



A University of Sussex DPhil thesis

Available online via Sussex Research Online:

<http://sro.sussex.ac.uk/>

This thesis is protected by copyright which belongs to the author.

This thesis cannot be reproduced or quoted extensively from without first obtaining permission in writing from the Author

The content must not be changed in any way or sold commercially in any format or medium without the formal permission of the Author

When referring to this work, full bibliographic details including the author, title, awarding institution and date of the thesis must be given

Please visit Sussex Research Online for more information and further details



University of Sussex

**Supersymmetry searches in events with
at least four leptons using the ATLAS
detector at the Large Hadron Collider**

Zara Grout

Declaration

I hereby declare that this thesis has not been and will not be submitted in whole or in part to another University for the award of any other degree.

Signature:

Zara Grout

UNIVERSITY OF SUSSEX

ZARA GROUT, DOCTOR OF PHILOSOPHY

SUPERSYMMETRY SEARCHES IN EVENTS WITH AT LEAST FOUR LEPTONS
USING THE ATLAS DETECTOR AT THE LARGE HADRON COLLIDER

SUMMARY

This thesis presents a search for supersymmetry using the dataset taken by ATLAS at the Large Hadron Collider with $\sqrt{s} = 8$ TeV during 2012. Events with four or more leptons are selected and required to satisfy additional kinematic criteria that define optimised signal regions. These criteria are chosen to reject the majority of events produced by Standard Model processes, whilst retaining a large fraction of events produced by a variety of proposed supersymmetry scenarios. The expected number of Standard Model events are estimated using a combination of Monte Carlo and data-driven methods, the predictions of which are tested against data in specifically designed validation regions. No significant deviations from the Standard Model estimations are observed within statistical and systematic uncertainties. Exclusion limits are then set at 95% confidence level (CL) on a wide range of R-parity conserving and R-parity violating supersymmetry simplified models, as well as models of general gauge mediated supersymmetry. In R-parity violating models, 95% CL exclusion limits of 1350 GeV and 750 GeV are set on the masses of gluinos and charginos respectively. Exclusion limits are also set at 95% CL up to 620 GeV on the mass of heavy neutralinos for an R-parity conserving scenario with decays via right-handed sleptons. Results are also presented for the combination of the four lepton analysis with another lepton-rich supersymmetry search.

Acknowledgements

There are many people who have contributed to me reaching the endpoint of my PhD, and I would like to acknowledge their help as best I can. Firstly I would like to thank my supervisor Antonella De Santo, who has provided guidance, encouragement and support throughout the last three and a half years without fail. My second supervisor Fabrizio Salvatore has also been a constant friendly presence and a pleasure to work with. Tina Potter was there from the beginning to provide answers to any questions I could think of, and solutions to many problems. A wealth of information was passed on to me from Mark Sutton.

The ATLAS group at the University of Sussex has grown to such an extent since the beginning of my PhD that I can no longer name everyone here, but I would like to thank them all for making it such a friendly and fun place to work. I will however give special thanks to Nicky Santoyo, Yusufu Shehu, and the newest ATLAS students Nicola, Olly, Giuseppe and Fab, as well as Stewart-Martin Haugh and Dan Gibbon, both of whom have since moved on from the group. The other EPP members Ed, James Sinclair, James Waterfield, Luke, Tristan and Mark have also made Sussex a great place to be.

The ATLAS four lepton analysis group was a wonderful community to work within, and I would like to thank Mike Flowerdew, Estel Perez, Lukas Marti and Max Goblirsch, and also Basil Schneider. There were many other ATLAS members who have helped me with many things over the years. I met too many great people during my time at CERN to name them all, but I would like to thank everyone who shared a coffee or beer when they were needed. I would also like to mention my CERN office mates Josh and Ian who were the source of answers to many questions.

I am very grateful to both of my parents, for always encouraging me to try and achieve whatever I wanted to.

Finally I would like to thank Dave, I could not have done it without him.

Contents

List of Tables	x
List of Figures	xiii
1 Introduction	1
2 The Standard Model of Particle Physics and Beyond	2
2.1 Introduction	2
2.2 Particle Content of the SM	3
2.3 Forces	5
2.3.1 Quantum Electrodynamics	6
2.3.2 Electroweak Unification and Symmetry Breaking	6
2.3.3 Quantum Chromodynamics	9
2.4 Problems with the Standard Model	10
2.5 Introduction to Supersymmetry and the MSSM	11
2.6 Soft Supersymmetry Breaking	14
2.7 MSSM Mass Spectrum	15
2.8 R-parity	17
2.9 Simplified Models	18
2.10 Status of Supersymmetry	19
3 The ATLAS Detector at the LHC	21
3.1 The Large Hadron Collider	21
3.2 The ATLAS Detector	23
3.3 ATLAS detector geometry and nomenclature	24
3.4 Magnet System	26
3.5 Inner Detector	26
3.5.1 Pixel Detector	27

3.5.2	Semiconductor Tracker	27
3.5.3	Transition Radiation Tracker	28
3.6	Calorimeters	29
3.6.1	Electromagnetic Calorimeter	30
3.6.2	Hadronic Calorimeter	32
3.7	Muon Spectrometer	33
3.8	Trigger and Data Acquisition System in Run 1	35
3.8.1	Level 1 Trigger	35
3.8.2	High Level Trigger	37
3.8.3	Trigger Chains, Streams and Menus	37
4	Generation, Simulation and Reconstruction of ATLAS Data	39
4.1	Event Generation	41
4.1.1	Parton Distribution Functions	42
4.1.2	Matrix Element	43
4.1.3	Parton Showers	44
4.1.4	Hadronisation	44
4.1.5	Underlying Event	44
4.2	Simulation	44
4.3	Digitisation	45
4.4	Reconstruction	46
4.4.1	Inner Detector Tracks	46
4.4.2	Vertices	47
4.4.3	Electron Reconstruction and Identification	48
4.4.4	Muon Reconstruction and Identification	49
4.4.5	Jet Reconstruction	50
4.4.6	Tau Reconstruction and Identification	51
4.4.7	Missing Transverse Energy	53
4.5	Object Selection	53
4.5.1	Baseline Electron/Muon Selection	54
4.5.2	Baseline Jet Selection	54
4.5.3	Baseline Tau Selection	54
4.5.4	Overlap Removal	55
4.5.5	Signal Electron Selection	56
4.5.6	Signal Muon Selection	57

4.5.7	Signal Jet Selection	57
4.5.8	Signal Tau Selection	58
5	Search for SUSY in Events with Four or More Leptons	59
5.1	Analysis Overview	60
5.2	Supersymmetry Signal Scenarios	60
5.2.1	$\tilde{\chi}_2^0 \tilde{\chi}_3^0$ Simplified Models	60
5.2.2	R-parity Violating Simplified Models	62
5.2.3	General Gauge Mediated Simplified Models	64
5.2.4	Signal MC Samples	65
5.3	Dataset and Event Selection	66
5.3.1	Trigger	67
5.3.2	Event Cleaning	67
5.3.3	Standard Model Background Samples	68
5.4	Signal Region Optimisation	69
5.4.1	Optimisation procedure	71
5.4.2	Z Boson Veto	72
5.4.3	Z Boson Selection	86
5.5	Signal Region Summary	88
6	Background Estimation and Systematic Uncertainties	99
6.1	Introduction	99
6.2	Weighting Method	103
6.2.1	Derivation and methodology	103
6.2.2	Required Components for Weighted Average Fake Ratios	105
6.3	Systematic Uncertainties	106
6.3.1	Irreducible Background	106
6.3.2	Reducible Background	110
6.3.3	Signal Systematic Uncertainties	111
6.3.4	Summary	112
6.4	Validating the Background Estimation	117
7	Results and Interpretation	123
7.1	Signal Region Results	123
7.2	Statistical Interpretation of Results	131
7.2.1	The CL_S Method	131

7.2.2	Combination of Signal Regions	133
7.2.3	Model-independent Limits	134
7.2.4	Limits on Supersymmetry Scenarios	134
7.3	Result Re-interpretations and Combinations with the Three Lepton Analysis	142
7.3.1	Introduction	142
7.3.2	Overview of Three Lepton Analysis	142
7.3.3	Combination in the $\tilde{\chi}_2^0\tilde{\chi}_3^0$ via Slepton Scenario	144
7.3.4	Combination in the GGM Scenario	148
7.3.5	Varying the Intermediate Slepton Mass	151
8	Conclusions	154
A	Inner Detector Tracking Performance	156
A.1	Introduction	156
A.2	Methodology	157
A.3	One-prong Tau Performance	157
B	Generation and Properties of $\tilde{\chi}_2^0\tilde{\chi}_3^0$ Grids	162
B.1	Introduction	162
B.2	Sample Generation	163
B.3	Properties of the $\tilde{\chi}_2^0\tilde{\chi}_3^0$ Grids	165
C	Systematic Uncertainties in the Signal Regions	171
	Bibliography	181

List of Tables

2.1	SM lepton properties.	4
2.2	SM quark properties.	4
2.3	SM gauge boson properties.	5
2.4	MSSM chiral supermultiplet particle content.	14
2.5	MSSM gauge supermultiplet particle content.	14
2.6	Free parameters introduced by SUSY breaking.	15
2.7	Mass eigenstates of the MSSM.	16
4.1	Baseline object selection.	55
4.2	Overlap removal summary.	56
4.3	Signal object selection.	58
5.1	$\tilde{\chi}_2^0 \tilde{\chi}_3^0$ mass ranges.	62
5.2	RPV λ_{ijk} couplings.	64
5.3	RPV mass ranges.	65
5.4	Analysis light lepton trigger chains.	68
5.5	Background datasets.	70
5.6	Signal region summary.	71
5.7	Signal region definitions.	89
5.8	MC event numbers in $4\ell 0\tau$ SRs for background and benchmark signal points.	96
5.9	MC event numbers in $3\ell 1\tau$ SRs for background and benchmark signal points.	97
5.10	MC event numbers in $2\ell 2\tau$ SRs for background and benchmark signal points.	98
6.1	Estimated background events in all SRs with statistical and systematic uncertainties.	117
6.2	Validation region summary.	118
6.3	Expected and observed events in all VRs.	121

7.1	Expected and observed events in all SRs.	125
7.2	Model-independent limits in all SRs.	135
7.3	Three lepton SR summary.	143
7.4	Observed and expected CL_S values for the $\tilde{\chi}_2^0\tilde{\chi}_3^0$ via slepton signal points with varying slepton mass.	152
B.1	Signal systematic uncertainties on the $\tilde{\chi}_2^0\tilde{\chi}_3^0$ stau points.	165
B.2	Properties of $\tilde{\chi}_2^0\tilde{\chi}_3^0$ via Z decays.	166
C.1	Systematics Summary SR0noZa.	172
C.2	Systematics Summary SR0noZb.	173
C.3	Systematics Summary SR0Z.	174
C.4	Systematics Summary SR1noZa.	175
C.5	Systematics Summary SR1noZb.	176
C.6	Systematics Summary SR1Z.	177
C.7	Systematics Summary SR2noZa.	178
C.8	Systematics Summary SR2noZb.	179
C.9	Systematics Summary SR2Z.	180

List of Figures

2.1	Higgs Potential.	8
2.2	Running of the gauge couplings.	13
2.3	Proton decay.	17
3.1	LHC layout.	22
3.2	LHC luminosity in 2011 and 2012.	23
3.3	Pile-up in 2011 and 2012.	24
3.4	ATLAS detector schematic.	25
3.5	ATLAS magnet system schematic.	27
3.6	Inner Detector schematic.	28
3.7	Cut-away of calorimeters.	29
3.8	Calorimeter thicknesses in radiation and nuclear interaction lengths.	31
3.9	ECAL module accordion diagram.	32
3.10	Muon cut-away	34
3.11	Trigger Flow-Chart.	36
4.1	MC simulation flow diagram.	40
4.2	Example of a DIS process.	41
4.3	HERAPDF1.0 PDFs for gluons, sea and valence quarks at $Q^2 = 10 \text{ GeV}^2$	43
4.4	Electron ID efficiency as a function of pile-up.	49
4.5	Muon reconstruction efficiency as a function of η	50
4.6	Signal tau selection efficiency as a function of p_T	52
5.1	$\tilde{\chi}_2^0 \tilde{\chi}_3^0$ Feynman diagrams.	61
5.2	RPV Feynman diagrams.	63
5.3	RPV $\tilde{\chi}_1^0$ decays.	64
5.4	GGM Feynman diagrams.	66
5.5	Radiative Z boson decay.	72

5.6	Invariant mass of lepton combinations in $4\ell 0\tau$ channel.	74
5.7	E_T^{miss} and Z_N vs E_T^{miss} distributions for $4\ell 0\tau$ N2N3 events.	75
5.8	E_T^{miss} or m_{eff} and Z_N vs E_T^{miss} or m_{eff} distributions for $4\ell 0\tau$ RPV events.	77
5.9	Invariant mass of lepton combinations in $3\ell 1\tau$ events.	79
5.10	E_T^{miss} and Z_N vs E_T^{miss} distributions for three light lepton one tau N2N3 events.	80
5.11	E_T^{miss} or m_{eff} and Z_N vs E_T^{miss} or m_{eff} distributions for three light lepton one tau RPV events.	82
5.12	Invariant mass of SFOS lepton pairs in $2\ell 2\tau$ channel.	83
5.13	E_T^{miss} and Z_N vs E_T^{miss} distributions for two light lepton two tau N2N3 events.	84
5.14	E_T^{miss} or m_{eff} and Z_N vs E_T^{miss} or m_{eff} distributions for two light lepton two tau RPV events.	85
5.15	Invariant mass for $4\ell 0\tau$ Z-rich events.	87
5.16	E_T^{miss} and Z_N vs E_T^{miss} distributions for four light lepton Z-rich events.	87
5.17	E_T^{miss} distributions for $3\ell 1\tau/2\ell 2\tau$ events with a Z-selection.	88
5.18	Significance Z_N for $4\ell 0\tau$ SRs.	90
5.19	Significance Z_N for $3\ell 1\tau$ SRs.	93
5.20	Significance Z_N for $2\ell 2\tau$ SRs.	95
6.1	Lepton origin in Z-veto regions.	100
6.2	Lepton origin in Z-selection regions.	101
6.3	Systematics summary in $4\ell 0\tau$ regions.	114
6.4	Systematics summary in $3\ell 1\tau$ regions.	115
6.5	Systematics summary in $2\ell 2\tau$ regions.	116
6.6	Distributions in VR0Z and VR2Z.	120
7.1	Distributions in $4\ell 0\tau$ SRs.	126
7.2	Distributions in $3\ell 1\tau$ SRs.	128
7.3	Distributions in $2\ell 2\tau$ SRs.	130
7.4	Exclusion limits on the RPV signal grids.	139
7.5	Exclusion limits on the N2N3 signal grids.	140
7.6	Exclusion limits on the GGM signal grids.	141
7.7	Combined exclusion limits on the N2N3 slepton signal grid.	146
7.8	Combined expected and observed CL_s values on the N2N3 slepton signal grid.	147

7.9	Combined exclusion limits on the GGM $\tan\beta = 30$ signal grid.	149
7.10	Combined expected and observed CL_S values on the GGM $\tan\beta = 30$ signal grid.	150
7.11	Cross-section limits on the $\tilde{\chi}_2^0\tilde{\chi}_3^0$ via slepton signal points with varying slepton mass.	153
A.1	Tau tracking efficiencies as a function of $\langle\mu\rangle$	159
A.2	Tau tracking efficiencies as a function of η and p_T	160
A.3	Tau tracking efficiencies as a function of ϕ	161
B.1	Cross-section of $\tilde{\chi}_2^0\tilde{\chi}_3^0$ via slepton and stau decay.	167
B.2	Acceptance of $\tilde{\chi}_2^0\tilde{\chi}_3^0$ via slepton and stau decay.	168
B.3	Efficiency of $\tilde{\chi}_2^0\tilde{\chi}_3^0$ via slepton and stau decay.	169
B.4	Uncertainty on $\tilde{\chi}_2^0\tilde{\chi}_3^0$ via slepton and stau decay.	170

Chapter 1

Introduction

The content of this thesis is taken from work carried out during the 3.5 years of my time undertaking a PhD on the ATLAS experiment at the Large Hadron Collider. The detailed analysis considers a search for supersymmetry using events containing four or more electrons, muons or taus, from the ATLAS dataset taken in 2012. The results from this analysis were made public in the Physical Review D journal in May 2014 [1]. Chapter 2 provides an overview of particle physics theory as it stands, the questions which remain unanswered, and an introduction to supersymmetry as an extension of the current model. Details of the Large Hadron Collider and the ATLAS detector used for producing and detecting the high energy data used by this analysis are included in Chapter 3. Chapter 4 then discusses the software required to process data collected at ATLAS, and to produce simulated events. The four lepton analysis is introduced in Chapter 5, including the dataset and simulated samples used, signal scenarios considered and the signal region optimisation. Chapter 6 discusses the background estimation and systematic uncertainties. The results of this analysis are then presented in Chapter 7, along with the results produced by combining these with the results from a trilepton supersymmetry analysis, and modifying some of the considered scenarios.

Chapter 2

The Standard Model of Particle Physics and Beyond

2.1 Introduction

The Standard Model (SM) of particle physics has remained the preferred theoretical model since its conception during the 1960's and 70's [2]. It is a gauge invariant quantum field theory with symmetry group $SU(3)_C \otimes SU(2)_L \otimes U(1)_Y$ which describes interactions of three of the four fundamental forces (weak, electromagnetic (EM), and strong). Symmetries are key to the SM, and are described mathematically by group theory. Each symmetry has a conserved property associated with it, as stated by Noether's theorem [3]. These symmetries can also be broken in nature, which leads to violation of conservation laws, and changes to the involved gauge fields.

The SM predicts many measurable quantities which have been well experimentally verified, and has predicted the existence of particles prior to their discovery, for example the W boson, Z boson and τ lepton. Most recently the Higgs Boson was discovered at the Large Hadron Collider (LHC) in 2012 [4,5], completing the observation of all particles expected by the SM. However, the description does not extend well to the higher energy regime. In particular, infinite divergences are introduced when considering the Higgs couplings which cannot be explained by the model, and suggest that some higher energy physics needs to be involved. There are other known problems with the SM: there is no known way to include the gravitational force, the values of the particle masses are not explained, and phenomena have been observed which are not consistent with the model as it stands.

A range of theories have been developed in the last few decades which approximate

the SM in the low energy regime, while extending it to higher energy regimes to explain some of these flaws. The most popular of these is *supersymmetry*, which postulates an additional symmetry resulting in a set of particles and associated new physics at higher energies [6]. These particles are more massive than those present in the SM, and so require higher energies in order to be produced at collider experiments and observed. The topic of this thesis is a search for evidence of these massive supersymmetric particles. This chapter will provide a brief overview of the SM, highlighting the areas where the description is incomplete. There will then be a general discussion of supersymmetry, including some specific formulations which are relevant to this analysis.

2.2 Particle Content of the SM

The particles present within the SM can be divided into two groups based on the values of their spin. Fermions have half-integer spin values, and comprise the matter component of the model, whilst bosons have integer-spin values. So-called gauge bosons form a subset of these with spin=1 and are *mediators* of the fundamental forces described. The fermions can be further subdivided into two groups of fundamental particles called quarks and leptons. These are both classified into three families or generations, consisting of SU(2) doublets. The masses of the particles in each family get progressively heavier. The three lepton families of electron e , muon μ , and tau τ , have doublets comprised of an electrically neutral neutrino ν and a charged lepton of the same flavour:

$$\begin{pmatrix} \nu_e \\ e^- \end{pmatrix}, \begin{pmatrix} \nu_\mu \\ \mu^- \end{pmatrix}, \begin{pmatrix} \nu_\tau \\ \tau^- \end{pmatrix}.$$

The properties of the leptons are summarised in Table 2.1. Each generation possesses a characteristic quantum number designated the electron (L_e), muon (L_μ), and tau (L_τ) lepton numbers.

The six quarks present in the SM are also arranged into SU(2) doublets of three families:

$$\begin{pmatrix} u \\ d \end{pmatrix}, \begin{pmatrix} c \\ s \end{pmatrix}, \begin{pmatrix} t \\ b \end{pmatrix}.$$

Some of the properties of these are summarised in Table 2.2. They have fractional electric charges of $\frac{2}{3}$ for the ‘‘up-type’’ quarks and $-\frac{1}{3}$ for the ‘‘down-type’’ quarks. These occupy the top and bottom positions in the doublets displayed above, respectively. All quarks possess an additional property, known as colour charge, which can have three different

Table 2.1: Some properties of the three generations of leptons present within the Standard Model [7].

Particle	Charge	Mass [MeV]	L_e	L_μ	L_τ
ν_e	0	$<2.25 \times 10^{-7}$	1	0	0
e^-	-1	0.51	1	0	0
ν_μ	0	$<0.19 \times 10^{-7}$	0	1	0
μ^-	-1	105.66	0	1	0
ν_τ	0	$<18.2 \times 10^{-7}$	0	0	1
τ^-	-1	1776.82	0	0	1

values labelled as “red”, “green” and “blue”. Due to *confinement*, which will be discussed in more detail in Section 2.3.3, quarks do not exist in isolation, and instead group together to form *hadrons*. A hadron containing three quarks is referred to as a baryon, and common examples are protons and neutrons. The quantum number listed in the final column of Table 2.2, known as the baryon number, will always be one for baryonic bound states.

Table 2.2: Some properties of the three generations of quarks present within the Standard Model [7].

Particle	Charge	Mass [MeV]	Baryon number
Down (d)	$-\frac{1}{3}$	4.8	$\frac{1}{3}$
Up (u)	$\frac{2}{3}$	2.3	$\frac{1}{3}$
Strange (s)	$-\frac{1}{3}$	95	$\frac{1}{3}$
Charm (c)	$\frac{2}{3}$	1275	$\frac{1}{3}$
Bottom (b)	$-\frac{1}{3}$	4180	$\frac{1}{3}$
Top (t)	$\frac{2}{3}$	173070	$\frac{1}{3}$

The properties of the integer-spin vector bosons present in the SM are summarised in Table 2.3. The photon is a massless, electrically neutral gauge boson which mediates electromagnetic (EM) interactions. Three massive bosons mediate the weak force, the charged W^+ and W^- bosons and the electrically neutral Z^0 boson. The mediator of the strong force, the gluon, is massless and electrically neutral, but carries colour charge. These bosons all have spin values of 1. A spin 2 mediator of gravity, the *graviton*, has also been proposed, although this has not yet been verified experimentally so is not included here [8].

Table 2.3: Some properties of the gauge bosons present in the SM and the forces which they mediate [7].

Gauge Boson	Mass [GeV]	Charge	Spin	Force
Photon γ	0	0	1	Electromagnetic
W^\pm	80.39	± 1	1	Weak
Z	91.19	0	1	
Gluon g	0	0	1	Strong

The SM also contains a scalar boson referred to as the Higgs boson, which has been very recently experimentally verified at the LHC [4, 5]. It is electrically neutral, with a spin value of 0 and mass of approximately 126 GeV [4, 5]. It is also a complex SU(2) doublet in the SM, which is key to generating fermion masses within the theory. This will be discussed in much more detail in Section 2.3.2.

The Dirac equation predicts an *antiparticle* for each particle [9], with identical mass and spin but opposite charge. The charged leptons each have an antiparticle with negative charge, denoted e^+ , μ^+ and τ^+ . This has not been experimentally validated for the neutrinos, and the theory that they could be their own antiparticles was proposed by Majorana in 1937 [10]. Anti-quarks not only have opposite electrical charge to their standard counterparts but also opposite colour charge, which is labelled as anti-red, anti-blue and anti-green.

2.3 Forces

The fermionic particles in the SM interact via the EM, weak and strong forces. These interactions are mediated by the bosonic particles, as has already been discussed. The EM force is associated with electric charge, and therefore affects the charged leptons and quarks but not the neutrinos which are electrically neutral. The weak force is related to particle *chirality* or handedness, and only the left-handed components of particles feel this interaction. The lepton and quark doublets which have been previously discussed are actually comprised of the left-handed components of the included particles. These are accompanied by the right-handed singlets: e_R^- , μ_R^- , τ_R^- ; and u_R , d_R , s_R , c_R , b_R , and t_R ; in the lepton and quark sectors respectively. Neutrinos have only ever been observed to have a left-handed component (and only a right-handed component in the case of anti-neutrinos). The selective action of the weak force on only left-handed particles violates

parity conservation, which is otherwise conserved within the SM. Quark states interacting via the weak force are mixtures of the mass eigenstates of the SM, defined by the CKM mixing matrix [11]. The strong force involves interactions between particles with colour charge, i.e. the quarks and the strong mediator, the gluon.

These interactions are described by the component gauge symmetries of the SM. Quantum electrodynamics (QED) provides an effective description of the EM force, and has displayed predictive power to a very high precision. The mathematical formulation will be covered in Section 2.3.1. The weak force, however, cannot be explained consistently with similar methods, and requires unification with the EM force, which will be discussed in Section 2.3.2. Finally, the strong interaction is described almost entirely independently with quantum chromodynamics (QCD), and does not unify with the other forces within the remit of the SM. QCD is discussed in Section 2.3.3.

2.3.1 Quantum Electrodynamics

QED was the first quantum field theory to be developed [12–14], and is invariant under the unitary gauge group $U(1)_Q$ [15]. The associated conserved quantity is the electric charge. An interaction between a charged spin- $\frac{1}{2}$ field Ψ with mass m and the EM field is described by the Lagrangian:

$$\mathcal{L} = -\frac{1}{4}F_{\mu\nu}F^{\mu\nu} + \bar{\Psi}(i\gamma^\mu D_\mu - m)\Psi. \quad (2.1)$$

The electromagnetic field tensor $F_{\mu\nu}$ [3] is defined in terms of the covariant four-potential of the EM field A_μ as:

$$F_{\mu\nu} = \partial_\mu A_\nu - \partial_\nu A_\mu, \quad (2.2)$$

where ∂_μ is the partial derivative $\frac{\partial}{\partial x_\mu}$. The gauge covariant derivative D_μ is defined as:

$$D_\mu = \partial_\mu + iqA_\mu, \quad (2.3)$$

where q is the electric charge of the spin- $\frac{1}{2}$ field. The $U(1)$ group is Abelian, meaning that the *generators* of the group all commute. The physical consequence of this is the electrical neutrality of the photon, and the fact that it does not self-interact. This is not the case for all of the fundamental forces in the SM.

2.3.2 Electroweak Unification and Symmetry Breaking

Formulating an equivalent description to QED for the weak interaction is problematic. The force has a short range (approximately 10^{-17} m) [2] which means it must be mediated by

massive gauge bosons (now known to be the W^\pm and Z). Theories which included these massive gauge bosons were formulated [16] but these are all plagued by a lack of gauge invariance or renormalisability. This led to theorists considering a gauge invariance which was hidden, due to the associated symmetry being broken above the observable energy scale (at the order of 100 GeV). This hidden gauge is of the group $SU(2)_L \otimes U(1)_Y$, and corresponds to the unification of the EM and weak interactions. The specific formulation of the breaking mechanism was proposed in the form of a scalar field which falls into a *vacuum expectation value* (VEV) below a certain energy threshold, spontaneously breaking the hidden gauge invariance [17–19]. This results in the only remaining gauge invariance at the observable energy scale being that which is seen in QED.

A mathematical description of unified electroweak interactions was first developed by Glashow [20], Salam [21] and Weinberg [22] in the 1960's. The generators of the $SU(2)$ and $U(1)$ components of the gauge theory are the third component of the weak isospin T^3 and the weak hypercharge Y . The isospin is related to chirality. The left-handed $SU(2)$ doublets which were introduced in Section 2.2 each contain a component with $T^3 = 1/2$ (the up-type quarks and the neutrinos) and a component with $T^3 = -1/2$ (the down-type quarks and the charged leptons). The right-handed $SU(2)$ singlets all have a T^3 value of zero, resulting in them not coupling to the weak force. The weak isospin and weak hypercharge generators are related to the electric charge generator seen in QED by the Gell-Mann-Nishijima formula [23, 24]:

$$Q = T^3 + \frac{1}{2}Y. \quad (2.4)$$

Three gauge fields W_μ^a ($a=1,2,3$) correspond to the exchange of T^3 , and have values of +1, 0 and -1. A fourth relates to the exchange of hypercharge, and is denoted B^0 . At this point, all of the gauge fields are massless.

The Higgs field is introduced as a complex scalar doublet, which will transform under $SU(2)_L$ as a $T^3 = 1/2$ doublet and has four real components, and hence four degrees of freedom. It has a potential (see Figure 2.1) with a non-zero vacuum expectation value (VEV) which forms a circular trough in the complex plane. Any point within this trough will be a minimum. The symmetry breaking is visualised by the arrow, which shows a movement from the centre of the potential where the symmetry is unbroken to a randomly chosen point in the minimum where this symmetry is no longer visible. The selection of a “direction” in which to reach the VEV breaks the symmetry. The interaction of the Higgs field at this VEV with the $SU(2)_W \otimes U(1)_Y$ gauge fields creates *screening currents* which result in the three W_μ^a fields acquiring mass. The fourth $SU(2)_W \otimes U(1)_Y$ gauge

field B^0 remains massless. In the process, the Higgs field is reduced to a spinless scalar, corresponding to a massive Higgs boson particle.

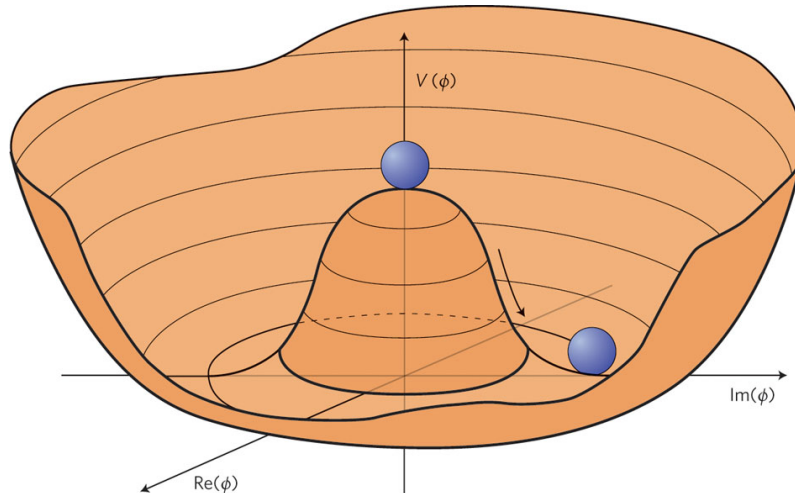


Figure 2.1: Higgs potential $V(\phi)$ in the complex plane. The vacuum corresponds to a randomly chosen point within the potential minimum, the movement from the centre of the potential to this point corresponds to a massive scalar Higgs boson. [25].

The W_μ^a and B^0 do not directly correspond to the charged W^\pm , Z^0 and photon gauge fields. Instead these are comprised of mixtures of the four given by:

$$W_\mu^\pm = \frac{W_\mu^1 \mp iW_\mu^2}{\sqrt{2}}, \quad (2.5)$$

$$Z_\mu = W_\mu^3 \cos\theta_W - B_\mu \sin\theta_W, \quad (2.6)$$

and

$$A_\mu = W_\mu^3 \sin\theta_W + B_\mu \cos\theta_W. \quad (2.7)$$

The variable θ_W is called the *Glashow-Weinberg angle* and relates the coupling constants of the weak and EM interactions. This can be used to relate the masses of the W and Z bosons:

$$M_Z = \frac{M_W}{\cos\theta_W}. \quad (2.8)$$

The inclusion of a B_μ component in the Z_μ field allows it to also couple to right-handed particles as observed in experiment, unlike the W^\pm fields. The fermions do not gain masses in the act of electroweak symmetry breaking but afterwards due to interactions with the Higgs boson.

2.3.3 Quantum Chromodynamics

Each quark in the SM has three associated fields corresponding to the different flavour states of red, green and blue. Quarks can be described as colour triplets e.g.

$$\mathbf{q} = \begin{pmatrix} q_r \\ q_g \\ q_b \end{pmatrix}.$$

These triplets are invariant under $SU(3)_c$ transformations, which describe strong interactions. There are eight generators associated with this group, which correspond to eight real and independent gluon gauge fields, each of which is defined by a linear combination of colour and anti-colour states. The group is non-Abelian, so these generators do not commute, corresponding to interaction terms between the gluons. The Lagrangian density of the strong force is defined as:

$$\mathcal{L} = -\frac{1}{4} \sum_{a=1}^8 G_{\mu\nu}^a G^{a\mu\nu} + \sum_{f=1}^6 [\bar{\mathbf{q}}_f i\gamma^\mu (\partial_\mu + ig\mathbf{G}_\mu)\mathbf{q}_f - m_f \bar{\mathbf{q}}_f \mathbf{q}_f], \quad (2.9)$$

where

$$\mathbf{G}_\mu = \frac{1}{2} \sum_{a=1}^8 G_\mu^a \lambda_a, \quad (2.10)$$

is a sum over all the gluon states and λ_a - the *Gell-Mann matrices*. The index f refers to the quark flavours, and \mathbf{q} are quark colour triplet states.

The coupling of strong interactions increases with increasing distance, corresponding to decreasing energy, and is smaller at short range, which corresponds to high energy. This is due to the gluon self-interaction loop processes and has two main consequences. It has already been mentioned that quarks can form bound states, but in fact it is impossible for them to remain “bare” and unbound in order to be observed. This is also the case for gluons. As the distance between them increases, it becomes more energetically favourable for the quarks to create a bound state with additional quarks than it is for them to remain free. This is referred to as *confinement* and results in coloured particles at collider experiments being observed as “jets” - sprays of hadronic particles which have formed in the detector. In addition to the baryons mentioned in Section 2.2 that consist of three bound quarks, they can also form mesons, which are quark anti-quark pairs. These are both colour-neutral states that can then be observed. The second consequence is that at higher energy the strong interaction is weaker (referred to as *asymptotic freedom*), which allows it to be calculated perturbatively, whereas at lower energy it cannot be.

2.4 Problems with the Standard Model

It was discussed in Section 2.3.2 that the fermion masses can be produced from coupling terms with the Higgs boson. However, the Higgs mass squared term receives corrections for each of these couplings due to additional higher order loops. The term due to fermionic loop coupling would be given by:

$$\Delta m_H^2 = -\frac{|\lambda_f|^2}{8\pi^2}\Lambda_{UV}^2 + \dots, \quad (2.11)$$

where additional higher order terms have been ignored in this case. $|\lambda_f|$ is the coupling between the fermionic and Higgs fields and Λ_{UV} is the ultraviolet momentum cut-off that has been selected as the cut-off value for the loop integral. This cut-off choice is required to correspond to the energy scale at which any new higher energy physics processes occur. The Higgs mass is therefore sensitive to the highest energy scale of a given theory and can be subject to quadratically divergent corrections, causing an infinite Higgs mass squared parameter.

New physics in the high energy regime is expected partly due to the difference in energy of sixteen orders of magnitude between electroweak theory and the Planck scale M_P [7]. This scale is the energy at which a quantum field theory description of gravity becomes possible. Not only is some extension or modification required in order to explain the relationship between the $SU(3)_c \otimes SU(2)_L \otimes U(1)_Y$ and gravity, but it is expected to be at a much higher energy. In fact as it stands, the EM and weak forces unify at around 100 GeV, but although the strong force coupling approaches that of the electroweak coupling in the SM, there is no further unification of these forces.

It was discussed earlier that the neutrinos do not have couplings to the Higgs boson as they lack a right-handed component, and they therefore have no mechanism for obtaining mass within the SM. However, the observation of the phenomenon of neutrino *oscillation* [26] suggests that they must have non-zero masses. Neutrinos produced with a given flavour were observed with a different flavour after propagating some distance. This can be explained by each of the flavour eigenstates being a superposition of the mass eigenstates. The phases of the three mass states propagate at different rates due to differences in the masses of the three neutrinos ν_e , ν_μ and ν_τ . This leads to the mass eigenstate mixture changing with distance travelled, and eventually this will correspond to a different flavour eigenstate or neutrino. Some extension is required in order to explain the origin of the neutrino masses.

Discrepancies in the expected and observed gravitational effects on large-scale astro-

nomical objects, for example the rotation curves of galaxies [27] and the gravitational lensing of galaxy clusters, most famously the *bullet cluster* [28], led to the postulation of *dark matter*. The velocity of matter within galaxies is predicted to decrease with distance from the galaxy centre, as the density of matter decreases. This was not consistent with measurements showing the velocity remaining relatively constant with distance, despite there being less observable matter in the outer regions of the galaxy. This suggested that something must be contributing additional mass in these regions, but which was not comprised of normal matter. The same conclusion can be reached when considering the gravitational lensing produced by gravitational clusters - the clusters do not contain sufficient observable matter to account for the expected mass. One of the most favoured theories for dark matter is that it consists of weakly interacting massive particles (WIMPs) whose presence would account for these observations. There is no candidate for these particles (or alternative DM candidates) within the SM as it stands, and it is widely accepted that some new physics is required to provide an explanation.

In addition to these issues, there are still a number of things which remain unexplained by the SM. The fermions are arranged into three generations, but there is no obvious cause behind this. The differences in mass between the fermions do not seem to follow any pattern, and the top quark is especially massive compared to all other fermions. There is also the problem referred to as *baryon asymmetry* [29]. The SM does not contain any mechanism which would explain the matter dominance of the universe, as matter and anti-matter would be expected to be produced in equal amounts during the Big Bang, which would result in everything annihilating. It has been postulated that this could be due to *CP violation*, allowing processes resulting in matter to occur more frequently than the corresponding antimatter processes. CP refers to the combined charge and parity, and it is expected that this combination will be conserved for interactions within the SM. As yet however this has not been confirmed experimentally to the degree which would be required for the level of asymmetry observed.

2.5 Introduction to Supersymmetry and the MSSM

Supersymmetry (SUSY) relates fermionic and bosonic particles, transforming between the two with a quantum operator Q :

$$Q|\text{boson}\rangle = |\text{fermion}\rangle, Q|\text{fermion}\rangle = |\text{boson}\rangle. \quad (2.12)$$

Each SM particle has a supersymmetric partner with a difference in spin of $\Delta s = \frac{1}{2}$, meaning SM fermions will have a bosonic superpartner and vice versa. The supersymmetric particles are referred to as *sparticles* and their symbols are identical to the SM convention but with an additional tilde. Each pair of partners is arranged in a *supermultiplet*, and due to their relation to the operator Q and its properties, the two components have identical masses and quantum numbers, with spin being the only exception.

There are two kinds of supermultiplet, the first is referred to as chiral or scalar, and the second is referred to as gauge or vector. Chiral supermultiplets contain a Weyl fermion and a complex scalar field, and they allow different transformations for right and left-handed components. All leptons and quarks are within chiral supermultiplets, and their superpartners are sleptons and squarks, where the “s” preceding the SM name stands for scalar. The sleptons and squarks participate in the same gauge interactions as their SM partners, e.g. the superpartners of the left-handed SM fermion components couple weakly, but the superpartners of the right-handed SM fermion components do not. The gauge supermultiplets contain a vector boson and two spin- $\frac{1}{2}$ fermions. All spin-1 bosons are arranged in gauge multiplets, and their superpartners, referred to as *gauginos*, are spin- $\frac{1}{2}$ fermions. The spin-0 Higgs boson has two supermultiplets containing sparticles with different weak isospin values, referred to as H_u and H_d . These are required to give mass to both the up-type and down-type sparticles. The supersymmetric Higgs partners are called the *Higgsinos*.

The introduction of these SUSY particles with $\Delta S = \frac{1}{2}$ compared to their SM partners naturally provides a solution to the hierarchy problem. The Higgs mass squared potential also receives corrections for the scalar partners of the SM fermions, of the form:

$$\Delta m_H^2 = -\frac{\lambda_S}{16\pi^2}[\Lambda_{UV}^2 - \dots]. \quad (2.13)$$

Each SM fermion has two complex scalar partners with a coupling of $\lambda_S = |\lambda_f|^2$ and a correction to the Higgs mass squared parameter as shown above. Comparing to Equation (2.11) which gives the correction of the SM fermion, one can see that the quadratically divergent term of an SM fermion is cancelled by its scalar superpartners. This is a strong motivation for theories of supersymmetry.

The Minimal Supersymmetric Standard Model (MSSM) is a supersymmetric extension to the SM which retains the $SU(3)_c \otimes SU(2)_L \otimes U(1)_Y$ and has minimal additional particle content. This additional particle content also has an effect on the “running of the gauge couplings” i.e. their strength as a function of momentum transfer. It was mentioned that one of the problems with the SM as it stands is the lack of unification of the strong

force with the electroweak, which can be seen by considering the running of the gauge couplings. These cross in the SM, but the strong coupling does not meet the others at the point where the electromagnetic and weak unify. Figure 2.2 shows the running of the

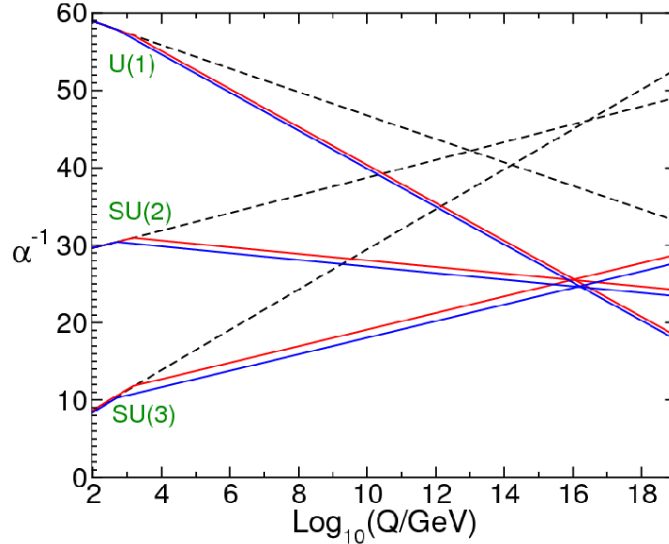


Figure 2.2: The running of the inverse gauge couplings of the strong, electromagnetic and weak interactions within the SM (dashed lines) and for the MSSM with two possible sparticle mass scales at 500 GeV and 1.5 TeV (red and blue solid lines) [6].

couplings for the SM and the MSSM, which has different coefficients due to the additional particles involved in the gauge interactions. This leads to the approximate unification of all three interaction coupling strengths, and although this could be “accidental” it can also be considered a strong indication that a grand unified theory (GUT) is attainable within a SUSY framework. Table 2.4 and Table 2.5 show the particle content of the MSSM arranged in the chiral and gauge supermultiplets respectively, along with some of their properties.

The equations used to describe the behaviour of quantum fields within the SM can be modified to describe the supermultiplets using *chiral superfields*. The *superpotential* - supersymmetric equivalent of the potential - which describes the general non-gauge interactions of the chiral supermultiplets within the MSSM can be defined as:

$$W_{MSSM} = \bar{u}Y_uQH_u - \bar{d}Y_dQH_d - \bar{e}Y_eLH_d + \mu H_uH_d \quad (2.14)$$

where Y_u , Y_d and Y_e are Yukawa couplings, and \bar{u} , Q , H_u , \bar{d} , H_d , \bar{e} and L are the chiral superfields corresponding to the supermultiplets described in Table 2.4 and Table 2.5.

Table 2.4: Particle content of the MSSM - chiral supermultiplets. The left-hand column gives the type of particle and the symbols used for the supermultiplets containing them. The second and third columns contain the spin-0 and spin- $\frac{1}{2}$ components of each of these supermultiplets. The first generation of the quarks and leptons are included as an example, and the other two generations follow the same convention.

Names		Spin-0	Spin- $\frac{1}{2}$
squarks, quarks ($\times 3$ families)	Q	$(\tilde{u}_L, \tilde{d}_L)$	(u_L, d_L)
	\bar{u}	\tilde{u}_R^*	u_R^\dagger
	\bar{d}	\tilde{d}_R^*	d_R^\dagger
sleptons, leptons ($\times 3$ families)	L	$(\tilde{\nu}, \tilde{e}_L)$	(ν, d_L)
	\bar{e}	\tilde{e}_R^*	e_R^\dagger
Higgs, higgsinos	H_u	(H_u^+, H_u^0)	$(\tilde{H}_u^+, \tilde{H}_u^0)$
	H_d	(H_d^0, H_d^-)	$(\tilde{H}_d^0, \tilde{H}_d^-)$

Table 2.5: Particle content of the MSSM - gauge supermultiplets. The left-hand column gives the name of the particles and the second and third columns contain the spin- $\frac{1}{2}$ and spin-1 components of each of the associated supermultiplets.

Names	Spin- $\frac{1}{2}$	Spin-1
gluino, gluon	\tilde{g}	g
winos, W bosons	$\tilde{W}^\pm, \tilde{W}^0$	W^\pm, W^0
bino, B bosons	\tilde{B}^0	B^0

2.6 Soft Supersymmetry Breaking

The fact that the supersymmetric particles have not been discovered at the mass scale of their SM partners indicates that these components of the supermultiplets are of a larger mass scale. If this is the case, then supersymmetry is not an exact symmetry, i.e. it is broken. The mechanism of symmetry breaking must be *soft* or *spontaneous* in order that the broken supersymmetry still provides a solution to the hierarchy problem. If the relationship between the fermionic and scalar couplings is altered, then the corrections to the Higgs mass squared parameter from SM fermions will not be cancelled by their SUSY partners correction terms. For the breaking mechanism to be spontaneous it must be analogous to the electroweak symmetry breaking discussed in Section 2.3.2, in that the symmetry is broken by a non-zero VEV. Many possible ways to incorporate this into SUSY

have been considered, all of them ultimately involve adding some new higher energy scale particles and interactions to the MSSM. This equates to adding terms to the Lagrangian which are gauge invariant and violate SUSY, but contain only masses and couplings with positive mass dimension. The total Lagrangian is defined as;

$$\mathcal{L} = \mathcal{L}_{\text{SUSY}} + \mathcal{L}_{\text{soft}}, \quad (2.15)$$

where all additional terms are contained within $\mathcal{L}_{\text{soft}}$, and the original SUSY invariant interaction terms are contained within $\mathcal{L}_{\text{SUSY}}$. This introduces a whole new set of parameters (around 100 of them, dependent of the method) into the theory, these are summarised in Table 2.6.

Table 2.6: Key free parameters introduced by soft supersymmetry breaking in the MSSM.

Parameters	Physical Meaning
M_1, M_2, M_3	Masses of the bino, wino and gluino.
$m_{\tilde{Q}_L}, m_{\tilde{u}_R}, m_{\tilde{d}_r}, m_{\tilde{L}_L}, m_{\tilde{e}_R}$	Masses of the left-handed squarks, up-type and down-type right-handed squarks, left-handed sleptons and right-handed sleptons.
$m_{H_u^2}, m_{H_d^2}, \mu , B$	Up and down-type higgsino mass squared parameters, the higgs-higgsino mass and the bilinear higgs term.
A_u, A_d, A_e	Up and down-type squark and sfermion Higgs interaction trilinear couplings.
$\tan\beta$	Ratio of the VEVs of the two higgs doublet fields.

The most successful mechanisms proposed for SUSY breaking involve extending the MSSM to couple to a separate *hidden sector* where supersymmetry breaking occurs. The effects of the SUSY breaking must then be communicated to the MSSM sector in some way. There are many possibilities for this, including gravity mediation [30, 31], gauge mediation [32–34], and extra-dimensional [35] or anomaly-mediation [36, 37]. This work considers some SUSY scenarios which specify gauge mediated SUSY breaking, where the *messenger fields* coupling the hidden sector to the MSSM sector are gauge fields.

2.7 MSSM Mass Spectrum

As with the gauge bosons in the SM, the gaugino masses are affected by electroweak symmetry breaking. The new mass terms which have been introduced in the $\mathcal{L}_{\text{soft}}$ mix to

form the mass eigenstates of the sparticles. The neutral winos \tilde{W}^0 , binos \tilde{B}^0 and higgsinos \tilde{H}^0 detailed in Tables 2.4 and 2.5 mix to form four neutral linear combinations called the *neutralinos*. These are denoted $\tilde{\chi}_1^0, \tilde{\chi}_2^0, \tilde{\chi}_3^0, \tilde{\chi}_4^0$ in increasing mass. The mixing can be represented by a matrix:

$$\begin{pmatrix} \tilde{\chi}_1^0 \\ \tilde{\chi}_2^0 \\ \tilde{\chi}_3^0 \\ \tilde{\chi}_4^0 \end{pmatrix} = \begin{pmatrix} M_1 & 0 & -c_\beta m_Z s_W & s_\beta m_Z s_W \\ 0 & M_2 & c_\beta m_Z c_W & -s_\beta m_Z c_W \\ -c_\beta m_Z s_W & c_\beta m_Z c_W & 0 & -\mu \\ s_\beta m_Z s_W & -s_\beta m_Z c_W & -\mu & 0 \end{pmatrix} \begin{pmatrix} \tilde{B}^0 \\ \tilde{W}^0 \\ \tilde{H}_u^0 \\ \tilde{H}_d^0 \end{pmatrix},$$

where c_β represents $\cos \beta$, s_β represents $\sin \beta$, c_W represents $\cos \theta_W$, and s_W represents $\sin \theta_W$. The charged winos \tilde{W}^\pm and charged higgsinos \tilde{H}^\pm mix to form two *charginos*, denoted as $\tilde{\chi}_1^\pm, \tilde{\chi}_2^\pm$, again in increasing mass. This mixing can be represented with the matrix:

$$\begin{pmatrix} \tilde{\chi}_1^\pm \\ \tilde{\chi}_2^\pm \end{pmatrix} = \begin{pmatrix} M_2 & \sqrt{2}M_W s_\beta \\ \sqrt{2}M_W c_\beta & \mu \end{pmatrix} \begin{pmatrix} \tilde{W}^\pm \\ \tilde{H}^\pm \end{pmatrix}.$$

The gluino does not mix with the other gauginos as it is a colour octet, and its mass is set by the parameter M_3 .

There is also mixing of the slepton and squark states due to electroweak symmetry breaking, although this is usually considered negligible with the exception of the third generation particles. The $\tilde{\tau}_L$ and $\tilde{\tau}_R$ states mix to give the mass eigenstates $\tilde{\tau}_1$ and $\tilde{\tau}_2$, the \tilde{b}_L and \tilde{b}_R states mix to give the mass eigenstates \tilde{b}_1 and \tilde{b}_2 and the \tilde{t}_L and \tilde{t}_R states mix to give the mass eigenstates \tilde{t}_1 and \tilde{t}_2 . It is conventional for the eigenstate with lower mass to have the lower index, as with the neutralinos and charginos. The Higgs sector is also affected, with five mass eigenstates arising. The resulting mass eigenstates which differ from the gauge eigenstates are given in Table 2.7.

Table 2.7: Mass eigenstates of the MSSM - only those which differ from the gauge eigenstates are listed.

Names	Gauge Eigenstates	Mass Eigenstates
Higgs	$H_u^0 H_d^0 H_u^+ H_d^-$	$h^0 H^0 A^0 H^\pm$
squarks	$\tilde{t}_L \tilde{t}_R \tilde{b}_L \tilde{b}_R$	$\tilde{t}_1 \tilde{t}_2 \tilde{b}_1 \tilde{b}_2$
sleptons	$\tilde{\tau}_L \tilde{\tau}_R \tilde{\nu}_\tau$	$\tilde{\tau}_1 \tilde{\tau}_2 \tilde{\nu}_\tau$
neutralinos	$\tilde{B}^0 \tilde{W}^0 \tilde{H}_u^0 \tilde{H}_d^0$	$\tilde{\chi}_1^0 \tilde{\chi}_2^0 \tilde{\chi}_3^0 \tilde{\chi}_4^0$
charginos	$\tilde{W}^\pm \tilde{H}_u^\pm \tilde{H}_d^\pm$	$\tilde{\chi}_1^\pm \tilde{\chi}_2^\pm$

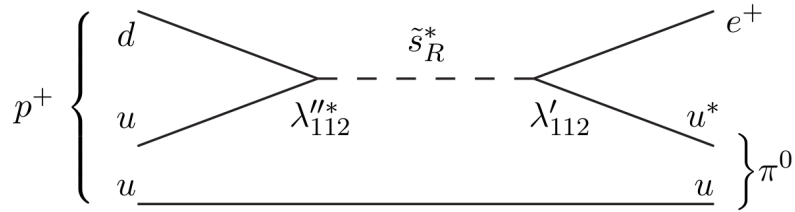


Figure 2.3: Decay of proton through a strange squark to produce an positron and a neutral pion. A violation of both $\Delta B = 1$ and $\Delta L = 1$ is required. Taken from [6].

2.8 R-parity

The superpotential given in Equation (2.14) is for the minimal SUSY extension to the SM, but there are additional terms which are gauge-invariant, which all violate lepton or baryon number by a unit of one, and have a superpotential term of:

$$W_{\text{RPV}} = \lambda_{ijk} L_i L_j \bar{e}_k + \lambda'_{ijk} L_i Q_j \bar{d}_k + \mu'_i L_i H_2 + \lambda''_{ijk} \bar{u}_i \bar{d}_j \bar{d}_k, \quad (2.16)$$

where the indices i , j , and k refer to flavour, and λ_{ijk} , λ'_{ijk} , λ''_{ijk} and μ'_i are coupling constants for the interactions between the chiral superfields. The first three terms violate lepton number conservation, and the final term violates baryon number conservation. The most current measurements of the proton lifetime as $> 5.8 \times 10^{29}$ years [7] put stringent limits on the possibility of the final coupling λ''_{ijk} and one of the other three couplings λ_{ijk} , λ'_{ijk} , or μ'_i existing simultaneously without either being strongly suppressed. As the proton is already comprised of the lightest combination of quarks, the only particles it would be able to decay into are lighter leptons. This would require violation of both baryon and lepton number, as the baryon number will change from 1 to 0 and the lepton number will change from 0 to 1. This can be seen in Figure 2.3, which gives an example of how proton decay could proceed if the λ''_{ijk} and λ'_{ijk} were both non-zero. In order to avoid the possibility of these terms in the superpotential at all, an additional quantum number can be introduced within the SUSY theoretical framework. Referred to as R-parity, this relates the baryon (B), lepton (L), and spin (S) quantum numbers of a particle as:

$$R_P = (-1)^{3(B-L)+2S}. \quad (2.17)$$

This will have a value of +1 for SM particles and -1 for SUSY particles. If it is conserved, SUSY particles are forbidden from decaying to SM particles, as this would lead to a change of $\Delta R_P = 2$. Consequently, the lightest supersymmetric particle (LSP) will be stable, as there will be no lighter particles with the same R_P number for it to decay into. This makes it a potential candidate for dark matter, especially in the instance that it is the lightest

neutralino, which is favourable for many SUSY models including the MSSM [38]. It also requires that SUSY particles are produced in SM particle-particle collisions in pairs, in order to maintain an even number of sparticles at each vertex. Similarly, heavier sparticles will eventually decay to a state with an odd number of LSPs.

The laws of conservation of baryon and lepton number in the SM do not arise from any symmetries but because all observed interactions are seen to obey them. There is therefore no mathematical motivation to forbid the R-parity violating terms in supersymmetry, although their couplings are limited by measurements like the proton lifetime. It is interesting and more rigorous to also consider instances of SUSY which violate R-parity in a way which agrees with current observation. The work detailed in this thesis considers examples of both R-parity conserving (RPC) and R-parity violating (RPV) models. The MSSM itself conserves R-parity, but can be extended to models where this is not the case.

2.9 Simplified Models

The MSSM contains 105 additional parameters with respect to the Standard Model, and there is no theoretical indication as to what the value of many of these should be. Experimental results constrain many properties, in particular those which have an effect on violation of flavour conservation. However, this still leaves a large number of free parameters. In order to deal with this at collider experiments it is necessary to reduce the number of these parameters and simplify matters. The simplified model approach [39, 40] is intended to provide *building blocks* for experimentalists which can then be developed upon when an observation is made. For each model, only a few sparticles are set to have accessible masses, and the branching ratios for a considered process are selected to be favourable. The mechanism for SUSY breaking, amongst other things, is therefore not a concern for simplified models, as the sparticle decays considered can originate from a range of different theories. They are not intended to be a representation of nature, but to allow a starting place for exploring the variation of many parameters more easily. The results for one or two-step simplified processes are transferable to more developed models, only requiring modification to account for differences in cross-section or branching ratios. Results on these grids are therefore arguably more useful than on more developed but very specific SUSY models. The signal scenarios considered in this work are all simplified models, and will be discussed in detail in Section 5.2.

2.10 Status of Supersymmetry

Indirect constraints on supersymmetric parameter values within specific models are placed by a number of measurements, for example the relic dark-matter density [41,42] and rates of rare B meson decays [43,44]. Additionally, direct limits are set by SUSY searches undertaken at particle colliders, like the work described in this thesis. Prior to the Large Hadron Collider (LHC), the most significant constraints came from searches at the Large Electron Positron (LEP) [45] collider, and the Tevatron [46] $p\bar{p}$ collider. These were generally interpreted on a simplified version of the MSSM, called the constrained MSSM (cMSSM) [47], or sometimes referred to as the Minimal Supergravity (mSUGRA) model. This provided a good benchmark with which to gauge the sensitivity of different searches and assess their performance. However, once results from the initial LHC data started to be analysed for SUSY searches, these cMSSM models became very constrained, rendering them rather useless for characterising search results. Additional constraints were introduced by the discovery of the Higgs boson [4,5], which ruled out any benchmark SUSY scenarios with Higgs mass parameters not consistent with a 126 GeV SM Higgs boson. This led to a move to include simplified models like those described above alongside the more popular SUSY models like cMSSM in order to make them more transferable and to cover a wider range of final states.

Summaries of the exclusion limits set for different sparticle masses from the initial LHC dataset (totalling approximately 5 fb^{-1} recorded at a centre-of-mass energy of 7 TeV in 2011) can be found for both ATLAS and CMS searches at [48] and [49] respectively. Coloured sparticles had particularly stringent limits set at around 1 TeV, depending on the scenario and production/decay modes considered. This is partly due to the LHC colliding protons, resulting in higher cross-sections for coloured sparticle production. More data is therefore required for electroweak SUSY searches to have equivalent sensitivity, and so SUSY searches in the electroweak sector were expanded for the 2012 dataset to complement the strong searches. In light of the agreement seen between the SM and the 2011 data, searches also began to consider versions of SUSY which were a bit more difficult to detect, or were less simplified in some way. This motivated the choice of models by the analysis in this thesis. R-parity violation is one possibility which deviates slightly from the simplest SUSY scenarios, and results in a different signature, which could be missed by the more standard searches. A total of twenty different R-parity violating simplified models are used in this analysis, covering a wide range of sparticle mass hierarchies and final states, the results for which can then be transferred to a plethora of SUSY scenarios. The R-parity

conserving models for lower cross-section processes like $\tilde{\chi}_2^0\tilde{\chi}_3^0$ production are also included, in order to take advantage of the increased dataset available from 2012. Using four leptons to select a final state in supersymmetry searches allows sensitivity to processes with lower production rates as the background processes which mimic them are very small.

Overall, the SUSY search strategy employed at the LHC aims to cover as many final state signatures as possible, and use these to set limits on simplified models for as many SUSY processes as possible, which are then easy to directly compare, and can be applied to interpretations on either new or existing popular SUSY models. No significant deviation has been seen between the data and SM expectations yet, and the exclusion limits set by ATLAS and CMS so far are summarised at [50] and [51] respectively.

Chapter 3

The ATLAS Detector at the LHC

3.1 The Large Hadron Collider

The Large Hadron Collider [52, 53] (LHC) is a circular particle accelerator and collider at CERN, the European Organisation for Nuclear Research, which started up in September 2008. Located on the Franco-Swiss border near Geneva, CERN has been conducting nuclear and particle physics experiments since the 1950s, and the tunnel in which the LHC operates is recycled from a previous experiment, the Large Electron-Positron collider (LEP) [45]. This tunnel is 27 km in circumference, and its depth varies between 40 m and 170 m below ground level.

The LHC was primarily designed to collide protons, which are supplied after passing through a chain of pre-existing smaller accelerators. The schematic layout of the full accelerator chain can be seen in Figure 3.1. The beams of protons begin at the linear accelerator LINAC 2, where they are accelerated to energies of 50 MeV. They are then passed on to the Proton Synchrotron Booster (PSB) where they reach energies of 1.4 GeV. This is followed by the Proton Synchrotron (PS), pushing energies up to 25 GeV, and then the Super Proton Synchrotron (SPS), at energies up to 450 GeV. Finally the proton beams are injected in bunches into the LHC, which circulates them in opposite directions, accelerating them to energies of (to date) 8 TeV before colliding them at four strategic positions around the ring. The LHC is also capable of colliding heavy ions, which are processed by LINAC 3 and LEIR (Low Energy Ion Ring) before they are passed to the PS and then follow the same path as the protons. Four large detectors are located at the collision points; the multi-purpose detectors ATLAS (A Toroidal LHC ApparatuS) [55] and CMS (Compact Muon Solenoid) [56], LHCb [57], which focuses on flavour physics, and ALICE (A Large Ion Collider Experiment) [58] which specialises in heavy ion physics.

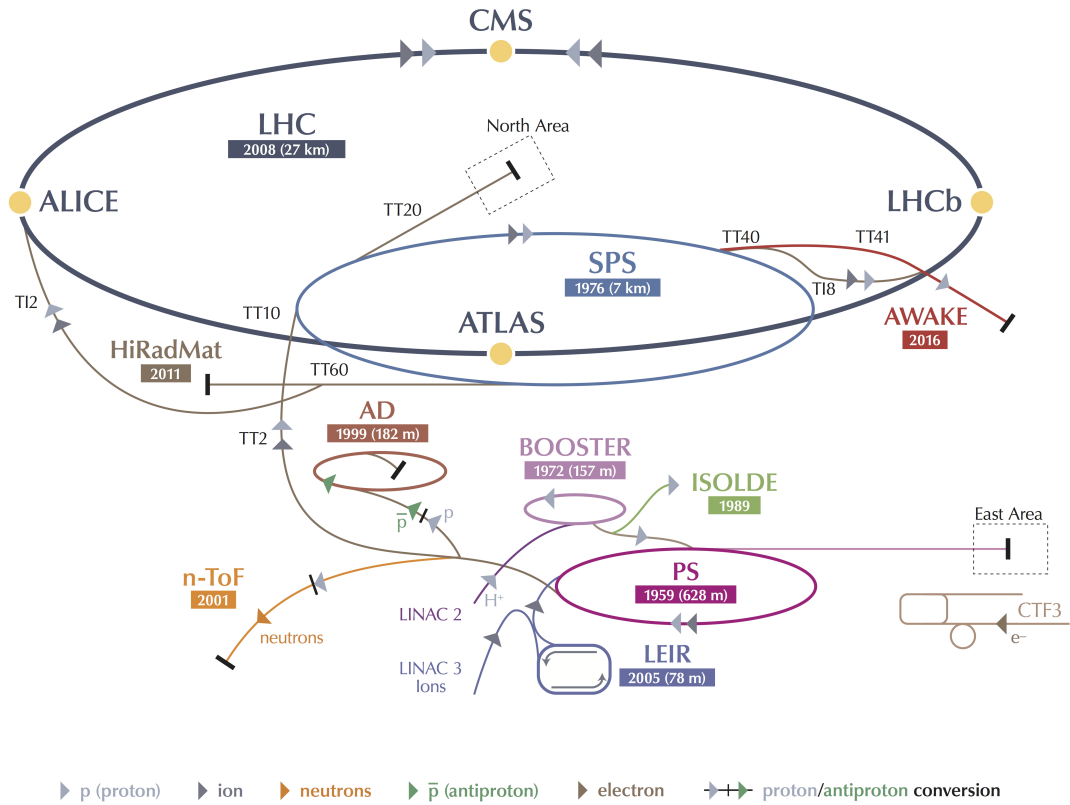


Figure 3.1: Diagram of the layout of accelerators connected to and including the LHC at CERN, as well as the locations of the four major detector sites [54].

There are also a number of smaller experiments located within these four caverns but these are not discussed here. In the original LHC design proposal protons collide at a centre of mass energy of $\sqrt{s} = 14$ TeV, achieving an instantaneous luminosity L of $1 \times 10^{34} \text{ cm}^2 \text{ s}^{-1}$. The luminosity is related to properties of the proton beam and bunches:

$$L = \frac{f N_1 N_2}{4\pi \sigma_x \sigma_y}, \quad (3.1)$$

where N_1 and N_2 are the number of protons per bunch in each of the colliding beams, f is the frequency of the bunch collisions, and σ_x and σ_y are the horizontal and vertical dimensions of the beam. In order to maximise values for the luminosity a small beam cross-section is required, as well as large numbers of protons in frequently collided bunches. For the 2011 and 2012 runs the beam was around 0.1 mm diameter in both x and y , and bunches of approximately 10^{11} protons with a nominal time spacing of 50 ns were collided with a frequency of 20 MHz. This resulted in peak instantaneous luminosities of $L = 3.7 \times 10^{33} \text{ cm}^{-2} \text{ s}^{-1}$ in 2011 and $L = 7.7 \times 10^{33} \text{ cm}^{-2} \text{ s}^{-1}$ in 2012. The integrated luminosities recorded by the LHC in 2011 and 2012 were approximately 5 fb^{-1} and 21 fb^{-1}

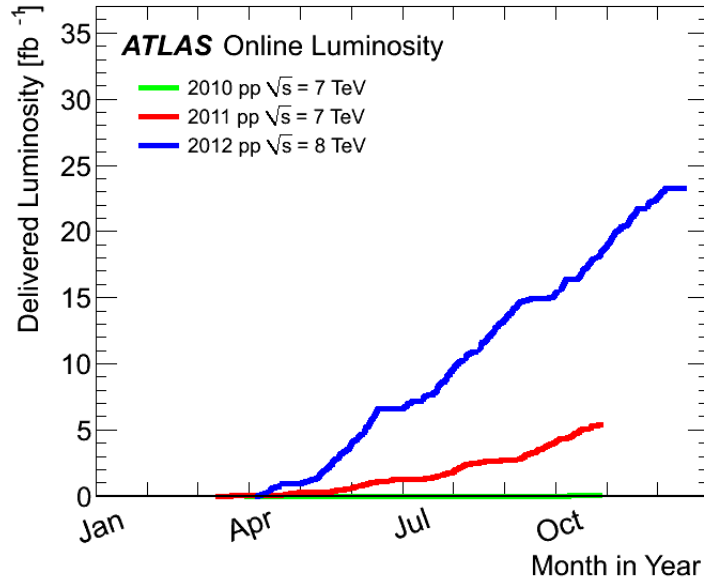


Figure 3.2: Instantaneous luminosity recorded as a function of time in 2010, 2011 and 2012 at the LHC from [?]

respectively, and the delivered instantaneous luminosity as a function of time can be seen in Figure 3.2 for 2011 and 2012, as well as the earlier run in 2010.

For each bunch crossing only some of the protons in the bunches will collide. The mean number of interactions, $\langle\mu\rangle$, is correlated with the instantaneous luminosity, and so this also increased between 2011 and 2012, as can be seen in Figure 3.3. The additional interactions in a bunch crossing which are not considered to be the *primary* interaction are referred to as *pile-up* [60]; an increasing challenge for modelling events as the running conditions approach the design conditions.

3.2 The ATLAS Detector

The ATLAS detector is one of two large multi-purpose detectors on the LHC ring at CERN. It has cylindrical symmetry, measuring 45 m in length and 25 m in diameter. Concentric layers of subdetectors surround the beam pipe, most of which contain modules in the central *barrel* region and on either end, the *endcaps*. Moving from the beam pipe outwards these consist of a set of tracking detectors, electromagnetic and hadronic calorimeters, and an outermost muon spectrometer system. A solenoid magnet surrounds the inner tracking detectors and a set of toroidal magnets are incorporated into the muon spectrometer. These components are displayed in Figure 3.4 and will be discussed in more detail in the following sections. This is preceded by a description of the geometry of the detector and

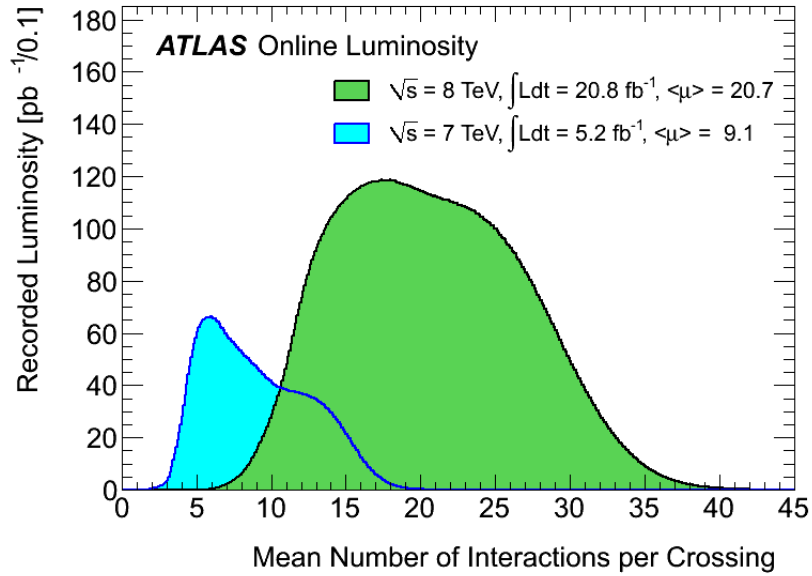


Figure 3.3: Mean number of interactions per bunch crossing weighted by the luminosity in 2011 and 2012 [59]. The mean average was taken from the Poisson distribution describing the number of interactions per crossing for each bunch, calculated using the instantaneous luminosity per bunch.

nomenclature associated with the kinematics.

3.3 ATLAS detector geometry and nomenclature

The nominal interaction point is defined as the origin of a right-handed cylindrical coordinate system describing the ATLAS detector. The beam line direction defines the z axis, and the x and y axes are defined as pointing into the centre of the LHC ring, and upwards, respectively. The detector is referred to as having a side A, the half with positive z , and a side C, which is the part with negative z , and these are roughly identical due to the symmetrical nature of the detector. The polar angle θ is measured from the beam axis, and the azimuthal angle ϕ is measured around the beam axis. Often the *pseudorapidity* is used in combination with ϕ as the spatial co-ordinates. Pseudorapidity is defined as:

$$\eta = -\ln \tan \frac{\theta}{2}, \quad (3.2)$$

which coincides with the rapidity y for massless particles, defined as follows for massive particles:

$$y = \frac{1}{2} \ln \frac{E + p_z}{E - p_z}, \quad (3.3)$$

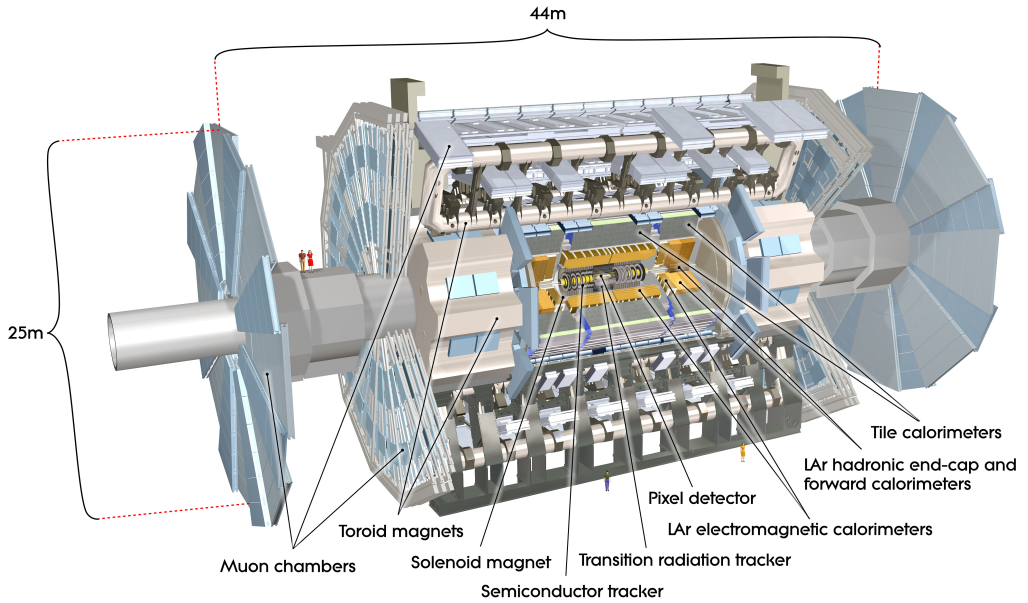


Figure 3.4: A schematic view of the sub-detectors and other components making up the ATLAS detector from [55].

where E is the particle's energy and p_z is the z -component of its momentum. The distance between two objects in the pseudo-rapidity-azimuthal angle space is defined as:

$$\Delta R = \sqrt{(\Delta\eta)^2 + (\Delta\phi)^2}, \quad (3.4)$$

where $\Delta\eta$ and $\Delta\phi$ are the distance in η and ϕ between the two considered objects. Requirements on spatial proximity between objects can then be made by imposing conditions on ΔR . The boundary of a ΔR condition describes a cone around the considered object. The *transverse momentum* is another important variable and is defined as:

$$p_T = \sqrt{p_x^2 + p_y^2}, \quad (3.5)$$

where p_x and p_y are the x and y components of the momentum. Overall, the initial momentum in the x - y plane of a proton-proton interaction can be taken to be zero, and therefore we expect the final total transverse momentum to also be zero, due to momentum conservation. If the total visible transverse momentum, p_T^{vis} is measured as non-zero, there is an indication that additional undetected particles were present in the event, resulting in an invisible p_T component which accounts for the observed imbalance. We refer to the magnitude of the momentum of any undetected particles as the missing transverse energy E_T^{miss} , defined as

$$\vec{E}_T^{\text{miss}} = -\vec{p}_T^{\text{vis}} = -\sum \vec{p}_T, \quad (3.6)$$

where the p_T of all visible particles are summed. Significant E_T^{miss} is expected from events containing neutrinos or mismeasured events, but is also very important for models predicting new electrically neutral particles, such as supersymmetry.

3.4 Magnet System

The magnet system incorporated into ATLAS allows key measurements for charged particles which are deflected by the magnetic fields within the detector. The direction and radius of curvature of the particles' subsequent paths are related to their charge and momentum. The solenoid magnet is located between the Inner Detector (ID) and the electromagnetic calorimeter (ECAL). It has an axial length of 5.8 m, and in order to cause as little obstruction as possible to the calorimeters, it has been designed to be as thin as possible, with an inner radius of 2.46 m and an outer radius of 2.56 m. Despite its compact nature it still provides a magnetic field of 2 T. The toroidal magnet system consists of a barrel and two endcaps, each made of eight coils, in the outer-most section of the detector. This system provides a magnetic field which is orthogonal to particle direction within the muon spectrometer, for measurements of the muon momenta. The barrel toroid has an axial length of 25.3 m, an inner diameter of 9.4 m and an outer diameter of 20.1 m, and delivers a 0.5 T magnetic field. The endcaps are 5 m in length and have inner and outer diameters of 1.65 m and 10.7 m respectively. These provide a magnetic field of 1 T. All components of the magnet system can be seen in Figure 3.5, along with the calorimeters. They are all formed of NbTi, a superconducting material, in order to achieve a high magnetic field with thin magnets, and are cooled to 4.5 K by liquid helium.

3.5 Inner Detector

The ID is comprised of three component detector systems which focus on the tracking of particles from the interaction point over a wide spacial area (within $|\eta| < 2.5$). Algorithms reconstruct the paths of particles, or tracks, from a number of high-resolution position spacepoints measured by each of these subdetectors. The inner-most component, the Pixel Detector (PD), is most useful for reconstructing both the primary interaction vertex and also secondary vertices in an event. The next layer, the Semiconductor Tracker (SCT), focuses primarily on accurate measurement of particle momenta. The final layer, the Transition Radiation Tracker (TRT), is key for particle identification. All three subdetectors have barrel and endcap components, and the positioning of these with respect

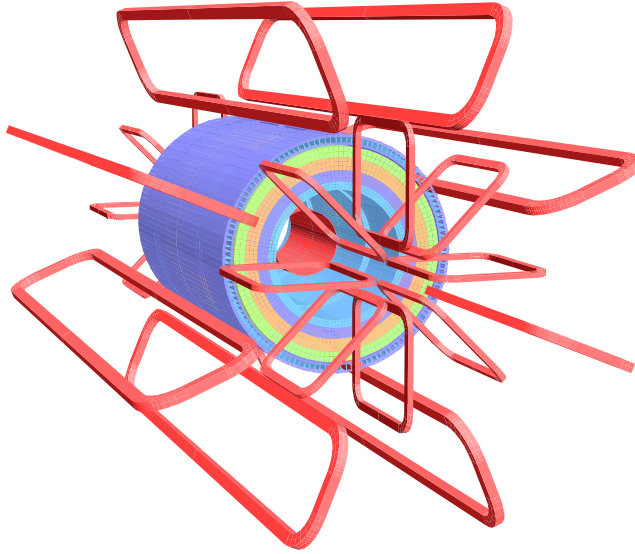


Figure 3.5: Schematic of the solenoid (inner-most red barrel) and toroidal magnets (red loops) in ATLAS, and including the electromagnetic and hadronic calorimeters (blue, orange and green rings). The outermost ring corresponds to the Tile Calorimeter, which returns the flux of the solenoid magnet due to its high steel content. Taken from [55].

to the beam line can be seen in Figure 3.6.

3.5.1 Pixel Detector

The PD has three layers of silicon pixel modules in both the barrel and end-caps, totalling 1744 modules and covering $|\eta| < 2.5$. Charged tracks are guaranteed to cross three of these layers, resulting in at least three space-points, provided they are within $|\eta| < 2.5$. Each module contains 46,080 pixels, each measuring $50 \times 400 \mu\text{m}$, which send information to 16 chips. Further details can be found in [61]. In preparation for Run 2, an additional layer of PD called the *Insertable B-Layer* [62] (IBL) has been added to the outside of the beam pipe. This will improve vertexing and impact parameter measurement, and therefore b-physics measurements.

3.5.2 Semiconductor Tracker

The SCT is a silicon strip detector containing a total of 4088 microstrip detector modules which are arranged in four layers in the barrel and nine layers in each of the endcaps. Each module contains back-to-back wafers set at a stereo angle of 40 mrad, with 786 strips on each side at an average pitch of $80 \mu\text{m}$. This also covers the range $|\eta| < 2.5$, and particles in this η range will pass through all four layers, leaving clusters of *hits* in one or more of

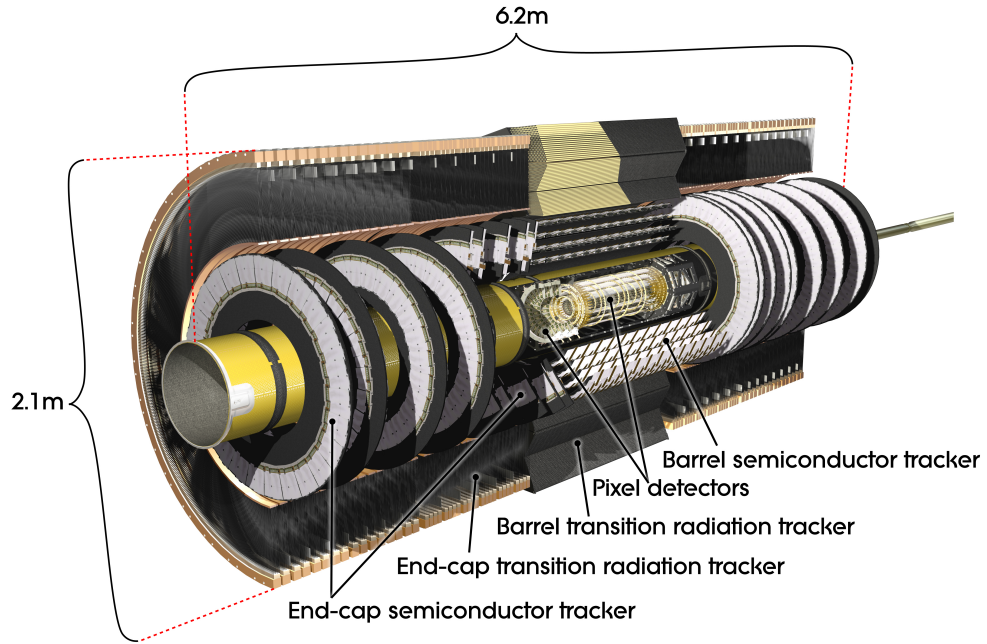


Figure 3.6: Schematic of the structure of subdetectors comprising the Inner Detector.

the strips on each side. These are later reconstructed as space-points used for the particle tracking.

3.5.3 Transition Radiation Tracker

Unlike the other ID subdetectors, the TRT uses 370,000 4 mm diameter straw drift-tubes, filled with a $\text{Xe}(70\%)\text{CO}_2(27\%)\text{O}_2(3\%)$ gas mixture. These are arranged parallel to the beam pipe in the barrel section, and radially in the endcaps. Each straw is coated with aluminium to form a cathode, and a gold-plated tungsten wire is threaded through the centre as an anode. Charged particles passing through the straw ionise gas atoms, which drift towards the anode, registering a *hit*. Compared to the three or four hits expected per track in the pixel and SCT subdetectors, about 30 hits are expected on average for a particle passing through the TRT. These hits help to improve the p_T resolution. In addition to this readout, the TRT also makes use of transition radiation emitted by charged particles for identification purposes. Polypropylene is interwoven between the straws, creating a varying dielectric constant as particles pass through the subdetector. This causes them to emit X-rays roughly proportional in energy to the particle's Lorentz factor ($\gamma = \frac{E}{m}$), which will then produce secondary, higher energy hits in the TRT, referred to as high-threshold hits. Electrons and pions can be distinguished for a p_T range of 1 GeV-150 GeV using the ratio of high-threshold to normal hits. Measurements of the $\frac{dE}{dx}$ can

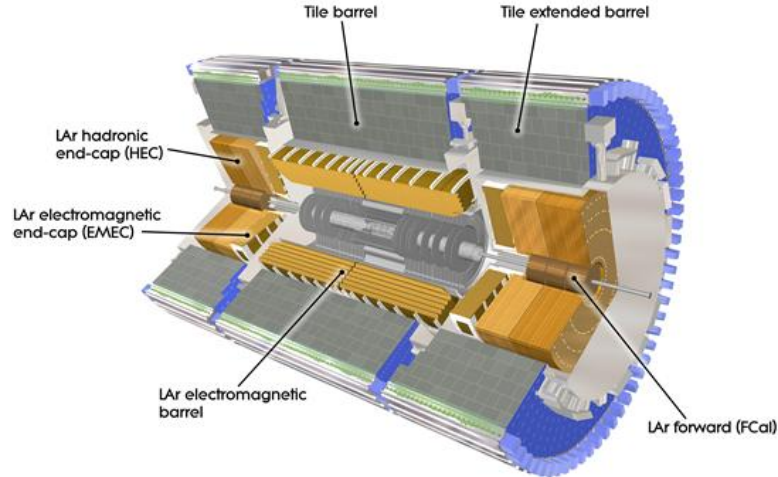


Figure 3.7: Cut-away diagram of the ATLAS calorimeter system, showing the LAr (liquid Argon) electromagnetic barrel and end-cap comprising the ECAL, and the Tile barrel, extended barrel and LAr hadronic end-cap making up the HCAL, as well as the forward calorimeter, FCal. Taken from [55].

also be used to distinguish protons and kaons with missing transverse momenta less than 10 GeV. The overall coverage of the TRT is $|\eta| < 2.0$.

3.6 Calorimeters

The ATLAS Calorimeter system consists of the electromagnetic calorimeter (ECAL) and hadronic calorimeter (HCAL), shown in Figure 3.7, which are designed to stop and measure the energy of EM and hadronic particles respectively. Altogether they give coverage of the region with $|\eta| < 4.95$. They are designed to be hermetic, allowing as accurate a measurement of the missing transverse energy as possible. All constituent calorimeters are ‘sampling’, meaning they have layers which initiate energy loss (absorber), alternated with layers which measure the energy of the resulting *showers* (sampler). The calorimeters use different technologies to target electromagnetic and hadronic particles specifically, and are non-compensating, meaning they respond differently to these particle types. It is important that showers are contained within the calorimeters, to improve energy measurements, but also to avoid any *punch-through* - i.e. continuation of the shower into the muon spectrometer.

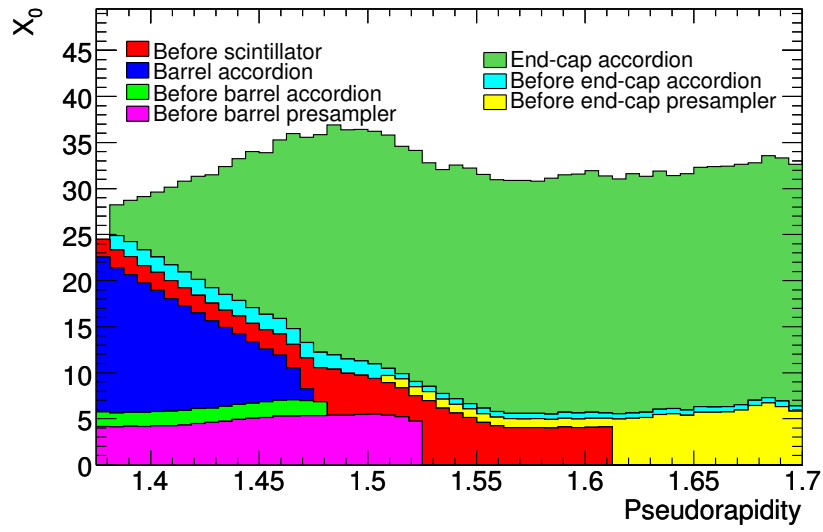
The radiation length (X_0) is defined as the distance over which an electron loses $\frac{1}{e}$ of its energy within a given material, and the equivalent for strongly interacting particles is the

nuclear interaction length (λ_I). The electromagnetic calorimeter is at least $22 X_0$ thick in the barrel, and $24 X_0$ in the end-caps (but thicker for some regions in $|\eta|$), and the hadronic calorimeter is $10 \lambda_I$ thick on average, although this varies with η . The average nuclear interaction length is much longer than the average radiation length (by about a factor of ten), hence hadronic particles are much more penetrating within the ATLAS detector than electromagnetic particles. The electromagnetic calorimeter is approximately $2 \lambda_I$ thick, and all material prior to the calorimeters themselves must of course be considered as well. Figure 3.8 shows the simulated thickness of material from the interaction point up to and including the calorimeters for both radiation lengths and nuclear interaction lengths.

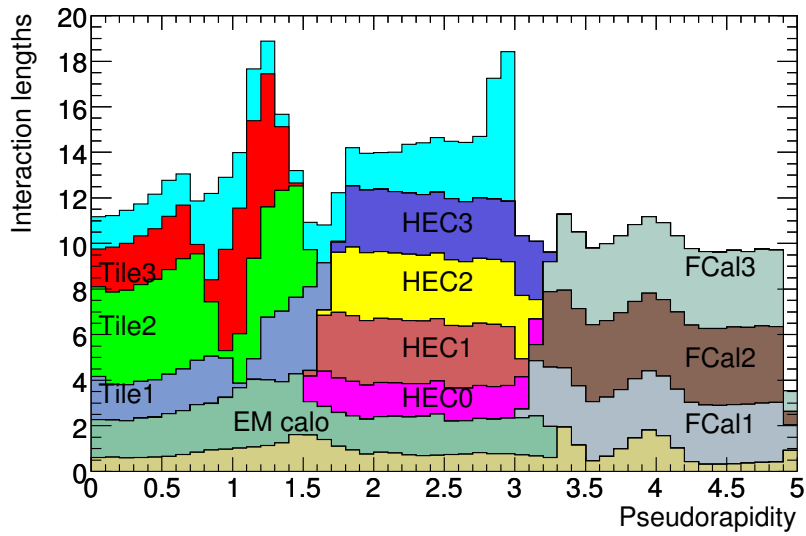
3.6.1 Electromagnetic Calorimeter

The electromagnetic calorimeter (ECAL) consists of modules containing alternating layers of lead absorber and liquid Argon (LAr) folded into an accordion shape as shown in Figure 3.9. This gives full ϕ coverage, and an even energy resolution throughout the calorimeters. The LAr is ionised by electromagnetic showers, and copper electrodes running through these layers then read out the signal. The modules are arranged into two symmetric ‘half-barrel’ components in the barrel section of the ECAL subdetector, and two co-axial wheels in the end-caps. The barrel covers the region $|\eta| < 1.475$ and the end-caps are at $1.375 < |\eta| < 3.200$. There is a region referred to as the *crack* region at the junction of the barrel and endcap components which is discarded in analysis due to the large volume of material obscuring it. In order to minimise material in front of the ECAL, a single shared vacuum vessel is used for the solenoid magnet and adjacent ECAL barrel.

For the majority of the half-barrel sections there are three layers of detector, although this varies with $|\eta|$, and in the region $|\eta| < 1.8$ there is an additional *presampler* layer. This consists of a thin (0.5 cm in the end-cap and 1.1 cm in the barrel) LAr layer with no absorber. The purpose of the presampler is to allow correction for energy lost upstream by taking a measurement just before the ECAL is reached and the majority of showering occurs. The first layer of the calorimeter proper is aimed at precision measurements, including distinguishing between prompt photons (single shower) and those from neutral pion decay (double shower). For this reason it has the finest granularity, i.e. the smallest measurable segment size in (η, ϕ) , of the three layers, at $\Delta\eta \times \Delta\phi = 0.025 \times 0.025$. The second layer will contain the largest fraction of energy deposited by an EM shower, and so is crucial for the energy measurement. The third layer will then contain only the tails of



(a)



(b)

Figure 3.8: (a) displays the cumulative amount of material in radiation lengths, X_0 , before and including the electromagnetic calorimeter components as a function of $|\eta|$. (b) shows the amount of material in nuclear interaction lengths for all components of the hadronic calorimeter is shown as a function of $|\eta|$. Also displayed is the ECAL, the material prior to the ECAL (beige), and the first layer of the muon spectrometer (light blue). From simulations, taken from [55].

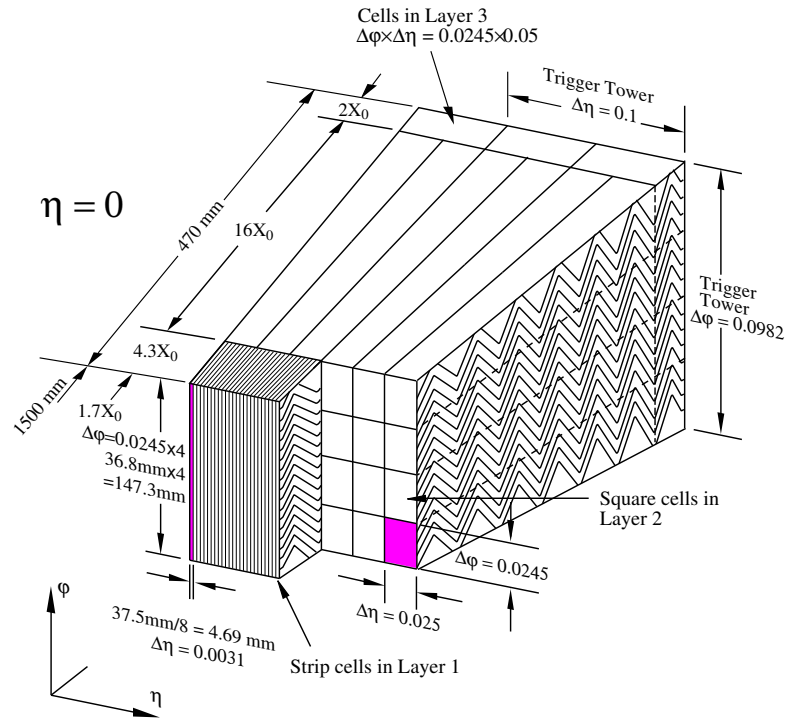


Figure 3.9: Diagram of a barrel module of the ECAL, where the accordion folding of the lead and LAr layers can be seen, as well as the differing η and ϕ granularity and thickness in radiation lengths of the three ECAL layers. Taken from [55].

an EM shower, if it is reached, and is therefore useful for distinguishing EM showers from hadronic showers, which are much more penetrating. It can afford a coarser granularity for this, and so only has $\Delta\eta \times \Delta\phi = 0.05 \times 0.025$.

3.6.2 Hadronic Calorimeter

The hadronic calorimeter (HCAL) uses slightly different materials and techniques to the ECAL, and these vary within the tile calorimeter, end-cap and forward calorimeter (FCAL) components. The barrel section at $|\eta| < 1.0$ and *extended barrel* sections at $0.8 < |\eta| < 1.7$ make up the tile calorimeter, which uses steel absorber layers and plastic scintillating tiles as the active medium. These are read out from both sides by wavelength-shifting fibers to photomultiplier tubes (PMTs). There are three layers of modules in each barrel section, these are 1.5-, 4.1-, and 1.8- λ_I thick in the barrel, and 1.5-, 2.6-, and 3.3- λ_I thick in the extended barrels. Module layers are offset with respect to the layers of their neighbours to increase granularity, which is $\Delta\eta \times \Delta\phi = 0.1 \times 0.1$ in the first two layers, and $\Delta\eta \times \Delta\phi = 0.1 \times 0.2$ in the final layer. The electronics are contained within supportive *girders* which also provide flux return for the central solenoidal magnetic field.

Each hadronic end-cap (HEC) consists of two wheels, each containing two layers of wedge-shaped modules which use copper absorber layers alternated with LAr. The end-caps cover the region $1.5 < |\eta| < 3.2$, overlapping slightly with both the tile calorimeter and FCALs in η . The FCAL is located at $3.1 < |\eta| < 4.9$, and uses an absorber metal matrix combined with rod and tube electrodes, where LAr fills all of the small gaps in between. It is comprised of three modules, the first using copper as the shower-initiating metal, which is focussed on EM measurements, and the final two which both use tungsten and are primarily for the measurement of hadronic energy.

3.7 Muon Spectrometer

Muons are the most penetrating particles detected by ATLAS; they lose far less energy through Brehmstrahlung than electrons due to their higher mass and their lifetime is “extended” by time dilation due to their relativistic momenta at the LHC. The muon spectrometer occupies the outermost region of ATLAS, and the tracks it measures are used in conjunction with charged tracks in the ID and small energy deposits in the Calorimeters for muon reconstruction. It is divided into the barrel, containing three layers at radius 5, 7.5, and 10 m in the region $|\eta| < 1.0$, and two endcaps, comprised of wheels at 7.4, 10.8, 14, and 21.5 m from the origin and covering the range $1.0 < |\eta| < 2.7$. A cut-away showing the structure and individual components can be seen in Figure 3.10. The magnetic field used to bend particle trajectories is provided by the barrel toroids for $|\eta| < 1.4$, by the end-cap toroids for $1.6 < |\eta| < 2.7$, and a combination of the two in the “transition” region $1.4 < |\eta| < 1.6$. As explained below, the muon spectrometer has four different types of component chambers, two for precision measurement and two for triggering. This is due to the readout time of the precision measurement chambers not reaching the required limit for triggering. In order to achieve the required performance it is important that the chambers are aligned accurately and that their position is well known. For this reason the muon system contains an optical alignment system both in and between the muon chambers, and this is complemented by track-based alignment.

The precision chambers used for the region $|\eta| < 2$ are Monitored Drift Tubes (MDTs), consisting of three to eight layers of 29.970 mm drift tubes, each filled with Ar/CO₂ gas and with a tungsten-rhenium wire through the center. The wire is kept at a potential to collect gas ionised by charged particles passing through. At the higher η range 2.0-2.7 different chambers are required to deliver a higher rate capability and better time resolution. These forward chambers use Cathode Strip Chambers (CSCs), which are multi-

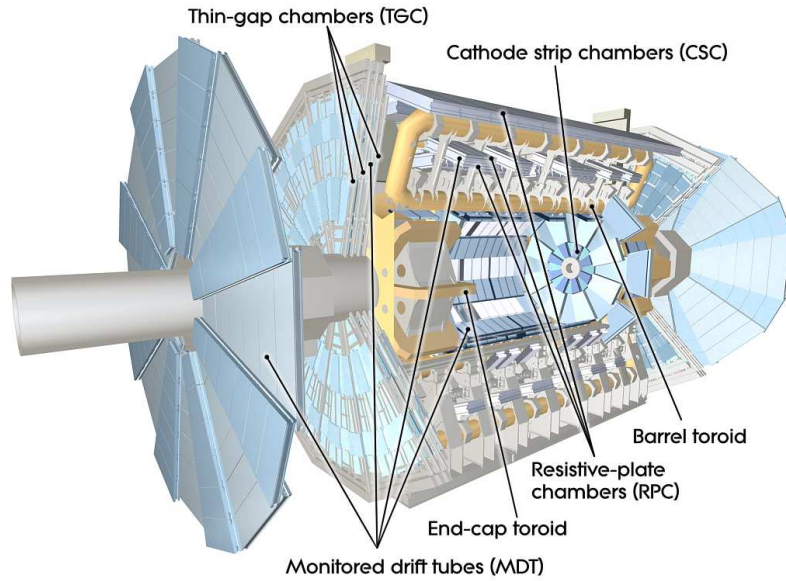


Figure 3.10: Cut-away showing the layout of the ATLAS muon subdetector system. Taken from [55].

wire proportional chambers filled with $\text{Ar}/\text{CO}_2/\text{CF}_4$ gas. Segmented cathode strips are arranged both parallel and perpendicular to the anode wires. This gives a high granularity and allows measurement of both the particle's co-ordinates to be calculated from the induced charge distribution.

The trigger chambers are operational in the region $|\eta| < 2.4$, and as with the MDTs and CSCs, there are two types of chamber employed due to increased rates in the forward region. The Resistive Plate Chambers (RPCs) are located in the barrel and cover the region $|\eta| < 1.05$, and the Thin Gap Chambers (TGCs) are in the end-caps covering $1.05 < |\eta| < 2.4$. As well as providing a fast enough read-out (less than 50 ns) for triggering, these also determine a second reading of the muon co-ordinate which is orthogonal and complementary to that taken by the precision chambers. The RPCs consist of parallel resistive plastic plates at a spacing of 2 mm and with a voltage across them of 4.9 kV/mm. Between them is a gas mixture of $\text{C}_2\text{H}_2\text{F}_4/\text{Iso-C}_4\text{H}_{10}/\text{SF}_6$, which forms ionising avalanches when a charged particle passes through. These are read off by metallic couplings on the outside of the resistive plates. The TGCs are multi-wire proportional chambers similar to the CSCs, with a higher granularity than the RPCs.

3.8 Trigger and Data Acquisition System in Run 1

The Trigger and Data Acquisition (TDAQ) system is responsible for reducing the event rate (which varies dependent on beam structure, but was around 20 MHz for most of Run 1) produced to approximately 200 Hz for recording by selecting and storing events which contain potentially interesting physics. It really consists of two subsystems: the trigger; and data acquisition; which handle the event selection and data flow respectively. The trigger during Run 1 was a three-tier system, consisting of the Level 1 (L1), Level 2 (L2), and Event Filter (EF), where L2 and EF collectively form the High Level Trigger (HLT). Each subsequent level of increasingly stringent criteria must be passed in order for an event to be accepted and stored, otherwise it is discarded permanently. Signatures of interest are identified, such as high momentum electrons, muons, hadronically decaying taus, jets, photons and large missing transverse energy, and used as criteria for event selection. The combination of these signature requirements is referred to as the *menu*, and can be changed depending on the run conditions.

The L1 trigger selects a region of interest (RoI) in η and ϕ based on these signatures using coarse granularity information from the calorimeters and muon detector. Whilst this decision is being made, the event information from the detectors is stored in front-end pipelines, and is then passed to the Read Out Buffers (ROBs) if the decision is positive, along with the RoI information from the L1. The L2 trigger is then “seeded” with this RoI, in which it accesses finer granularity calorimeter and muon detector information, with the addition of tracking information from the ID. All of this information is read from the ROBs, which retain the event fragments for the bunch crossing until the L2 has reached a decision. If it is accepted, the data is passed to the Event Builder for combination and stored in the Full Event Buffer. It is accessed by the EF, which uses algorithms based on offline software, and has access to full detector granularity and a higher latency in order to achieve a more accurate reconstruction. If the event is accepted by EF then it is passed from the Full Event Buffer on to permanent storage. Figure 3.11 shows a flowchart representing this process.

3.8.1 Level 1 Trigger

The L1 trigger uses custom fast electronics to read data directly from the detectors and pass its decision to the Central Trigger Processor (CTP). Muon candidates are identified using the three layers of RPCs and TGCs in the barrel and endcap of the muon spectrometer. Coarse granularity segments of the HCAL and ECAL referred to as *trigger towers*

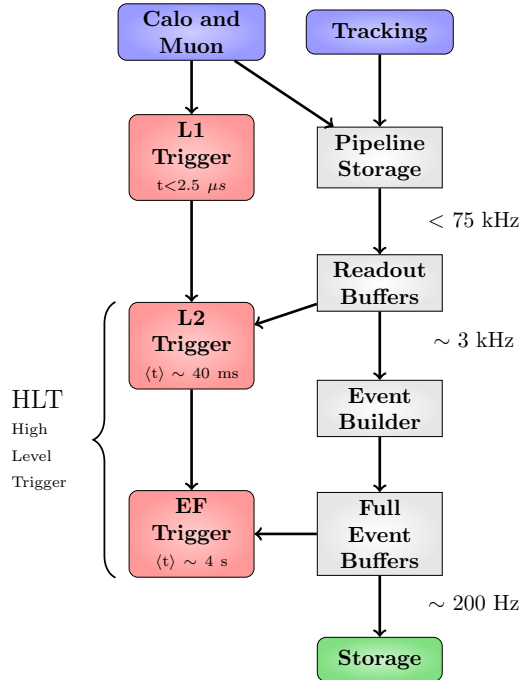


Figure 3.11: Flow chart showing the movement of data (black arrows) through the TDAQ system. Numbers quoted are the design goals taken from [63] and in some cases differ from those for 2011 and 2012.

are used to identify RoIs for electrons, photons, taus and jets. These towers cover blocks of size $\Delta\eta \times \Delta\phi = 0.1 \times 0.1$ in the central calorimeters, and up to $\Delta\eta \times \Delta\phi = 0.4 \times 0.4$ in the forward calorimeters. Energy measurements from the muon detector and calorimeters are used to select on transverse energy, E_T , or missing transverse energy, E_T^{miss} . Data from the subdetectors are stored in front-end pipelines located on or near to them whilst L1 processing occurs. The time between the collision and the L1 decision, or the latency, is required to be $< 2.5 \mu s$, and the resultant data rate is decreased to 75 kHz.

The CTP can process 256 different conditions in combination by taking the logical OR of each. In addition to the physics objects and properties discussed above, triggers which are random or periodic are also included for use with calibration and monitoring of the trigger. If an event passes the L1 trigger requirements, an *accept* signal is sent to the CTP. To prevent too greater rate of data flow through the front-end buffers, the CTP enforces two types of dead-time; simple and complex. The simple dead time requires a given period to pass after an accept decision from the L1 before another is allowed. In 2011 and 2012 this was five bunch crossings. The CTP will veto any L1 accept signals falling within this time period. The complex dead time sets a limit on the number of accepts allowed within a given period, which was set to 8 accepts per 416 bunch crossings for 2011 and 2012.

3.8.2 High Level Trigger

The High Level Trigger (HLT) is comprised of a combination of the L2 and EF triggers, both of which are software based and run on standard PCs in L2 and EF “farms”. The L2 trigger uses signature-based algorithms which have a limited precision in order to operate on a short timescale. It has a latency of approximately 40 ms and reduces the rate further, in 2011 to 5.5 kHz and in 2012 to 6.5 kHz. It typically accesses the full granularity detector information only within the RoI provided by L1, thus reducing the data to be processed to 2-6 % of the total event. In addition to the muon detector and calorimeter data, the L2 also has access to the tracking information from the ID. This is used to select electrons, muons and taus and to distinguish them from background processes based on track properties. For example, for the tau triggers, the isolation and impact parameter of considered tracks was key to rejecting signal from pile-up jets.

Two strategies were used for the L2 fast tracking algorithms in Run 1, one of which performed better for electron and muon tracks, and the other for tau and jet tracks. These both involve grouping together the space-points from the hits in the pixel and SCT subdetectors based on their η and/or ϕ values, and using these to identify the z co-ordinate value for the primary vertex. The space points are then further combined using criteria based on the primary vertex position, and the groups are then filtered to remove the sets which produce the worst fits. All track candidates selected by one of these algorithms are then processed with a Kalman filter [64] to produce the final tracks.

The Event Filter has access to the full granularity data from the whole event, rather than being restricted to the RoIs. It uses the standard ATLAS offline reconstruction algorithms wherever possible, with very similar criteria to those described in Section 4.4. The design processing time of 4 s allows this to be possible, although the average time for 2011 and 2012 was only around 1 s. The average rate after the EF decision in was approximately 400 Hz 2011 and approximately 1kHz in 2012.

3.8.3 Trigger Chains, Streams and Menus

The full sequence of algorithms for the L1, L2 and EF triggers which must be satisfied to make a specific trigger selection is referred to as a *chain*. For each signature used for triggering, for example muons or missing transverse energy, a set of chains is defined. Primary chains are physics-based chains used for analyses, backup chains have a higher threshold than the primary chains and can be used if the detector malfunctions or the luminosity increases unexpectedly, supporting chains provide support for physics analyses

for e.g. background estimation methods, and the monitoring chains are used to monitor data performance, for example the ID tracking performance. Appendix A describes studies performed by myself using the tau monitoring chains to measure the performance of the ID tracking used for taus in Run 1.

An example of a primary chain is EF_mu24i.tight, which is one of the trigger chains used by the analysis discussed in this thesis. The level one condition for this chain is L1_MU15, which requires the muon trigger chambers to select an object with $p_T > 15$ GeV consistent with a muon. The RoI information for this object is then provided to the L2 trigger - L2_mu22i.tight, which requires the identified muon to satisfy $p_T > 22$ GeV. Finally at the EF stage, EF_mu24i.tight, the reconstructed muon is required to satisfy $p_T > 24$ GeV and $\Sigma p_T^{trk}/p_T < 0.12$, where Σp_T^{trk} is the sum of transverse momenta of all ID tracks within a $\Delta R < 0.2$ cone of the muon ID track. This final condition results in an isolated muon, signified by the “i” in the trigger chain name. Details of all chains used by this analysis will be discussed in Section 5.3.1.

Events which have passed the EF are classified into *streams* depending on which category of trigger chain accepted the event. These are inclusive, meaning an event can be contained within more than one stream, although the overlap is intended to be minimal, and is approximately 10-15% at most. There are four physics streams; muon, electron/photon, jet/tau/missing transverse energy and minimum bias. Signatures which are related are grouped together. Data from these streams are recorded separately, allowing analyses to consider only events which contain e.g. muons. In addition to the physics streams there are also data collections for calibration and an *express* stream used for fast reprocessing in order to validate the recorded data.

The total collection of all trigger chains used for all signatures during data taking is called the trigger menu. Different menus are defined in order to deal with the varying running conditions, for example the loss of luminosity during data-taking with one set of beams, or the increase in luminosity with subsequent periods of data-taking. Any changes in the collision energy or amount of pile-up will affect the input and output rates of the various triggers included, requiring an alteration to the trigger menu. A new menu will be defined for data taking during Run 2, which will operate at a higher centre-of-mass energy.

Chapter 4

Generation, Simulation and Reconstruction of ATLAS Data

Data which has been recorded by the ATLAS detector requires processing to reconstruct physics objects for use in analysis. The ATLAS software framework Athena [65], which is based on the Gaudi [66] framework developed by LHCb [57], is used to do this. For consistency and ease, this framework deals with all aspects of the experiment software including triggering and the processing required for simulated data. Monte Carlo (MC) simulated data used to model background and signal process events are produced in a number of stages, as shown in Figure 4.1, before being output in a format which can be used by analysers. This chapter follows these stages in the subsequent Sections - Event Generation (Section 4.1), Event Simulation (Section 4.2) and Digitisation (Section 4.3). Objects in both real data and simulated MC events are then reconstructed using the same algorithms, as described in Section 4.4. Finally, a set of selection criteria are applied to reconstructed objects to identify those suitable for use in analysis, as detailed in Section 4.5.

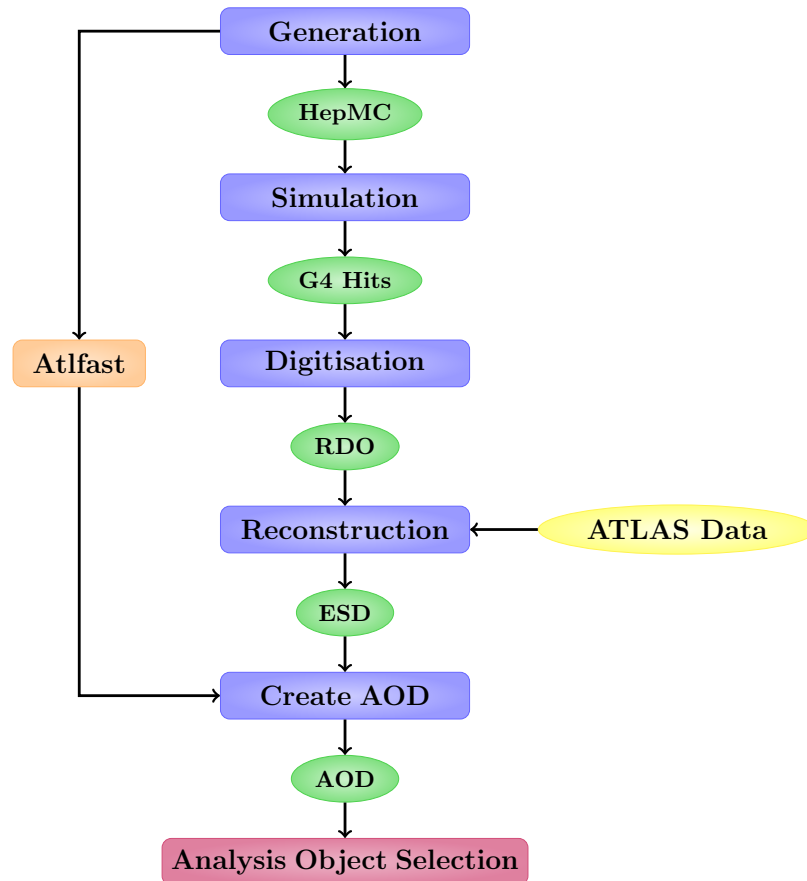


Figure 4.1: Flow diagram showing the various stages required to produce analyseable simulated and real data formats. Blue boxes show processes, and their output format is shown in green ellipses. RDO output are raw data objects, ESD are event summary data, and AOD are analysis object data. The orange box shows the alternative simulation method ATLFAST [67], which will be discussed in Section 4.2. The yellow box shows the point at which real data events begin processing - at the reconstruction stage.

4.1 Event Generation

MC event generators simulate physics processes in order to produce randomly distributed events containing final state particles. The physics processes involved in proton-proton collisions result from interactions between the constituent *partons* making up both hadrons. These partons include the three quarks (uud) which are referred to as the *valence* quarks; gluons mediating strong interactions between the valence quarks; and *sea* quarks which are produced in virtual $q\bar{q}$ pairs by interactions of the gluons. These interactions are called Deep Inelastic Scattering (DIS) processes, as the substructure of the proton is probed (deep) and the proton's momentum is not conserved (inelastic). Figure 4.2 shows an annotated Feynman diagram of the DIS of a proton by an incoming positron. Although at the LHC this positron will be replaced by a parton from the other proton, the physics remains the same. The interacting parton has a fraction of the proton's momentum x , called the scaling variable, and the measure of momentum transfer in the event Q^2 is related to the momentum transferred by the exchanged boson q by:

$$Q^2 = -q^2. \quad (4.1)$$

To effectively model interactions of the protons their parton content must be mathemat-

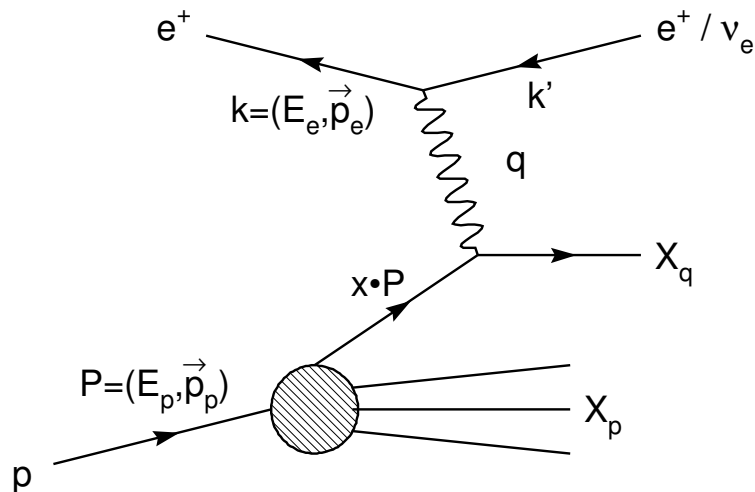


Figure 4.2: Example of a Deep Inelastic Scattering event involving a proton and an incident positron. The four-momentum of the incoming proton is denoted P , and the proportion of this carried by the incident parton is x . The four-momentum of the incoming and scattered positron are given by k and k' , and the momentum of the exchanged boson is given by q .

ically described using parton distribution functions (PDFs) which will be briefly described

in Section 4.1.1.

Scattering interactions involving protons at the LHC can be categorised as either *hard* processes, which can be described with perturbation theory, or *soft* processes, which involve non-perturbative QCD effects. Each p-p collision will typically contain a hard scattering process between two partons - one from each proton, and a number of soft processes, which can include *Initial State Radiation* (ISR), *Final State Radiation* (FSR), and the *Underlying Event* (UE). ISR refers to particles radiated by the partons which will interact in the hard process prior to their scattering. The remnant partons which are not involved in the hard scatter form the UE. Particles radiated from the final state products of the hard scatter are labelled as FSR. Coloured particles in the event are capable of radiating gluons and/or producing $q\bar{q}$ pairs, a process referred to as *parton showering*. Due to confinement, the products of these showers will undergo *hadronisation* to form colourless hadron states when Q^2 is of the order of 1 GeV.

Sections 4.1.2, 4.1.3 and 4.1.4 briefly describe the techniques used to model the hard process, parton showering and hadronisation within the event. The modelling of the UE is then considered in Section 4.1.5. A more detailed discussion of the techniques employed to calculate these components and incorporate them into generation programs for use at the LHC can be found in [68] and a thorough review of the processes involved in [69].

MC samples are categorised based on the hard-process which is specified before generation, allowing analysers to use samples which are relevant for a specific purpose. It is also possible to filter events to only produce a given final state, for example to request the inclusion of at least two electrons or muons. This is very useful for analyses which require for example two electrons or muons, as more events which can directly be used can be generated, without wasting time and disk space on events which would not be eligible in any case. This improves the available statistics, and a filter efficiency is then applied to account for this when the physics analysis is carried out. The simulated data output from the generation stage is saved in the HepMC [70] format.

4.1.1 Parton Distribution Functions

PDFs [69] describe the probability density of constituent partons of the interacting protons to have a proportion x of the overall momentum. They are also dependent on the parton type (valence quark, gluon, or sea quark), and the momentum transfer Q^2 . It is not possible to calculate the PDFs perturbatively, but the dependence as a function of Q^2 for a given parton can be obtained using the DGLAP [71,72] evolution equations, using a range

of hard scattering data from both fixed target and collider experiments. These equations describe the evolution of the structure functions of the constituent quarks and gluons as a function of the “running” strong coupling α_s - here running refers to a dependence on Q^2 . Figure 4.3 shows example PDFs for u and d valence quarks, gluons, and sea-quarks, calculated with input from HERA and CTEQ at $Q^2 = 10 \text{ GeV}^2$. A range of PDF sets are used by the MC samples considered by this analysis.

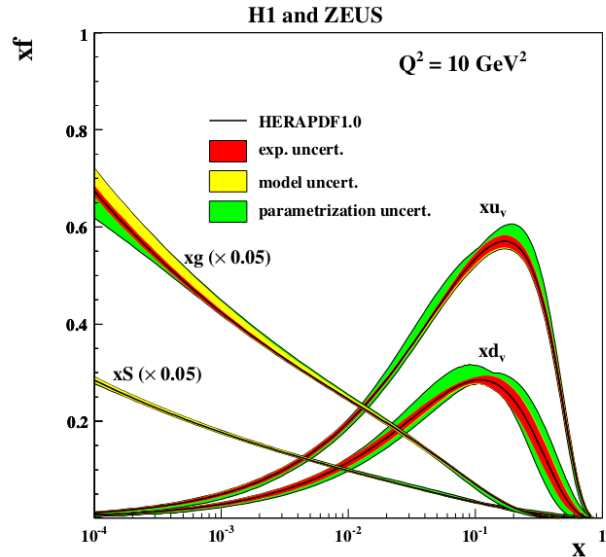


Figure 4.3: Parton distribution functions produced by HERAPDF1.0 for up and down valence quarks xu_v and xd_v , gluons xg , and sea quarks $xS = 2x(\bar{U} + \bar{D})$, using a momentum transfer of $Q^2 = 10 \text{ GeV}^2$. Taken from [73].

4.1.2 Matrix Element

The matrix element calculation involves standard perturbative quantum field theory calculations, used to simulate the high Q^2 ($> O(1 \text{ GeV})$) hard process. They are still not simple to perform however, and are usually only carried out to leading order (LO) or next-to-leading order (NLO) in an expansion in α_s . Additions can be made to the matrix element to include *hard emission*, which refers to the production of high momentum quarks and gluons in the event. This includes a number of processes; a gluon splitting into two gluons ($g \rightarrow gg$), a gluon decaying to a quark-antiquark pair ($g \rightarrow q\bar{q}$), and a quark radiating a gluon ($q \rightarrow qg$). These processes can repeat, and they will be included in the matrix element calculation as long as they are at high Q^2 .

4.1.3 Parton Showers

The processes $g \rightarrow gg$, $g \rightarrow q\bar{q}$ and $q \rightarrow gq$ also occur at lower energies, but they cannot still be modelled by the matrix element calculation due to their non-perturbative nature. They are instead dealt with by parton shower (PS) phenomenological modelling, which is valid for Q^2 values above $O(\text{GeV})$, the QCD scale. The algorithms used to simulate parton showers are based on a Markov chain [74]: using probabilities that a gluon is radiated or $q\bar{q}$ pair produced, a decision is made at each point in the chain whether or not these processes will occur. Eventually the energy of the involved partons will decrease below 1 GeV and they will undergo hadronisation, which is modelled separately.

4.1.4 Hadronisation

Modelling of bound state production, or hadronisation, relies on phenomenological modelling, as the threshold is at low energies. These models involve many more parameters than the parton showering, and they are *tuned* using data. Differing versions of hadronisation models are produced by SHERPA [75], HERWIG [76] and PYTHIA [77].

4.1.5 Underlying Event

Spectator partons, which are not involved in the hard process of an event, are referred to collectively as the Underlying Event (UE) [78]. They can hadronise to form colour-singlet states, and a number of behaviours are considered in the phenomenological models. Versions of these are provided by SHERPA, JIMMY [79] and PYTHIA. As with the standard hadronisation, the modelling involves a lot of additional free parameters, which are tuned to data. The nature and behaviour of the UE is discussed in [78].

4.2 Simulation

Generated events need to be passed through an accurate simulation of the ATLAS detector, which is modelled with GEANT4 [80]. The subsequent interaction with the detector is recorded equivalently to the real data, in the form of “hits” in the subdetectors. These provide information on where particles traversed within the detector and how much energy was deposited where. The model is initially calibrated for energy loss and radiation within the various layers of subdetectors using test beam experiment data. The detector geometry and alignment measurements are also input, as well as the location of any dead material within the detector. Simulations of the three levels of the trigger, L1, L2 and EF, are

then applied using very similar selections to the online trigger, and each event saves a pass or fail flag corresponding to each trigger. It is possible to simulate MC using fast simulation software called ATLFASTII [67], which does not run all of these stages for simulation. Instead, parameterised response functions are developed and applied for showers in the hadronic and electromagnetic calorimeters, and a simplified geometry is applied. Scattering of particles within the inner detector is considered using a simplified model too. This software is very useful for requests for large MC samples, e.g. signal requests for a very large number of events, and it has now been well validated against the full simulation samples.

4.3 Digitisation

The hits produced during simulation are subjected to a simulation of the detector response, producing digitised values for associated times, voltages, etc. Effects like noise and cross-talk within the detector are included. Hits produced from background events, for example minimum bias, beam halo and the cavern background are independent of the event itself, and so do not need to be simulated each time, but can be overlaid at this stage. The same method is used for hits resulting from pile-up. This greatly reduces the CPU required, as the simulation for these effects need only be run once and added later to each event simulation. The MC is then output in a raw data object (RDO) format, which contains equivalent information to that recorded by the detector for real data. This stage also produces a simulated data object (SDO) format, which contains a *truth* record for the samples. This retains information on the “true” identity of particles at each vertex, and any tracks and decays for these. These truth objects will not necessarily correspond exactly to the objects reconstructed from the RDO, for example an electron may be mistakenly identified as a photon. Maintaining the truth information for these particles allows analysers to study behaviour of the detector, such as the misreconstruction rates of various particles. In order to “match” a reconstructed object to the true object in the original simulation a minimum ΔR between the objects is required. This can also be used to re-trace the decay chain and identify the “parent” of a particle, using the vertex and particle ID information.

4.4 Reconstruction

Reconstruction algorithms are run on both the data and simulated events to produce physics objects (electrons, muons, hadronically decaying taus, jets and missing transverse energy) from the detector information to be used in analysis. The code makes use of reconstructed vertices and inner detector tracks, and initially defines loose enough objects to suit many analyses. More stringent requirements can then be applied in addition to suit the needs of individual analyses, which will increase the purity of selected objects but also decrease the selection efficiency.

ATLAS provides guidelines based on the performance of these varying object definitions which are used by the analysis considered here. In this section the treatment of each object will be discussed separately, including any specific selection used by this analysis.

In all cases, a discriminatory algorithm is first used to identify an appropriate seed for reconstruction by rejecting candidates which do not satisfy the required criteria. There are two forms of discriminative algorithm used here. Cut-based algorithms use physically motivated properties to distinguish “signal” from “background” candidates, optimising the cut values for the variables by hand from pure samples of both. Multivariate methods are more complex, and involve forming a discriminant from multiple physically motivated properties, which quantifies the performance of the variables given certain cut values. These values are selected using a multi-dimensional algorithm, with inputs for the signal and background samples. The cut value is chosen based on both the power to reject fake objects, and also the efficiency of selecting true objects. More than one value can be defined for varying purity of the sample (i.e. a higher proportion of true to fake objects selected) versus the selection efficiency (i.e. a higher number of the total true objects selected). The reconstruction algorithms then begin with the selected seed or seeds to construct a new object using an iterative process.

4.4.1 Inner Detector Tracks

The pixel, SCT and TRT components of the ID register “hits” as a charged particle traverses the detector, which are then reconstructed into a “track” tracing the particle’s trajectory. There are a number of different algorithms used for this, the most widely used being the “inside-out” method. This initially groups together hits in the pixel and SCT subdetectors, working outwards from the center to produce a track. If this track is then compatible with hits in the TRT detector, then these hits are also included and the track is accepted. The back-tracking algorithm uses the same approach, but in the opposite

order, working from the TRT to the SCT and Pixel detectors, and tracks can also be reconstructed using only the hits in the TRT.

The ID tracks are then matched up with candidates for charged particles produced from signals in other parts of the detector, for example the ECAL cluster for an electron. A number of selection cuts are made on the tracks before this stage to ensure that they are of the required quality. The tracks are assigned values of η and ϕ using their direction with respect to the origin in the right-handed co-ordinate system described in Section 3.3. The origin is taken to be the position of the primary interaction, as discussed in Section 4.1. In addition, d_0 is defined as the distance of closest approach between the track and the origin, and z_0 is defined as the z -plane component of d_0 . The parameter $z_0 \sin \theta$ gives the projection of d_0 onto the z -axis, and is also used. The transverse momentum p_T of a track is related to the magnetic field B , and the bending radius R , which quantifies the bending of the track trajectory due to B . The relationship is given as p_T (GeV) = $0.3 \times B$ (T) $\times R$ (m). The following cuts are applied to all tracks referred to after this point, unless otherwise specified:

- $p_T > 1$ GeV,
- $|\eta| < 2.5$,
- $d_0 < 1.5$ mm,
- $z_0 \sin \theta < 1.0$ mm,
- Number of hits in the pixel detector ≥ 2 ,
- Number of hits in the SCT detector ≥ 7 .

4.4.2 Vertices

Vertices correspond to decays of single particles, or interactions between more than one particle, and are reconstructed by extrapolating ID tracks. As the primary vertex is taken to represent the hardest interaction within the event, it is defined as the vertex with the largest summed track p_T . In the analysis discussed here, events must have at least five tracks originating from the primary vertex to be accepted, in order to suppress background from events without a p-p collision. Secondary vertices can be reconstructed from the decays of particles with sufficient lifetime for the decay length to be measurable at ATLAS, e.g. b-quarks, which travel a few millimetres. These secondary vertices will

therefore be displaced with respect to the primary vertex, due to the distance travelled by the decaying particle, and are important for identification.

4.4.3 Electron Reconstruction and Identification

Electrons are reconstructed by identifying a seed within the ECAL with the *sliding-window* algorithm [81], which is then geometrically matched to an ID track before being used to form a full “cluster”. First, a window defined as 3×7 ECAL towers is moved across the whole ECAL a step at a time in either η or ϕ , at a granularity corresponding to that of the middle ECAL layer ($\Delta\eta \times \Delta\phi = 0.025 \times 0.025$). If a window contains a local energy maximum greater than 2.5 GeV it is identified as a “pre-cluster”. If this is within a minimum $\Delta\eta$ and $\Delta\phi$ of an ID track then it is rebuilt with the cluster reconstruction algorithm. Cells of size 3×7 (5×5) are used in the barrel (endcaps) of the calorimeter, and the cluster position is varied to reflect the distribution of energy deposition. The efficiency of the cluster reconstruction was at least 96% in 2012, and increased to 99% for electrons with a transverse energy of 15 GeV or more [82]. The η and ϕ of the reconstructed electron are set as those of the corresponding matched ID track. The electron energy is calculated as the energy deposited within the cluster plus a factor to account for energy deposited outside of the cluster, referred to as leakage. This includes contributions from energy deposited prior to the ECAL, within the ECAL but outside of the cluster, and beyond the ECAL.

Objects reconstructed by the cluster algorithm are not all electrons, further cuts must be made to reduce the contributions from background processes. These can include electrons from photon conversions, pion decays, or heavy flavour hadronic decays, and misidentified hadronic jets. ATLAS uses cut-based identification algorithms for this, with three increasingly stringent options, LOOSE++, MEDIUM++ and TIGHT++ [83]. Each option defines a set of cuts which build upon those of the looser options, such that tight electrons are a subset of medium electrons, which are a subset of loose electrons. The efficiency for each of the three identifications can be seen in Figure 4.4 as a function of the number of vertices, which is a measure of pile-up, for 2011 and 2012 data. The loose selection uses cuts on the shower shape relating to energy leakage, and makes loose requirements on the track quality and cluster matching. The medium selection tightens these track quality and matching requirements, and introduces a cut on the ratio of high-threshold to normal TRT hits, which is expected to differ for electrons due to Bremstrahlung. The tight selection tightens all of these cuts, as well as rejecting events if the electron is matched to a photon

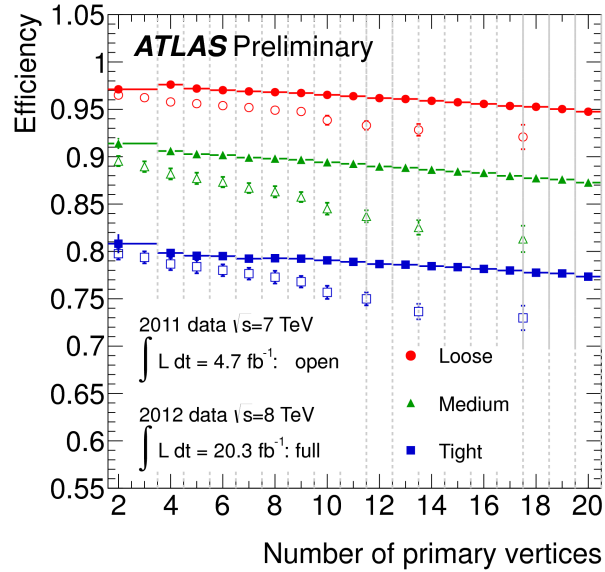


Figure 4.4: Electron reconstruction efficiency for the loose, medium and tight settings of the electron identification algorithm as a function of the number of primary vertices measured in data events for the 2011 and 2012 datasets. Taken from [82].

conversion vertex reconstructed in the ID. More detail of all three levels of identification is given in [83].

4.4.4 Muon Reconstruction and Identification

The majority of information used for muon reconstruction comes from the muon spectrometer, which is not reached by any other detectable particles, although an independent measurement of the track will be recorded in the ID, and small energy deposits within the calorimeters. Muons in this analysis are reconstructed using the STACO [84] (statistical combination) algorithm, complemented by the MuTAG [84] algorithm in regions of the detector which contain fewer chambers. STACO reconstructs straight track segments in the MS chambers using pattern recognition algorithms on the hits, beginning in the outer layer and working inwards. All tubes crossed by a segment must contain a hit for the track to be considered. These are then extrapolated back to the ID, where they are geometrically matched to independently reconstructed ID tracks, on the condition that their properties, e.g. p_T , are compatible. The statistical combination of the parameters of both tracks takes advantage of the momentum sensitivity of both the ID and MS systems, which is why this method was preferred by the analysis contained in this work. The MuTAG algorithm works in a similar but reversed way, beginning with ID tracks, which are extrapolated to the MS and then matched to straight track segments. This relies less heavily

on the hits in the muon spectrometer, which is why it is useful for regions where there are less chambers present to contain hits, or for low p_T muons which do not pass through the full MS, therefore accumulating less hits there. The energy lost between ID and MS is applied as a correction to the reconstructed muons in data, and simulated muons have their energy distributions *smeared* to reflect this. The reconstruction efficiency for muons with the methods described here was approximately 98% for muons with a p_T above 10 GeV in 2012, as can be seen in Figure 4.5, which displays results from a tag and probe study in $Z \rightarrow \mu\mu$ events.

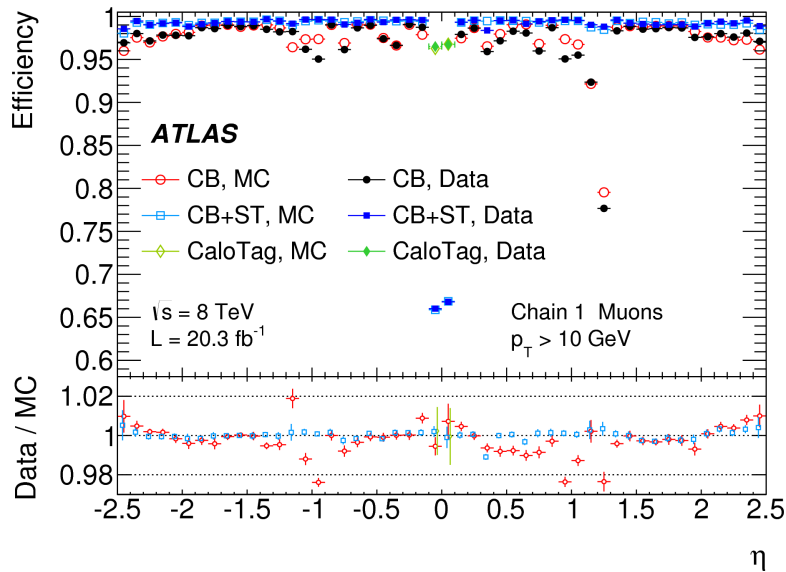


Figure 4.5: Muon reconstruction efficiency as a function of η for MC and data events in a $Z \rightarrow \mu\mu$ tag and probe study documented in [85]. CB muons refer to STACO muons, CB+ST refer to MuTAG muons and CaloTag muons are not considered in this work.

Unlike electrons, muons only have one set of identification criteria available. Their background comes mostly from charged pions, which do not tend to reach the MS, and leave much larger energy deposits in the calorimeters. Muons must pass the STACO requirements, although those in the region $|\eta| < 1.05$ can also pass the MuTAG requirements.

4.4.5 Jet Reconstruction

Jet reconstruction begins with the formation of *topological* clusters in the hadronic calorimeter [86] using the topological algorithm [87]. The algorithm begins with a seed cell, selected if it has a signal S to noise N ratio $S/N \geq 4$, and then proceeds iteratively, adding any neighbouring cells which satisfy $S/N \geq 2$. The mass of the resulting topological cluster is taken to be zero, the energy is taken to be the sum of the constituent cells, and the η

and ϕ are calculated from the weighted average of the values of the constituent cells. The topological clusters need to be calibrated before being used as input for the anti- k_T [88] recombination algorithm. Local cluster weighting (LCW) calibration first identifies topological clusters as originating from either EM or hadronic showers, and then applies the corresponding correction to the energy deposits [89] (EM scale and jet energy scale respectively). The anti- k_T algorithm then takes these clusters, and iteratively combines the two with the lowest value of $d_{i,j}$, defined as:

$$d_{i,j} = \left(\frac{1}{k_{Ti}^2}, \frac{1}{k_{Tj}^2} \right) \frac{\Delta R_{ij}}{R^2}, \quad (4.2)$$

where i and j are indices of different topological clusters, k_T is the transverse momentum of a cluster, ΔR_{ij} is the angular distance between the two clusters, and R is a specified distance parameter. For this analysis the value of R is set at 0.4 for jet reconstruction. Clusters formed from the combination of two topological clusters can still then be combined with either original topological clusters or other combined clusters, and this will continue until the distance between all the clusters is greater than R . The resulting combined objects are returned as reconstructed jets.

4.4.6 Tau Reconstruction and Identification

Taus produced during the interaction will decay within the ATLAS detector, but their lifetime is sufficiently short that this occurs within the beampipe itself. In the case that the decay products are light leptons (electrons and muons), which occurs approximately 35% [7] of the time, they are therefore virtually indistinguishable from light leptons produced promptly in the event. In this analysis any light leptons originating from taus will just be reconstructed as normal light leptons.

The only taus which will be reconstructed as taus are those which decay hadronically. The hadronic decays considered are subdivided into “one-prong” and “three-prong” decays, where the number corresponds to the charged particles produced in the decay. Decays to one-prong final states have a branching ratio of approximately 50% [7], and the branching ratio to three-prong states is approximately 15%. Decays producing more than three charged particles are not considered by ATLAS due to their very small branching ratios and the increased difficulty of reconstructing them into taus.

The tau reconstruction algorithm is seeded with anti- k_T reconstructed (and therefore calibrated) jets which have $p_T > 10$ GeV and $|\eta| < 2.5$. The η and ϕ values for the tau are taken as those of the jet, which have previously been calculated using the weighted

topological cluster values. Due to the specific mix of charged and neutral pions produced by hadronic tau decays, the energy calibration applied differs from the general hadronic energy calibration scale. It includes additional p_T and η dependent terms calculated using semi-leptonic $Z \rightarrow \tau\tau$ decays [90]. Tracks within $\Delta R < 0.2$ of the axis of the seed jet (referred to as within the *core cone*) are associated to the tau candidate, and define the number of prongs of the decay. They must also satisfy the quality criteria described in Section 4.4.1.

Tau candidates can result from mis-reconstructed muons, electrons or jets. There are three separate methods used to discriminate against these: separate boosted decision trees (BDTs) are used for the electrons and the jets, and muons are rejected with a cut-based approach [91]. These methods use a number of different track and cluster properties, including the proportion of energy deposited in the ECAL and HCAL, and the ratio of normal to high threshold TRT deposits. Full details of all variables used in these selections can be found in [92]. Tracks within $0.2 < \Delta R < 0.4$ of the central jet axis (outside of the core cone, and referred to as within the “isolation annulus”) are used for calculating some of these properties. All three discriminating algorithms are available as loose, medium or tight, with varying resultant efficiencies for one- and three-prong tau candidates [93]. An example can be seen in Figure 4.6 for the electron veto BDT efficiency as a function of p_T in $Z \rightarrow \tau\tau$ simulated events.

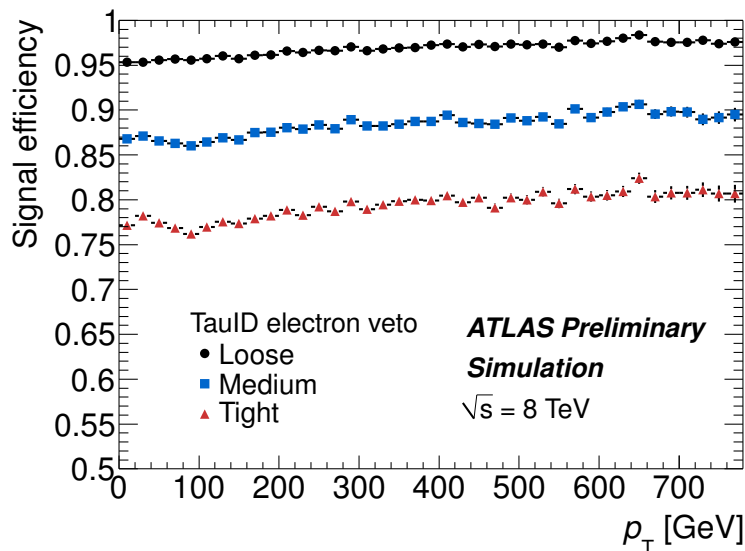


Figure 4.6: Signal selection efficiency as a function of p_T for all three settings of the electron veto BDT used for tau identification, using a tag and probe method in $Z \rightarrow \tau\tau$ MC events [94].

4.4.7 Missing Transverse Energy

The missing transverse energy refers to the magnitude of momentum imbalance in the plane transverse to the beam axis, as explained in Section 3.3. It is reconstructed by taking the vector sum of all energy deposits in the detector calorimeters and muon spectrometer [95]. These are summed in the following order for the x and y axes:

$$E_{x(y)}^{\text{miss}} = - \left(E_{x(y)}^e + E_{x(y)}^\gamma + E_{x(y)}^\tau + E_{x(y)}^{\text{jets}} + E_{x(y)}^{\text{softjets}} + E_{x(y)}^{\text{calo}\mu} + E_{x(y)}^{\text{cellout}} + p_{x(y)}^{\text{MS}\mu} \right). \quad (4.3)$$

The first three terms give the energies from topological clusters associated to electrons, photons and hadronically decaying taus respectively. The energy term for jets includes all deposits for jets with $p_T > 20$ GeV, whilst *soft jets* with $10 \text{ GeV} < p_T < 20$ GeV are added separately. Energy lost by muons within the calorimeters is included in the “calo μ ” term, and all clusters not associated to reconstructed objects are also summed and included in the “cell out” term. These terms together give the total energy deposited in the calorimeter subsystems. Finally, the sum of transverse momenta of all muons in the muon spectrometer is added, to give the total energy deposited in the detector. The energies of the electrons, muons, taus and jets have already been calibrated, and no calibration is required for the soft jet or cell out terms [95]. The missing transverse energy is now calculated using the energy in the x and y axes:

$$E_T^{\text{miss}} = \sqrt{(E_x^{\text{miss}})^2 + (E_y^{\text{miss}})^2}. \quad (4.4)$$

The azimuthal component, ϕ^{miss} is given by:

$$\phi^{\text{miss}} = \arctan \left(\frac{E_y^{\text{miss}}}{E_x^{\text{miss}}} \right). \quad (4.5)$$

4.5 Object Selection

The reconstructed objects read from data storage files are not used directly by analysers, instead they are selected using a further set of criteria. “Baseline objects” are defined first, these then undergo the “overlap removal” procedure, before having more stringent cuts applied to them to define “signal objects”. Taus are an exception to this ordering, as signal taus are used as the input to overlap removal, rather than baseline taus.

Signal objects are therefore a subset of baseline objects which have a higher purity (i.e. more of them are correctly identified) and are well isolated (well separated in space within the detector). These signal objects are used in the main body of analyses, whilst baseline objects can be used for secondary purposes like background estimation or validation. It can

be useful to look at differences between the objects passing these two levels of selection, and is particularly important for contributions to background estimates from “fake” sources. This procedure is prescribed by ATLAS and baseline objects are the selected with the same criteria for all analyses. The exact cut values and selection of cuts used for the signal object selection can vary slightly from one analysis to another. The criteria described here refer to those used by the work considered in this thesis, and are described in the order that they are applied. A summary of baseline object selection cuts can be found in Table 4.1, a summary of overlap removal in Table 4.2, and a summary of signal selection cuts in Table 4.3.

4.5.1 Baseline Electron/Muon Selection

Electrons and muons are all required to have $p_T > 10$ GeV. Muons must have a pseudorapidity $|\eta| < 2.50$, and the ECAL cluster of an electron must have pseudorapidity $|\eta| < 2.47$. In addition electrons are required to pass the MEDIUM++ identification criteria described in Section 4.4.3. Muons are required to pass a loose identification criteria within the STACO algorithm described in Section 4.4.4 and have specific hits present in the ID, as well as requests based on the number of normal hits in the TRT compared to outliers. The total number of hits n is defined as the sum of the normal and outlier hits, and the condition $n > 5$ must be satisfied. In addition, the proportion of outliers must be less than 90%.

4.5.2 Baseline Jet Selection

Baseline jets must have $p_T > 20$ GeV and $|\eta| < 4.5$, and are reconstructed as described in Section 4.4.5.

4.5.3 Baseline Tau Selection

Baseline taus are seeded from jets which must have $p_T > 10$ GeV and $|\eta| < 2.5$ as described in Section 4.4.6. The taus themselves are then required to satisfy $p_T > 20$ GeV and $|\eta| < 2.5$. They must also have either one or three tracks associated with them, corresponding to a one or three prong tau decay. No identification criteria are required at this stage.

Table 4.1: Summary of cuts used to define baseline objects in this analysis. $n_{b\text{-layer}}$ refers to the number of hits in the layer of the pixel detector closest to the beam pipe, n_{pixel} refers to the total number of hits in the pixel detector, n_{SCT} refers to the total number of hits in the SCT, and $n_{\text{holes}(\text{pix+SCT})}$ refers to the number of layers without a hit in the pixel and SCT subdetectors. $n_{\text{TRT}}^{\text{total}}$ refers to the total number of hits in the TRT, and $n_{\text{TRT}}^{\text{outliers}}$ refers to outlier hits in the TRT.

Object	η	$p_{\text{T}}/E_{\text{T}}$ [GeV]	Identification	Other
Electron	$\eta^{cl} < 2.47$	$E_{\text{T}} > 10$	medium++	
Muon	$ \eta < 2.5$	$p_{\text{T}} > 10$	STACOLoose	$n_{b\text{-layer}} \geq 1, n_{\text{pixel}} \geq 1,$ $n_{\text{SCT}} \geq 6, n_{\text{holes}(\text{pix+SCT})} < 3$ $n_{\text{TRT}}^{\text{total}} > 5, \frac{n_{\text{TRT}}^{\text{outliers}}}{n_{\text{TRT}}^{\text{total}}} < 0.9$
Jet	$\eta < 4.5$	$p_{\text{T}} > 20$	-	-
Tau	$\eta < 2.5$	$p_{\text{T}} > 20$	-	$n_{\text{tracks}} = 1 \text{ or } 3,$ charge = ± 1

4.5.4 Overlap Removal

Due to spatial resolution and reconstruction efficiency of event objects, selections on the spatial proximity of objects depending on their type are made, in order to identify them more accurately. This removes any possible ambiguity arising from multiple objects in the same spatial region of the detector. This selection is made using the ΔR variable introduced in Section 3.3. Selections are applied in the order they are described using baseline electrons, muons and jets, but signal taus, as defined in Section 4.5.8.

If two electrons are found with $\Delta R < 0.5$, the electron with the lower energy is discarded. If an electron and a jet are found within $\Delta R < 0.2$, the jet reconstruction algorithm could have also picked up the electron, and so the jet is discarded but the electron is kept. Objects identified as taus can be incorrectly reconstructed electrons or muons, and so are discarded if they are $\Delta R < 0.2$ from the closest light lepton. Leptons can sometimes be contained within jets due to semi-leptonic decays of hadrons containing the bottom or charm quarks. To neglect these, leptons within $\Delta R < 0.4$ of a jet are discarded. If a baseline electron is found within $\Delta R < 0.01$ of a baseline muon, both are discarded, as these can arise from the mis-reconstruction of a Brehmstrahlung photon as an electron. Muons are required to be separated by at least $\Delta R > 0.05$ from each other, as occasionally multiple copies of the same muon can be reconstructed. Finally, if a tau and a jet are found with $\Delta R < 0.02$ between them, the jet is discarded and the tau kept. These cuts are also summarised in Table 4.2. After overlap removal a final request is made, that any

same flavour opposite sign (SFOS) lepton pairs with an invariant mass below 12 GeV are discarded, to suppress Drell-Yan backgrounds and decays from particles with low mass.

Table 4.2: Summary of overlap removal cuts used in this analysis, in the order that they are applied.

Overlap Removal Cut	Result
$\Delta R_{e_1, e_2} < 0.05$	Lowest p_T electron discarded
$\Delta R_{e_1, jet} < 0.02$	Jet discarded
$\Delta R_{\tau, (e/\mu)} < 0.02$	Tau discarded
$\Delta R_{(e/\mu), jet} < 0.04$	Light lepton discarded
$\Delta R_{e, \mu} < 0.01$	Both discarded
$\Delta R_{\mu_1, \mu_2} < 0.05$	Both discarded
$\Delta R_{\tau, jet} < 0.02$	Jet discarded

4.5.5 Signal Electron Selection

Signal electrons are now required to pass the more stringent TIGHT++ [83] identification criteria, in addition to isolation and d_0 and $z_0 \sin \theta$ conditions:

$$\frac{|d_0|}{\sigma(d_0)} < 5, z_0 \sin \theta < 0.4 \text{ mm.} \quad (4.6)$$

The isolation conditions for the electrons are two-fold, with one requirement for the track and one for the cluster in the calorimeter. The track isolation requires that:

$$\frac{p_T^{30}}{E_T} < 0.16, \quad (4.7)$$

where E_T is the transverse energy of the electron, and p_T^{30} is the combined transverse p_T of all tracks within $\Delta R \geq 0.3$ of the electron track. These tracks must satisfy the following cuts to be included -

- $p_T > 1 \text{ GeV}$
- $|d_0| < 1 \text{ mm}$
- $|z_0 \sin \theta| < 1 \text{ mm}$
- At least one hit in the ID b-layer
- At least seven hits in the ID silicon detectors.

The cluster isolation requires:

$$\frac{E_T^{30\text{corr}}}{E_T} < 0.18, \quad (4.8)$$

where the energy-density corrected isolation, $E_T^{30\text{corr}}$, is defined as:

$$E_T^{30\text{corr}} = E_T^{30} - A \times N_{\text{vtx}}. \quad (4.9)$$

N_{vtx} is the number of vertices with at least 5 associated tracks and A is a scale factor to account for energy leakage in the calorimeter and additional deposits from pile-up collisions. Values of 20.15 MeV for data and 17.97 MeV for MC simulation are used, due to differences between the modelling and data measurement. E_T^{30} is defined equivalently to p_T^{30} , as the combined E_T of all tracks within $\Delta R \geq 0.3$ of the electron track. Baseline electrons must satisfy all of these criteria in order to be accepted as signal electrons.

4.5.6 Signal Muon Selection

Signal muons do not require any additional identification criteria, but they do have similar cuts on $|d_0|$ and $|z_0 \sin \theta|$ defined as:

$$\frac{|d_0|}{\sigma(d_0)} < 3, z_0 \sin \theta < 1mm. \quad (4.10)$$

They also have an isolation requirement of:

$$\frac{p_T^{30\text{corr}}}{p_T} < 0.12, \quad (4.11)$$

where similarly

$$p_T^{30\text{corr}} = p_T^{30} - A \times N_{\text{vtx}}, \quad (4.12)$$

and for muons the values used for A are 10.98 MeV for data and 6.27 MeV for MC simulation. Only baseline muons surviving overlap removal and which pass all of these criteria are included within the subset of signal muons.

4.5.7 Signal Jet Selection

Baseline jets are further required to satisfy the cuts

$$p_T > 20 \text{ GeV}, |\eta| < 2.5 \text{ and } \text{JVF} > 0.5, \quad (4.13)$$

where JVF refers to the Jet Vertex Fraction, which gives a measure of the probability that the jet originated from a given vertex. This is used in order to discriminate between jets originating from the primary interaction, and those produced by pile-up. The JVF requirement is only applied to jets which have $p_T < 50$ GeV and $|\eta| < 2.4$.

4.5.8 Signal Tau Selection

Signal taus are required to pass the additional medium [93] identification criteria. This requires the muon veto to be passed, in addition to the loose definition of the electron BDT selection, and the medium Jet BDT selection, all of which are described in Section 4.4.6. All baseline taus passing these criteria are defined as signal taus, and these are then used as input for the overlap removal described in Section 4.5.4.

Table 4.3: Summary of cuts used to define signal objects in this analysis. These cuts are applied to objects which already satisfy the baseline cuts summarised in Table 4.1 and with the exception of taus, the overlap removal procedure summarised in Table 4.2.

Object	η	Identification	Isolation	Other
Electron	-	tight++	$\frac{p_T^{30}}{E_T} < 0.16, \frac{E_T^{30\text{corr}}}{E_T} < 0.18$	$\frac{ d_0 }{\sigma(d_0)} < 5,$ $z_0 \sin \theta < 0.4 \text{ mm}$
Muon	-	-	$\frac{p_T^{30\text{corr}}}{p_T} < 0.12$	$\frac{ d_0 }{\sigma(d_0)} < 3,$ $z_0 \sin \theta < 1 \text{ mm}$
Jet	$\eta < 2.5$	-	-	JVF > 0.5 (applied if $p_T < 50$ and $\eta < 2.4$)
Tau	-	medium - pass muon veto, ElectronBDTLoose and JetBDTMedium	-	-

Chapter 5

Search for SUSY in Events with Four or More Leptons

A four-lepton final state can be produced at the LHC by many supersymmetric scenarios, and has the benefit of very low background rates from SM processes. This chapter details the strategies developed to search for the RPV, $\tilde{\chi}_2^0\tilde{\chi}_3^0$ and GGM scenarios described in Section 5.2 - all of which produce four leptons and missing transverse energy. The following two chapters will then detail the background estimation methods and systematic uncertainty treatment (6) and the results and interpretation of them (7). Everything shown in this thesis uses the full ATLAS dataset from 2012, produced at a centre-of-mass energy of 8 TeV. The results for this search were published in a paper in the Physical Review D in May 2014 [1]. Previous versions of the analysis were also made using the 2011 dataset at a centre-of-mass energy of 7 TeV, published in the Journal of High Energy Physics [96], and with an earlier subset of the 2012 dataset, documented in an ATLAS conference note [97]. I was involved in the production of all of these versions, and present the most recent analysis here, as it is an updated, improved and extended version of the earlier work.

These three chapters will place more emphasis on areas of the analysis for which I was responsible, whilst providing an overview for the reader to follow. I was responsible for optimising the search strategy and all plots and tables included in this chapter were produced by me for documentation of the analysis. I was also responsible for the MC estimates for the number of events in the search regions, and the composition of the backgrounds (Section 6.1). I produced systematic uncertainties for some of the simplified model samples, as discussed in more detail in Appendix B. I was a main contributor to the introduction of new simplified model scenarios and the generation of the associated MC,

as also detailed in Appendix B. I carried out studies for the initial inclusion of tau leptons (earlier versions of this analysis used only electrons and muons) which affected the trigger choices discussed in Section 5.3.1 and object selection for taus, as detailed in Section 4.5. Content which was not produced myself is clearly labelled as the work of other analysis team members, all other included results have been produced by myself.

5.1 Analysis Overview

SM background processes which result in four lepton final states are not very abundant, which makes this a powerful channel with which to search for SUSY scenarios which have lower E_T^{miss} or object p_T in their final states. Events from SM background processes can be suppressed with a well-chosen set of cuts yielding simple, “clean” search regions with few expected background events.

When discussing this analysis, the term lepton refers to electrons, muons, or hadronically decaying taus (taus for short), whilst electrons and muons are also collectively referred to as “light leptons”. Selected events are split into *channels* containing different light lepton and tau multiplicities. Further kinematic requirements are then made to discriminate between signal and background - leading to the definition of a number of dedicated “Signal Regions” (SRs), detailed in Section 5.4. The background contributions in these SRs are estimated using a combination of MC and data-driven methods, described in detail in Section 6.2. The performance of these estimation methods will later be “validated” in separate dedicated regions containing a high proportion of background events, as described in Section 6.4.

5.2 Supersymmetry Signal Scenarios

5.2.1 $\tilde{\chi}_2^0\tilde{\chi}_3^0$ Simplified Models

Supersymmetry models which solve the hierarchy problem most cleanly (referred to as “natural” models) generally require relatively light electroweak sparticles. Neutralinos can decay into final states which contain two leptons, so pair production of neutralinos is a SUSY process which can be targetted with the four lepton analysis more effectively than any lower lepton multiplicity. A set of simplified models are constructed to consider pair production of mass-degenerate $\tilde{\chi}_2^0$ and $\tilde{\chi}_3^0$ particles, where these are assumed to be the next-to-lightest sparticles (NLSP)s. These then decay to the LSP, which is the lightest neutralino, $\tilde{\chi}_1^0$, as is commonly the case. R-parity is conserved in the considered models,

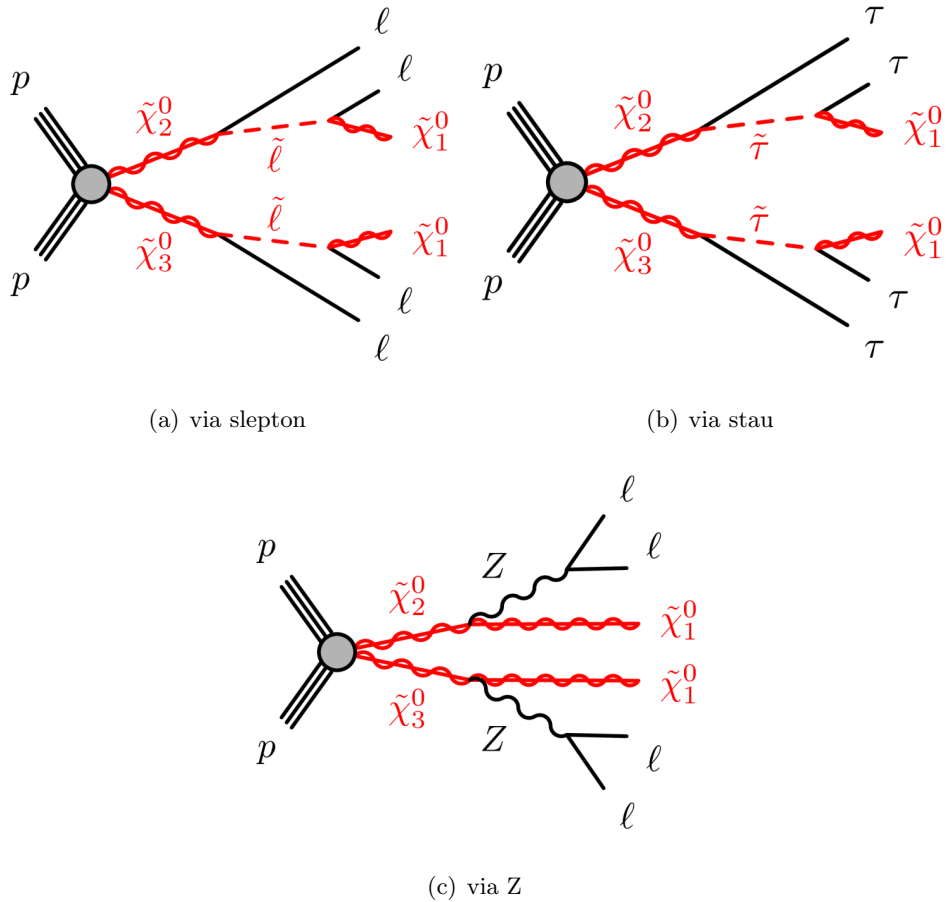


Figure 5.1: Feynman diagrams of the decays considered for simplified RPC models with $\tilde{\chi}_2^0 \tilde{\chi}_3^0$ production.

so the LSP is stable. Three possible decay mechanisms are considered for the NLSPs: via right-handed sleptons, via staus, and finally via Z bosons. All of these produce a total of four or more leptons in the final state, as illustrated by the Feynman diagrams in Figure 5.1.

The mixing of the neutralinos (described in Section 2.7) is such that the $\tilde{\chi}_1^0$ is bino-like and both $\tilde{\chi}_2^0$ and $\tilde{\chi}_3^0$ are higgsino-like. Their decay branching ratios are set to 100% via the respective process. The mass of the co-NLSPs $\tilde{\chi}_2^0$ and $\tilde{\chi}_3^0$ is varied, along with the mass of the $\tilde{\chi}_1^0$, to cover a range of values. The collection of possible scenarios generated by this variation are referred to as a *grid*, and the same nomenclature is used for the collections of points of the other SUSY signals.

For the slepton and stau models the intermediate sparticle masses are set to be halfway between the LSP and NLSP masses, and the masses of all other sparticles are set to 1 TeV. All other parameters introduced in this formulation of SUSY are set to values which are favourable for production and detection of this process at the LHC and agree with any

existing experimental data, e.g. the Higgs mass. The mass parameter space for each scenario which is considered in these models is listed in Table 5.1. The range of masses considered for each model is based on sensitivity studies discussed in Appendix B and reflect the regions of the parameter space where the four lepton analysis is able to make a statistically meaningful statement about the model.

Table 5.1: Masses considered in each of the three $\tilde{\chi}_2^0\tilde{\chi}_3^0$ models.

Decay Mode	$\tilde{\chi}_1^0$ Masses [GeV]	$\tilde{\chi}_{2/3}^0$ Masses [GeV]	Mass Splittings [GeV]
slepton	0-575	110-812.5	20-750
stau	0-100	100-350	50-300
Z	0	100-400	100-400

5.2.2 R-parity Violating Simplified Models

A set of simplified models that include decays resulting from non-zero R-parity violating couplings are also considered. When the RPV superpotential terms defined in Equation 2.16 are included in the MSSM, an additional 48 parameters are introduced. Due to the experimental restrictions on multiple non-zero couplings discussed earlier, and the desire for multiple leptons in the final state, only the coupling λ_{ijk} is given a non-zero value. This also means that sparticles can still be pair produced at the LHC for this scenario, making a multilepton final state easier to achieve from SUSY decay.

A bino-like $\tilde{\chi}_1^0$ is selected as the LSP. As the model considered violates R-parity, the decay of pair produced $\tilde{\chi}_1^0$ s would already give a four lepton signature. However, the pair production cross-section for $\tilde{\chi}_1^0$ at the LHC is rather small, and so a selection of different NLSPs with higher pair production cross-sections are also included in the process. All other sparticle masses are set to 4.5 TeV. The four different NLSPs and their corresponding fixed cascade decays to the LSP are given below.

- Wino: $\tilde{\chi}_1^\pm \rightarrow W^\pm\tilde{\chi}_1^0$
- Slepton: $\tilde{\ell} \rightarrow l\tilde{\chi}_1^0$ (where l is e , μ or τ .)
- Sneutrino: $\tilde{\nu}_l \rightarrow \nu_l\tilde{\chi}_1^0$ (where l is e , μ or τ .)
- Gluino: $\tilde{g} \rightarrow q\bar{q}'\tilde{\chi}_1^0$ (q, q' can be u, d, c, s .)

Figure 5.2 shows the Feynman diagrams for each of these processes. For the slepton NLSP, left and right-handed sleptons are considered separately, as the cross-section is different

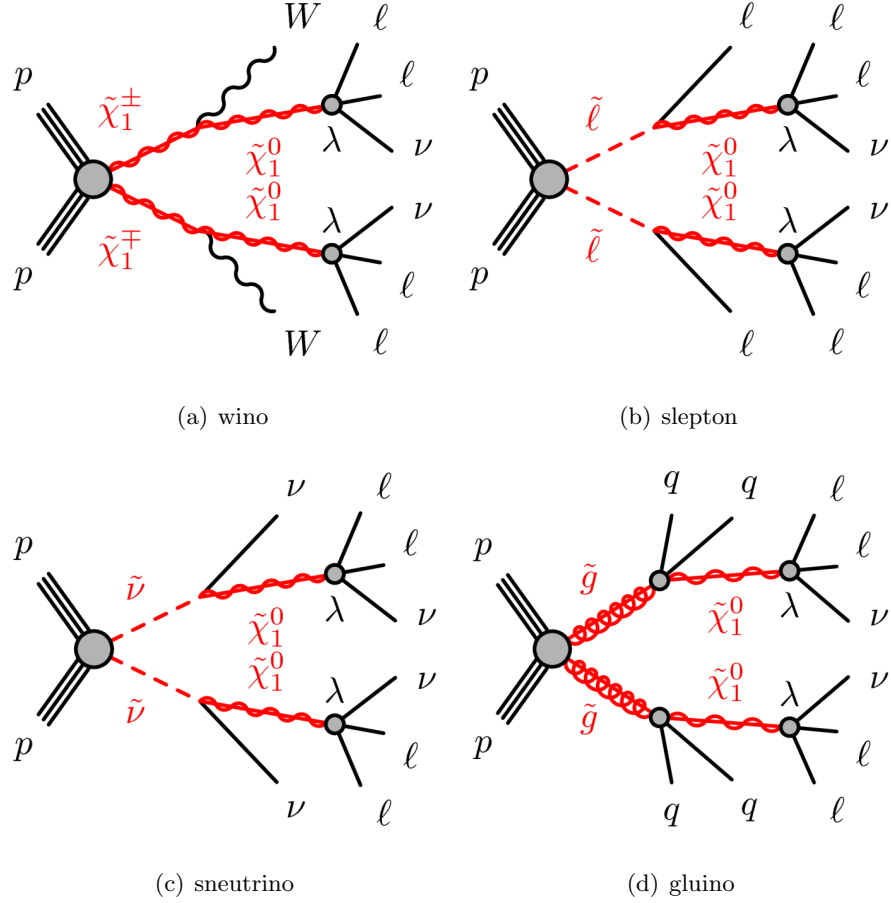


Figure 5.2: Feynman diagrams of the simplified RPV model cascade decays for all NLSPs considered.

for the two cases, resulting in a different phenomenology. The SUSY decays all proceed via the electroweak interaction, with the exception of the case with a gluino NLSP. The different NLSP choices give different final state products in addition to those from the LSP: the wino produces a W boson in the decay chain, the slepton produces another light lepton, the sneutrino produces a neutrino and the gluino produces jets. The LSP decay products always include two leptons and a neutrino, but the flavours of these products depends on the indices of the coupling λ_{ijk} . The decay products resulting from all possible indices is given in Table 5.2, where each has two possible final states depending on which flavour the neutrino takes. The non-zero couplings considered for these models are λ_{121} , λ_{122} , λ_{133} and λ_{233} , which cover instances where the final state can contain electrons and muons, electrons and taus, and muons and taus. An example of the resulting final states which can be produced for a non-zero λ_{121} coupling can be seen in Figure 5.3.

The LSP and NLSP masses are the varied parameters for every model, with the other parameters remaining fixed. There are a total of twenty different grids resulting from

Table 5.2: Decay products resulting from all possible i, j, k values of λ_{ijk} .

	$i, j = 1, 2$	$i, j = 1, 3$	$i, j = 2, 3$
$k = 1$	$ee\nu/e\mu\nu$	$ee\nu/e\tau\nu$	$e\mu\nu/e\tau\nu$
$k = 2$	$e\mu\nu/\mu\mu\nu$	$e\mu\nu/\mu\tau\nu$	$\mu\mu\nu/\mu\tau\nu$
$k = 3$	$e\tau\nu/\mu\tau\nu$	$e\tau\nu/\tau\tau\nu$	$\mu\tau\nu/\tau\tau\nu$

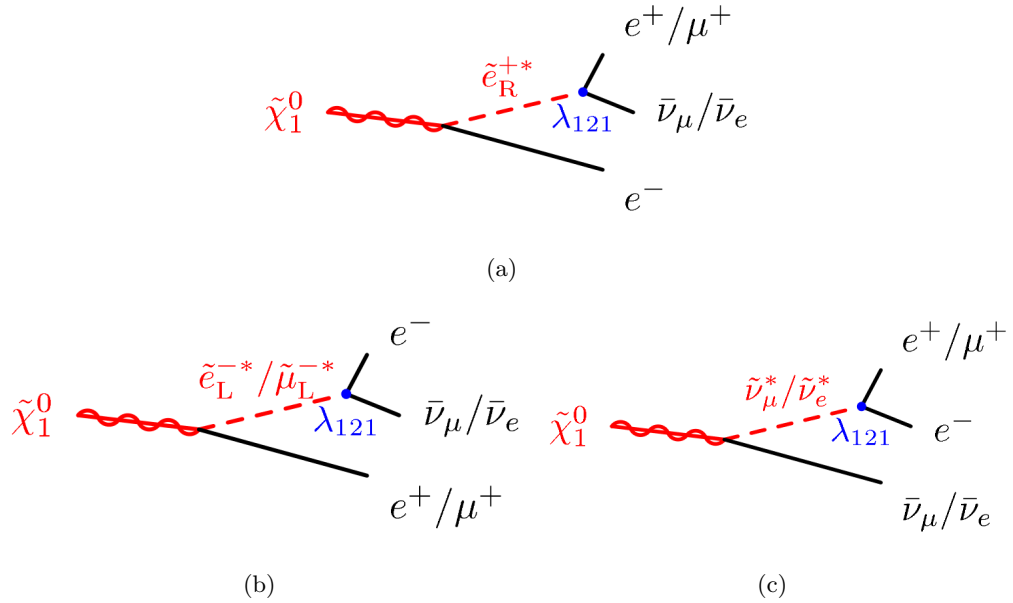


Figure 5.3: Illustration of $\tilde{\chi}_1^0$ decays for a non-zero λ_{121} coupling. In all cases, the charge conjugate decay is implied.

the combination of each of the five NLSP choices with each of the four possible non-zero couplings. The mass ranges considered for these grids depend on the expected sensitivity of the analysis and existing limits if these have been set. The mass ranges are summarised for each grid in Table 5.3.

5.2.3 General Gauge Mediated Simplified Models

General Gauge Mediation (GGM) [98] is a generalised form of gauge-mediated supersymmetry breaking (GMSB) [99]. The symmetry breaking takes place in a *hidden sector* and the *messenger* fields required to couple to both the hidden and separate SM sectors are gauge fields. GGM maintains the properties which are shared by all gauge mediated SUSY models, whilst avoiding any of the specifics which vary from scenario to scenario. The hidden sector is entirely arbitrary, and neither the mechanism of SUSY breaking nor the interaction coupling the gauge fields to the hidden sector is specified. The key assumption that the hidden sector decouples as the MSSM gauge couplings approach zero is

Table 5.3: Masses considered in each of the RPV grids.

NLSP	λ_{ijk} indices	NLSP Mass Range [GeV]	$\tilde{\chi}_1^0$ Mass Range [GeV]
wino	all	200-1000	10-990
slepton	all	75-600	10-590
sneutrino	121,122	75-600	10-590
sneutrino	133,233	75-500	10-490
gluino	all	500-1700	490-1690

upheld, and the LSP is a massless gravitino. The masses of the supersymmetric particles result from higher order interactions with the messenger particles. The mass hierarchy has lighter electroweak sparticles and heavier coloured sparticles.

There are still a number of free parameters in GGM models, some of which are fixed in the scenarios considered, while others are varied. Two sets of models are considered here, and for both cases the gaugino masses M_1 and M_2 are set to 1 TeV. The properties of the NLSP have a significant impact on phenomenology. In this case we consider the higgsino-like $\tilde{\chi}_1^0$, $\tilde{\chi}_2^0$ and $\tilde{\chi}_1^\pm$ as co-NLSPs. The average decay length of the NLSP, $c\tau_{NLSP}$, another free parameter, is set to 0.1 mm for both grids. The gluino is also set to be light, and its mass $m_{\tilde{g}}$ (M_3) is varied within a certain range, along with the higgsino mass parameter μ . The chosen values of μ are such that the $\tilde{\chi}_1^0$ NLSP decay dominates.

For the first grid, the ratio of Higgs VEVs is set to $\tan\beta = 1.5$. This results in a 97% branching ratio of the neutralino to a Z boson and the gravitino ($\tilde{\chi}_1^0 \rightarrow Z\tilde{G}$). For the second grid $\tan\beta = 30$. This gives a higher branching ratio of the NLSP to a Higgs boson and the gravitino ($\tilde{\chi}_1^0 \rightarrow h\tilde{G}$) which increases with increasing μ . Values of μ from 200 GeV to 900 GeV are considered, and gluino masses from 400 (600) GeV to 1.2 TeV for the $\tan\beta = 30$ (1.5) grid. Figure 5.4 shows weak and strong production processes which occur in the GGM. While the strong production dominates in the bulk of the grid, at higher gluino masses the contribution from weak production increases.

5.2.4 Signal MC Samples

Samples for the $\tilde{\chi}_2^0\tilde{\chi}_3^0$ models were generated using MADGRAPH [100], additional details of the generation of these samples are given in Appendix B, where personal contributions are also highlighted. The RPV samples were generated using HERWIG++2.5.2 [101], and the GGM samples were generated using PYTHIA [77]. All three scenarios used the PDF set CTEQ6L1 [102] and have cross-sections calculated to next-to-leading order (NLO)

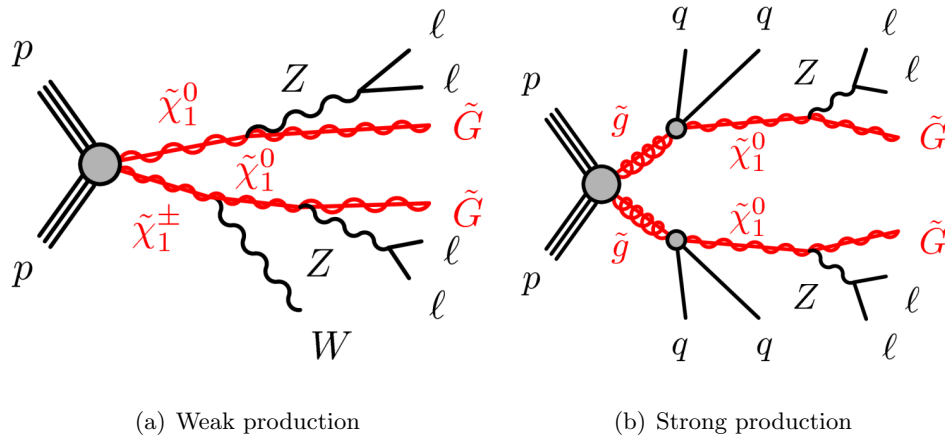


Figure 5.4: Feynman diagrams of production processes in the GGM models.

produced in PROSPINO2 [103]. Each sample corresponds to a sample with a different set of values for the varied parameters of that model, for example specific masses for the LSP and NLSP, defining a point on the parameter space. If multiple values of an additional parameter are considered, then a grid of points is defined for each additional parameter value. For example for the RPV samples, different grids are defined for different values of the i, j, k indices in the λ_{ijk} coupling parameter. The considered mass value ranges for each of these grids depends on the expected sensitivity, so this is different for grids with different phenomenology. Datasets are produced with parameter values which are designed to give finer granularity of MC in the regions of parameter space which are more important for the analysis. For example a grid may have datasets separated by 20 GeV in LSP and NLSP mass parameter values for the majority of the grid, but use a 10 GeV spacing in the region where the sensitivity is expected to vary more as a function of these parameters.

5.3 Dataset and Event Selection

Data used for this analysis was collected during 2012 at $\sqrt{s} = 8$ TeV, totalling an integrated luminosity of $\mathcal{L} = 20.3 \text{ fb}^{-1}$ which satisfied the so-called “Good Runs List” data quality criteria. These criteria require the LHC beams to be stable, all of the ATLAS subdetectors to have normal operating voltages, and the toroidal and solenoidal magnetic fields to be of the correct strength. The dataset is subdivided into *periods* consisting of a specific set of runs, which were labelled A-M from the beginning to end of running in 2012. Periods F and K did not involve any LHC collisions, and period M involved heavy ion collisions, rather than p-p collisions. These three periods are therefore disregarded from the total

dataset considered.

Events of interest are then selected using leptonic triggers, as detailed in Section 5.3.1. Further data quality event selection cuts, referred to as “cleaning cuts” are also applied, as described in Section 5.3.2. The combination of these event selection cuts and the object selection described in Section 4.5 is often referred to as the “preselection” - after which the analysis specific event selection is applied.

5.3.1 Trigger

The set of trigger chains used to select events for this analysis require signatures containing either one or two light leptons, applying the lowest p_T thresholds possible to the lepton p_T . A logical OR combination of all trigger chains listed in Table 5.4 is made. For any event passing one of these trigger chains, the light leptons in the event must also pass the corresponding offline p_T thresholds in order to be accepted. These thresholds are chosen such that the particle p_T is within the plateau of efficiency for the trigger it has fired. These offline values therefore vary depending on the trigger selections, and are listed in Table 5.4 for all selections considered.

If a specific trigger lists “loose”, “medium” or “tight”, this applies a criteria similar to the offline identification used - see Section 4.5. The “vh” label identifies triggers where electrons are vetoed at the L1 stage if they have left significant deposits within the hadronic calorimeter. An “i” in the chain name refers to an isolation requirement, specifically that the sum of track p_T within $\Delta R < 0.2$ of a candidate lepton must be less than 10% (12%) of the lepton p_T if it is an electron (muon).

Although the analysis presented here includes events with taus, triggering using hadronically decaying tau leptons is not included. This is because tau-based triggers have a slower increase in efficiency with increasing object p_T (“turn-on”). Additionally, the taus used for the background estimation methods (described in Section 6.2) require very loose identification criteria, which are not met by the trigger, therefore resulting in a bias.

5.3.2 Event Cleaning

“Event cleaning” refers to the removal of events where the quality of the reconstruction is lowered or partial due to a malfunctioning in some part of the detector, or any other condition that would invalidate the event for physics analysis. These events are removed with ATLAS recommended procedures for all analyses before any analysis specific cuts are made.

Table 5.4: Light lepton trigger chains used for this analysis, all combined using a logical OR. Where two numbers are given in the Offline P_T Threshold column, the first refers to the lepton listed first in the corresponding trigger chain name, and the second number applies to the lepton listed second. In some instances both leptons have the same threshold applied, and are preceded by a 2 in the chain name.

Object Type	Trigger Detail	Offline P_T Threshold [GeV]
Single e	EF_e24vhi_medium1	25
Single μ	EF_mu24i_tight	25
Double e	EF_2e12Tvh_loose1	14, 14
	EF_e24vh_medium1.e7_medium1	25, 10
Double μ	EF_2mu13	14, 14
	EF_mu18_tight_mu8_EFFS	18, 10
Combined $e\mu$	EF_el2Tvh_medium1_mu8	14, 10
	EF_mu18_tight.e7_medium1	18, 10

The event cleaning procedure removes events where a timing, trigger and control processing partition has restarted, resulting in missing detector information, or where errors or bursts of noise have been reported in the LAr calorimeters, as well as events where data from the Tile calorimeter has become corrupted. Events where jets point to some problematic (η, ϕ) region of the Tile calorimeter are also vetoed. Jets are rejected if they could potentially have originated from detector effects. Background from cosmic muons is suppressed by rejecting events where muons have either an impact parameter d_0 satisfying $|d_0| > 0.2$ mm, or a projection of the impact parameter onto the z axis $z_0 \sin \theta$ satisfying $z_0 \sin \theta > 1$ mm. Additionally, to suppress events where muons have been poorly reconstructed due to mis-measurement, they are required to satisfy

$$\frac{\sigma_{q/p}}{|q/p|} \geq 0.2, \quad (5.1)$$

where q is the muon charge, p is muon momentum, and $\sigma_{q/p}$ is the uncertainty on the measurement of q/p .

5.3.3 Standard Model Background Samples

Once events with at least four leptons have been selected, contamination from SM processes is very small. The SM processes that contribute to the four lepton background are all detailed below, along with information on the generators used for each sample and the

corresponding cross-section calculation. A summary of relevant information can be found in Table 5.5. The composition of the SM backgrounds varies greatly depending on the number of light leptons and taus in the event.

Diboson processes $WZ/W\gamma^*$ and $ZZ/Z\gamma^*$ were simulated using POWHEG [104] at NLO, and showering was carried out by PYTHIA8 [105]. In addition, gg2ZZ [106] was used to generate the process $gg \rightarrow ZZ/Z^*$, using HERWIG [76] for showering. These samples include the following final states $4e$, 4μ , $2e2\mu$, $2e2\tau$ and $2\mu2\tau$ (4τ is not included). For calculating generator uncertainties (described in Section 6.3) samples were also generated for $ZZ/Z\gamma^*$ using aMC@NLO [107]. The triboson processes $WWW \rightarrow \nu\nu\nu\nu$, $ZWW \rightarrow \nu\nu\nu\nu$ and $ZZZ \rightarrow \nu\nu\nu\nu$ were generated with MADGRAPH [100] at LO, and processes resulting in two bosons and two jets were simulated using SHERPA [75] at LO but normalised to NLO. The processes $t\bar{t} + Z(+ \text{jets})$ and $t\bar{t} + W(+ \text{jets})$ were generated by ALPGEN [108] at LO, and MADGRAPH was used to generate samples for $t\bar{t} + W$, tWZ and tZ . Samples for $t\bar{t} + Z(+ \text{jets})$ and $t\bar{t} + W(+ \text{jets})$ were also generated with MADGRAPH for use calculating generator systematic uncertainties as described in Section 6.3. Production of $t\bar{t}$ was simulated using POWHEG, and single tops with MC@NLO and ACERMC [109]. The cross-sections for top pair production were calculated at NNLO with NNLL corrections, and the single top cross-sections were calculated at NNLO+NNLL precision. Samples of $Z/\gamma^* + \text{jets}$ and $W + \text{jets}$ processes are generated using ALPGEN and PYTHIA6 [77]. The LO ALPGEN cross-sections are scaled to NNLO. For $Z/\gamma^* + \text{LF jets}$ samples where the invariant mass of the produced leptons satisfies $10 \text{ GeV} < m_{ll} < 60 \text{ GeV}$, referred to as ‘‘Drell-Yan’’ production, ALPGEN and HERWIG were used. Higgs samples including five different production mechanisms are included: gluon fusion (ggF), vector boson fusion (VBF), associated production with a W (HW) or Z (HZ), and associated production with a $t\bar{t}$ pair ($t\bar{t}H$). These were generated using a mix of POWHEG+PYTHIA8 and just PYTHIA8, to NNLO QCD and NLO EW precision, except for $t\bar{t}H$ which is only to NLO QCD.

5.4 Signal Region Optimisation

Starting from events that pass the basic quality requirements, *signal regions* (SRs) to discriminate SUSY scenarios from known SM processes can then be defined. These regions require a set of selections or cuts on various properties of the event, which are optimised using the significance, Z_N . This gives a statistical measure of how relevant an observation

Table 5.5: Summary of MC background samples used in this analysis, including the generator used for production and the precision to which the cross-section is calculated.

Process	Generator	Cross-section
WZ, ZZ $gg \rightarrow ZZ$	Powheg + Pythia8 gg2ZZ + Herwig	NLO QCD
WWW, ZWW, ZZZ $VVV \rightarrow VVjj$	MadGraph Sherpa	LO + NLO normalisation
$t\bar{t}Z, t\bar{t}W$ $t\bar{t}WW, tWZ, tZ$	ALPGEN MadGraph	LO + NLO normalisation
$t\bar{t}$ t (includes Wt)	POWHEG MC@NLO + AcerMC	NNLO + NNLL corrections
$Z/\gamma^* + \text{jets}, W + \text{jets}$ $Z/\gamma^* + \text{jets DY}$	ALPGEN + Pythia6 ALPGEN + Herwig	LO scaled to NNLO
ggF, VBF higgs HW, HZ $t\bar{t}H$	PowhegPythia8 Pythia8 Pythia8	NNLL QCD + NLO EW NNLL QCD + NLO EW NNLO QCD

would be for a given region, and is defined as:

$$Z_N = \sqrt{2} \operatorname{erf}^{-1}(1 - 2p(S + B, B, \delta B)), \quad (5.2)$$

where erf is the error function, p is the background only p-value, S is the number of expected signal events, B is the number of expected background events and δB is the uncertainty on the background MC estimation, assumed to be 50% based on statistical uncertainties for previous four lepton analyses. The p-value gives the probability of observing the number of signal events expected or higher, given the background-only hypothesis. The background-only hypothesis here is the SM, represented by the MC samples. Therefore the larger the gap between the number of events expected from SM and signal is, the higher the significance will be. The observed number of events is set by summing the number of expected background and signal events. Using this p-value estimate to calculate the significance gives a measure of how strong a statistical statement could be made if the expected signal was observed in a given SR. The aim of the optimisation is to maximise this property for each region, based on the events observed for MC background and signal samples. This is done using MC predictions, adopting a *blind* analysis strategy - meaning the data in the signal regions is not observed until these SRs have been decided based on expectation only. Data is used in other areas of the analysis for the background estimation (control regions) and background validation (validation regions) but must not

overlap with the data within these regions.

5.4.1 Optimisation procedure

Events are first classified into separate channels depending on the light lepton and tau multiplicities, with a total of four leptons always required overall. Additional leptons may be allowed but are never explicitly requested. Three channels are considered: four or more light leptons ($4\ell 0\tau$); three light leptons plus one or more taus ($3\ell 1\tau$); and two light leptons plus two or more taus ($2\ell 2\tau$). Channels requiring more than two taus are not considered. These channels are then further subdivided according to additional criteria in order to target scenarios characterised by a range of properties, such as the amount of missing transverse energy in the event. A total of nine signal regions are defined, and their main properties and targeted SUSY scenarios are listed in Table 5.6. A detailed description of the optimisation for each signal region will be covered in the following. Firstly the regions which include a Z boson veto will be discussed in Section 5.4.2, split by lepton multiplicity and into the “a” or “b” regions. Then the regions which request the presence of a Z boson will be discussed in Section 5.4.3, split by lepton multiplicity. Finally, the exact selection criteria chosen for each of the nine signal regions will be summarised in Section 5.5.

Table 5.6: Summary of signal regions used in this analysis. The names are related to the cuts; the number following SR denotes the required tau multiplicity, Z or noZ refers to either a Z-veto or Z request respectively, and the a and b regions denote a softer and harder set of cuts, targeting slightly different scenarios.

Channel	Signal Region	Z boson	E_T^{miss}	m_{eff}	Target
$4\ell 0\tau$	SR0noZa	Veto	Moderate	-	$\tilde{\chi}_2^0 \tilde{\chi}_3^0$ via ℓ
	SR0noZb	Veto	High	High	RPV
	SR0Z	Request	High	-	GGM (and $\tilde{\chi}_2^0 \tilde{\chi}_3^0$ via Z)
$3\ell 1\tau$	SR1noZa	Veto	Moderate	-	$\tilde{\chi}_2^0 \tilde{\chi}_3^0$ via $\tilde{\tau}$
	SR1noZb	Veto	High	High	RPV
	SR1Z	Request	High	-	-
$2\ell 2\tau$	SR2noZa	Veto	Moderate	-	$\tilde{\chi}_2^0 \tilde{\chi}_3^0$ via $\tilde{\tau}$
	SR2noZb	Veto	High	High	RPV
	SR2Z	Request	High	-	-

5.4.2 Z Boson Veto

Events containing four or more leptons are most commonly produced by background processes involving the leptonic decay of Z bosons. It may therefore be beneficial to implement a so-called “Z-veto” algorithm in order to suppress these background processes, for signal events that do not themselves contain leptonically decaying Z bosons. A pair of light leptons from a Z boson decay are required to have the same flavour but opposite charge (i.e. e^-e^+ or $\mu^-\mu^+$), in order to conserve lepton number. The invariant mass of these lepton pairs has a prominent peak corresponding to the Z boson mass, 91.2 GeV, which from now on will be referred to as m_Z . The Z-veto makes use of these properties in order to tag and possibly reject events containing leptons which were likely produced by a Z boson decay. The variable m_{SFOS} is defined as the invariant mass of a same-flavour opposite-sign (SFOS) light lepton pair. All possible SFOS combinations within an event are considered, and the pair with invariant mass m_{SFOS} closest to m_Z is examined for further selection. If the mass difference $|m_{\text{SFOS}} - m_Z|$ for the selected pair is less than 10 GeV and the Z-veto is implemented, the event is rejected.

The Z boson can also decay radiatively to produce a total of four light leptons, as seen in Figure 5.5, and in some instances, one of these leptons will be too low in p_T to be reconstructed. These radiative leptonic Z boson decays will contribute to the background in the $4\ell 0\tau$ and $3\ell 1\tau$ channels. In order to suppress these processes an “extended” version of the Z-veto is also defined. In addition to considering m_{SFOS} for all SFOS light lepton pairs, the invariant mass is also calculated with the inclusion of an additional light lepton ($m_{\text{SFOS}+1}$) or additional SFOS pair ($m_{\text{SFOS}+\text{SFOS}}$) in the event. All possible combinations are considered, and whichever resultant mass is closest to that of the Z boson is then used to calculate the mass difference from m_Z for further event selection.

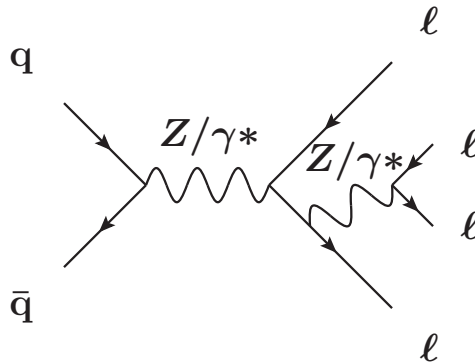


Figure 5.5: Example of a radiative Z boson decay resulting in four light leptons.

5.4.2.1 $4\ell 0\tau$ Z Veto Signal Regions

After the preselection and the four light lepton multiplicity requirement, the majority of background events remaining come from fully leptonic ZZ production. Smaller contributions also come from processes containing one leptonically decaying Z boson, e.g. WZ and $t\bar{t}Z$. The Z-veto SRs target these background processes with the extended Z-veto described above. Any events where the mass difference between m_Z and m_{SFOS} , $m_{\text{SFOS}+1}$ or $m_{\text{SFOS}+\text{SFOS}}$ is less than 10 GeV are discarded. Distributions of the m_{SFOS} , $m_{\text{SFOS}+e}$, $m_{\text{SFOS}+\mu}$ and $m_{\text{SFOS}+\text{SFOS}}$ for the background processes and a number of representative signal scenarios can be seen in Figure 5.6.

The RPV benchmark signals are chosen from the grid with a wino NLSP and a non-zero coupling to light leptons, λ_{121} . These points are used for the majority of the optimisation of the $4\ell 0\tau$ channel. The behaviour for the RPV grids with slepton or sneutrino NLSPs is found to be relatively similar, although the cross-sections differ. For instances where some signal points display different behaviour to the majority, a point which is representative of this behaviour is also included in the optimisation. The points selected lie in the region of the wino λ_{121} grid where the border between easily excluded points and those with a lower sensitivity lies. This emphasises the effect of varying an SR definition on the expected statistical sensitivity. The $\tilde{\chi}_2^0\tilde{\chi}_3^0$ via slepton grid also uses the Z-veto regions, and two points are displayed for this scenario which are also not yet excluded but hopefully can be with sufficient SR optimisation.

The invariant mass of SFOS pairs with an additional light lepton has been separated based on the lepton flavour, but it can be seen that the overall shape of the background and signal processes are the same for both. The plots are made consecutively, so that the m_{SFOS} is plotted at the $4\ell 0\tau$ stage, and the $m_{\text{SFOS}+e}$, $m_{\text{SFOS}+\mu}$ and $m_{\text{SFOS}+\text{SFOS}}$ distributions are plotted after the m_{SFOS} has already been used to veto events. The peak in the mass distributions coming from background processes containing Z bosons, in particular ZZ which is displayed with WZ in the ‘‘diboson’’ category, can be seen clearly between 80 and 100 GeV. This corresponds to the 10 GeV mass difference cut used in the Z-veto.

Once the Z-veto has been implemented, kinematic properties of the remaining events are used to define two different signal regions in order to target the RPV and $\tilde{\chi}_2^0\tilde{\chi}_3^0$ via slepton signals most effectively. The optimisation of the latter region, SR0noZa will be discussed first, before moving on to the slightly more complex SR0noZb optimisation.

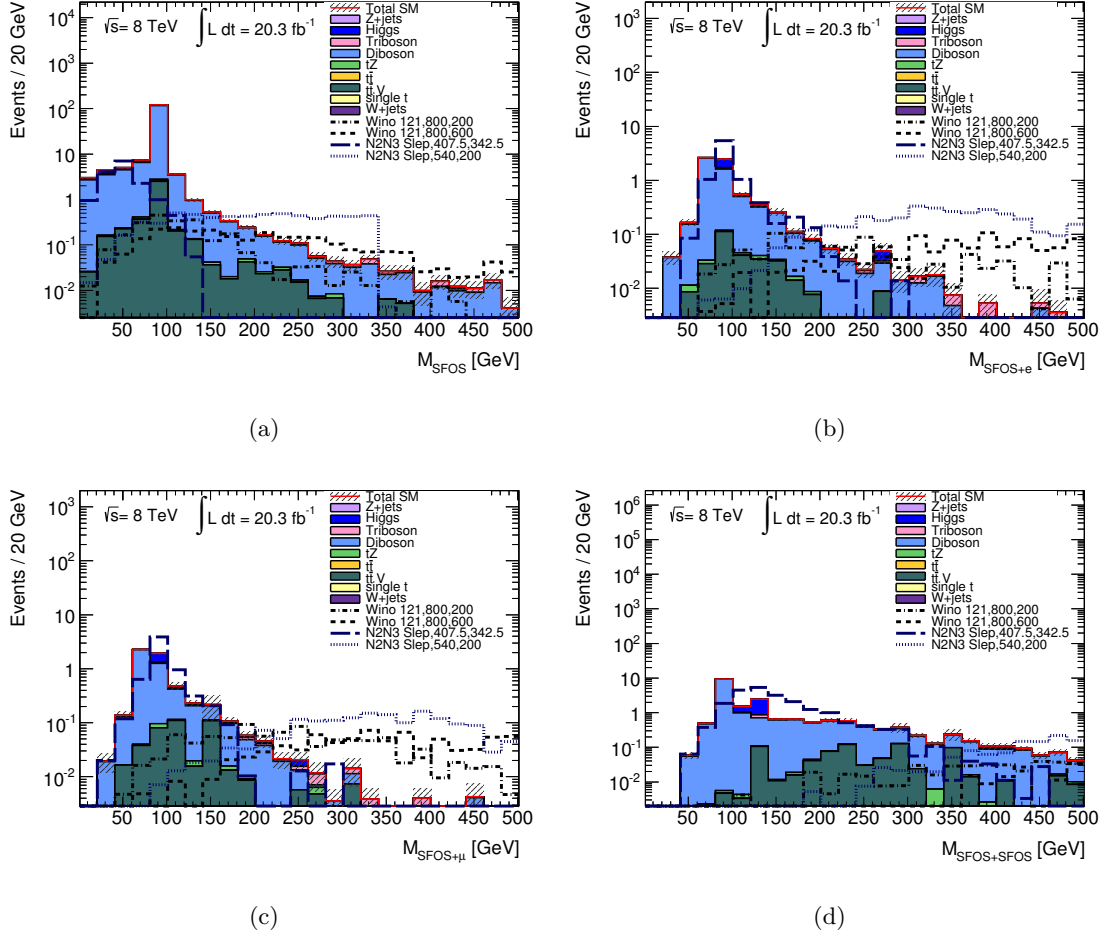


Figure 5.6: Distributions of the (a) m_{SFOS} , (b) $m_{\text{SFOS}+e}$, (c) $m_{\text{SFOS}+\mu}$, and (d) $m_{\text{SFOS}+\text{SFOS}}$ for all background processes and a selection of representative RPV wino and $\tilde{\chi}_2^0\tilde{\chi}_3^0$ via slepton signal points in events with four or more light leptons. In events with multiple SFOS pairs, SFOS+l or SFOS+SFOS, the combination with invariant mass closest to the Z boson mass is plotted.

SR0noZa

The $\tilde{\chi}_2^0\tilde{\chi}_3^0$ via slepton SUSY scenario produces four light leptons and two neutralino LSPs in the final state. The LSP in this model is stable, so the energy carried by these supersymmetric particles will be undetected by ATLAS. This signal should therefore be sensitive to a moderate requirement on missing transverse energy E_T^{miss} (defined in Section 3.3). Figure 5.7 includes two plots which were used to optimise the value of the E_T^{miss} cut for this signal region, both of which are produced after four light leptons are required and the extended Z-veto is applied. Figure 5.7(a) shows the E_T^{miss} distribution for all background processes compared to some benchmark $\tilde{\chi}_2^0\tilde{\chi}_3^0$ via slepton signal points. Figure 5.7(b) shows the significance Z_N as a function of E_T^{miss} for a number of $\tilde{\chi}_2^0\tilde{\chi}_3^0$ via

stopion signal benchmark points. The first and second numbers given in the legend entries for each point refer to the masses of the $\tilde{\chi}_{2/3}^0$ (NLSP) and $\tilde{\chi}_1^0$ (LSP) respectively. It can be seen that these points are selected to display a range of sensitivity, one already has more events than the background processes in the E_T^{miss} distribution, whilst the other two only dominate for higher E_T^{miss} values. The background processes peak below 50 GeV on the distribution, and a cut here removes the majority of background events, primarily from diboson processes. The significance for the majority of the points considered is at a maximum for a cut value of 50 GeV. The significance decreases with increasing E_T^{miss} above this point, with the exception of the point with masses 532.5 GeV and 467.5 GeV, which is not excluded for any value of E_T^{miss} . The final requirement of this signal region after four light leptons have been selected and an extended Z-veto applied is to request at least 50 GeV of missing transverse energy in the event.

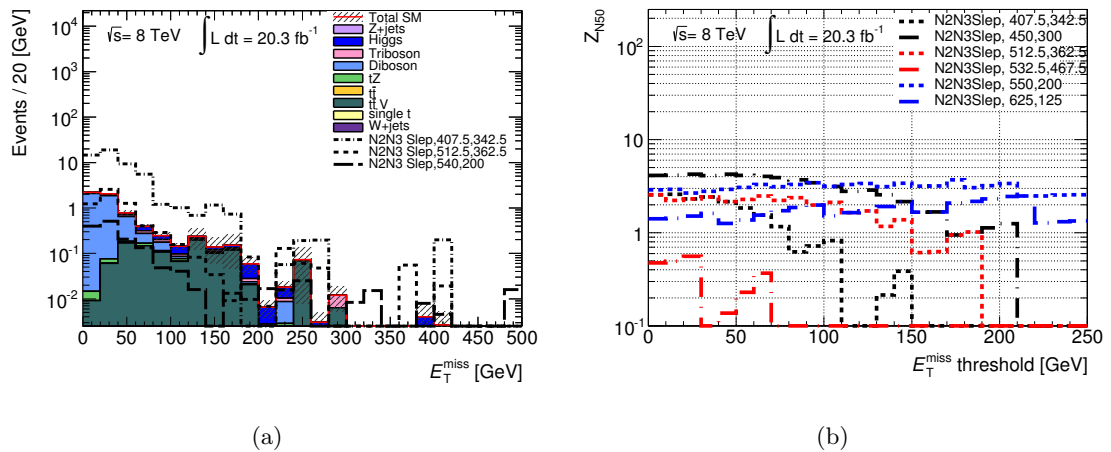


Figure 5.7: Distribution of (a) the E_T^{miss} for all background processes and a selection of representative $\tilde{\chi}_2^0\tilde{\chi}_3^0$ via slepton signal points and (b) Z_N as a function of E_T^{miss} for the same signal points in events with four light leptons after the Z-veto has been applied.

SR0noZb

A second signal region for the $4\ell 0\tau$ channel with a Z-veto is defined to target the RPV models with non-zero couplings for LSP decays to light leptons. All RPV models considered have at least two neutrinos in the final state, and the sneutrino NLSP scenario has an additional neutrino produced by each sparticle decay. These are a source of missing transverse energy as they pass through ATLAS undetected, making E_T^{miss} a good discriminating variable for these scenarios. In addition, the model with a gluino NLSP has an abundance of jets produced in the cascade, meaning that a related variable, the effective

mass, m_{eff} is also important. The m_{eff} represents the total mass contained within the event, and is defined as:

$$m_{\text{eff}} = E_T^{\text{miss}} + p_T^{\text{leptons}} + p_T^{\text{jets with } p_T > 40 \text{ GeV}}. \quad (5.3)$$

Due to the correlation between E_T^{miss} and m_{eff} , a cut value for each variable is optimised independently, and these are then implemented with a logical OR. An event can therefore pass either one of the cuts in order to be accepted and does not necessarily have to satisfy both simultaneously.

Figure 5.8 shows distributions of the E_T^{miss} and m_{eff} variables for background processes and a selection of RPV model benchmark points, and the corresponding significance Z_N for the benchmark signals. Considering first the E_T^{miss} distribution, it can be seen that at low values of E_T^{miss} events from SM background processes dominate, whereas at larger values the signal points have a higher yield. Although the desire is to achieve a high signal to background event ratio, it must be taken into consideration that this analysis involves very small yields, and if less than one background event is predicted in any of the SRs the statistical uncertainty becomes very high. It is therefore important to not be too extreme in rejecting background events, in order to prevent this from happening. In this instance a cut on E_T^{miss} at 75 GeV removes the bulk of the background events whilst maintaining sufficient background levels to allow estimation with a reasonable uncertainty. Considering now the accompanying significance plot, the significance for some points is still increasing at 75 GeV, but for others it is beginning to drop, so this is a good value to choose in order to maximise overall sensitivity. The majority of the benchmark points selected to optimise this cut were from the wino λ_{121} grid, with the inclusion of a point from the slepton λ_{121} grid to represent cases where a lower E_T^{miss} cut is preferred.

A set of benchmark points from the gluino RPV grid is used to optimise the m_{eff} cut value, as this is the scenario where it is most important due to the jets present in the final state. Figure 5.8(c) shows clearly how well this variable can be used to discriminate between the background and signal points on the gluino grid. The vast majority of background processes have less m_{eff} in an event than any of the signal points considered. The significance presented in Figure 5.8(d) shows an increase with increasing m_{eff} cut value for all points, so the selection is limited most by the need to maintain enough background events to keep the statistical uncertainty under control. The optimal requirement is found to be $m_{\text{eff}} \geq 600$ GeV when all these points are taken into consideration.

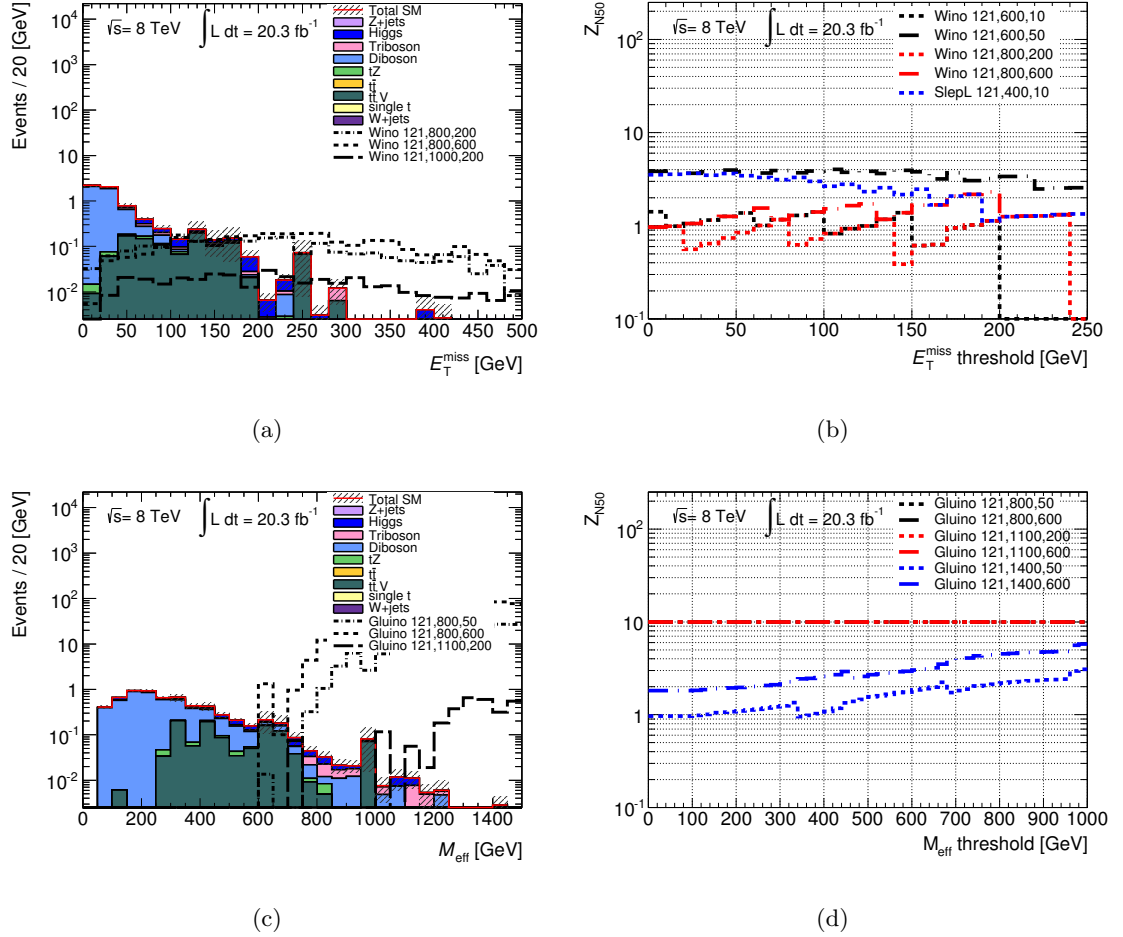


Figure 5.8: Distribution of (a) the E_T^{miss} for all background processes and a selection of representative RPV wino signal points, and (b) Z_N as a function of E_T^{miss} for a selection of RPV wino signal points, in events with four light leptons and a Z-veto. Also presented are the distributions of (c) the m_{eff} for background and a set of benchmark RPV gluino signal points, and (d) Z_N as a function of m_{eff} for a selection of benchmark RPV gluino signal points, in events with four light leptons and a Z-veto.

5.4.2.2 $3\ell 1\tau$ Z Veto Signal Regions

Events with three light leptons and one or more taus still have a large contribution from ZZ . Other important backgrounds are WZ and $Z + jets$. These processes can also be targeted effectively by a Z-veto, due to the common presence of a Z boson. Three light leptons can also be produced by one of the radiative Z boson decay processes, so the Z-veto is extended to include additional combinations of SFOS pairs plus a light lepton in this channel. Distributions of the m_{SFOS} , $m_{\text{SFOS}+e}$ and $m_{\text{SFOS}+\mu}$ for background and signal processes with three light leptons and one or more taus can be seen in Figure 5.9. Benchmark points from the RPV wino grid with a non-zero coupling λ_{133} (resulting in taus in the final state) are used for optimisation, as well as benchmark points from the $\tilde{\chi}_2^0\tilde{\chi}_3^0$ via stau decay scenario. Neither of these models involve any Z boson decays in their cascades. The background processes have a flatter dependence on the invariant mass for this channel than $4\ell 0\tau$, but there are still peaks visible between 80 and 100 GeV, and it is found that this is still the optimal cut window to use for the Z-veto.

SR1noZa

The SR1noZa signal region is defined to target the $\tilde{\chi}_2^0\tilde{\chi}_3^0$ via stau scenario once three light leptons and one or more taus have been selected and the extended Z-veto applied. The LSP is a stable neutralino in this model, and therefore a source of E_T^{miss} in the signal events. A selection of benchmark points from this grid are used to optimise a cut on the E_T^{miss} variable, as shown in Figure 5.10. It can be seen from the E_T^{miss} distribution in Figure 5.10(a) that the signal scenario has relatively small E_T^{miss} , but there is still some discrimination compared to the background processes, which are more peaked in events with $E_T^{\text{miss}} < 50$ GeV. Considering the significance for a selection of $\tilde{\chi}_2^0\tilde{\chi}_3^0$ via stau signal points shown in Figure 5.10(b), 50 GeV is an optimal place to cut on this variable, before the significance begins to drop dramatically. The SR1noZa signal region is set to require $E_T^{\text{miss}} > 50$ GeV in any events passing the $3\ell 1\tau$ lepton multiplicity and extended Z-veto requirements.

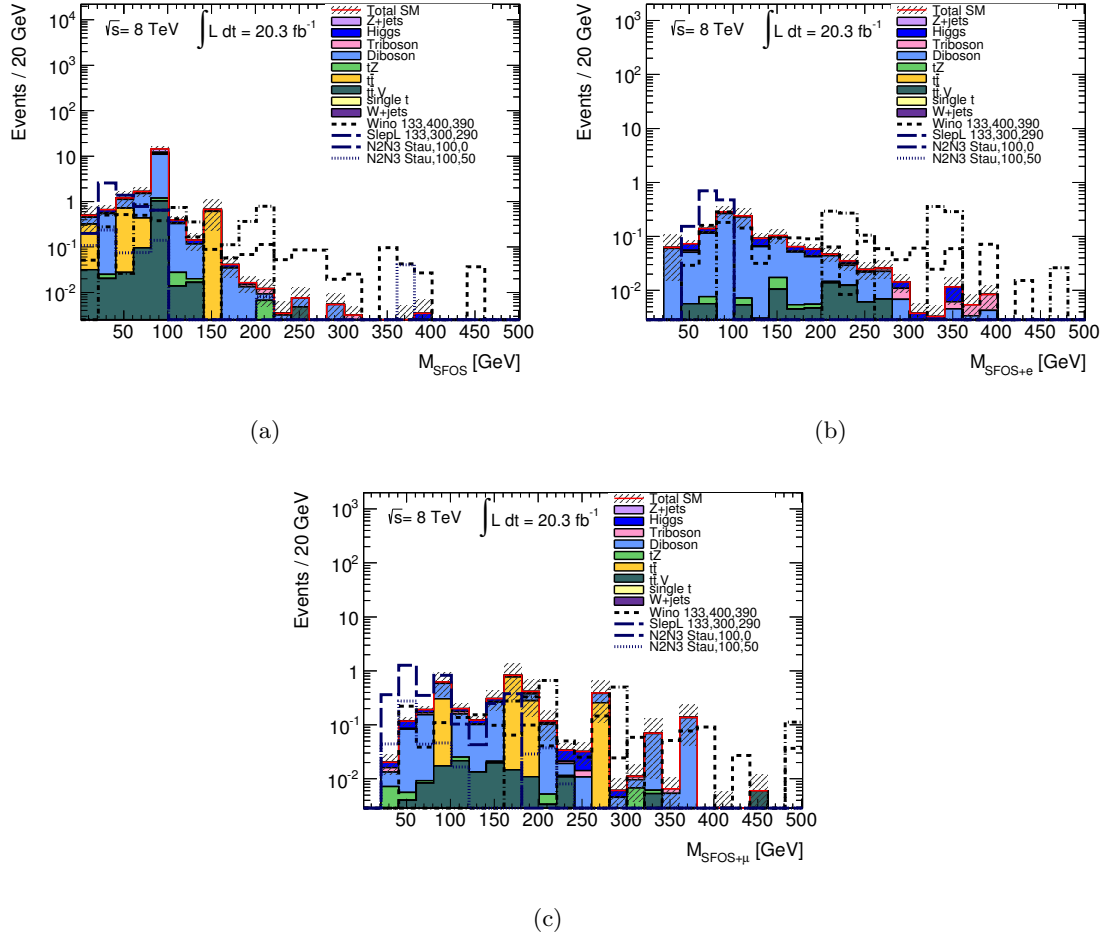


Figure 5.9: Distributions of the (a) m_{SFOS} , (b) $m_{\text{SFOS}+\text{electron}}$ and (c) $m_{\text{SFOS}+\text{muon}}$ for all background processes and a selection of representative RPV and $\tilde{\chi}_2^0 \tilde{\chi}_3^0$ via stau signal points for events with at least three light leptons and one tau. In events with multiple SFOS pairs or SFOS plus 1, the combination with invariant mass closest to the Z boson mass is plotted.

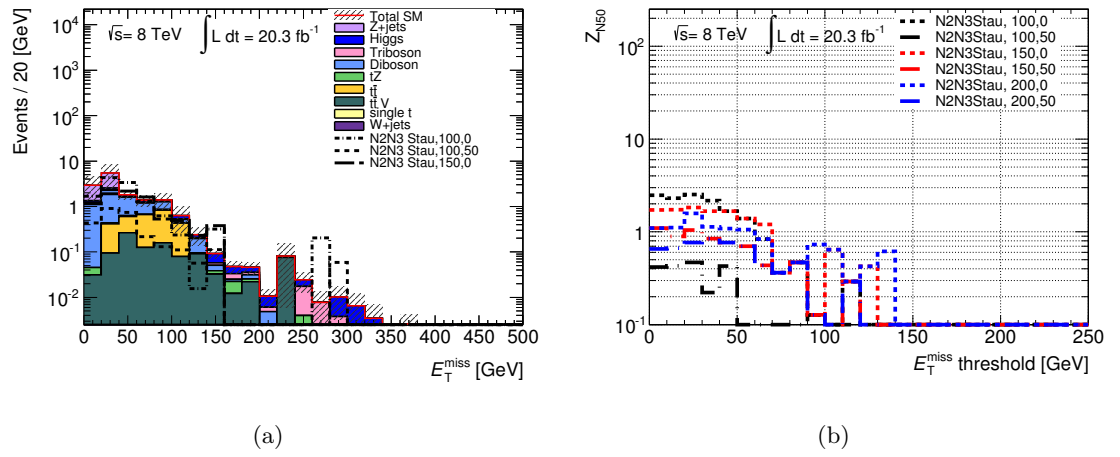


Figure 5.10: Distribution of (a) the E_T^{miss} for all background processes and a selection of representative $\tilde{\chi}_2^0 \tilde{\chi}_3^0$ via stau signal points and (b) Z_N as a function of E_T^{miss} for the same signal points in events with three light leptons, one tau and a Z-veto.

SR1noZb

A second region SR1noZb is defined for the $3l0\tau$ channel with a Z-veto in order to target the RPV scenarios with non-zero couplings which cause the LSP decay products to include taus. This follows the same format as SR0noZb. The variables E_T^{miss} and m_{eff} are optimised separately using signal points from the wino and gluino grids respectively, and combined together in one cut using a logical OR. Figure 5.11 shows the distributions for both variables, and the corresponding significance values for a range of benchmark signal points. Figure 5.11(a) shows the E_T^{miss} distribution for background processes and signal points from the wino and slepton RPV grids. This plot shows that the majority of background events have E_T^{miss} values below 100 GeV, and beyond this point the distribution is dominated by the signal events. The significance as a function of E_T^{miss} shown in Figure 5.11(b) confirms for the majority of the wino and slepton points considered that a requirement of 100 GeV is optimal, with one exception from the slepton grid. The slepton points were also included here as the E_T^{miss} values varied on this grid compared to the other RPV models. One of these points, with slepton and neutralino masses of 75 GeV and 10 GeV respectively, has a much higher significance for a lower cut of 50 GeV. This is not beneficial for the other points, so a cut is defined at $E_T^{\text{miss}} > 100$ GeV, and there is the option to use SR1noZa with the lower E_T^{miss} cut for the problematic slepton point. This will be discussed in more detail in Section 7.2.

Figure 5.11(c) of the m_{eff} distribution of the background and RPV gluino signal processes shows a distinct cross-over at 500 GeV from complete domination of the background to a very high proportion of signal events. However, it is found that this cut value discards more background events than desired for the statistical uncertainty of the background estimation. The significance for the RPV gluino points shown in the Figure 5.11(d) continues to increase with increasing m_{eff} . A cut value of 400 GeV balances both of these factors. The signal region SR1noZb requires three light leptons and one or more taus, an extended Z-veto, and either $E_T^{\text{miss}} > 100$ GeV or $m_{\text{eff}} > 400$ GeV.

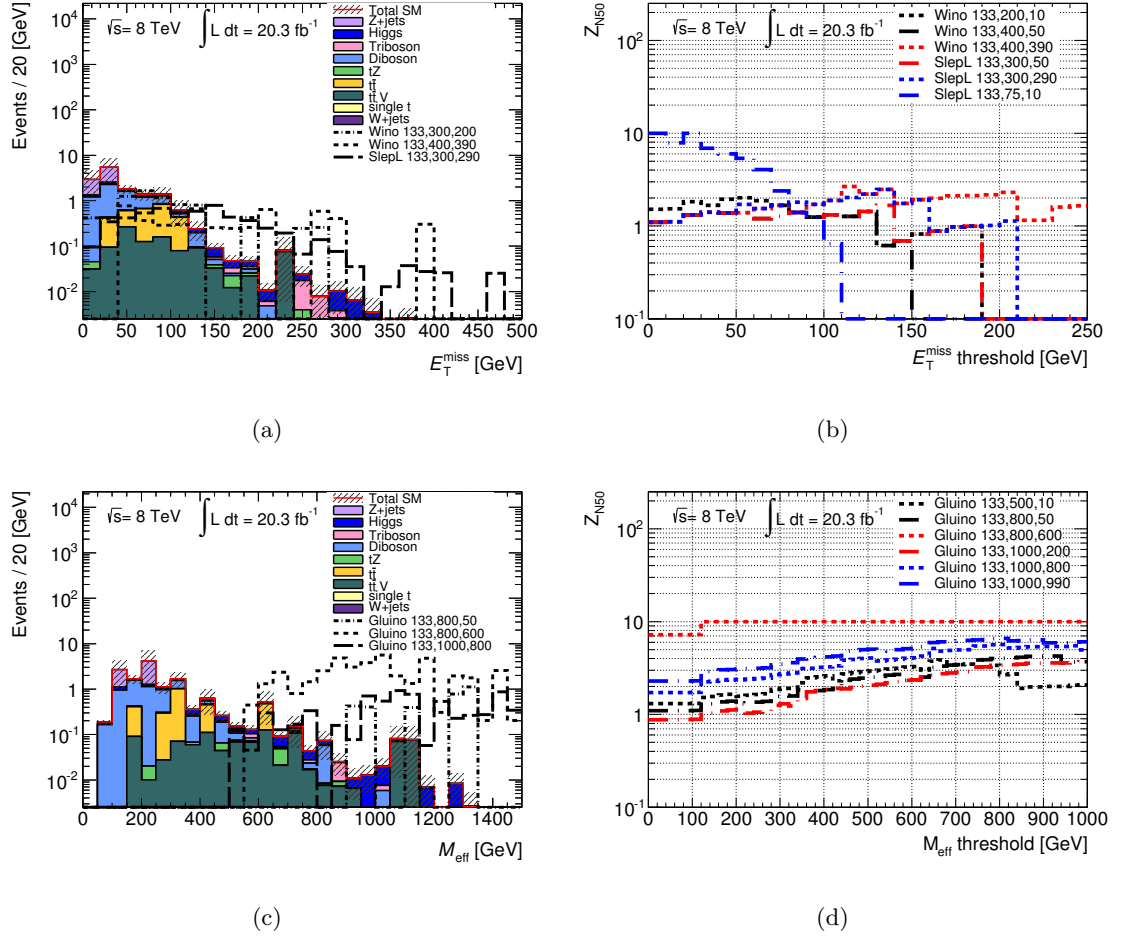


Figure 5.11: Distribution of (a) the E_T^{miss} for all background processes and a selection of representative RPV signal points, and (b) Z_N as a function of E_T^{miss} for a selection of RPV signal points, for events with three light leptons, one or more taus and a Z-veto. Also presented are the distributions of (c) the m_{eff} for all background processes and a selection of benchmark RPV gluino signal points, and (d) Z_N as a function of m_{eff} for a selection of RPV gluino signal points, in events with three light leptons, one or more taus and a Z-veto.

5.4.2.3 $2\ell 2\tau$ Z Veto Signal Regions

The Z-veto is also beneficial for $2\ell 2\tau$ events as the background in this channel is completely dominated by $Z + jets$ processes. As only two light leptons are present in these events, backgrounds with additional light leptons coming from radiative decays of the Z will not contribute, so an extended Z-veto is not implemented. A distribution for the invariant mass of SFOS pairs in background and signal events is shown in Figure 5.12. The distinctive peak in the background at 80-100 GeV can be seen again, as well as the little effect that the Z-veto has on the signal samples displayed. The signal regions for the $2\ell 2\tau$ channel then follow the same format as the others, defining one region targeting the $\tilde{\chi}_2^0 \tilde{\chi}_3^0$ scenarios and one region targeting the RPV scenarios.

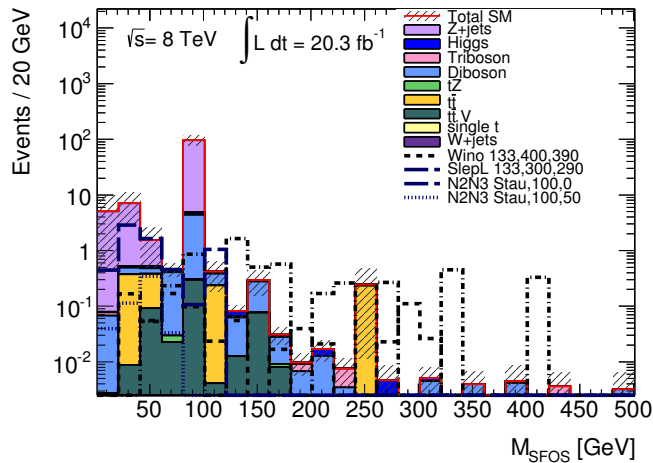


Figure 5.12: Distribution of the m_{SFOS} variable for all background processes and a selection of representative RPV and $\tilde{\chi}_2^0 \tilde{\chi}_3^0$ via stau signal points in events with two light leptons and two or more taus. In events with multiple SFOS pairs, the combination with invariant mass closest to the Z boson mass is plotted.

SR2noZa

This signal region targets $\tilde{\chi}_2^0 \tilde{\chi}_3^0$ via stau decays, and is complementary to SR1noZa, covering the instances where two taus decay hadronically rather than just one. The variable E_T^{miss} is used to define this region as well, as there is moderate E_T^{miss} from the LSP in the signal scenarios, which is typically greater than the E_T^{miss} in background events. This can be seen in Figure 5.13(a), where the majority of background events have $E_T^{\text{miss}} < 50$ GeV and events from signal then begin to dominate. Figure 5.13(b) shows the significance as a function of E_T^{miss} , and indicates that a slightly harder cut at 75 GeV is preferable for

the range of points considered, and sufficient background events remain with this choice. Signal region SR2noZa requires any events passing the $2\ell 2\tau$ lepton multiplicity and Z-veto to satisfy a criteria of $E_T^{\text{miss}} > 75$ GeV.

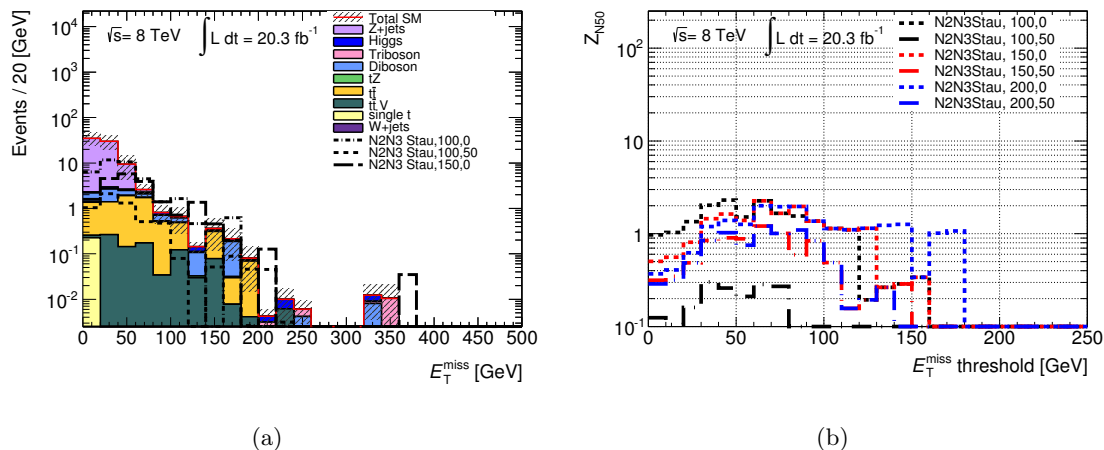


Figure 5.13: (a) Distribution of E_T^{miss} and (b) Z_N as a function of E_T^{miss} for all background processes and a selection of representative $\tilde{\chi}_2^0 \tilde{\chi}_3^0$ via stau signal points in events with two light leptons, two taus and a Z-veto.

SR2noZb

All tau-rich RPV models are also targeted by the SR2noZb signal region, which is complementary to the $3l0\tau$ region SR1noZb, in the case that two of the produced taus decay hadronically and two decay leptonically. Cut values are optimised for the E_T^{miss} and m_{eff} variables using a range of RPV signal points, and the two requirements are then combined with a logical OR to form the signal region. Figure 5.14 shows the distributions of E_T^{miss} and m_{eff} and the significance of a number of benchmark signal points as a function of both variables. The distribution of E_T^{miss} in Figure 5.14(a) shows the signal processes beginning to dominate in terms of number of events once the E_T^{miss} is at around 100 GeV. Figure 5.14(b) shows the significance as a function of E_T^{miss} , demonstrating that this cut value is optimal for the majority of the benchmark points considered. As mentioned when discussing the $3\ell 1\tau$ channel, SUSY scenarios that have a much softer E_T^{miss} distribution (e.g. those from the RPV slepton grid) can also make use of the SR2noZa region. A requirement of $E_T^{\text{miss}} > 100$ GeV is optimal when these points are disregarded. Figure 5.14(c) presents the m_{eff} distribution for the background processes and a selection of RPV gluino points, showing that this is a powerful discriminating variable in this channel as well. There is a good separation between background and signal events, and a cut around 500-

600 GeV seems adequate, whereas above 700 GeV there would be very few background events remaining. The significance versus m_{eff} distribution in Figure 5.14(d) shows that significance increases with increasing m_{eff} cut values for all scenarios, the only limitation being maintaining sufficient background events. With this in mind the cut is set at 600 GeV, and SR2noZb requires either $E_T^{\text{miss}} > 100$ GeV or $m_{\text{eff}} > 600$ GeV in addition to the lepton multiplicity and Z-veto requirements.

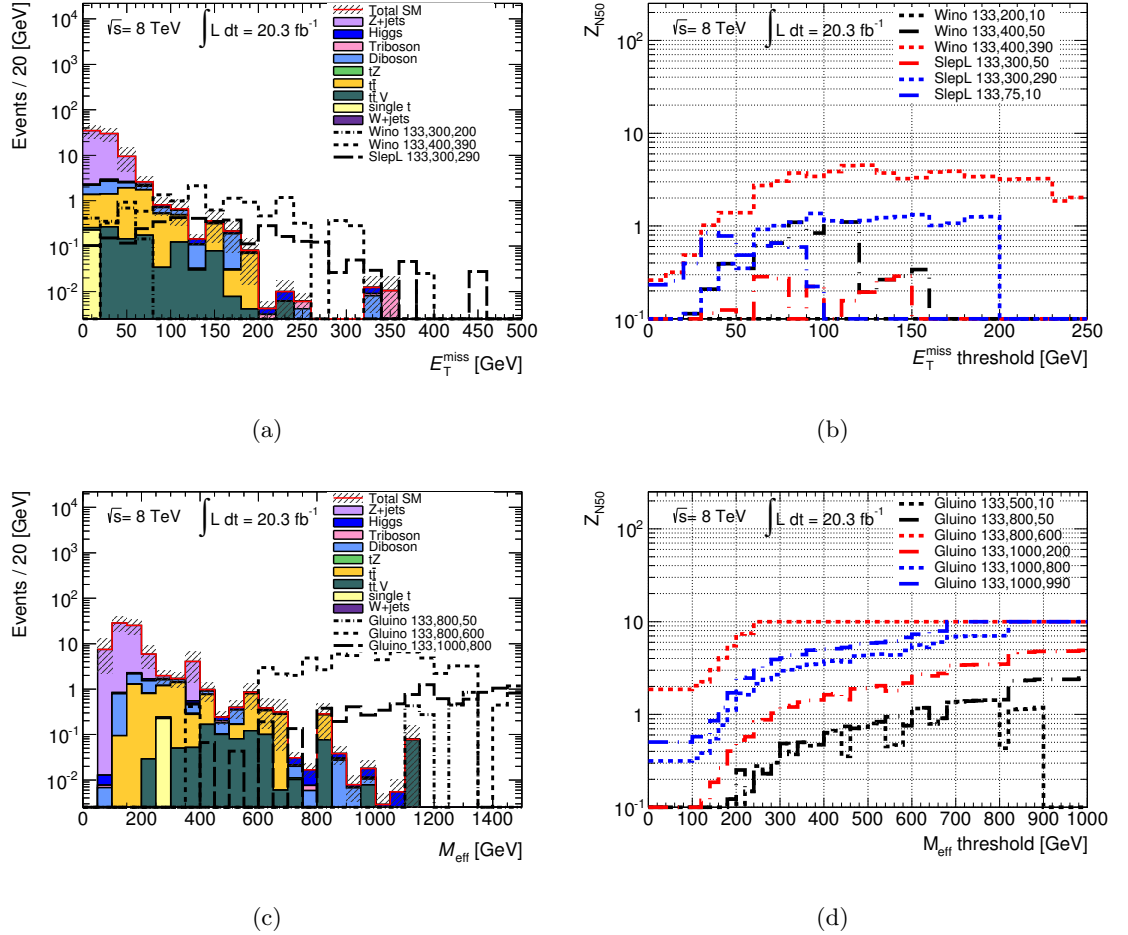


Figure 5.14: Distributions of (a) the E_T^{miss} for all background processes and a selection of representative RPV wino signal points, and (b) Z_N as a function of E_T^{miss} for a selection of RPV signal points, in events with two light leptons, two or more taus and a Z-veto. Also presented are the distributions of (c) the m_{eff} for all background processes and a selection of benchmark RPV gluino signal points, and (d) Z_N as a function of m_{eff} for a selection of benchmark RPV gluino signal points, in events with two light leptons, two or more taus and a Z-veto.

5.4.3 Z Boson Selection

While the use of a Z-veto is very effective at suppressing SM background processes contributing to four lepton events, there are also SUSY scenarios considered where Z bosons are produced in the decay chain. This is the case for the GGM models and the $\tilde{\chi}_2^0\tilde{\chi}_3^0$ via Z decays scenario. In order to target these signals an SR must be defined where events containing Z bosons are selected, rather than vetoed. A Z request requires the presence of SFOS light lepton pairs whose invariant mass is within 10 GeV of the Z boson mass, i.e. events are required to satisfy $|m_{\text{SFOS}} - m_Z| \leq 10$ GeV. A “Z-rich” signal region is hence defined for each of the three channels.

5.4.3.1 $4\ell 0\tau$ Z Selection Signal Region

Both the GGM and $\tilde{\chi}_2^0\tilde{\chi}_3^0$ via Z models produce four light leptons in the final state, and the signal region SR0Z is defined to target them. Figure 5.15 displays the invariant mass m_{SFOS} distribution for background processes and two benchmark points from each of the signals. The peak at around m_Z is visible for all benchmark points, and there is a higher signal-to-background ratio in this region. Once the Z-selection is made, a cut on E_T^{miss} is used to suppress the remaining background. Figure 5.16 shows the distribution of E_T^{miss} in background and signal events, and the corresponding significance. Benchmark points from both the $\tilde{\chi}_2^0\tilde{\chi}_3^0$ via Z and GGM grids are included in the E_T^{miss} distribution in Figure 5.16(a) for reference, but only the GGM points were used to optimise the cut. The number of background events begins to decrease below the number of GGM signal events at around 75 GeV. For the majority of signal points shown in Figure 5.14(b) the significance is maximal at 75 GeV, with some peaking at slightly higher values and some at slightly lower values. A requirement of $E_T^{\text{miss}} > 75$ GeV is made to define this signal region, once four light lepton events have passed the Z-selection.

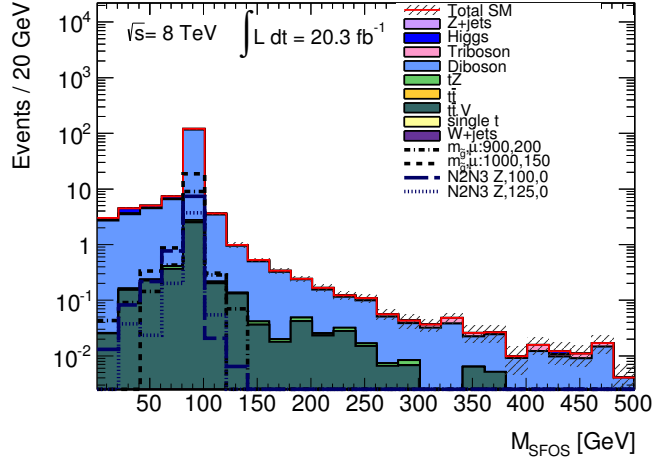


Figure 5.15: The distribution of the m_{SFOS} for all background processes and a representative selection of $\tilde{\chi}_2^0 \tilde{\chi}_3^0$ via Z and GGM signal points in events with at least four light leptons.

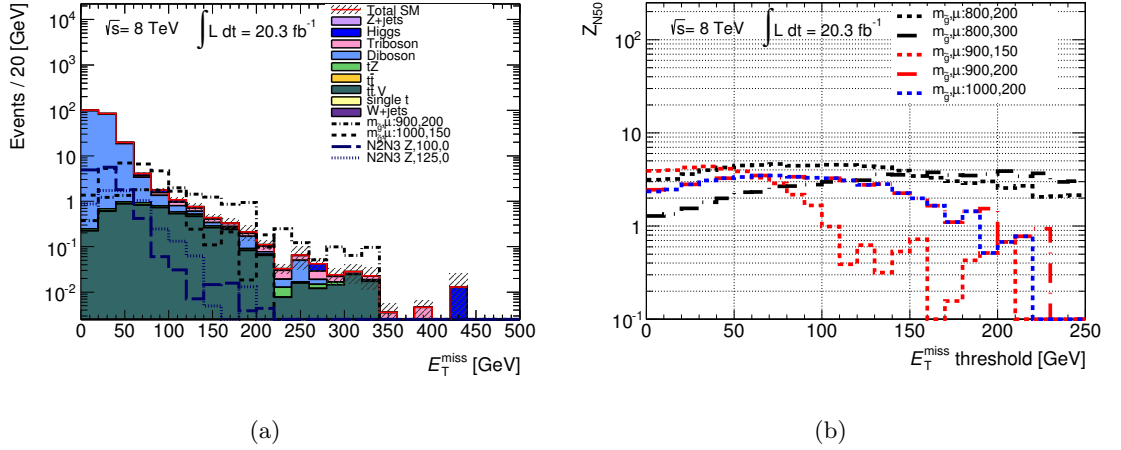


Figure 5.16: Distribution of (a) the E_T^{miss} of all background processes and a selection of representative GGM and $\tilde{\chi}_2^0 \tilde{\chi}_3^0$ via Z signal points and (b) Z_N as a function of E_T^{miss} for a selection of representative GGM signal points in events with four light leptons and a Z-selection.

5.4.3.2 $3\ell 1\tau$ and $2\ell 2\tau$ Z Selection Signal Regions

There are no specific signals considered by this analysis which are Z-rich and produce taus in the final state, but a Z-rich signal region is defined for each of the $3\ell 1\tau$ and $2\ell 2\tau$ channels (SR1Z and SR2Z respectively) to maintain a broad set of selections. These are used in combination with other signal regions when producing the final results, as is explained in Section 7.2. Figure 5.17 shows the E_T^{miss} distributions of background processes once a Z-selection has been required for the $3\ell 1\tau$ and $2\ell 2\tau$ channel events. Based on Figure 5.17(a) SR1Z requires $E_T^{\text{miss}} > 100$ GeV, which removes the majority of the SM background. Similarly SR2Z is defined to require $E_T^{\text{miss}} > 75$ GeV based on Figure 5.17(b), as the vast majority of background processes are below 75 GeV. Both regions maintain sufficient background events to contain the effect of systematic uncertainties associated with limited statistics.

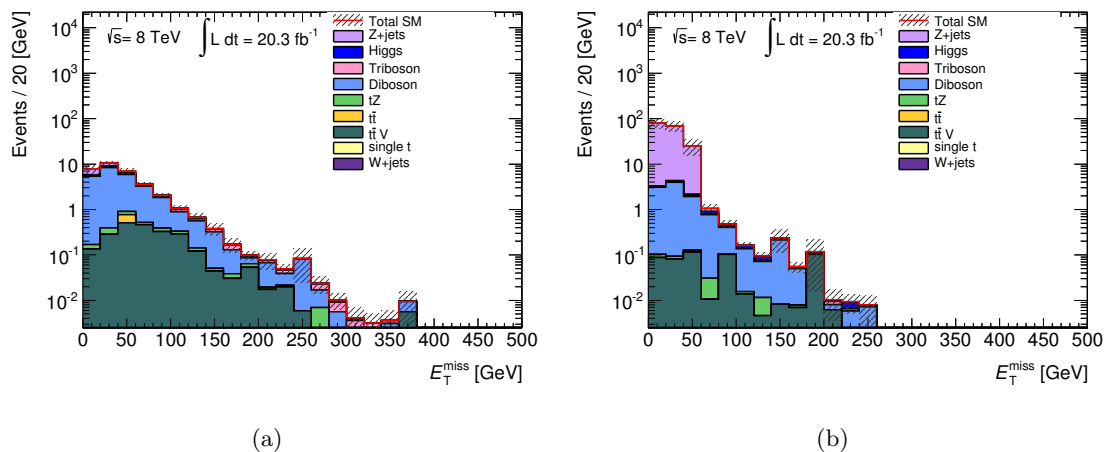


Figure 5.17: Distribution of E_T^{miss} for all background processes in events with (a) three light leptons, one tau and a Z-selection and (b) two light leptons, two taus and a Z-selection.

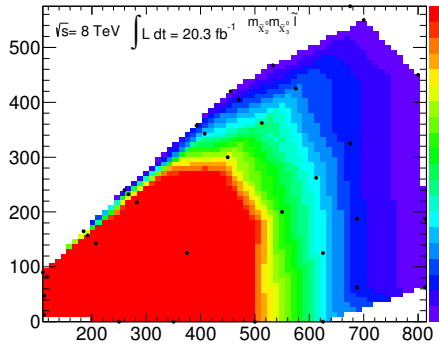
5.5 Signal Region Summary

The final optimised cuts for each of the nine signal regions are detailed in Table 5.7. An estimation of the performance of each signal region on a specific SUSY scenario is made by calculating the significance Z_N for each point and filling a histogram with the significance as a function of the parameter space. The x and y axes display whichever two parameters are varied in the scenario considered, usually the LSP and NLSP masses, and the z axis displays the significance. Delaunay triangulation [110] is used to interpolate the significance values for bins in between the points where signal samples exist so that

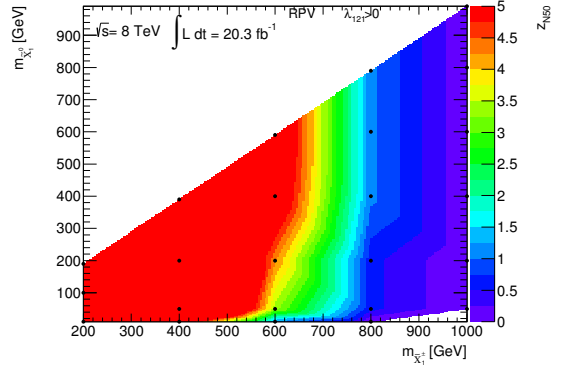
Table 5.7: Summary of SRs used in this analysis, including number of light leptons and taus requested, leptons used for Z-veto or selection and E_T^{miss} OR m_{eff} requests.

SR	$N(l)$	$N(\tau)$	Z-veto	E_T^{miss} [GeV]	OR m_{eff} [GeV]
SR0noZa	≥ 4	≥ 0	SFOS,(SFOS + l),(SFOS + SFOS)	> 50	-
SR0noZb	≥ 4	≥ 0	SFOS,(SFOS + l),(SFOS + SFOS)	> 75	> 600
SR1noZa	$= 3$	≥ 1	SFOS,(SFOS + l)	> 50	-
SR1noZb	$= 3$	≥ 1	SFOS,(SFOS + l)	> 100	> 400
SR2noZa	$= 2$	≥ 2	SFOS	> 75	-
SR2noZb	$= 2$	≥ 2	SFOS	> 100	> 600
SR	$N(l)$	$N(\tau)$	Z-selection	E_T^{miss} [GeV]	OR m_{eff} [GeV]
SR0Z	≥ 4	≥ 0	SFOS	> 75	-
SR1Z	$= 3$	≥ 1	SFOS	> 100	-
SR2Z	$= 2$	≥ 2	SFOS	> 75	-

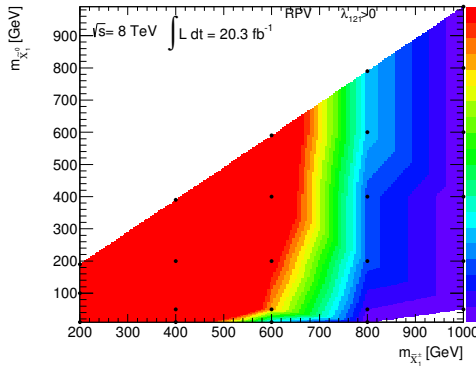
the significance changes smoothly as a function of x and y . A significance value of 1.64 or greater corresponds to an exclusion of the signal scenario considered with 95% confidence level [111].



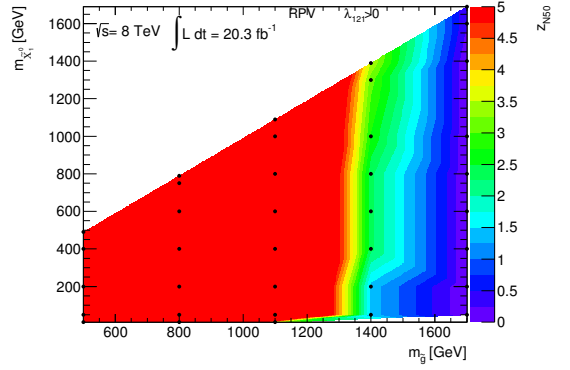
(a) SR0noZa



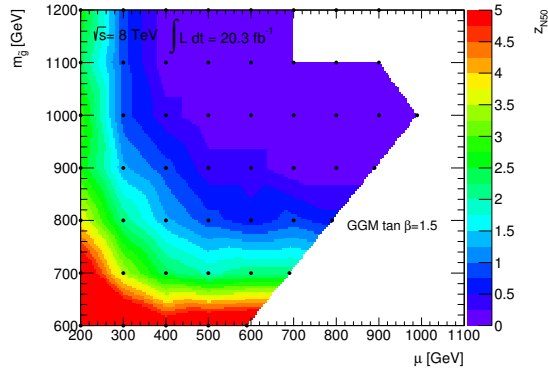
(b) SR0noZa



(c) SR0noZb



(d) SR0noZb



(e) SR0Z

Figure 5.18: Figures showing the significance Z_N for SR0noZa on (a) the $\tilde{\chi}_2^0\tilde{\chi}_3^0$ via slepton grid and (b) the wino λ_{121} grid, for SR0noZb on (c) the wino λ_{121} grid and (d) the gluino λ_{121} grid, and for SR0Z on (e) the GGM grid with $\tan\beta = 1.5$.

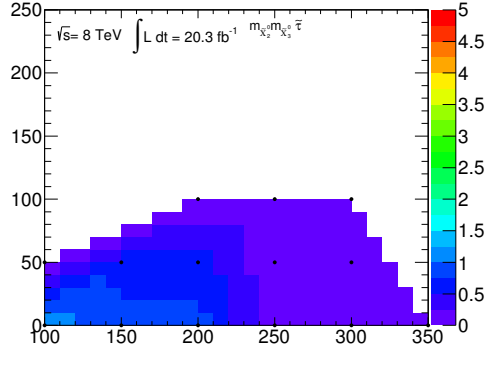
Figure 5.18 displays two-dimensional significance histograms for the SR0noZa, SR0noZb, and SR0Z signal regions on example signal grids that they were optimised to target. The significance of signal region SR0noZa on the points of the $\tilde{\chi}_2^0\tilde{\chi}_3^0$ via slepton decays scenario is shown in Figure 5.18(a). This is the main target of this signal region and the scenario which was used to optimise it. The drop in significance close to the top edge of the considered grid is due to the decreasing mass difference between the NLSP and the LSP (“mass splitting”). The smallest mass splitting included in the grid produced for the $\tilde{\chi}_2^0\tilde{\chi}_3^0$ scenario is 20 GeV. For these points, the majority of the mass of the decaying NLSP is required to produce the LSP, with only 20 GeV remaining to contribute to the p_T of the produced particles (neglecting the masses of the other decay products). This means the decay products will generally have a lower p_T than for a point where the mass splitting is say 50 GeV. This makes it more difficult for the leptons produced to be detected and reconstructed, which impacts on the sensitivity of the analysis, as less signal events will pass the selection criteria for the SRs. The decrease in significance with increasing NLSP mass is caused by decreasing cross-section for the considered process. The cross-section values for each point for this grid can be found in Appendix B.

Figure 5.18(b) shows the significance of the same signal region SR0noZa on the RPV wino λ_{121} grid. Although the RPV grids were not used to optimise this region, it will be useful for any scenario where the missing transverse energy does not satisfy the higher 75 GeV cut required by SR0noZb. It is therefore reasonable to expect that this SR will have some exclusion power on regions of the RPV grids where this is likely. This plot can be compared to Figure 5.18(c), which shows the significance for the same wino λ_{121} grid, but using the SR0noZb region. The latter gives slightly higher significance values for the row of points with NLSP mass of 800 GeV, at approximately 1.5 rather than approximately 1. Based on this, it would be expected that SR0noZb will produce an exclusion limit up to slightly higher mass values than SR0noZa (both just under 800 GeV). As the LSP in these RPV scenarios decays, the energy of the resultant leptons is dependent on the mass of the LSP, rather than the mass splitting. Hence the significance does not decrease for the parameter space closer to the diagonal like it does for $\tilde{\chi}_2^0\tilde{\chi}_3^0$ in Figure 5.18(a). The cross-section for this process also decreases as the NLSP mass is increased. Considering the significance at higher NLSP mass (from around 550 GeV), there is a decrease for the region with low LSP mass (below 250 GeV) compared to the region with LSP mass greater than 250 GeV. For example the point with an NLSP mass of 600 GeV and LSP mass of 50 GeV has a significance of approximately 4, whereas the point with an NLSP mass of

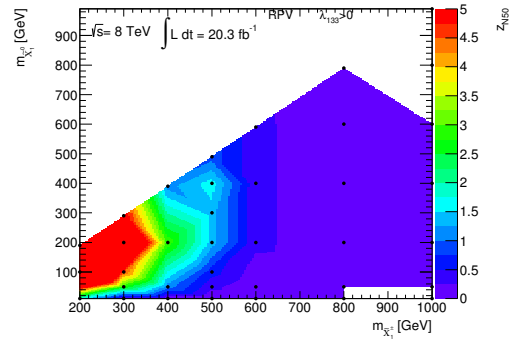
600 GeV and LSP mass of 200 GeV is between 4.5 and 5. This difference can be attributed to the difficulty reconstructing lower p_T leptons resulting from a light LSP decay, making it more difficult to achieve an equivalent significance.

Figure 5.18(d) shows the significance of the SR0noZb region on the RPV gluino λ_{121} grid, which was the scenario used to optimise the m_{eff} value for this SR. The significance is high for the majority of points on this signal grid, with the exception of the highest NLSP mass points due to the falling cross-section. The significance is also lower in the low LSP mass (less than approximately 200 GeV) high NLSP mass (above approximately 1100 GeV) region, for the same reasons as the wino grid, lower production cross-section and lower p_T of decay products.

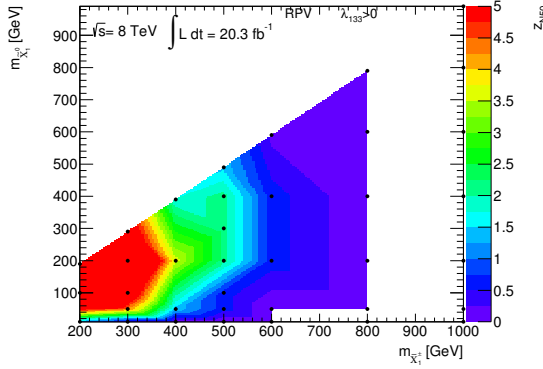
Figure 5.18(e) shows the significance of SR0Z for all points on the GGM $\tan\beta = 1.5$ grid used to optimise it due to the presence of a Z boson in the sparticle decay chain. In this case the vertical axis gives the gluino mass M_3 and the horizontal axis shows the Higgs mass parameter μ , both of which are varied for this scenario. When μ is high, the strong processes involved in this model will dominate, but at lower μ the electroweak processes are dominant (as explained in Section 5.2.3), which explains the high significance along the left-hand side of the grid. The total cross-section is highest for low μ , low LSP mass, and lowest for high μ and high NLSP mass. This also contributes to the decrease in significance for high LSP mass points with increasing μ .



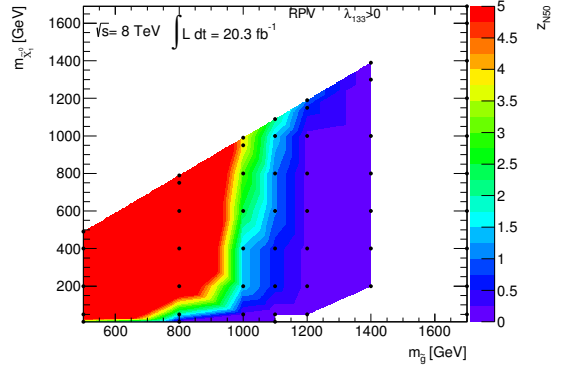
(a) SR1noZa



(b) SR1noZa



(c) SR1noZb



(d) SR1noZb

Figure 5.19: Figures showing the significance Z_N for SR1noZa on (a) the $\tilde{\chi}_2^0\tilde{\chi}_3^0$ via stau grid and (b) the wino λ_{133} grid, and for SR1noZb on (c) the wino λ_{133} grid and (d) the gluino λ_{133} grid.

An equivalent set of example significance plots for the $3\ell 1\tau$ SRs are displayed in Figure 5.19. Figure 5.19(a) shows the significance of region SR1noZa on the $\tilde{\chi}_2^0\tilde{\chi}_3^0$ via stau grid which it was optimised to target. The significance is 1.5 or less for all points on this grid with this SR, and so no region of this parameter space is expected to be excluded. This signal process does not have as high a cross-section as the decay via a slepton, and in addition a request for three light leptons requires three of the produced taus to decay leptonically. As the branching ratio for a tau decaying to a lepton is approximately 35% [7], this leaves less events which are accessible with this signal region.

In Figure 5.19(b) the significance of the same signal region SR1noZa is shown on the RPV scenario with a wino NLSP and λ_{133} . If compared to the significance of SR1noZb on the same grid shown in Figure 5.19(c), it appears that the significance of SR1noZa is less powerful, but for the lowest LSP and NLSP mass point SR1noZa has a significance of

approximately 2 compared to just 0.5 for SR1noZb. There are other signal points on the RPV grids where the “a” regions perform better than the “b” regions, particularly for a slepton NLSP, but this serves as a good example.

Figure 5.19(d) gives the significance values for the RPV gluino scenario when using the signal region SR1noZb. As was seen for the scenarios with λ_{121} in the four lepton channel, the sensitivity on the gluino grid extends to higher NLSP masses than for the wino. This is because gluino pair production has a higher cross-section from a proton-proton collision than pair production of electroweak sparticles.

The significance values for exactly the same signal samples using the $2\ell 2\tau$ SRs are displayed in Figure 5.20. It can be seen from Figure 5.20(a) that the SR2noZa SR is more powerful than SR1noZa, and expects to exclude three signal points with an LSP mass of 0 GeV from the $\tilde{\chi}_2^0\tilde{\chi}_3^0$ via stau grid. Requiring two leptonically decaying taus in the final state rather than one decreases the branching ratio to the final state, but this is counteracted by the higher reconstruction efficiency of light leptons compared to taus. Figure 5.20(b) shows the significance of SR2noZa on the RPV wino λ_{133} grid, and Figure 5.20(c) shows the significance values for the same grid using signal region SR2noZb. Overall SR2noZb appears to have greater exclusion power, comparing the set of points with an NLSP mass of 500 GeV: these are approximately 1.5-1.75 for SR2noZb, whereas for SR2noZa they have values of approximately 1.25-1.5. However there are some points where this is reversed, for example the point with NLSP mass of 400 GeV and LSP mass of 50 GeV, which is approximately 1.25 for SR2noZa, but approximately 1 for SR2noZb. The significance of region SR2noZb is also shown in Figure 5.20(d) for the RPV gluino grid, which was used to optimise the m_{eff} cut value. The shape is similar to the other RPV gluino significance distributions, decreasing towards higher NLSP masses, and decreasing for very low LSP masses.

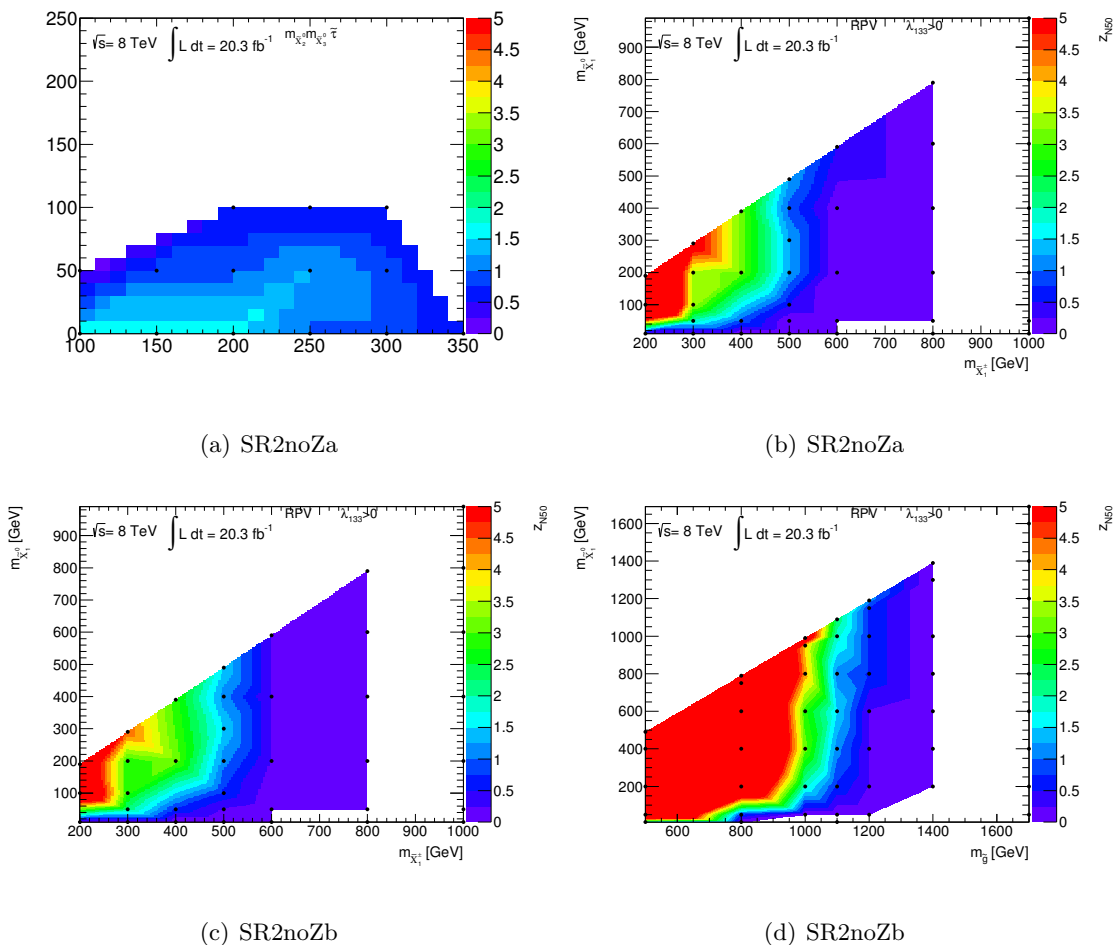


Figure 5.20: Figures showing the significance Z_N for SR2noZa on (a) the $\tilde{\chi}_2^0\tilde{\chi}_3^0$ via stau grid and (b) the wino λ_{133} grid, and for SR2noZb on (c) the wino λ_{133} grid and (d) the gluino λ_{133} grid.

Table 5.8 gives the number of background events expected from MC after the lepton multiplicity requirement, Z-veto or selection requirement, and each of the SR selections have been made for the $4\ell 0\tau$ channel. The numbers demonstrate very clearly the effectiveness of the Z-veto, which greatly decreases the ZZ background events from 216.87 to 4.50, and also removes most of the contributions from WZ , triboson, $t\bar{t}Z$, tZ and Higgs processes. Signal region SR0noZa has 1.81 expected background events in total, and 6.93 events expected for a benchmark point from the $\tilde{\chi}_2^0\tilde{\chi}_3^0$ via slepton scenario. This benchmark point has NLSP mass 550 GeV, and LSP mass 200 GeV, and is selected due its position close to the edge of the region of expected exclusion (based on Figure 5.18). The number of events remaining for this benchmark point after the $4\ell 0\tau$ and Z-veto requirements show that only a small number are discarded, compared to the much larger effect on the number of background events. SR0noZb requires a higher value of E_T^{miss} , so it is

expected that this region will have less background events, which total 1.43. The benchmark signal point included to demonstrate this signal region is from the RPV wino λ_{121} grid with NLSP mass of 600 GeV and LSP mass of 400 GeV. This is within the bulk of the region which is expected to be excluded, as can be seen by the large number of events with respect to the background. When a Z-selection is made instead of a Z-veto, the majority of four light lepton background events remain. The SR0Z region removes most of this with the E_T^{miss} requirement, but there are still 5.72 expected background events, considerably more than in the Z-veto regions. The benchmark point chosen for this signal region is from the GGM $\tan\beta=30$ scenario, with LSP mass of 1000 GeV and μ of 200 GeV. This point is from the region of parameter space where electroweak processes dominate, making it the main region targeted by this analysis.

Table 5.8: Number of SM MC background events and events from benchmark SUSY scenarios which survive event selection criteria in the $4\ell 0\tau$ channel. Uncertainties are statistical only. Numbers given in the benchmark point descriptions give the mass of the NLSP and LSP respectively for the RPV wino and $\tilde{\chi}_2^0\tilde{\chi}_3^0$ via slepton scenarios, and the LSP mass and μ value for the GGM scenario.

Process	$\geq 4l+0\tau$	Z-veto	SR0noZa	SR0noZb	Z request	SR0Z
ZZ	216.87 \pm 0.68	4.50 \pm 0.10	0.31 \pm 0.03	0.20 \pm 0.02	200.03 \pm 0.65	1.08 \pm 0.05
WZ	0.77 \pm 0.20	0.03 \pm 0.03	0.03 \pm 0.03	0.03 \pm 0.03	0.64 \pm 0.18	0.26 \pm 0.12
WW	0.00 \pm 0.05	0.00 \pm 0.05	0.00 \pm 0.05	0.00 \pm 0.05	0.00 \pm 0.05	0.05 \pm 0.05
Triboson	3.68 \pm 0.07	0.30 \pm 0.02	0.15 \pm 0.01	0.14 \pm 0.01	3.11 \pm 0.06	0.73 \pm 0.03
$t\bar{t}$	0.00 \pm 0.20	0.00 \pm 0.20	0.00 \pm 0.20	0.00 \pm 0.20	0.00 \pm 0.20	0.00 \pm 0.20
$t\bar{t}Z$	6.05 \pm 0.38	0.91 \pm 0.17	0.80 \pm 0.17	0.68 \pm 0.17	4.87 \pm 0.33	2.68 \pm 0.26
$t\bar{t}W$	0.29 \pm 0.15	0.15 \pm 0.11	0.15 \pm 0.11	0.09 \pm 0.09	0.09 \pm 0.09	0.09 \pm 0.09
$t\bar{t}WW$	0.02 \pm 0.01	0.01 \pm 0.01	0.01 \pm 0.01	0.01 \pm 0.01	0.00 \pm 0.00	0.00 \pm 0.00
single t	0.00 \pm 0.02	0.00 \pm 0.02	0.00 \pm 0.02	0.00 \pm 0.02	0.00 \pm 0.02	0.00 \pm 0.02
tZ	0.68 \pm 0.03	0.08 \pm 0.01	0.06 \pm 0.01	0.04 \pm 0.01	0.55 \pm 0.03	0.27 \pm 0.02
Z+jets	0.00 \pm 0.02	0.00 \pm 0.02	0.00 \pm 0.02	0.00 \pm 0.02	0.00 \pm 0.02	0.00 \pm 0.02
Higgs	8.68 \pm 0.16	0.53 \pm 0.05	0.31 \pm 0.04	0.24 \pm 0.03	5.90 \pm 0.15	0.60 \pm 0.07
Σ SM(MC)	237.04 \pm 3.17	6.51 \pm 0.85	1.81 \pm 0.68	1.43 \pm 0.60	215.20 \pm 2.66	5.72 \pm 1.01
RPV wino λ_{121} 600, 400	19.64 \pm 0.82	17.32 \pm 0.78	-	17.05 \pm 0.77	-	-
GGM $\tan\beta=30$ 1000, 200	15.12 \pm 0.77	-	-	-	14.45 \pm 0.74	9.18 \pm 0.60
$\tilde{\chi}_2^0\tilde{\chi}_3^0$ slepton 550, 200	7.98 \pm 0.22	7.28 \pm 0.21	6.93 \pm 0.20	-	-	-

Table 5.9 and Table 5.10 present the equivalent figures for the signal region selection

criteria in the $3\ell 1\tau$ and $2\ell 2\tau$ channels respectively. The same benchmark points are included for comparison for both channels, a point from the RPV wino λ_{133} scenario with NLSP mass 400 GeV and LSP mass 200 GeV, and a point from the $\tilde{\chi}_2^0\tilde{\chi}_3^0$ via stau scenario with NLSP mass 100 GeV and LSP mass of 0 GeV. The wino benchmark point is towards the edge of the expected exclusion region, and the $\tilde{\chi}_2^0\tilde{\chi}_3^0$ stau point is that with the highest expected significance on this grid, as this scenario is more challenging. The effect of the Z-veto and subsequent SR region criteria can be seen to reduce the backgrounds significantly, with a minimal decrease from the signal samples displayed. In both cases the expected background events are also displayed after a Z-selection and the Z-rich signal region criteria have been applied. No signal scenarios are displayed for these regions as they do not target a specific model.

Table 5.9: Number of SM MC background events and events from benchmark SUSY scenarios which survive event selection criteria in the $3\ell 1\tau$ channel. Uncertainties are statistical only. Numbers given in the benchmark point descriptions give the mass of the NLSP and LSP respectively for the RPV wino and $\tilde{\chi}_2^0\tilde{\chi}_3^0$ stau scenarios.

Process	$3l+\geq 1\tau$	Z-veto	SR1noZa	SR1noZb	Z request	SR1Z
ZZ	18.75 ± 0.22	2.99 ± 0.09	0.57 ± 0.04	0.28 ± 0.03	14.56 ± 0.20	0.56 ± 0.04
WZ	11.61 ± 0.80	2.01 ± 0.33	1.11 ± 0.26	0.19 ± 0.11	9.37 ± 0.72	0.98 ± 0.23
WW	0.06 ± 0.04	0.06 ± 0.04	0.00 ± 0.05	0.00 ± 0.05	0.00 ± 0.05	0.00 ± 0.05
<i>Triboson</i>	1.54 ± 0.09	0.33 ± 0.03	0.18 ± 0.02	0.12 ± 0.02	1.17 ± 0.08	0.28 ± 0.04
$t\bar{t}$	2.76 ± 0.93	2.22 ± 0.85	1.56 ± 0.71	0.69 ± 0.49	0.26 ± 0.26	0.00 ± 0.20
$t\bar{t}Z$	3.20 ± 0.26	0.90 ± 0.17	0.74 ± 0.17	0.74 ± 0.17	2.25 ± 0.20	0.59 ± 0.09
$t\bar{t}W$	0.14 ± 0.10	0.08 ± 0.08	0.00 ± 0.00	0.00 ± 0.00	0.06 ± 0.06	0.00 ± 0.00
$t\bar{t}WW$	0.01 ± 0.00	0.00 ± 0.00	0.00 ± 0.00	0.00 ± 0.00	0.00 ± 0.00	0.00 ± 0.00
single t	0.00 ± 0.02	0.00 ± 0.02	0.00 ± 0.02	0.00 ± 0.02	0.00 ± 0.02	0.00 ± 0.02
tZ	0.64 ± 0.05	0.15 ± 0.02	0.10 ± 0.02	0.09 ± 0.02	0.49 ± 0.04	0.10 ± 0.02
Z+jets	15.02 ± 6.58	1.59 ± 1.59	0.00 ± 0.02	0.00 ± 0.02	3.85 ± 2.01	0.00 ± 0.02
Higgs	2.37 ± 0.09	0.94 ± 0.06	0.53 ± 0.05	0.37 ± 0.04	1.30 ± 0.06	0.15 ± 0.02
Σ SM(MC)	56.11 ± 6.92	11.29 ± 2.13	4.80 ± 1.11	2.51 ± 0.87	33.31 ± 2.55	2.65 ± 0.61
RPV wino λ_{133} 400,200	17.15 ± 2.36	15.01 ± 2.20	-	11.49 ± 1.89	-	-
N2N3 stau 100,0	10.68 ± 1.77	9.17 ± 1.65	5.50 ± 1.30	1.47 ± 0.68	-	-

Table 5.10: Number of SM MC background events and events from benchmark SUSY scenarios which survive event selection criteria in the $2\ell 2\tau$ channel. Uncertainties are statistical only. Numbers given in the benchmark point descriptions give the mass of the NLSP and LSP respectively for the RPV wino and $\tilde{\chi}_2^0\tilde{\chi}_3^0$ stau scenarios.

Process	$2l+\geq 2\tau$	Z-veto	SR2noZa	SR2noZb	Z request	SR2Z
ZZ	11.47 ± 0.18	2.14 ± 0.07	0.17 ± 0.02	0.12 ± 0.02	9.33 ± 0.16	0.68 ± 0.04
<i>Triboson</i>	0.40 ± 0.04	0.21 ± 0.03	0.07 ± 0.02	0.05 ± 0.01	0.19 ± 0.03	0.05 ± 0.01
$t\bar{t}Z$	1.21 ± 0.24	0.67 ± 0.17	0.17 ± 0.07	0.38 ± 0.15	0.54 ± 0.17	0.24 ± 0.13
$t\bar{t}WW$	0.00 ± 0.00	0.00 ± 0.00	0.00 ± 0.00	0.00 ± 0.00	0.00 ± 0.00	0.00 ± 0.00
WZ	1.99 ± 0.35	1.15 ± 0.26	0.34 ± 0.16	0.28 ± 0.16	0.83 ± 0.24	0.20 ± 0.12
$t\bar{t}W$	0.22 ± 0.14	0.22 ± 0.14	0.13 ± 0.11	0.12 ± 0.11	0.00 ± 0.00	0.00 ± 0.00
$t\bar{t}$	6.71 ± 1.36	6.71 ± 1.36	1.44 ± 0.62	1.15 ± 0.55	0.00 ± 0.20	0.00 ± 0.20
tZ	0.19 ± 0.03	0.11 ± 0.02	0.04 ± 0.01	0.03 ± 0.01	0.07 ± 0.02	0.01 ± 0.01
Z +jets	200.14 ± 28.75	40.24 ± 11.93	0.00 ± 0.02	0.00 ± 0.02	159.90 ± 26.15	0.00 ± 0.02
single t	0.23 ± 0.23	0.23 ± 0.23	0.00 ± 0.02	0.00 ± 0.02	0.00 ± 0.02	0.02 ± 0.02
WW	0.23 ± 0.23	0.23 ± 0.23	0.00 ± 0.02	0.00 ± 0.02	0.00 ± 0.02	0.00 ± 0.02
Higgs	1.72 ± 0.06	0.79 ± 0.06	0.25 ± 0.03	0.18 ± 0.02	0.94 ± 0.03	0.14 ± 0.01
Σ SM(MC)	224.53 ± 28.82	52.70 ± 12.05	2.68 ± 0.85	2.33 ± 0.76	171.83 ± 26.18	1.344 ± 0.50
RPV wino λ_{133} 400,200	16.15 ± 2.36	15.69 ± 2.32	-	9.53 ± 1.83	-	-
N2N3 stau 100,0	23.86 ± 2.74	23.86 ± 2.74	6.15 ± 1.33	-	-	-

Everything presented so far has used MC samples to estimate the number of expected events from different SM background processes, however, this is not always sufficient, and for some processes a data-driven estimation is made. The reasoning behind this and details of the methodology used to estimate the background events in this analysis are discussed in the following chapter.

Chapter 6

Background Estimation and Systematic Uncertainties

6.1 Introduction

This chapter discusses aspects of the analysis relevant to estimating the background events and calculating the systematic uncertainties affecting the analysis. First, the processes contributing to background events expected by the Standard Model are considered in more detail in this section, followed by a description of the data-driven “weighting method” background estimation technique in Section 6.2, and finally a discussion of the sources of systematic uncertainty affecting background processes estimated with MC, with the weighting method, and the expected signal events is made in Section 6.3. I made small contributions to these studies, including the plots in this introduction, and some of the systematic uncertainty calculations. Any content not identified as produced by other analysis team members has been produced by myself.

Background processes yielding events surviving in the defined signal regions can produce the required lepton multiplicity with either *real* or *fake* objects. A lepton referred to as “real” is required to have been produced promptly, and then reconstructed correctly. Promptly produced leptons come from the decays of W, Z, or Higgs bosons and taus, whilst the decay products of long-lived b- and c-quarks are classified as non-prompt. A “fake” lepton can be a non-prompt genuine lepton or it can be a different object which has been mis-reconstructed as a lepton. Sources of fakes are semi-leptonically decaying b-quark or c-quark (“heavy flavour”) jets, “light flavour” u-quark, d-quark, or s-quark jets which are mis-reconstructed as leptons, or photons which convert to electrons within the detector.

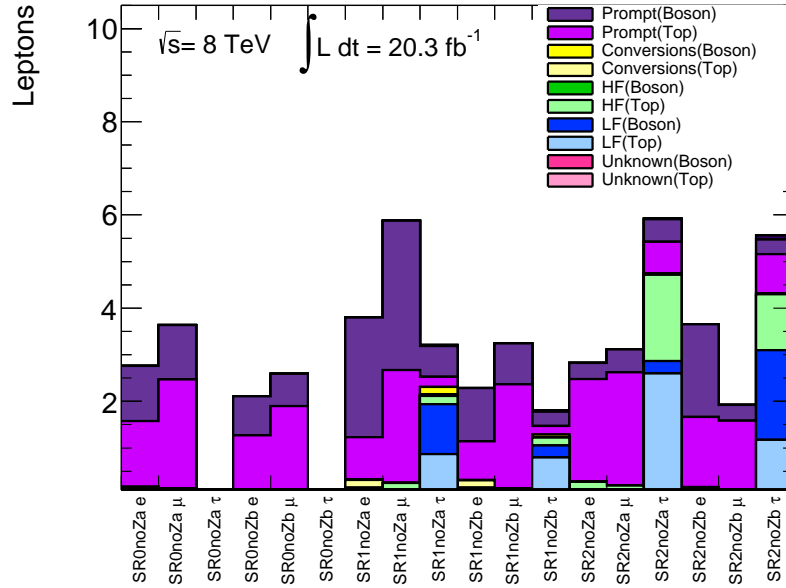


Figure 6.1: Source of leptons in signal regions which include a Z-veto, split by lepton flavour and into backgrounds containing top quarks or bosons. Any background process containing both is classified as “top”.

In Figure 6.1 and Figure 6.2 the sources of leptons from MC backgrounds are displayed in the Z-veto and Z-selection search regions respectively. Each lepton flavour is listed separately, as fake electrons, muons and taus can be produced by different processes and in different proportions. The background processes are separated into *top* which includes any process with a top quark included, and *boson* which includes any non-top process involving bosons. The leptons are classified by finding a *truth* object as defined in Section 4.3 within a specified ΔR distance of a reconstructed lepton, and using the truth vertex and decay information to trace backwards to its “parent” particle. Leptons are labelled as *HF* if the parent is a b or c quark, *LF* for light-flavour quarks, *Conversion* if the parent is a photon, *Prompt* if it is a W, Z, Higgs or tau, or *Unknown* if the source cannot be traced. It is very unlikely that the source will be unknown, hence no contribution is visible in the figures, although it can amount to a few % for tau leptons in the tau-rich SRs. For light leptons this occurs less than 1% of the time. Taus are marked as originating from a conversion if they are within a distance of $\Delta R < 0.2$ from a truth electron whose parent is a photon.

The majority of light leptons in all of the considered signal regions are produced promptly from either boson or top decays. In SR0noZa about 55% of electrons and approximately 65% of muons are produced promptly from top processes, and the remainder come from prompt boson decays. In SR0noZb the proportion of electrons (muons) ori-

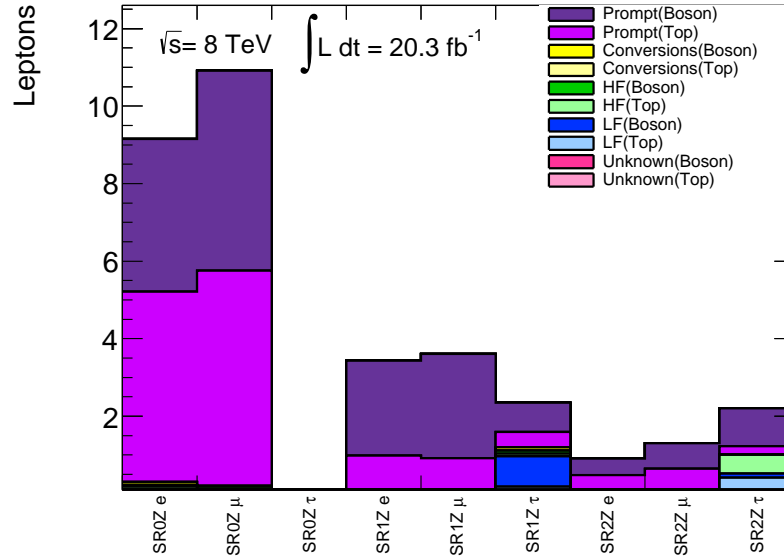


Figure 6.2: Source of leptons in signal regions which include a Z-selection, split by lepton flavour and into backgrounds containing top quarks or bosons. Any background process containing both is classified as “top”.

ginating promptly from top processes is 55% (75%), again the remainder are produced promptly from boson processes. Comparatively in SR0Z, 55% of electrons and 50% of muons originate from prompt top processes and the remainder are produced promptly from boson processes, with the exception of approximately 1% of electrons, which are produced by a conversion from a boson process.

Approximately 8% of electrons in SR1noZa and approximately 16% in SR1noZb are marked as conversions which come from top decays. Heavy flavour decays in top processes account for approximately 7% of electrons in the SR2noZa region and approximately 3% of muons in both SR1noZa and SR2noZa. The muons in SR1noZb and electrons and muons in SR2noZb are produced promptly, with a higher proportion from top processes in SR2noZa and SR2noZb (45-85% of electrons and 80-85% of muons) than there are in SR1noZa and SR1noZb (25-45% of electrons and 40-65% of muons). This behaviour is also seen in the Z-rich, tau-rich, SRs where all electrons and muons are produced promptly and top processes contribute about 30% in the SR1Z and about 55% in SR2Z.

Taus within the signal regions have a much higher proportion of fake sources. In SR1noZa only approximately 30% of taus are produced promptly, the majority of fake taus come from light flavour jets, 20% of taus are from top process LF jets, and 40% are from boson LF jets. The remainder of fake taus are produced by conversions in bo-

son processes and heavy flavour jets from top processes, both of which contribute about 5%. The proportions of sources for taus in SR1noZb is very similar, with the exception that more LF jets produced taus come from top processes, which make up approximately 43% of the total. About 50% of taus in SR2noZa come from LF jets, 42% from top processes. 30% originate from HF jets in top processes, and the remaining 20% are produced promptly from top and boson processes in equal amounts. The sources vary in proportion in SR2noZb, which comprises 20% from LF top, 35% from HF top, 22% from HF top and 23% produced promptly. In the Z-rich tau SRs approximately 50% of the taus are promptly produced. In SR1Z the main fake source is LF boson processes, which produce about 40% of taus, and the remainder come from small contributions from boson process conversions, boson process heavy flavour jets and LF jets from top processes. In SR2Z heavy flavour jets from top processes are the main fake source, producing approximately 25% of taus. LF jets from top and boson processes make up approximately 20% and 5% of the total.

Background processes are classified as *irreducible* if all four leptons are real and prompt or *reducible* if at least one lepton is fake. Background processes which fall into the irreducible category are ZZ/γ^* , ZZZ , ZWW , $t\bar{t}+Z/WW$, $t+WZ$ and Higgs processes involving decays through ZZ/γ^* or produced in association with either a Z or $t\bar{t}$ (dileptonic). The most significant contributions come from ZZ/γ^* , the triboson processes, $t\bar{t}+Z$ and Higgs. The reducible background can be further split by the number of fake leptons produced. Backgrounds containing three real leptons and one fake are WZ/γ^* , WWW , $t\bar{t}+Z/WW$ (if $t\bar{t}$ is not dileptonic) and $t+Z$. Events with two real leptons and two fake leptons can come from Z/γ^*+jets , $t\bar{t}$, single top (Wt), and WW . It is in principle possible to produce events which contain only one real lepton and three fakes from either single top (the s- or t-channel) or W, but the contribution from these is negligible and so they are not considered in the estimation.

Irreducible backgrounds are well modelled by MC, whereas for reducible backgrounds a data-driven estimation called the *Weighting Method* is used. This is required to account for the production of fakes, which is complex and dependent on a wide range of variables. This method will be detailed in Section 6.2. At this stage the sources of systematic uncertainty need to be identified and evaluated, as detailed in Section 6.3. Once the total background estimation is made, it is tested by comparing the number of predicted background events to the number of events observed in data. Additional regions called *validation regions* (VRs) are specially defined for this purpose, and they are required to test the estimation

of all of the main background processes without revealing any of the data events contained within the signal regions. The region definitions and results for the validation can be found in Section 6.4.

6.2 Weighting Method

In order to estimate the contribution to the signal regions from reducible backgrounds, a “weighting method” is used to predict the likelihood for a fake lepton to be reconstructed as a signal lepton, and thus accepted into an SR. In this method, leptons are defined as being either *tight* or *loose*. Tight leptons are taken to coincide with signal leptons as defined previously in this analysis: they satisfy all identification, overlap, isolation, and impact parameter requirements discussed in Section 4.5. On the other hand, loose leptons pass the baseline cuts and overlap removal, but will fail one or more of the identification, isolation or impact parameter cuts required of signal leptons. *Control regions* (CRs) are then defined in which to observe the number of events which pass similar requirements to those made in the SRs or VRs, but contain one or more loose leptons. The numbers of events are then weighted to estimate events coming from fake lepton sources within the SRs and VRs used in the analysis.

6.2.1 Derivation and methodology

Firstly, the probability \bar{f} for a fake lepton to be reconstructed as a loose lepton and the probability f for a fake lepton to be reconstructed as a tight lepton are defined. Similarly, e and \bar{e} identify the probability that a real lepton is reconstructed as either a tight or loose lepton respectively. To conserve total probability, these must be related by: $\bar{f} = (1 - f)$ and $\bar{e} = (1 - e)$. In the following, f is also referred to as the “fake rate” and e as the “reconstruction efficiency”. These probabilities can then be combined with the number of events in the control regions to calculate the number of events in a signal or validation region. Considering a two lepton scenario with only light leptons for simplicity, the following relationship between the numbers of loose (l) and tight (L) to real (R) and fake (F) leptons can be constructed:

$$\begin{pmatrix} N_{LL} \\ N_{Ll} \\ N_{lL} \\ N_{ll} \end{pmatrix} = \begin{pmatrix} e_1 e_2 & e_1 f_2 & f_1 e_2 & f_1 f_2 \\ e_1 \bar{e}_2 & e_1 \bar{f}_2 & f_1 \bar{e}_2 & f_1 \bar{f}_2 \\ \bar{e}_1 e_2 & \bar{e}_1 f_2 & \bar{f}_1 e_2 & \bar{f}_1 f_2 \\ \bar{e}_1 \bar{e}_2 & \bar{e}_1 \bar{f}_2 & \bar{f}_1 \bar{e}_2 & \bar{f}_1 \bar{f}_2 \end{pmatrix} \begin{pmatrix} N_{RR} \\ N_{RF} \\ N_{FR} \\ N_{FF} \end{pmatrix}. \quad (6.1)$$

In the left-hand vector, N_{ij} refers to the number of events containing leptons i and j which are either loose or tight. These are related to the right-hand vector which gives N_{kl} for leptons k and l which are either real or fake. The indices on the fake rates and reconstruction efficiencies in the matrix give an index for the lepton which corresponds to the ordering used in N_{kl} - i.e. a rate or efficiency with a subscript of 2 will relate to a lepton with index l .

The size of this matrix would become much larger (11×11) when the full four lepton relationship is written out, including a maximum of two light leptons, but the method remains the same. The total number of events with two tight leptons can be written as:

$$N_{LL} = e_1 e_2 N_{RR} + e_1 f_2 N_{RF} + f_1 e_2 N_{FR} + f_1 f_2 N_{FF}, \quad (6.2)$$

in terms of events with different numbers of real and fake leptons. This can be redefined to give the reducible contribution in terms of the number of events with one or more loose leptons:

$$N_{LL}^{red} = (N_{Ll} - e_1 \bar{e}_2 N_{RR}) \frac{f_2}{\bar{f}_2} + (N_{lL} - \bar{e}_1 e_2 N_{RR}) \frac{f_1}{\bar{f}_1} - (N_{ll} - \bar{e}_1 \bar{e}_2 N_{RR}) \frac{f_1}{\bar{f}_1} \frac{f_2}{\bar{f}_2}. \quad (6.3)$$

The ratio f_i/\bar{f}_i gives the probability for a fake lepton i to be reconstructed as a tight lepton. Considering the first term, the number of events where the first lepton is tight and the second is loose N_{Ll} is multiplied by the probability for the loose lepton to be reconstructed as tight f_2/\bar{f}_2 . Any contribution coming from real sources where one real lepton is reconstructed as a loose lepton ($e_1 \bar{e}_2 N_{RR}$) is then subtracted so that only the reducible contribution is counted. The same pattern is then followed for events where the first lepton is loose and the second is tight, and where both are loose. The final term ensures that double counting of events with two fake leptons is avoided. This leaves the number of events with at least one loose lepton where at least one of the leptons was faked, weighted by the probability that these events will be accepted into a region requesting two tight leptons.

The control region CR1 is defined to contain one loose lepton, and so the number of events in this region would be equal to the sum of N_{lL} and N_{Ll} . The control region CR2 is defined to contain two loose leptons, and the number of events in CR2 is therefore represented by N_{ll} . Equation 6.3 can then be written in terms of the number of data events in these control regions CR1 and CR2 to give the number of reducible events in a given signal or validation region, N_{red} :

$$N_{red} = \left(N_{data}^{CR1} - N_{irr}^{CR1} \right) \times \frac{f_i}{\bar{f}_i} - \left(N_{data}^{CR2} - N_{irr}^{CR2} \right) \times \frac{f_1}{\bar{f}_1} \times \frac{f_2}{\bar{f}_2}. \quad (6.4)$$

N_{data}^{CR1} and N_{data}^{CR2} give the number of data events observed in CR1 and CR2. The irreducible components N_{irr}^{CR1} and N_{irr}^{CR2} are estimated with MC samples, and these events are then subtracted from the data events to leave an estimation of the reducible component in each control region. The fake ratio denoted f_i/\bar{f}_i represents the correct ratio being applied dependent on whether the first or second lepton is loose for each instance. In order to perform this calculation, the fake ratios to weight the number of reducible events in the CRs are now required. The following section describes how these fake ratios are obtained and what additional measurements are required in order to estimate them.

6.2.2 Required Components for Weighted Average Fake Ratios

The fake ratios are control region specific, and they also depend on the lepton flavour, the type of fake (i.e. whether the fake lepton comes from a conversion, heavy flavour jets or light flavour jets) and the background process being estimated. Background processes involving top quarks can produce objects with different properties to those produced by a background process involving bosons, for example the kinematics of jets will be quite different. Background processes are therefore separated into those containing tops, and those containing bosons but no top quarks. The fake ratios for each process are taken from MC for each lepton type. These have additional dependencies which vary for each lepton flavour. For muons the ratios are measured as a function of muon p_T , whilst for electrons they are measured as a function of both η and p_T , which is possible due to the large number of candidate electrons available to extract this information from. Taus are split into one-prong or three-prong due to differences in the fake processes coming from each, and the fake ratio for each is then measured dependent on p_T and η .

Scale factors s^i for a given fake type i are measured by defining regions where leptons are dominantly produced by this fake process and comparing events seen in data and MC. These are used to correct any differences between MC samples and the data. They are assumed to be independent of the background process or the signal or validation region considered, however different flavour fake leptons are produced predominantly by different processes, so each lepton flavour is also considered separately.

Next, the abundance of each kind of fake origin within a given control region for each of the lepton flavours needs to be considered, and the fake ratios weighted accordingly. These weights are called *process fractions* R_{ij} defined as:

$$R_{ij} = \frac{N_{ij}\epsilon_j}{\sum_{kl} N_{kl}\epsilon_l}, \quad (6.5)$$

where the index i runs over the fake types, the index j runs over the background processes,

N_{ij} is the number of events measured in a given CR if the kinematic cuts on E_T^{miss} and/or m_{eff} are removed and the efficiency for the omitted cuts ϵ_j is then applied to correct for this. These modified versions of the CR requirements are used in order to increase the number of events available in these regions to draw more statistically accurate conclusions. The efficiencies themselves are calculated per region in events with loose fake leptons using the E_T^{miss} and m_{eff} distributions, separately for each lepton flavour and as a function of lepton p_T .

The process fractions R_{ij} are then applied to the fake ratios F_{ij} , along with the scale factors s^i , to give a weighted average fake ratio:

$$F^l = \sum_{i,j} (R^{ij} \times s^i F^{ij}), \quad (6.6)$$

for a given lepton flavour l as a sum over all fake types i and background processes j . A weighted average fake ratio is calculated for each lepton flavour for each signal or validation region.

6.3 Systematic Uncertainties

As the irreducible and reducible backgrounds are estimated with different methods, their systematic uncertainties are calculated separately and involve different considerations. These will therefore be discussed separately in Section 6.3.1 and Section 6.3.2 respectively. Sources of systematic uncertainty for the expected signal events are discussed in Section 6.3.3. All uncertainties are propagated through to the statistical interpretation used to produce exclusion limits and included in the calculation as individual nuisance parameters, which will be discussed later in Section 7.2.

6.3.1 Irreducible Background

The procedures evaluating systematic uncertainties on the irreducible backgrounds follow prescriptions that are common to all ATLAS analyses. The various sources of uncertainty and how they are estimated for irreducible backgrounds are given below.

MC Cross-section

The uncertainties on the calculated cross-sections corresponding to a certain background process are provided centrally by ATLAS, together with the generated MC samples. These could have been estimated for example by comparing the results using different generators and in some cases the effects of using different PDF sets is also considered. In addition,

all perturbative QCD calculations are dependent on the choice of a few parameter values. The *renormalisation scale* μ gives the scale of dependence for the running strong coupling $\alpha_s(\mu^2)$, and is normally set to be equal to the momentum transfer Q of the scattering. However, this does not have to be the case, and varying the choice for this parameter effects the predictions of the calculation e.g. the cross-section. The *factorisation scale* refers to the scale at which the hard scattering effects of a QCD interaction are separated from the PDF. This is often set to be equal to μ , but again this can be varied, and the variation will have an effect on the outcome and therefore the cross-section. The strong coupling constant at the renormalisation scale $\alpha_s(\mu^2)$ must also be defined but can be varied. The cross-section uncertainties for MC samples include the effect of variations of all three of these QCD perturbation theory properties.

For $t\bar{t} + Z/W/WW$ backgrounds the cross-section uncertainty is 30% [112], [113], for ZZ this is 5% [114], for WZ it is 7% [114], and for all triboson processes, which are known less precisely, a conservative 50% uncertainty is recommended. Higgs samples for the VH and VBF processes all have uncertainties of 20% [115], while those for the $t\bar{t}H$ and ggF processes have a higher associated uncertainty of 100% [115].

MC Generator

This was calculated by the four lepton analysis group in order to account for the choice of an MC sample using one generator rather than another for the ZZ and $t\bar{t}Z$ backgrounds. This uncertainty involves considering the *acceptance* of four lepton events, which is defined as the ratio of four lepton events to the total events in the sample. This is calculated using the truth information in the MC samples, and producing a close emulation of the analysis selections which uses truth objects.

For the ZZ background, the acceptance was compared for samples generated with Powheg, which is used for the background estimation, and with the alternate samples produced using aMC@NLO. This comparison is made as a function of E_T^{miss} and m_{eff} , due to the insufficient number of events available if the kinematic cuts of the analysis SRs using these variables are applied. The E_T^{miss} is corrected (“smeared ” [116]) in order to emulate the detector response as observed in data. The uncertainty in each signal region is calculated by scaling the difference seen between generators when four light leptons and a Z-veto or selection is applied, using the E_T^{miss} and/or m_{eff} dependence. Similarly for the $t\bar{t}Z$ background the Alpgen generated used in the background estimation was compared to alternate samples generated with Madgraph. However, the MC generated with Madgraph

only contains on-shell Z bosons, so to make a fair comparison, any regions with a Z-veto had a Z-selection applied instead.

The resulting uncertainties for the ZZ MC are relatively small, between approximately 5% and 20% depending on the region. For $t\bar{t}Z$ the uncertainties in the $4l0\tau$ regions are of a similar magnitude, but the regions containing one or two taus have uncertainties of approximately 15%-40% and 40%-100% respectively. This is due to the presence of very few events from this background process being present in these tau-rich channels. However for the same reason the higher uncertainties on $t\bar{t}Z$ in the tau-rich SRs are not a problem as the contribution from $t\bar{t}Z$ in these regions is very small.

PDF

A number of PDF “sets” exist, providing distributions for each of the partons using input from different experimental measurements e.g. data taken at HERA or the LHC and with different values of Q^2 [73]. The uncertainty associated with the choice of PDF set is evaluated for the ZZ sample in terms of the acceptance, using the PDF4LHC method [117, 118] on the full eigenset of the PDF set CT10 [102]. The free parameters in the PDF set are each varied up and down by 1σ and the resulting differences in observables are combined to give the total uncertainty. The other MC samples have this accounted for in the cross-section uncertainty, and so this method is not required.

Electrons

There are two sources of uncertainty on the electron energy, the electron energy scale (EES) and the electron energy resolution (EER). The first, EES, covers the uncertainty arising from any miscalibration of the electron energy using MC, and the latter, EER, considers the resolution of the ECAL subdetector itself. Both are calculated using an E_T and η dependent function to select W and Z events from data, and J/Ψ events to estimate this for low- p_T electrons [119]. The resulting uncertainties are applied to both the electrons and their associated component in the E_T^{miss} . The electron scale factor (ESF) accounts for uncertainty in the efficiency of reconstruction and identification of electrons. It is also E_T and η dependent, and is calculated by the ATLAS electron working group using W and Z events.

Muons

The muon energy scale (MES) uncertainty has contributions from both the inner detector track, referred to as Muon Inner Detector (MID), and the muon spectrometer track, referred to as Muon Muon Spectrometer (MMS). These are calculated using data events for $J/\Psi \rightarrow \mu\mu$, $Z \rightarrow \mu\mu$ and $\Upsilon \rightarrow \mu\mu$ compared to MC [120]. The resulting uncertainties are applied to both muons and their corresponding E_T^{miss} contribution. The muon scale factor (MSF) uncertainty, which considers the efficiency of muon reconstruction, has been calculated as a function of muon p_T in the same publication [120].

Taus

The tau energy scale (TES) uncertainties are calculated with a function dependent on the tau p_T , η , and the number of tracks associated to it, provided by the Tau Working Group and detailed in [121]. These uncertainties are only applied to taus which are identified as true by matching them within $\Delta R < 0.2$ of a truth tau in the MC. The tau identification scale factor (TSF) uncertainty [122] includes the uncertainty in the tau BDT identification and the BDT used to veto electron candidates, and is also only applied to true taus. It is calculated using tag and probe studies of $Z \rightarrow \tau\tau$ and $W \rightarrow \tau\nu$ events and the resulting uncertainty recommendations are provided by the Tau Working Group.

Jets

The Jet Energy Scale (JES) uncertainty [123] is accounted for with a prescribed ATLAS tool and applied to jets with $p_T > 15$ GeV and $|\eta| < 4.5$, and their corresponding E_T^{miss} components. The jet energy resolution (JER) uncertainty is estimated by smearing the p_T of each jet to a Gaussian distribution with unit mean and width, using a resolution function dependent on the p_T and η [124].

Missing Transverse Energy

The uncertainty in the pileup-suppressed soft term $E_{x(y)}^{\text{softjets}}$ (Section 4.4.7) can be estimated by adjusting the energy scale and the resolution of this term and recalculating the total resulting E_T^{miss} . The uncertainty in the other contributions to the E_T^{miss} are already accounted for in the uncertainties of the objects associated with them, as described above. The soft term uncertainty is found to be negligible for all MC samples considered, so it is not applied for this analysis.

Trigger

An uncertainty of 5% is applied to all events in order to account for small differences in efficiency of the lepton triggers observed when data $Z + jets$ events were compared to MC.

Luminosity

An uncertainty of 2.8% is prescribed for the ATLAS 2012 dataset based on preliminary calibration of the luminosity scale using beam separation scans run in 2012 [125].

6.3.2 Reducible Background

The uncertainty on the reducible background had to be calculated by the four lepton analysis team, as the method has been specifically developed as part of this analysis. The sources can be separated into uncertainties affecting the weighted average fake ratios, and those on the method as a whole, listed first below.

Five Lepton Events

The weighting method only accounts for events with four signal leptons, whereas the analysis is inclusive, and does not veto events which contain additional signal leptons. These events only account for about 2% or less of the total, and the conservative uncertainty adopted to cover this is set at 5%.

Closure Test

The weighting method is applied to Monte Carlo as it would be to data, with the exception of the corrective scale factors which are not included. The test “closes” (i.e. agrees with the expected result) within the statistical uncertainty, but it is not possible to assess the degree of agreement beyond this limit. Therefore the associated uncertainty is set to the statistical uncertainty on the MC used.

Uncertainties on the Weighted Average Fake Ratios

Systematic uncertainties affecting the weighted average fake ratios specifically are listed below. These are added in quadrature to give the total uncertainty on the average fake ratios.

Fake Ratio Scale Factors

These are varied by one sigma for each fake type and then the weighting method is recalculated, propagating the uncertainty through to the weighted average fake ratios. The differences in the resulting ratios are then summed in quadrature to give the total uncertainty in the estimate.

Region Selection Efficiency

The efficiencies for the signal region cuts are varied for each process and each fake type by a factor of two, before summing the resulting variations on the weighted average fake ratios in quadrature to give the resulting uncertainty.

Fake Ratio

The fake ratio calculation involved applying p_T -independent corrections to the region selection efficiencies due to differences for loose and tight fakes. The low numbers of events in many of the tight regions did not facilitate p_T -dependent corrections being applied. The p_T dependence of these corrections were then studied in regions where the number of events are sufficiently large, in order to estimate the uncertainty associated with not including the p_T dependence. The resulting differences showed that the correction varies by up to 20% at most, and so a conservative uncertainty of 20% is applied to all fake ratios.

Low MC Statistics

There are a number of bins within the process fraction calculation which are unpopulated due to low numbers of MC events. The uncertainty caused by this is obtained by setting all unpopulated bins to contain one event, and then recalculating the weighted average fake ratios. The variations in each resulting weighted average fake ratio are summed in quadrature to give a single error.

6.3.3 Signal Systematic Uncertainties

There are also a number of sources of uncertainty to be included on the signal samples.

Cross-section

The uncertainty on the MC cross-sections are taken directly from the Prospino [103] calculation itself, which varies PDF sets, factorisation scale and renormalisation scale to establish the effect. The method details can be found in [126].

Initial and Final State Radiation

Initial State Radiation (ISR) and Final State Radiation (FSR) refer to jets being produced from either the incoming partons or outgoing particles of the primary interaction, respectively. Parameters related to the probability of this radiation occurring are varied by one sigma for both ISR and FSR separately. The exact implementation of this variation will depend on the generator used - in all cases radiation from coloured particles typically occurs for high α_s values, but this is not necessarily directly varied. A comprehensive description of these parameters and their treatment can be found in [127]. The generator-level samples are produced once these parameter variations are made, and the acceptance of four lepton events for these are compared to the nominal samples in order to extract two systematic uncertainties. This is done for a selection of signal points, and the mean uncertainty was taken and applied for all points in each scenario, as it was seen to not vary greatly as a function of the various model parameters.

Matching Scale

The MadGraph [100] generator used in this analysis for signal MC production contains a parameter called the “matching” scale, which defines which event contents are dealt with by the matrix element, and which by the parton shower. These are simulated respectively by MadGraph itself and by Pythia. The variation of the matching scale is also related to the renormalisation and factorisation scales required for the generation, but these are not directly varied. The scale parameter is varied by one sigma in either direction before regenerating samples and comparing the four lepton acceptance to that of the nominal samples. As with the ISR and FSR uncertainties, the average of the variations seen for a number of signal sample points is taken and applied for all points of each SUSY scenario.

6.3.4 Summary

A summary of the systematic uncertainties on the irreducible and reducible background processes are shown for each SR in Figures 6.3-6.5. In the $4l0\tau$ SRs shown in Figure 6.3, the uncertainties on the weighting method appear very large, but the contribution from reducible background in these regions is very small, as can be seen from the yields in the plot legends. The largest contributions to the total uncertainty come from the theoretical cross-sections, the generator uncertainties for the $t\bar{t}Z$ and ZZ samples, and the statistical uncertainty on the MC samples. For SRs containing taus (see Figures 6.4 and 6.5), these uncertainties remain large, but much more of a contribution comes from uncertainties on

the weighting method. These vary slightly from region to region, but the average fake ratio uncertainty on τ_{aus} and the uncertainty from the weighting method closure test tend to be the largest. Tables containing the numbers for the breakdown of systematic uncertainties for each SR can be found in [Appendix C](#).

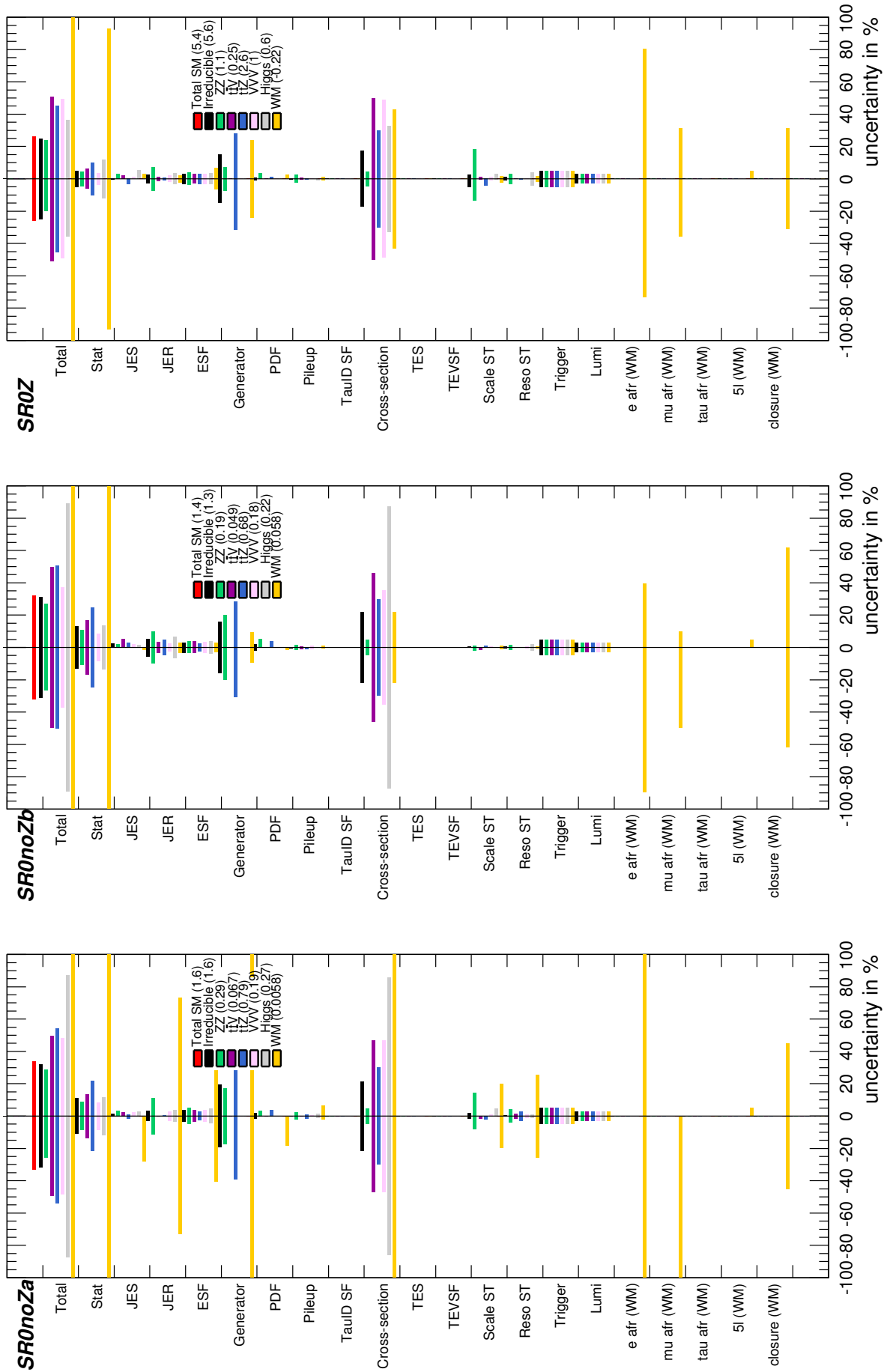


Figure 6.3: Summary of systematic uncertainties as defined in Section 6.3 on the estimated background in SR0noZa, SR0noZb, and SR0Z given as percentages. The reducible background is estimated with the weighting method, and the irreducible from MC, displayed as a total and separated by background process. The total uncertainty on the total estimated background is also shown in red. The yields from each background process in this SR are shown in brackets in the plot legend entries.

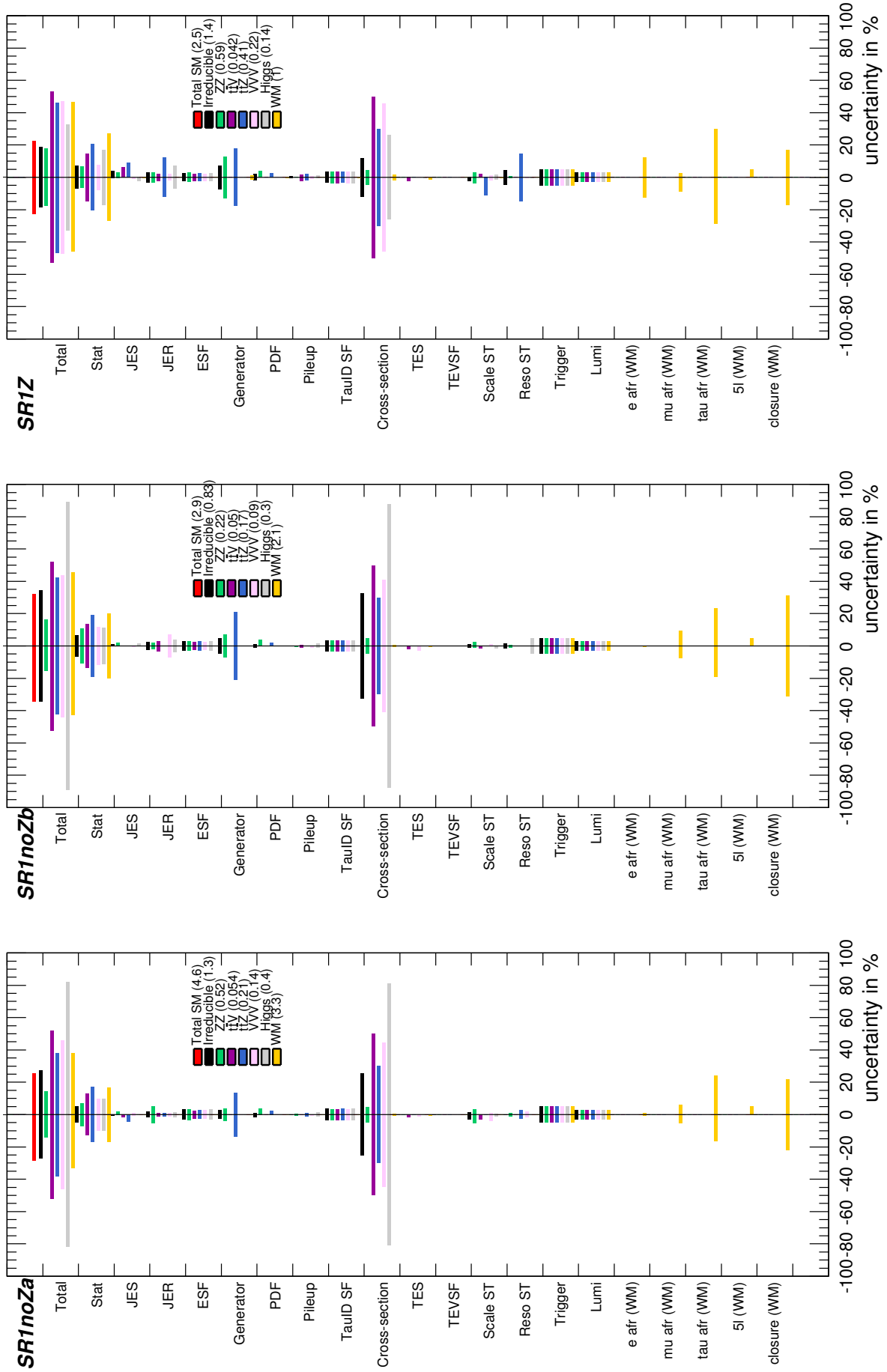


Figure 6.4: Summary of systematic uncertainties as defined in Section 6.3 on the estimated background in SR1noZa, SR1noZb and SR1Z given as percentages. The reducible background is estimated with the weighting method, and the irreducible from MC, displayed as a total and separated by background process. The total uncertainty on the total estimated background is also shown in red. The yields from each background process in this SR are shown in brackets in the plot legend entries.

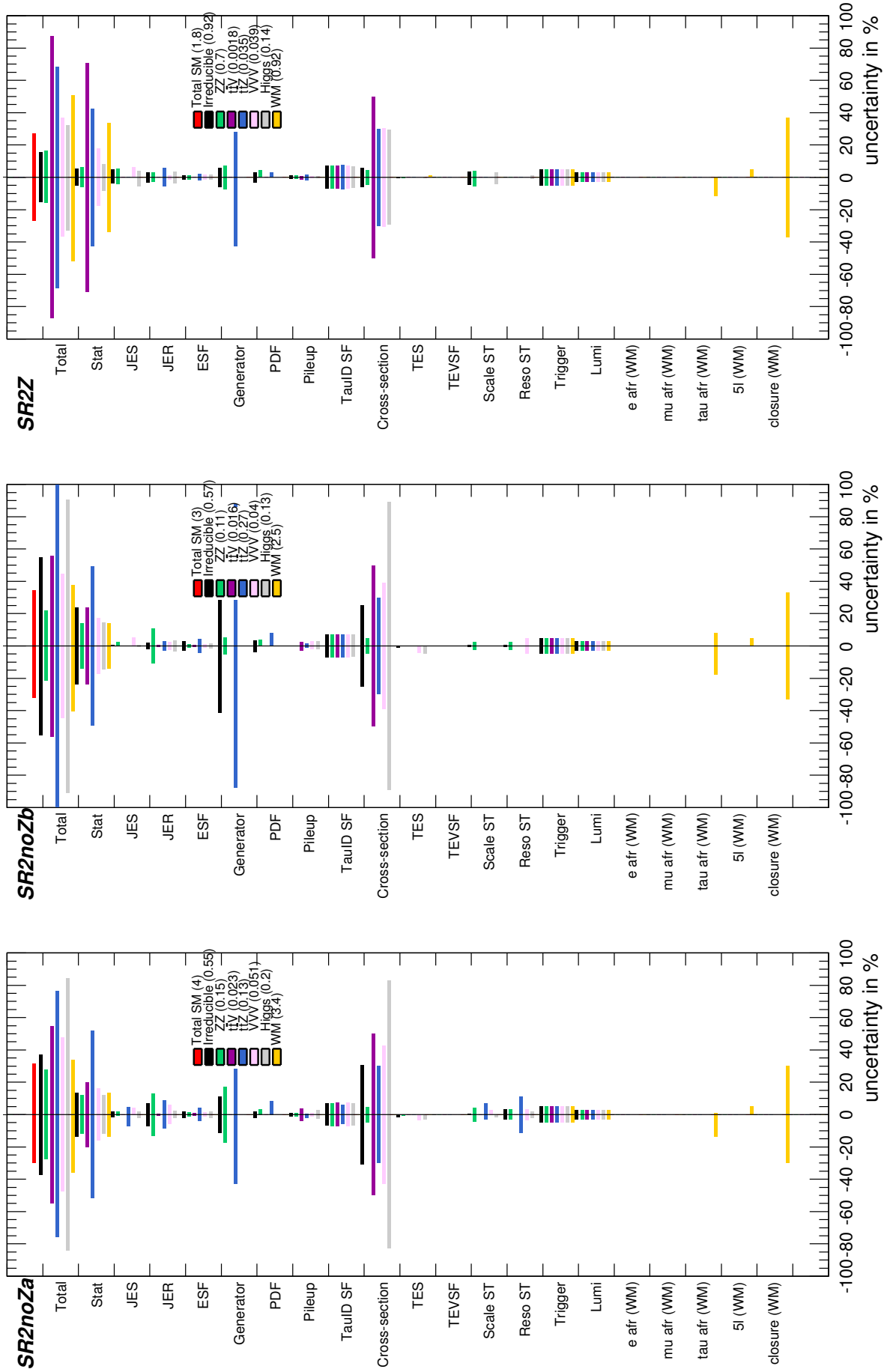


Figure 6.5: Summary of systematic uncertainties as defined in Section 6.3 on the estimated background in SR2noZa, SR2noZb and SR2Z given as percentages. The reducible background is estimated with the weighting method, and the irreducible from MC, displayed as a total and separated by background process. The total uncertainty on the total estimated background is also shown in red. The yields from each background process in this SR are shown in brackets in the plot legend entries.

6.3.4.1 Estimated Background in the Signal Regions

Table 6.1 displays the complete background estimation in the SRs with full statistical and systematic uncertainties included. The background processes have been separated into the irreducible processes, which are estimated individually with MC samples, and the reducible background processes, which are all estimated using the weighting method.

Table 6.1: Number of expected background events in each of the nine SRs including irreducible processes estimated with MC and the full weighting method estimation for the reducible backgrounds. Statistical and systematic uncertainties are included.

SR	ZZ	$t\bar{t}b + V$	$t\bar{t}b + Z$	VVV	Higgs	Red.	Σ SM
SR0noZb	$0.19^{+0.05}_{-0.05}$	$0.049^{+0.024}_{-0.024}$	$0.68^{+0.34}_{-0.34}$	$0.18^{+0.07}_{-0.07}$	$0.22^{+0.20}_{-0.20}$	$0.06^{+0.14}_{-0.14}$	$1.4^{+0.4}_{-0.4}$
SR1noZb	$0.219^{+0.036}_{-0.035}$	$0.050^{+0.026}_{-0.026}$	$0.17^{+0.07}_{-0.09}$	$0.09^{+0.04}_{-0.04}$	$0.30^{+0.26}_{-0.26}$	$2.1^{+0.4}_{-0.4}$	$2.93^{+0.33}_{-0.33}$
SR2noZb	$0.112^{+0.025}_{-0.024}$	$0.016^{+0.009}_{-0.009}$	$0.27^{+0.28}_{-0.15}$	$0.040^{+0.018}_{-0.018}$	$0.13^{+0.12}_{-0.12}$	$2.5^{+0.4}_{-0.4}$	$3.0^{+0.4}_{-0.4}$
SR0noZa	$0.29^{+0.08}_{-0.08}$	$0.067^{+0.033}_{-0.033}$	$0.8^{+0.4}_{-0.4}$	$0.19^{+0.09}_{-0.09}$	$0.27^{+0.23}_{-0.23}$	$0.006^{+0.161}_{-0.161}$	$1.6^{+0.5}_{-0.5}$
SR1noZa	$0.52^{+0.07}_{-0.07}$	$0.054^{+0.028}_{-0.028}$	$0.21^{+0.08}_{-0.11}$	$0.14^{+0.07}_{-0.07}$	$0.40^{+0.33}_{-0.33}$	$3.3^{+0.6}_{-0.6}$	$4.6^{+0.4}_{-0.4}$
SR2noZa	$0.15^{+0.04}_{-0.04}$	$0.023^{+0.012}_{-0.012}$	$0.13^{+0.10}_{-0.07}$	$0.051^{+0.024}_{-0.024}$	$0.20^{+0.16}_{-0.16}$	$3.4^{+0.5}_{-0.5}$	$3.97^{+0.30}_{-0.30}$
SR0Z	$1.09^{+0.26}_{-0.22}$	$0.25^{+0.13}_{-0.13}$	$2.6^{+1.2}_{-1.3}$	$1.0^{+0.5}_{-0.5}$	$0.60^{+0.22}_{-0.21}$	$0.0^{+0.0}_{-0.0}$	$5.4^{+1.4}_{-1.4}$
SR1Z	$0.59^{+0.11}_{-0.10}$	$0.042^{+0.022}_{-0.022}$	$0.41^{+0.19}_{-0.22}$	$0.22^{+0.11}_{-0.11}$	$0.14^{+0.05}_{-0.05}$	$1.05^{+0.29}_{-0.29}$	$2.45^{+0.29}_{-0.28}$
SR2Z	$0.70^{+0.12}_{-0.11}$	$0.0018^{+0.0015}_{-0.0015}$	$0.035^{+0.024}_{-0.031}$	$0.039^{+0.014}_{-0.014}$	$0.14^{+0.04}_{-0.05}$	$0.92^{+0.31}_{-0.31}$	$1.83^{+0.17}_{-0.17}$

6.4 Validating the Background Estimation

The performance of the background estimation is tested by comparing the total number of events predicted to the number of data events. As the analysis is blind, this cannot be done in the SRs, and so a number of validation regions (VRs) are defined for this purpose. These are designed to target specific background processes, whilst maintaining similarity to the signal regions. Because the analysis is blinded, they must be completely disjoint from the SRs. Only once the performance of the background estimation in the validation regions is satisfactory will the data be observed in the signal regions. Selection criteria are chosen in order to cover values of E_T^{miss} and m_{eff} which are complementary to those used by the signal regions. In total six validation regions are defined, and the cuts defining them are summarised in Table 6.2.

The validation region VR0noZ selects events containing four or more light leptons which do not contain a SFOS pair with an invariant mass within 10 GeV of m_Z , and requires that either the E_T^{miss} is less than 50 GeV or the m_{eff} is less than 400 GeV. This region is designed to target ZZ background processes, and will see contributions from these when the decaying Z bosons are off-shell, such that they are unaffected by the Z-

Table 6.2: Selection requirements and main background processes targeted for each of the six validation regions defined in this analysis. Nomenclature is the same as for the signal regions. 0, 1 and 2 within the region names refers to the number of taus. The exact cuts for the Z-veto and selection requirements for each channel are identical to those made for the SRs, detailed in Section 5.4. Where a m_{eff} cut is defined, this is applied as a logical or with the E_T^{miss} cut.

	$N(l)$	$N(\tau)$	Z boson cut	E_T^{miss} [GeV]	m_{eff} [GeV]	Target Process
VR0noZ	≥ 4	≥ 0	Z-veto	< 50	< 400	$Z^* Z^*$
VR1noZ	$= 3$	≥ 1	Z-veto	< 50	< 400	$Z^* Z^*, W Z^*, Z^* + \text{jets}$
VR2noZ	$= 2$	≥ 2	Z-veto	< 50	< 400	$Z^* + \text{jets}$
VR0Z	≥ 4	≥ 0	Z-selection	< 50	–	ZZ
VR1Z	$= 3$	≥ 1	Z-selection	< 50	–	$ZZ, W Z, Z + \text{jets}$
VR2Z	$= 2$	≥ 2	Z-selection	< 50	–	$Z + \text{jets}$

veto. Table 6.3 shows the number of events expected from the background estimation compared to the number of events observed in data for all of the VRs. The irreducible background estimated from MC is split by process, and the reducible backgrounds are all estimated together by the weighting method. The number of expected SM events in this region is 4.4, 3.6 of which come from ZZ processes, corresponding to a purity of approximately 80% for this VR. Small contributions of less than 0.1 events come from the tWZ , $t\bar{t}$ and triboson backgrounds, and 0.18 events are expected from Higgs MC. The second largest number of events is 0.5, predicted by the weighting method for all reducible processes. VR0Z also requires four light leptons, but applies the Z-selection and an E_T^{miss} of less than 50 GeV. No m_{eff} requirement is made as the Z-rich SRs do not consider this variable. This VR targets ZZ background processes as well, but the Z bosons in this instance will need to be on-shell in order to pass the Z-selection. The total number of expected events in this region is 193, 184 of which are from ZZ MC (see Table 6.3). This gives a purity of 95% for ZZ , which is higher than in VR0noZ. Minimal contributions from tWZ (0.13), $t\bar{t}$ (1.2) and triboson (2.13) are expected, and the reducible prediction in this VR is very low at 0.5 events. Higgs processes contribute the second largest number of events at 4.7, which is approximately 2.5% of the total.

Equivalent VRs are defined to complement the $3l1\tau$ signal regions. VR1noZ selects events which have $E_T^{\text{miss}} < 50$ GeV or $m_{\text{eff}} < 400$ GeV which have passed the $3l1\tau$ multiplicity and Z-veto requirements. This targets a mixture of ZZ , WZ and $Z + \text{jets}$ background processes, where any Z bosons must be off-shell. Considering Table 6.3, the

largest number of estimated events come from ZZ (1.43) and reducible (7.1) which will include both WZ and $Z + jets$ processes. This gives the VR a purity of approximately 96% for targeting these three backgrounds. VR0Z selection criteria are defined as three light leptons, one or more taus, a Z-selection and $E_T^{\text{miss}} < 50$ GeV. This targets the same ZZ , WZ and $Z + jets$ background processes as VR1noZ but in instances that the Z bosons are on-shell. As shown in Table 6.3, 31 events are expected in the VR, with 8.8 originating from ZZ background and 21 from reducible processes. This gives a purity of approximately 96%.

VR2noZ applies the $2l2\tau$ lepton multiplicity and Z-veto cuts and then requests that events have either $E_T^{\text{miss}} < 50$ GeV or $m_{eff} < 400$ GeV. This region targets the reducible background process $Z + jets$ with off-shell Z boson decays, and it can be seen in Table 6.3 that 32.5 out of the 35.1 events expected from background come from the reducible background estimation. There is also a significant contribution of 1.53 events expected from ZZ background, and minimal contributions of 0.3 events or less from the other reducible background sources. The purity is high at 95%, assuming all reducible events are attributable to $Z + jets$ events, although in practice the reducible processes are all calculated together. Finally region VR2Z requires the same $2l2\tau$ multiplicity criteria in addition to a Z-selection, and E_T^{miss} less than 50 GeV in the event. This targets on-shell Z boson decays in association with jets, and reducible background events make up 90 of the 99 expected events in this region. This gives a slightly lower purity of 91%, with the main contamination coming from 8.2 ZZ events, approximately 8% of the total.

Good agreement is seen within the systematic uncertainties between the number of expected background events and the number of data events in all six validation regions. In order to verify that the predicted events are also well described in terms of their event and object properties, a range of distributions for the predicted background events are also compared to those from data. Distributions of the E_T^{miss} and m_{eff} in two of the six validation regions, VR0Z and VR2Z, are shown in Figure 6.6. In Figure 6.6(a) and (b) displaying distributions for VR0Z the dominance of the irreducible ZZ background process can be seen clearly, and this region tests the performance of the MC samples used to estimate the irreducible background processes. The bottom boxes on each plot give the ratio of observed data events to estimated background events in each histogram bin, where the error bars on the points represent the full systematic uncertainty on the data, and the hashed area shows the systematic uncertainty on the background. For the vast majority of bins there is agreement within these systematic uncertainties, and the MC

background estimation appears to perform well. Figure 6.6(c) and (d) show the equivalent distributions in the VR2Z validation region, which contains a much larger contribution from reducible backgrounds due to the two requested taus. This provides a good measure of the performance of the weighting method to estimate these reducible background processes. The number of expected and observed events agree within systematic uncertainties and the weighting method and MC background estimation perform well together in this region.

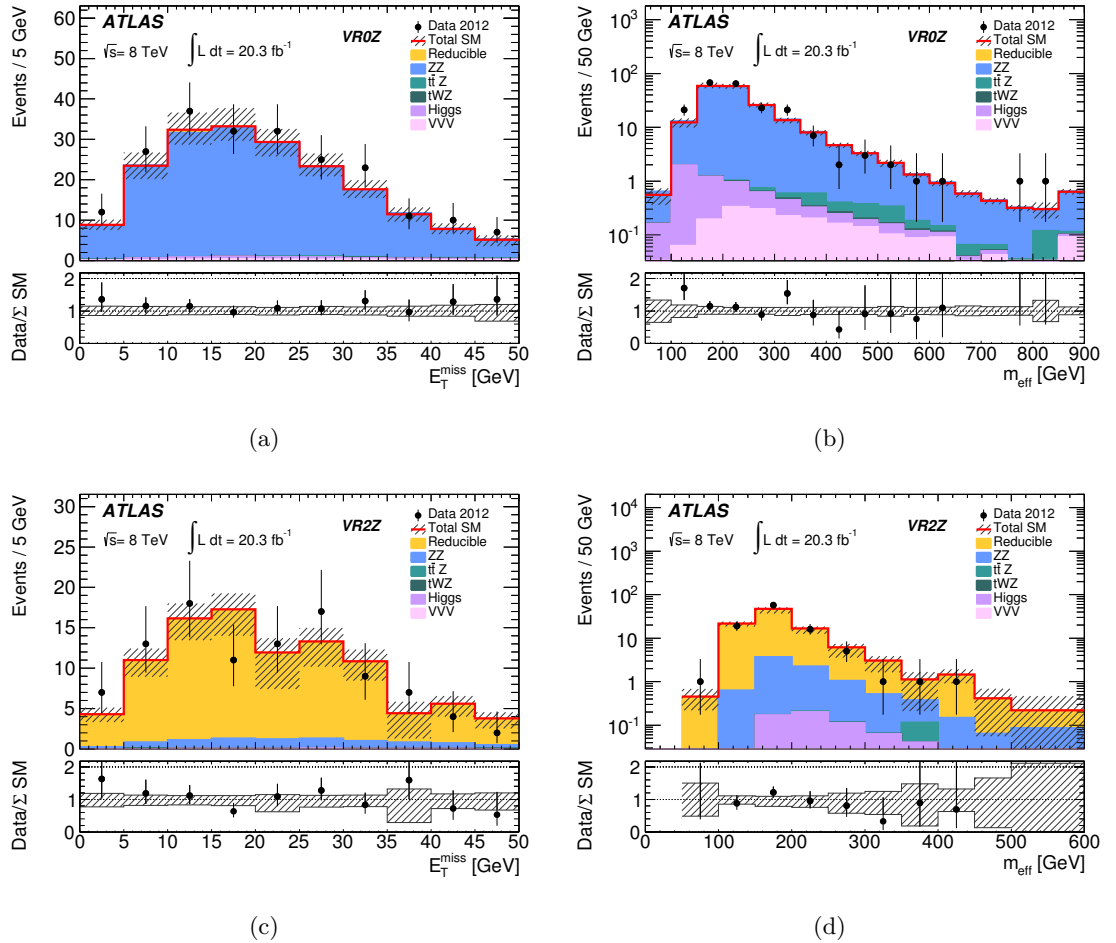


Figure 6.6: Distributions of (a) the E_T^{miss} and (b) m_{eff} for all SM background processes and data in VR0Z, and (c) E_T^{miss} and (d) m_{eff} for all background processes and data in VR2Z. Produced by other analysis team members and presented in [1].

Table 6.3: Table of expected and observed events in the validation regions, including full statistical and systematic uncertainties. Reducible background is estimated using the weighting method as described in Section 6.2

	ZZ	tWZ	$t\bar{t}Z$	Triboson	Higgs	Reducible	Σ SM	Data
VR0noZ	3.6 ± 0.7	0.017 ± 0.010	$0.034^{+0.036}_{-0.033}$	$0.090^{+0.032}_{-0.033}$	0.18 ± 0.13	$0.5^{+0.4}_{-0.5}$	4.4 ± 0.9	3
VR1noZ	1.43 ± 0.27	0.010 ± 0.006	0.033 ± 0.022	0.071 ± 0.029	0.28 ± 0.19	$7.1^{+1.8}_{-1.7}$	$8.9^{+1.8}_{-1.7}$	7
VR2noZ	$1.53^{+0.18}_{-0.17}$	0.007 ± 0.004	$0.025^{+0.031}_{-0.025}$	0.051 ± 0.020	0.29 ± 0.13	$33.2^{+3.3}_{-7.3}$	$35.1^{+3.4}_{-7.4}$	32
VR0Z	184^{+20}_{-19}	0.13 ± 0.07	1.2 ± 0.6	2.13 ± 0.33	4.7 ± 3.4	$0.5^{+3.1}_{-0.5}$	193^{+21}_{-19}	216
VR1Z	8.8 ± 0.9	0.039 ± 0.021	0.28 ± 0.11	0.19 ± 0.08	0.63 ± 0.16	21 ± 4	31 ± 4	32
VR2Z	$8.2^{+1.0}_{-1.0}$	0.0027 ± 0.0021	$0.09^{+0.12}_{-0.09}$	0.069 ± 0.013	0.61 ± 0.14	90^{+8}_{-22}	99^{+8}_{-22}	101

Good agreement within uncertainties of the yield and shape is seen between the background estimation and the observed data for all validation regions. This is consistent when considering different values of event properties, e.g. the transverse momentum of the leading lepton, or the missing transverse energy. It can be concluded that the background events are well modelled, and that there is a good understanding of all the associated uncertainties. The background estimation method is considered validated. This means that the data events within the SRs can be observed, and compared to the expected events predicted by the SM. This is referred to as “opening the box” within communities using blinded analyses. The following section documents the data events observed in the signal regions, before these are interpreted statistically in Section [7.2](#).

Chapter 7

Results and Interpretation

7.1 Signal Region Results

The data events observed in the signal regions are displayed in Table 7.1. No excess in the number of events is observed when comparing to the expected SM background. In general the agreement is good within systematic uncertainties, with some upwards and downwards fluctuations that are in line with expectations. How the differences between the number of expected and observed events can be quantified at a statistical level will be discussed in more detail in Section 7.2. As with the validation regions, it is also interesting to compare the shape of the distributions of important kinematic and event properties. The E_T^{miss} and m_{eff} distributions are shown in Figures 7.1, 7.2 and 7.3 for the $4l0\tau$ SRs, the $3l1\tau$ SRs, and the $2l2\tau$ SRs respectively. In some bins the solid red line denoting the total SM background contribution can appear lower than the top of the stacked separate background processes. This is due to possible negative contributions from the weighting method, which can arise due to the subtraction carried out to avoid double counting of events containing two fake leptons.

Figures 7.1(a) and (b) show the E_T^{miss} and m_{eff} distributions for the background and observed data in the signal region SR0noZa. The benchmark signal point included is from the $\tilde{\chi}_2^0\tilde{\chi}_3^0$ via slepton grid, which is the main target of this SR and has NLSP and LSP masses of 450 GeV and 300 GeV respectively. This point is within the region of parameter space expected to be excluded by the analysis, and clearly displays the difference between the signal and background distributions. Although the three data events observed in this region all fall into one bin for both distributions, this is also the bin with the highest expected SM background content in both cases.

SR0noZb has only one observed data event, which agrees well within uncertainties

with the estimated SM background shown in Figures 7.1(c) and (d). A benchmark signal point from the RPV wino λ_{121} scenario with NLSP mass of 600 GeV and LSP mass of 400 GeV is also included for comparison. The shape of the m_{eff} distribution in particular is quite different for the signal, for which the majority of events are expected to have $m_{eff} > 500$ GeV, corresponding to the tail of the SM background distribution.

The signal region SR0Z has 6 observed events in data, whose E_T^{miss} and m_{eff} distributions are displayed in Figures 7.1(e) and (f), along with the estimated SM background and a benchmark signal point from the GGM scenario. The latter has a \tilde{g} mass of 1000 GeV and μ of 200 GeV, corresponding to the region of parameter space where the electroweak sparticle decay process dominates. In both cases, the distributions seen in data agree within systematic uncertainty with the SM background distributions.

Table 7.1: Expected and observed number of events in each of the nine signal regions; combined statistical and systematic uncertainties are shown.

	ZZ	tWZ	$t\bar{t}Z$	Triboson	Higgs	Reducible	Σ SM	Data
SR0noZa	0.29 ± 0.08	0.067 ± 0.033	0.8 ± 0.4	0.19 ± 0.09	0.27 ± 0.23	$0.006^{+0.164}_{-0.006}$	1.6 ± 0.5	3
SR1noZa	0.52 ± 0.07	0.054 ± 0.028	0.21 ± 0.08	0.14 ± 0.07	0.40 ± 0.33	$3.3^{+1.3}_{-1.1}$	$4.6^{+1.3}_{-1.2}$	4
SR2noZa	0.15 ± 0.04	0.023 ± 0.012	0.13 ± 0.10	0.051 ± 0.024	0.20 ± 0.16	3.4 ± 1.2	$4.0^{+1.2}_{-1.3}$	7
SR0noZb	0.19 ± 0.05	0.049 ± 0.024	0.68 ± 0.34	0.18 ± 0.07	0.22 ± 0.20	$0.06^{+0.15}_{-0.06}$	1.4 ± 0.4	1
SR1noZb	$0.219^{+0.036}_{-0.035}$	0.050 ± 0.026	0.17 ± 0.07	0.09 ± 0.04	0.30 ± 0.26	$2.1^{+1.0}_{-0.9}$	$2.9^{+1.0}_{-0.9}$	1
SR2noZb	$0.112^{+0.025}_{-0.024}$	0.016 ± 0.009	$0.27^{+0.28}_{-0.27}$	0.040 ± 0.018	0.13 ± 0.12	$2.5^{+0.9}_{-1.0}$	3.0 ± 1.0	6
SR0Z	$1.09^{+0.26}_{-0.21}$	0.25 ± 0.13	2.6 ± 1.2	1.0 ± 0.5	$0.60^{+0.22}_{-0.21}$	$0.00^{+0.09}_{-0.00}$	5.6 ± 1.4	7
SR1Z	$0.59^{+0.11}_{-0.10}$	0.042 ± 0.022	0.41 ± 0.19	0.22 ± 0.11	0.14 ± 0.05	1.0 ± 0.5	2.5 ± 0.6	3
SR2Z	$0.70^{+0.12}_{-0.11}$	0.0018 ± 0.0015	0.035 ± 0.024	0.039 ± 0.014	$0.14^{+0.04}_{-0.05}$	0.9 ± 0.5	1.8 ± 0.5	1

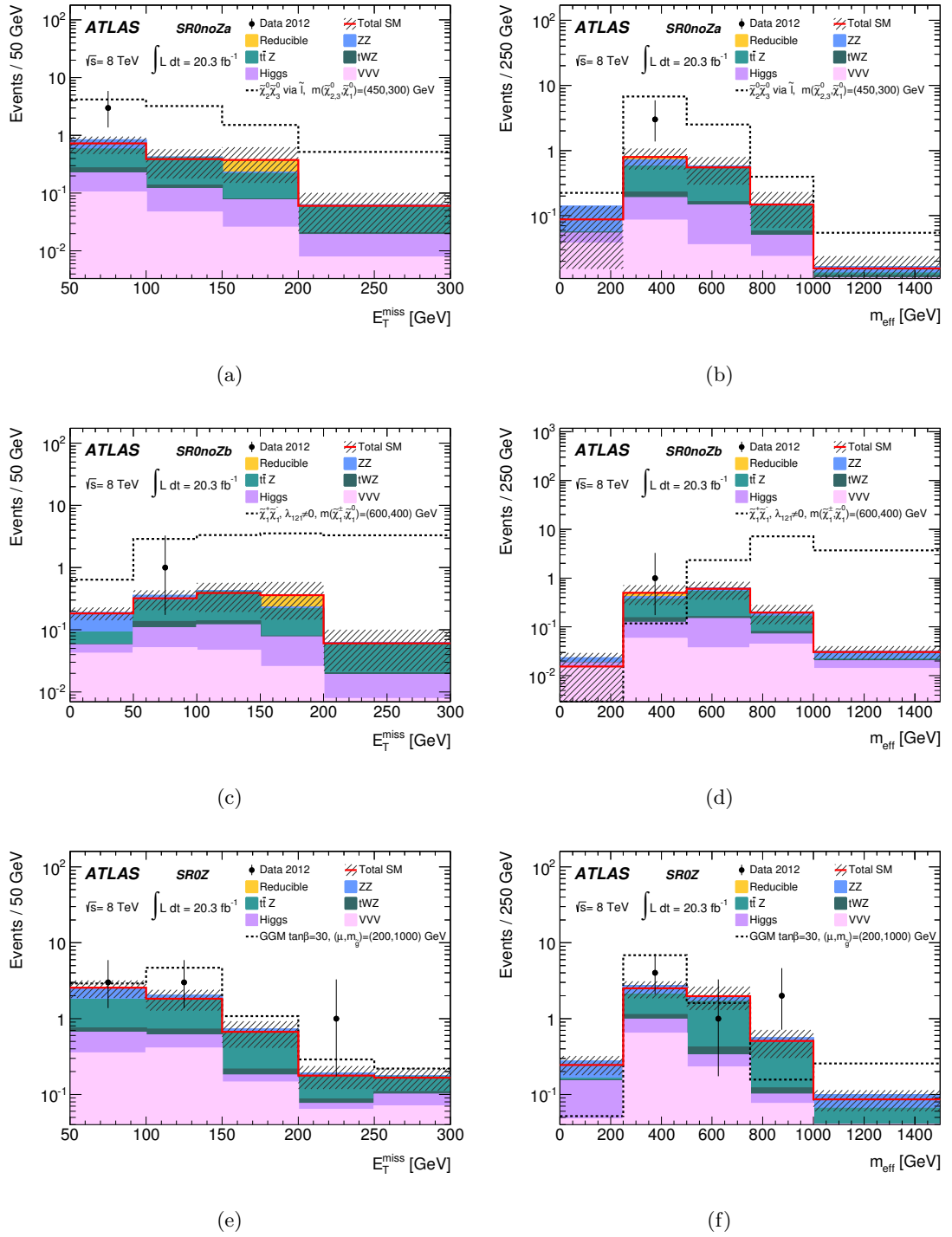


Figure 7.1: Distributions of (left) the E_T^{miss} and (right) the m_{eff} for all estimated SM background, data, and an example signal point in (a) and (b) for SR0noZa, in (c) and (d) for SR0noZb and in (e) and (f) for SR0Z. Produced by other analysis team members and presented in [1].

Figures 7.2(a) and (b) display the E_T^{miss} and m_{eff} distributions of the estimated SM background, observed data events and a benchmark SUSY point from the RPV wino λ_{133} scenario with NLSP mass 225 GeV and LSP mass 100 GeV in the signal region SR1noZa. A total of 4 events were observed in this region, which agrees well with the expected 4.6 events from SM backgrounds but within systematic uncertainties. It can be seen in both distributions that there is very good agreement between the data and SM expectations, with the data events sitting in the bins with highest expected contributions from the SM background events in both histograms. The shape of the signal distribution is less peaked at low E_T^{miss} and m_{eff} values and has a higher number of expected events. It is very clear in this region that the data events agree much better with the SM background than the expected signal. This is also the case for the signal region SR1noZb E_T^{miss} and m_{eff} distributions presented in Figures 7.2(c) and (d). There is good agreement within the systematic uncertainties between the 2.9 events expected from SM backgrounds and 1 event observed. The data events are located in the bins where the E_T^{miss} or m_{eff} is peaked for the estimated background distribution, and there is very good separation with the benchmark SUSY point, in this instance from the RPV gluino λ_{133} grid with NLSP(LSP) mass of 800(400) GeV. Figures 7.1(e) and (f) show the E_T^{miss} and m_{eff} distributions for expected background events, data events and a benchmark signal point in region SR1Z. This signal region also has very good agreement between the 2.5 expected background events and the 3 observed events. The data distributions agree within systematic uncertainty with the SM background distributions, and the shapes are similar. The benchmark signal point presented for this signal region is the RPV wino λ_{133} point used in Figures 7.2(a) and (b), as there are no Z-rich scenarios which contain taus in the final state considered in this analysis.

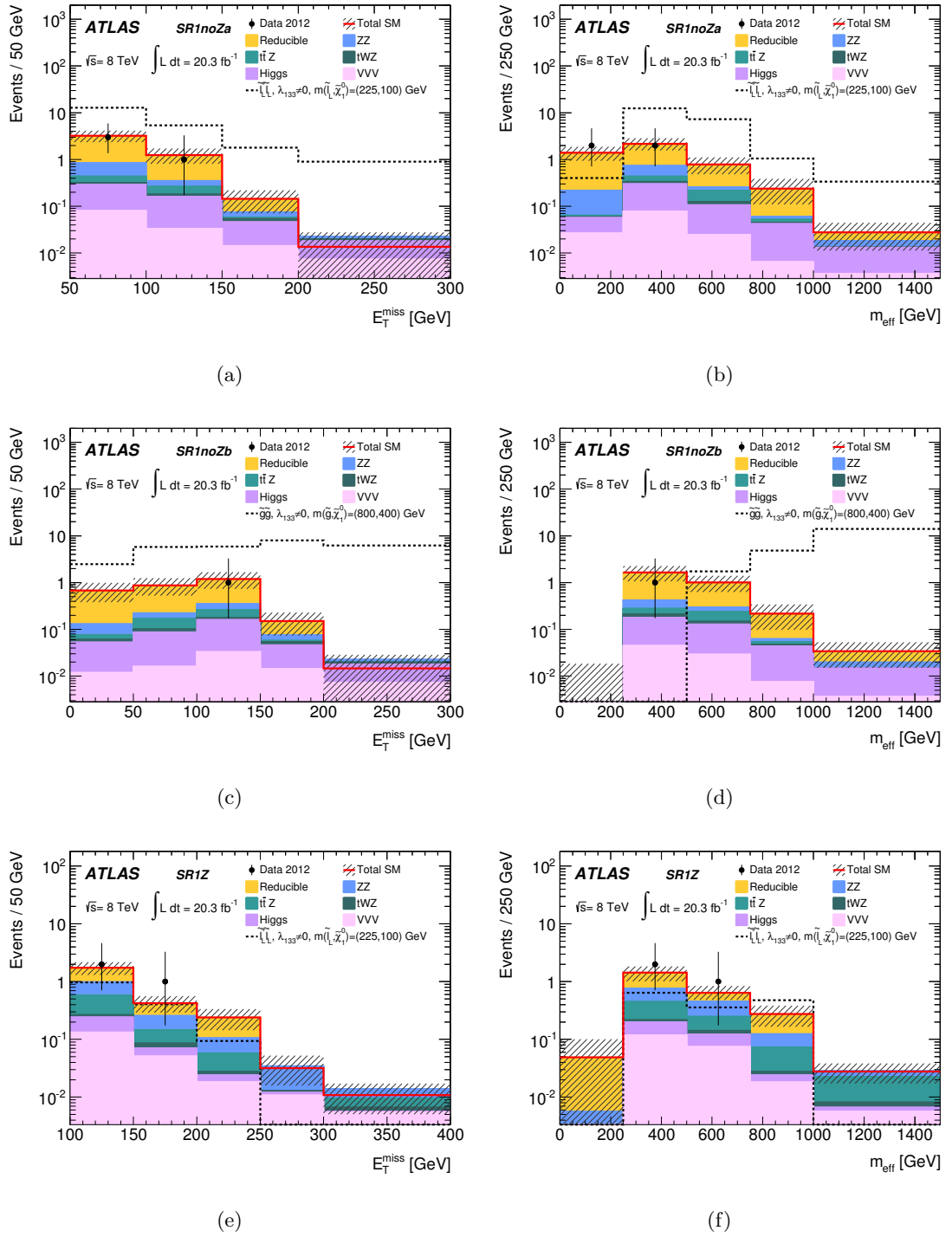


Figure 7.2: Distributions of (left) the E_T^{miss} and (right) the m_{eff} for all estimated SM background, data, and an example signal point in (a) and (b) SR1noZa, in (c) and (d) for SR1noZb and in (e) and (f) for SR1Z. Produced by other analysis team members and presented in [1].

The corresponding distributions for the $2l2\tau$ signal regions are presented in Figure 7.3. In Figures 7.3(a) and (b) the E_T^{miss} and m_{eff} distributions are shown for SM background, data and a benchmark signal point in the SR2noZa region. For this region the benchmark point is chosen from the $\tilde{\chi}_2^0\tilde{\chi}_3^0$ via stau grid, as this is the region with the best estimated sensitivity to this scenario. The point has an NLSP mass of 100 GeV and massless LSP, which had the highest significance of the grid for this signal region. There is not such a good discrimination between the signal and background in this instance, as not many of the signal events pass the signal region criteria compared to the background, even after optimising the cuts. The data events agree with the estimated background distributions within systematic uncertainty, although there were 7 events observed and only 4.0 expected from background processes. The E_T^{miss} and m_{eff} for SR2n0Zb are similarly presented in Figures 7.3(c) and (d), using the signal point from the same RPV wino λ_{133} as a benchmark again. In this signal region 3.0 events are expected from SM backgrounds and 6 events are observed. The data distributions are in good agreement with those of the expected background within uncertainties. The signal is not greatly dissimilar but expects more events with larger E_T^{miss} and m_{eff} . Figure 7.3(e) and (f) present the E_T^{miss} and m_{eff} distributions for data, background and the same RPV wino λ_{133} benchmark signal point in SR2Z. The E_T^{miss} distribution shows very good agreement between the expected and observed events, and although the agreement is not as good for the m_{eff} distribution, this is not particularly surprisingly given that only 1 event is observed in this SR, and the agreement is still within systematic uncertainties. The data is not compatible with the signal distribution, although this does not expect a very large number of events in this region due to the Z request.

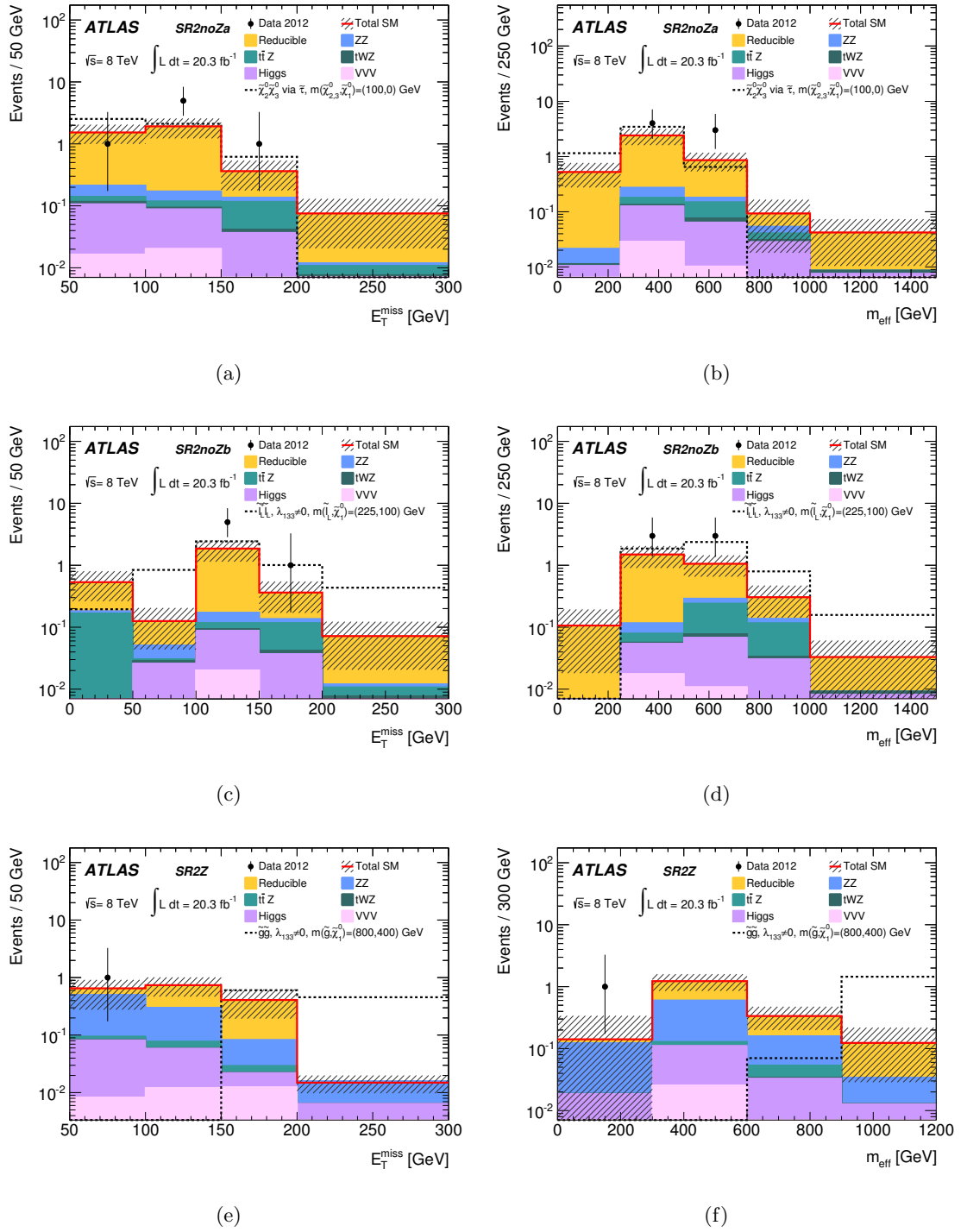


Figure 7.3: Distributions of (left) the E_T^{miss} and (right) the m_{eff} for all estimated SM background, data, and an example signal point in (a) and (b) for SR2noZa, in (c) and (d) for SR2noZb and in (e) and (f) for SR2Z. Produced by other analysis team members and presented in [1].

Overall the data which has been observed in each of the nine SRs is in good agreement with what was expected based on the estimated SM background events. There are no significant excesses observed in the number of events, and no values of E_T^{miss} and m_{eff} where a systematic disagreement is observed, with the majority of distributions agreeing very well. The discussion will now move to more advanced statistical treatment of these observations, in order to draw conclusions on the impact on the SUSY models considered and BSM physics in general which these observations have.

7.2 Statistical Interpretation of Results

7.2.1 The CL_S Method

In order to distinguish the background-only hypothesis b from a SUSY scenario corresponding to the signal plus background hypothesis $s + b$, the CL_S method [128] can be used. A test statistic q is defined to represent the two hypotheses and determine which best describes the observed data. This function q contains all the model parameters and observables of the theory, for example any mass parameters and existing restraints on them from previous experimental measurements. The p-value is then defined as a function of q , and gives the probability of obtaining a test statistic as extreme or more so than the one observed, given that the background-only hypothesis is true. The discovery p-value, p_μ , gives the compatibility of an observation with the $s + b$ hypothesis and is defined as:

$$p_\mu = P(n \geq n_{obs} | \mu), \quad (7.1)$$

where n is number of events predicted by the $s + b$ hypothesis, and n_{obs} is the number of observed events. The parameter μ is the “signal strength” which will be 0 if the background-only (SM) hypothesis is true and 1 if the considered SUSY scenario hypothesis is true. Hence the compatibility of the background-only hypothesis with observed data is given by the background-only p-value:

$$p_0 = P(n \leq n_{obs} | \mu = 0), \quad (7.2)$$

where in this instance n represents the number of events predicted by the background-only hypothesis.

Using the Confidence Level (CL) interpretation, a signal is said to be excluded at 95 % CL if the discovery p value is less than 0.05. However, it is possible that this can lead to a signal being incorrectly excluded in the case that the analysis does not expect a large ratio of signal to background events in the observed region - i.e. the analysis has a low

sensitivity to the considered signal. To protect against this, a variation of the CL method, namely the CL_S method, is used. This is defined as the ratio:

$$CL_S = \frac{CL_{s+b}}{CL_b}, \quad (7.3)$$

and includes the confidence level for the background-only hypothesis CL_b as well. This means that the background-only hypothesis will need to be supported to a high CL in addition to the signal hypothesis having a low CL value. It can also be written in terms of the signal and background-only p-values;

$$CL_S = \frac{p_{s+b}}{1 - p_b}. \quad (7.4)$$

This analysis then interprets the satisfaction of the condition:

$$CL_S \leq 0.05 \quad (7.5)$$

to signify the signal hypothesis being excluded with 95 % confidence level.

This analysis uses a profile log-likelihood ratio formalism to define a test statistic q which is then used to obtain the relevant p-values and the CL_S value. The likelihood is given by:

$$L(n_{obs}|\mu S, B, \eta) = P(n_{obs}|\mu S + B) \times \prod_{\eta} G_{syst}(\eta^0, \eta), \quad (7.6)$$

where S is the number of signal events, B is the number of expected background events, and η are the various systematics, described as nuisance parameters. $P(n_{obs}|\mu S + B)$ is the Poisson distribution for the expected events in a signal region, given the expected signal and background, and $G_{syst}(\eta^0, \eta)$ is a Gaussian, which is centered on the nominal value η^0 , around which the nuisance parameters can be varied when maximising the likelihood. Each nuisance parameter is described as a separate Gaussian, with $\sigma=1$, and the product of these is then taken.

The likelihood can be written in a more concise form as $L(\mu, \nu(\mu))$, where ν represents the full signal plus background model, which is a function of the signal strength μ . In this notation, the profile likelihood ratio $\lambda_p(\mu)$ is given by

$$\lambda_p(\mu) = \frac{L(\mu, \hat{\nu}(\mu))}{L(\hat{\mu}, \hat{\nu}(\hat{\mu}))}. \quad (7.7)$$

Here, $\hat{\nu}$ represents using an “unconditional” likelihood fit to maximise the the likelihood, which means that μ and ν are both varied simultaneously, whilst $\hat{\nu}$ represents a “conditional” maximisation of the likelihood, which entails fixing μ while ν is varied. These maximisation procedures convert the likelihoods to *estimators* [111] which are independent of the nuisance parameters.

The test statistic, q , is defined as a function of the log likelihood ratio $\lambda_p(\mu)$ given by:

$$q = \begin{cases} -2 \ln \lambda_p(\mu) & \hat{\mu} \leq \mu \\ 0 & \hat{\mu} > \mu, \end{cases} \quad (7.8)$$

where $\hat{\mu}$ is an estimator of the signal strength μ . The probability of observing the number of events predicted by the signal hypothesis or more given the signal strength has been used to define the discovery p-value. It is now possible to express this using the probability density function of the test statistic for a given μ value $f(q|\mu)$. An integration of this probability distribution function is made between the limits of the test statistic using the observed values q_{obs} and infinity in order to evaluate the total probability of obtaining a higher number of events than those observed. This gives a definition of the discovery p-value in terms of the log-likelihood ratio $\lambda_p(\mu)$:

$$p_\mu = \int_{q_{obs}}^{\infty} f(q|\mu) dq. \quad (7.9)$$

The p-value is ‘‘one-sided’’ [111], as an excess of events constitutes a signal, but an under-fluctuation does not. The background-only p-value can be similarly defined, in order to calculate the CL_s values as described in Equation 7.4.

7.2.2 Combination of Signal Regions

For all signal scenarios considered, it is beneficial to use a combination of more than one of the signal regions. For SRs which are orthogonal, this is carried out in the form of a statistical combination, where a combined likelihood is defined as:

$$L(\mu, \nu) = \prod_i^N L_i(\mu, \nu_i), \quad (7.10)$$

for N signal regions. If a signal region has no sensitivity to a given signal, the corresponding likelihood will not be a function of μ , and therefore it will not contribute to the combined likelihood for that signal scenario. Not all signal regions are orthogonal however - the SRXnoZa and SRXnoZb regions have some overlap, as they differ only in the value of E_T^{miss} required and an additional cut on m_{eff} in the case of the SRXnoZb regions. For these SRs, a graphical combination method is used, the effect of which is similar to adding together the areas excluded by each SR individually to give the total excluded region. The SR to use for each point of a signal scenario is selected based on which SR has the lowest expected p-value, and the exclusion limit is then produced as normal. The method used for each signal depends on which SRs have sensitivity to the scenario, for some statistical

combination methods are used, and for some a mixture of both statistical and graphical combinations are required.

7.2.3 Model-independent Limits

As well as considering the interpretation for the specific SUSY scenarios that this analysis was optimised for, we can also consider how compatible the observed data was with the background-only hypothesis b . As discussed previously, this corresponds to $\mu = 0$. We can consider how many events can be observed in each signal region before they are no longer compatible with the SM and set this as an upper limit, which is useful for an estimate of the sensitivity to any new physics scenarios. We also set an upper limit on the visible cross-section for any new physics scenarios. This will correspond to the product of the production cross-section for some new physics scenario with the acceptance and efficiency in the SR for the required objects produced by this scenario. If these three components are calculated, then the visible cross-section limit can be used to test scenarios not considered in this work using the data observed in the SRs of this analysis. This limit is set by varying the value of μ from a large, excluded value to one where the discovery p-value p_μ is less than 0.05. The upper limits on the number of events and production cross-section are displayed for all signal regions in Table 7.2, along with the expected and observed events, the background-only p-value, and the significance of any observed upward fluctuations.

7.2.4 Limits on Supersymmetry Scenarios

When placing 95% CL exclusion limits on the SUSY scenarios considered in this work, it is important to also take into account potential contamination from signal events within the CRs used for the weighting method. This is dealt with by modifying the weighting method slightly to include the subtraction of signal contamination events, such that equation 6.4 becomes:

$$N_{red} = \left(N_{data}^{CR1} - N_{irr}^{CR2} - \mu \times s^{CR1} \right) \times F - \left(N_{data}^{CR1} - N_{irr}^{CR2} - \mu \times s^{CR2} \right) \times F_1 \times F_2. \quad (7.11)$$

This subtraction can cause the weighting method to produce an estimate for a negative number of events, but this is not the case in any of the SRs where the reducible background processes contribute a significant number of events, and the estimate always remains within 1σ of the original uncorrected value. A systematic uncertainty is also included to account for the accuracy of this method. For the regions which use four light leptons, the weighting

Table 7.2: For each signal region, the number of events expected from the background estimation and the number of observed data events are listed. The observed $N_{\text{BSM}}^{\text{obs}}$ and expected $N_{\text{BSM}}^{\text{obs}}$ 95% CL upper limits on the number of signal events and the observed $\sigma_{\text{vis}}^{\text{obs}}$ and expected $\sigma_{\text{vis}}^{\text{exp}}$ 95% CL upper limits on the visible cross-section are then given. The background-only p-value p_0 is included (truncated at 0.5) and when $p_0 < 0.5$ the significance of the difference between the observed and expected events is expressed as a number of standard deviations N_σ . Numbers produced by other analysis team members and presented in [1].

	Σ SM	Data	$N_{\text{BSM}}^{\text{obs}}$	$N_{\text{BSM}}^{\text{exp}}$	$\sigma_{\text{vis}}^{\text{obs}}$ [fb]	$\sigma_{\text{vis}}^{\text{exp}}$ [fb]	p_0	N_σ
SR0noZa	1.6 ± 0.5	3	5.9	$4.4_{-1.0}^{+1.6}$	0.29	$0.22_{-0.05}^{+0.08}$	0.15	1.02
SR1noZa	$4.6_{-1.2}^{+1.3}$	4	5.7	$5.9_{-1.5}^{+2.5}$	0.28	$0.29_{-0.07}^{+0.12}$	0.50	–
SR2noZa	$4.0_{-1.3}^{+1.2}$	7	9.2	$6.1_{-1.4}^{+2.5}$	0.45	$0.30_{-0.07}^{+0.12}$	0.13	1.14
SR0noZb	1.4 ± 0.4	1	3.7	3.9 ± 1.4	0.18	0.19 ± 0.07	0.50	–
SR1noZb	$2.9_{-0.9}^{+1.0}$	1	3.5	$4.7_{-1.2}^{+1.9}$	0.17	$0.23_{-0.06}^{+0.09}$	0.50	–
SR2noZb	3.0 ± 1.0	6	8.7	$5.6_{-1.3}^{+2.3}$	0.43	$0.28_{-0.06}^{+0.11}$	0.10	1.30
SR0Z	5.6 ± 1.4	7	8.1	$6.7_{-1.6}^{+2.7}$	0.40	$0.33_{-0.08}^{+0.13}$	0.29	0.55
SR1Z	2.5 ± 0.6	3	5.3	$4.7_{-1.1}^{+1.9}$	0.26	$0.23_{-0.05}^{+0.09}$	0.34	0.40
SR2Z	1.8 ± 0.5	1	3.5	$4.1_{-0.8}^{+1.7}$	0.17	$0.20_{-0.04}^{+0.08}$	0.50	–

method estimate is very close to zero, and so for these regions, the contribution was set to zero, with an upper uncertainty of the original uncorrected value.

For each point of each signal scenario considered the CL_S value is calculated using the expected and observed events and the methods described in Section 7.2.1. The CL_S values for parameter space between the points are interpolated to produce smooth contours of both expected and observed 95% CL exclusion limits. These are always denoted by a dashed line for the expected exclusion limit, with a solid uncertainty band corresponding to 1σ variation of the background model uncertainties, and a solid line for the observed exclusion limit, with dashed uncertainty bands corresponding to a 1σ variation of the signal uncertainties.

7.2.4.1 Limits on R-parity Violating Models

The SRXnoZb regions were optimised to give maximal sensitivity on the RPV grids, but for a number of points the SRXnoZa regions are better. These regions are not orthogonal, so for each point, either the a or b region is chosen for use in the limit calculation. The selection is made based on the expected CL_S values of each SR on each point. All RPV signal scenarios use the same selection process, such that the final result is produced by

statistically combining the three Z-rich SRs with either the “a” or “b” region for each lepton multiplicity channel. For example the statistical combination of regions SR0Z, SR1Z, SR2Z, SR0noZa, SR1noZb, and SR2noZb could be used. The Z-selection regions are included as they are orthogonal with all other SRs and have some sensitivity to these scenarios. This procedure yields the best possible limits, as even if one particular region is not sensitive to a given scenario, it will not affect the final outcome, as the associated likelihood profile will not contribute to the sum.

The exclusion limits are displayed in the same parameter plane as the significance plots used for the SR optimisation. For these RPV scenarios, the two parameters which are varied are the LSP mass and the NLSP mass, displayed on the vertical and horizontal axes of the plots respectively. Figure 7.4 shows the 95% CL exclusion limits placed on each of the 20 different RPV signals considered, split by NLSP identity. Four separate bands can be seen on each plot, and these correspond to the four different $\lambda_{ijk} > 0$ couplings considered. In every case the dashed band displays the expected exclusion limit, with a solid band for the associated uncertainty, and the solid line represents the exclusion limit observed in data, with a dashed band to show the corresponding uncertainty. The area contained to the left of each band is the region of excluded parameter space. The mass limits set on the scenarios with non-zero couplings λ_{133} and λ_{233} which produce taus in the final state are lower than the light lepton only scenarios. This was expected from the signal region optimisation stage and is a result of the lower production cross-sections for these scenarios, as well as the lower reconstruction efficiency for tau leptons in the ATLAS detector and the higher number of background events in the tau channels, which make them more difficult to target. The region excluded is affected by the LSP mass approaching the NLSP mass in some of the tau-rich scenarios, for example in Figures 7.4(a),(c) and (e). SM particles resulting from the NLSP decay chain rather than the LSP become softer in this area of parameter space. The exclusion limit also does not cover the region where the LSP has low (< 50 GeV) mass in all scenarios, due to the decay products resulting from the LSP having a lower momentum, which makes them less likely to pass the SR criteria.

For the scenarios with non-zero tau-rich couplings, exclusion limits are set up to masses of 450 GeV for a wino NLSP, 950 GeV for a gluino NLSP, and 300(240) GeV for a left-(right-)handed slepton NLSP. These exclusion limits cover regions of parameter space not considered by any previous analysis, probing entirely new signal scenario interpretations. When the non-zero couplings considered produce electrons and muons from the LSP decay, exclusion limits are set up to masses of 750 GeV for a wino NLSP, 1350 GeV for a gluino

NLSP, 490(410) GeV for a left-(right-)handed slepton NLSP and 400 GeV for a sneutrino NLSP. These exclusions surpass the existing limits from previous searches at the LHC by a significant amount, for the wino NLSP scenario the previous exclusion from ATLAS was up to a mass of 540 GeV [96], whilst the previous exclusion for the gluino NLSP mass in this scenario was at 1 TeV, set by the CMS collaboration [129].

7.2.4.2 Limits on $\tilde{\chi}_2^0\tilde{\chi}_3^0$ Models

The SRXnoZa regions were optimised to target the $\tilde{\chi}_2^0\tilde{\chi}_3^0$ grids via slepton and stau decay, but for the slepton scenario the SRXnoZb regions have better sensitivity for the higher NLSP mass points. For this grid the statistical combination is taken with all the SRXZ regions and either all of the SRXnoZa regions or all of the SRXnoZb, depending on which set produces the best expected sensitivity. The 95% CL exclusion limit contour produced by this combination can be seen in Figure 7.5(a). The masses of the $\tilde{\chi}_1^0$ LSP and the $\tilde{\chi}_{2/3}^0$ NLSP are displayed on the vertical and horizontal axes respectively. The dashed black line shows the expected exclusion limits with a yellow band to show the uncertainty, and the red solid line presents the observed exclusion limit, with associated uncertainty given by the red dashed line. The region of parameter space for this scenario which falls beneath and to the left of these lines is excluded. The sensitivity is seen to decrease towards the diagonal as the mass of the LSP approaches that of the NLSP, and any leptons resulting from the NLSP \rightarrow LSP decay become lower in p_T and no longer pass the requirements of the SRs. Cases where the NLSP mass is below 620 GeV in this scenario are excluded, provided the LSP mass is below 300 GeV, with a maximum exclusion in the LSP mass plane of 340 GeV.

For the $\tilde{\chi}_2^0\tilde{\chi}_3^0$ via stau and via Z grids the statistical combination is taken for all SRXnoZa and all SRXZ regions. As no points are excluded for these grids, 95% CL upper limits are instead set on the production cross-sections. These can be seen in Figure 7.5(b) and (c) for the stau and Z scenario respectively. The points included for both grids all have an LSP mass of 0 GeV and varying NLSP mass, shown along the horizontal axis. The expected limit and associated uncertainty are again represented with a dashed line and yellow band, and the observed limit with a solid red line. Production cross-sections for this process above the line are excluded by this analysis. The solid black line gives the theoretical production cross-sections for these processes at the LHC calculated for these specific scenarios, and the green band shows the uncertainty on this calculation. If the observed limit passes beneath the theoretical cross-section this would correspond to an

exclusion for that NLSP mass in this scenario.

Existing limits from LEP exclude cases where the NLSP mass is around 100 GeV [130–133], which cannot be improved upon by the stau or Z models considered here, but a significant improvement is made for the slepton decay mode.

7.2.4.3 Limits on the GGM Models

All processes within the GGM models are mediated via either a Z or Higgs boson, and so the Z-veto regions (SRXnoZa and SRXnoZb regions) have no sensitivity at all. Therefore only the SRXZ regions are statistically combined for use on these two grids. 95% CL exclusion limits are displayed in Figure 7.6(a) and (b) for the GGM grids with $\tan\beta = 1.5$ and $\tan\beta = 30$ respectively. The blue area represents excluded parameter space, and the same convention for the expected and observed exclusion limit lines is used. The exclusion limits are presented as a function of the varied parameters $m_{\tilde{g}}$ on the vertical axis and μ on the horizontal axis, and an additional axis is inset to show the corresponding variation of the $\tilde{\chi}_1^0$ sparticle mass to enable comparison with other limits.

For the scenario with $\tan\beta = 1.5$ gluino masses less than 700 GeV are excluded for all considered μ values. Gluino masses below 1200 GeV are excluded for μ values between 200 and 250 GeV, due to the dominant production of electroweak sparticles in this region of the parameter space. The exclusion limits are slightly weaker for the $\tan\beta = 30$ scenario, which includes a proportion of Higgs bosons in the decays as well as Z bosons. Gluino masses less than around 650 GeV are excluded for all μ values in this signal model, and an exclusion upper limit of 900 GeV in gluino mass is reached for μ values close to 200 GeV. These complement recent results from an ATLAS supersymmetry search targeting the right-hand side of this grid where the strong processes dominate, using events with two leptons, jets and missing transverse energy [134]. They produce exclusion limits up to a gluino mass of 850 GeV when $\mu > 450$ GeV on the $\tan\beta = 1.5$ grid, and up to a gluino mass of 820 GeV when $\mu > 600$ GeV on the $\tan\beta = 30$ grid.

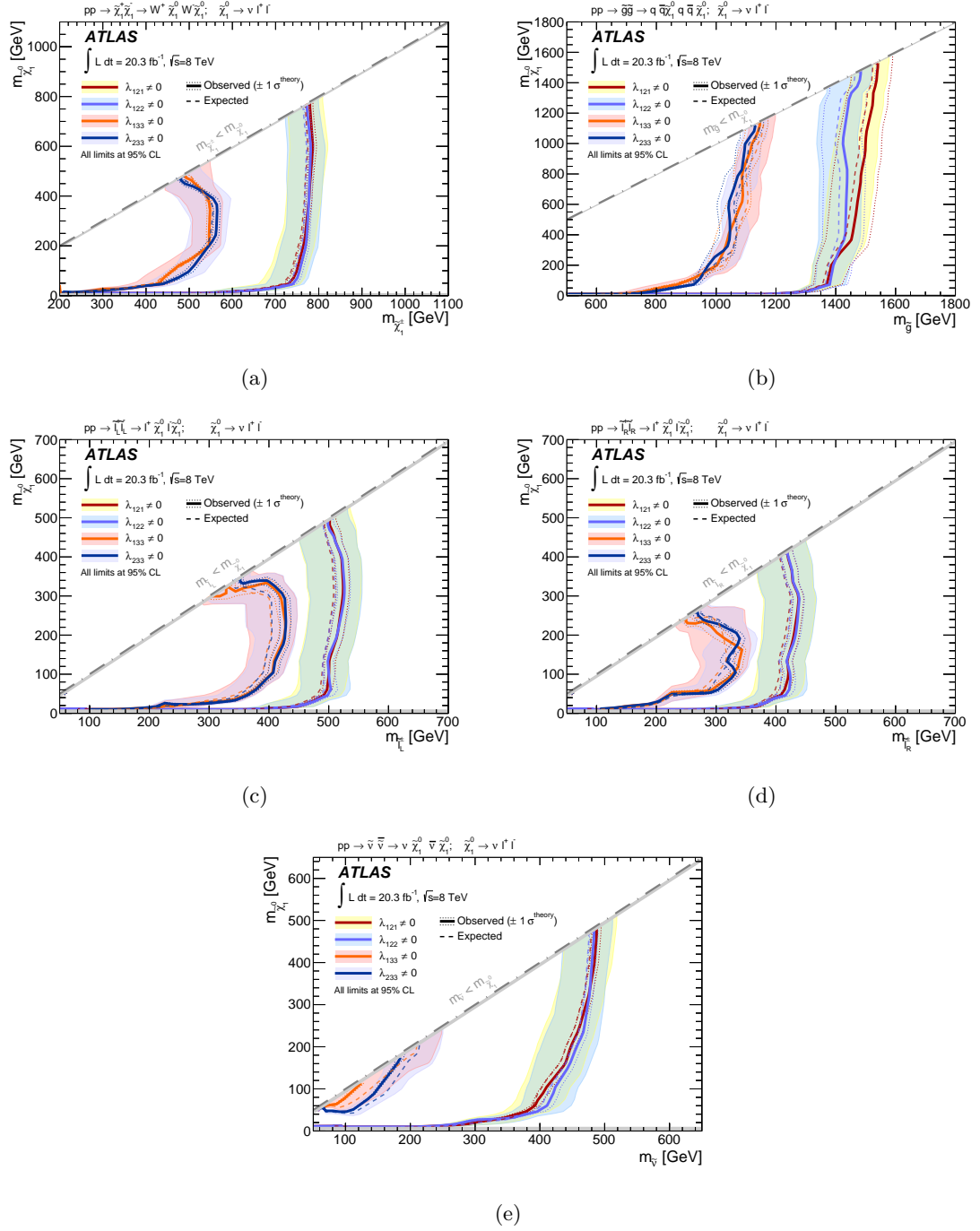


Figure 7.4: The 95% CL exclusion limit contours for all RPV grids, for scenarios where the NLSP is (a) a wino, (b) a gluino, (c) a left-handed slepton, (d) a right-handed slepton and (e) a sneutrino. Each plot displays limits for all four couplings considered to be non-zero, λ_{121} , λ_{122} , (via electrons and muons only) and λ_{133} and λ_{233} (including taus in the final state). Produced by other analysis team members and presented in [1].

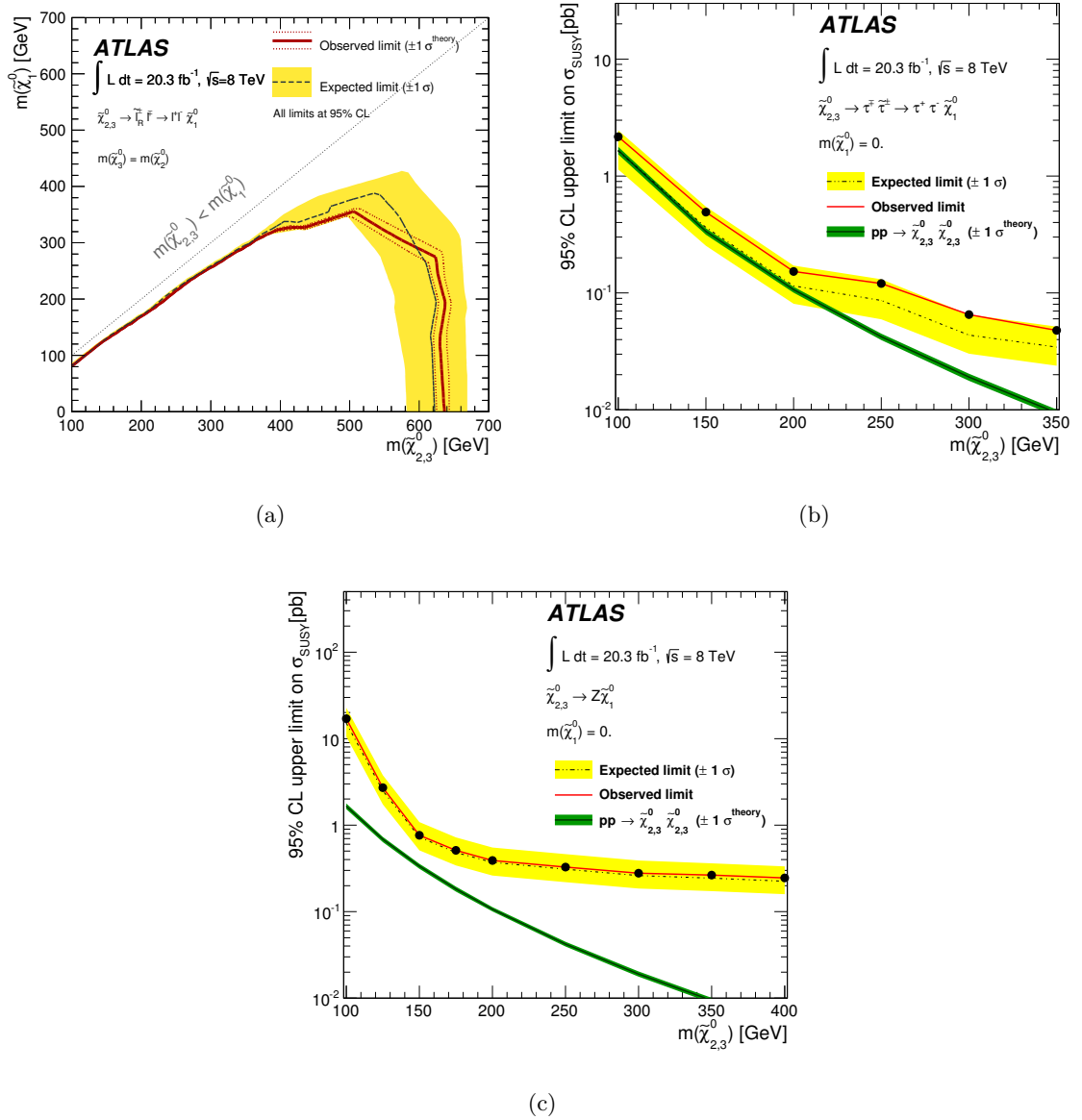


Figure 7.5: The 95% CL exclusion limit expected and observed contours are shown for (a) the $\tilde{\chi}_0^2\tilde{\chi}_0^3$ via slepton grid. The 95% CL cross-section limits are displayed for (b) the $\tilde{\chi}_0^2\tilde{\chi}_0^3$ via stau grid and (c) the $\tilde{\chi}_0^2\tilde{\chi}_0^3$ via Z grid. Produced by other analysis team members and presented in [1].

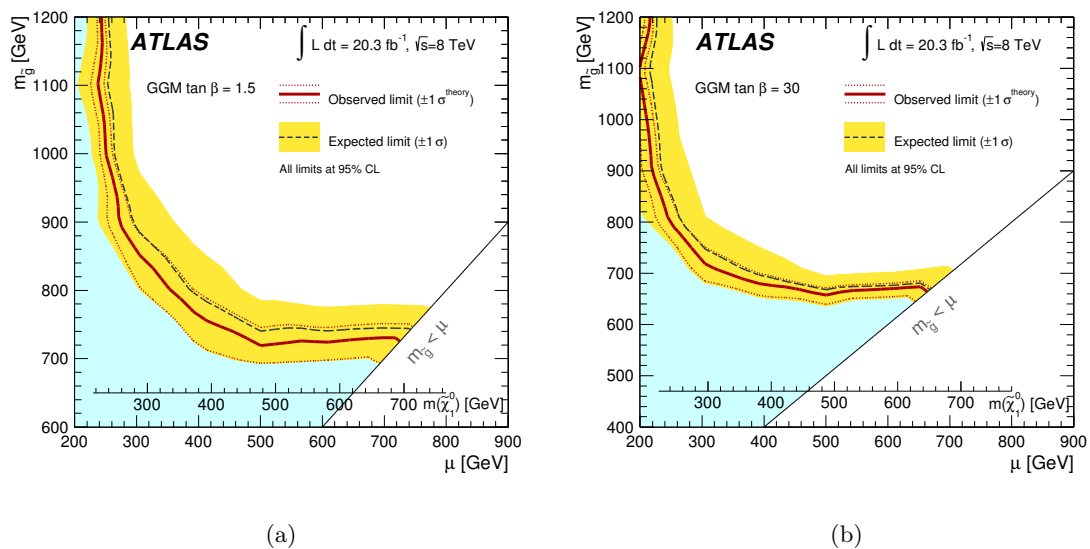


Figure 7.6: The 95% CL exclusion limit expected and observed contours are shown for the GGM grids (a) $\tan\beta = 1.5$ and (b) $\tan\beta = 30$. Produced by other analysis team members and presented in [1].

7.3 Result Re-interpretations and Combinations with the Three Lepton Analysis

7.3.1 Introduction

In the same way that the exclusion power of the analysis was improved by statistically combining signal regions, combining these results with signal regions from other analyses can also boost the sensitivity. In particular it is useful to consider analyses which require a lower lepton multiplicity, as their criteria will allow events from the signal scenarios where one of the leptons is “lost”, for example by having a p_T value too low to pass the trigger. As this is often beneficial, ATLAS analyses for electroweak SUSY searches are generally constructed to avoid overlap between each others signal regions wherever possible. All combinations presented here are produced by including an electroweak SUSY search analysis which requires exactly three light leptons [135]. A statistical combination of the SRs from both analyses is made and used on a number of the signal scenarios already considered by the four lepton analysis discussed in this thesis. All figures presented in this section were produced by myself, and are preliminary, pending approval. I also carried out all stages of the statistical analysis required to produce them. The input files required for this statistical analysis were produced and provided by the three and four lepton groups. At the time of writing, the publication in which these results will be included has not yet been made public but will be in the near future.

7.3.2 Overview of Three Lepton Analysis

The three-lepton (3L) analysis is optimised to target electroweak SUSY scenarios including $\tilde{\chi}_1^\pm \tilde{\chi}_2^0$ production with decays via sleptons, staus, a WZ pair, or a Wh pair. Five signal regions are defined which contain exactly three leptons with either zero, one or two taus included. All SRs implement a veto on events containing b-jets, in order to suppress background from $t\bar{t}$ processes. Using the nomenclature from the publication [135], the region SR0 τ a requires exactly three light leptons, two of which must form an SFOS pair, and is then subdivided into twenty disjoint “bins” requesting different values of m_{SFOS} , E_T^{miss} and transverse mass of the unpaired lepton m_T . This is defined as:

$$m_T = \sqrt{2p_T^l E_T^{miss} - 2\vec{p}_T^l \cdot \vec{p}_T^{miss}}, \quad (7.12)$$

where p_T^l is the missing transverse momentum of the lepton not included in the SFOS pair. A second region SR0 τ b requiring three light leptons is also defined by the analysis.

This SR vetoes events containing SFOS pairs (making it orthogonal to SR0 τ a), sets lower limits on the allowed E_T^{miss} in an event and p_T of the lowest- p_T lepton and requires the minimum distance in ϕ between opposite sign leptons to be less than 1. The signal region SR1 τ requests two same sign leptons and an opposite sign tau. The invariant mass of any same sign lepton pairs must fall more than 10 GeV from m_Z , the invariant mass of lepton-tau pairs closest to the Higgs mass must be less than 120 GeV, and cuts are then made on the scalar sum of lepton p_T and the p_T of the lowest- p_T lepton. SR2 τ a selects events containing two taus and one light lepton, and requests a high E_T^{miss} and “stransverse mass” m_{T2} . This variable is defined as:

$$m_{T2} = [\max(m_T(\vec{p}_{T,1}, \vec{q}_T), m_T(\vec{p}_{T,2}, \vec{r}_T))], \quad (7.13)$$

where $\vec{p}_{T,1}$ and $\vec{p}_{T,2}$ are the transverse momenta of two leptons, and \vec{q}_T and \vec{r}_T satisfy the relation $\vec{q}_T + \vec{r}_T = \vec{p}_T^{miss}$ and correspond to momenta of undetected particles, chosen to minimise the value of missing transverse momentum. The m_{T2} is calculated for all combinations of light leptons and taus and then the maximum value is used. The final region SR2 τ b also selects events with two taus and one lepton but it is not orthogonal to SR2 τ a and is not used in this work so will not be described here. A summary of the definitions of the three lepton SRs used in this chapter is presented in Table 7.3.

Table 7.3: The selection requirements for the 3L signal regions used in this chapter, as detailed in [135].

Signal Region	SR0 τ a	SR0 τ b	SR1 τ	SR2 τ a
ℓ flavour/sign	SFOS- ℓ	$\ell^\pm \ell^\pm \ell^\mp$	$\tau^\pm \ell^\mp \ell^\mp$	$\tau\tau\ell$
b -tagged jet	veto	veto	veto	veto
E_T^{miss}	binned	> 50 GeV	> 50 GeV	> 50 GeV
Other	m_{SFOS} binned	$p_T^{3rd \ell} > 20$ GeV	$p_T^{2nd \ell} > 30$ GeV	$m_{T2}^{max} > 100$ GeV
	m_T binned	$\Delta\phi_{ll}^{min} \leq 1.0$	$\sum p_T^l > 70$ GeV	–
	–	–	$m_{l,t} < 120$ GeV	–
	–	–	m_{ee} Z-veto	–

In general the 3L SRs contain higher numbers of expected events than the four-lepton regions, ranging from 3.8 to 10.3 in the un-binned SRs, and the bins in SR0 τ a contain between 0.29 and 715 expected background events. These are estimated in a similar way to the four-lepton analysis, using MC for the irreducible processes and a data-driven method for the reducible processes. This estimation is tested in a number of validation regions which are orthogonal from the 3L SRs but maintain kinematic similarity of the events. These all request exactly three leptons as well, and so are orthogonal from all regions

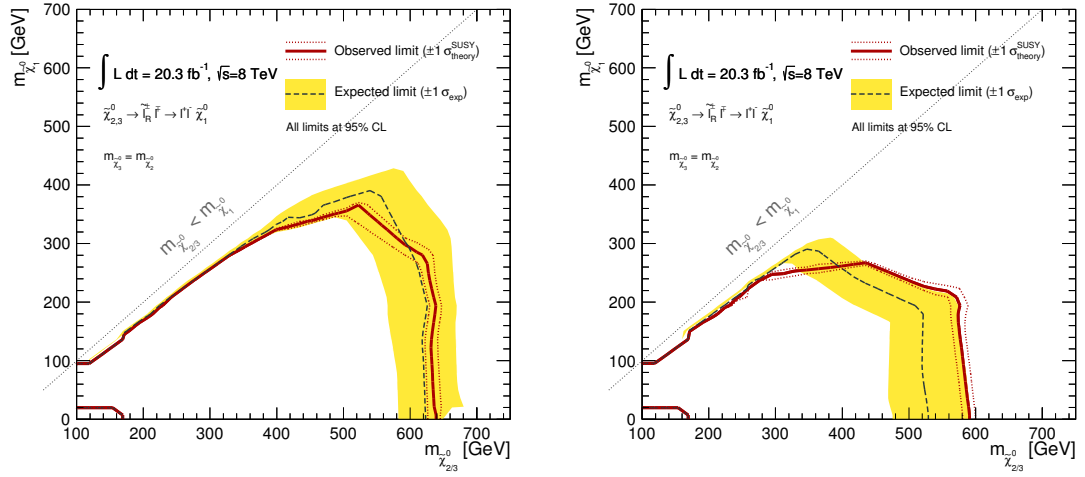
used in the four-lepton analysis. The majority of systematic uncertainties affecting the 3L analysis are shared with the four-lepton analysis, with the exception of uncertainties arising from the different background estimation methods and to account for the efficiency of the b-jet tagging algorithm which is only used by the 3L analysis. When combining the results from the two analyses, sources of uncertainty which are common are correlated within the statistical framework.

7.3.3 Combination in the $\tilde{\chi}_2^0\tilde{\chi}_3^0$ via Slepton Scenario

If one of the four leptons produced in the decay of a $\tilde{\chi}_2^0\tilde{\chi}_3^0$ pair via sleptons was not reconstructed, an SR requesting exactly three light leptons could be sensitive to the event. The region SR0 τ a from the 3L analysis can be used to target these instances, as the bins allow for a lot of variation in the event and object properties. For the lower mass splitting points on the grid, the bin with m_{SFOS} between 12 and 40 GeV, $m_T < 80$ GeV and E_T^{miss} between 50 and 90 GeV gives the best results. When the LSP mass is close to the NLSP mass, the invariant mass of the leptons would be expected to be small, as would the lepton p_T , resulting in lower values of transverse mass. This region is also most likely to benefit from a three lepton signal region, as the leptons are soft, so the lowest p_T lepton is more likely to fail the trigger or SR selection requirements for the four lepton analysis. However the SR0 τ a bins also have sensitivity to the higher NLSP mass points on the grid, in this region the bin requesting $m_{SFOS} > 120$ GeV, $m_T > 180$ GeV and E_T^{miss} between 50 GeV and 120 GeV tends to be most sensitive. There is a larger mass splitting between the NLSP and LSP for these points, and the decay products will be more energetic and have higher m_{SFOS} values.

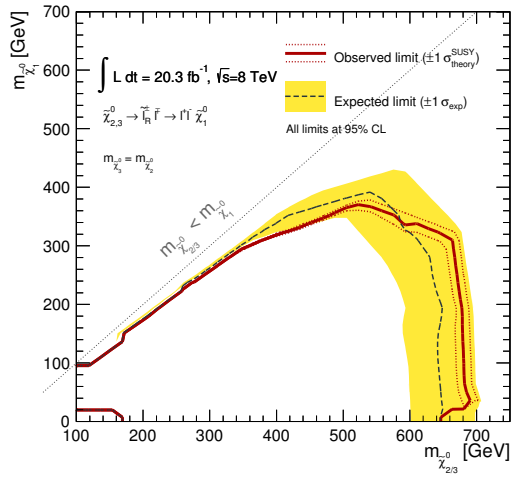
When using SR0 τ a all 20 of the orthogonal bins are statistically combined to obtain the best possible results. The four lepton result is produced by statistically combining SR0Z, SR1Z, SR2Z and either SR0noZa, SR1noZa and SR2noZa, or SR0noZb, SR1noZb and SR2noZb, as described in Section 7.2.4.2. The statistical combination of the results for both the 3L and four lepton analyses was then calculated, using the HISTFITTER [136] framework. Figures 7.7(a) and (b) show the 95% CL exclusion limit set by the four lepton analysis and three lepton analysis separately, and Figures 7.7(c) shows the 95% exclusion limit produced by statistically combining the two analyses. The same convention is used as in the four lepton analysis results: a dashed line shows the expected limit with uncertainty represented by the yellow band, and the solid red line shows the observed limit with the theoretical uncertainty represented by the red dashed bands. The area below and to the left

of the exclusion limit is the parameter space excluded. The small hole in the bottom left of all three plots is the result of the distribution of sample points in this corner, rather than a genuine gap in the exclusion produced. The observed limit for the 3L analysis does not reach as high in LSP mass as the expected limit, meaning the contribution of this analysis to the combined sensitivity close to the diagonal is not quite as good as was predicted. The limit is stronger in NLSP mass than expected though, reaching masses around 45 GeV lower than the existing four lepton limit. The combined exclusion limit reaches slightly closer to the diagonal of the grid, and increases the upper NLSP mass limit of the exclusion to around 680 GeV, 40 GeV higher than the original limit. The region with high NLSP mass and LSP masses of 250-300 GeV is also improved. These differences can be seen more quantitatively in Figure 7.8 which displays the CL_S values for each signal sample on the grid, and the interpolated CL_S values across the entire parameter space, using a colour scale on the z-axis. Three points located closest to the diagonal with (NLSP,LSP) masses of (185 GeV,165 GeV), (260 GeV,240 GeV) and (392.5 GeV,357.5 GeV) have lower expected CL_S values for the 3L analysis (0.01, 0.43 and 0.42 respectively) than from the four lepton analysis (0.32, 0.77 and 0.43 respectively). Although the observed CL_S values were not as favourable as the expected values, the combined results for these three points (0.22, 0.63 and 0.58 respectively) are still an improvement on those observed by the four lepton analysis (0.5, 0.82 and 0.63 respectively). Although the 3L analysis does not expect better CL_S values than the four lepton analysis elsewhere on the grid, it has a comparable sensitivity for some points, and still improves upon the existing values when a combination is made. In particular, the points located at (NLSP,LSP) masses (700 GeV,550 GeV), (687.5 GeV,187.5 GeV) and (687.5 GeV,62.5 GeV) have CL_S values of 0.16, 0.17 and 0.16 observed with the four lepton analysis, and these are improved to 0.09, 0.08 and 0.07 when combined with the three lepton results.



(a) 4 lepton

(b) 3 lepton



(c) Combined

Figure 7.7: 95% CL exclusion limits are also shown for the $\tilde{\chi}_2^0 \tilde{\chi}_3^0$ via \tilde{l} model for (a) the four lepton analysis (b) the three lepton analysis and (c) the statistical combination of the two.

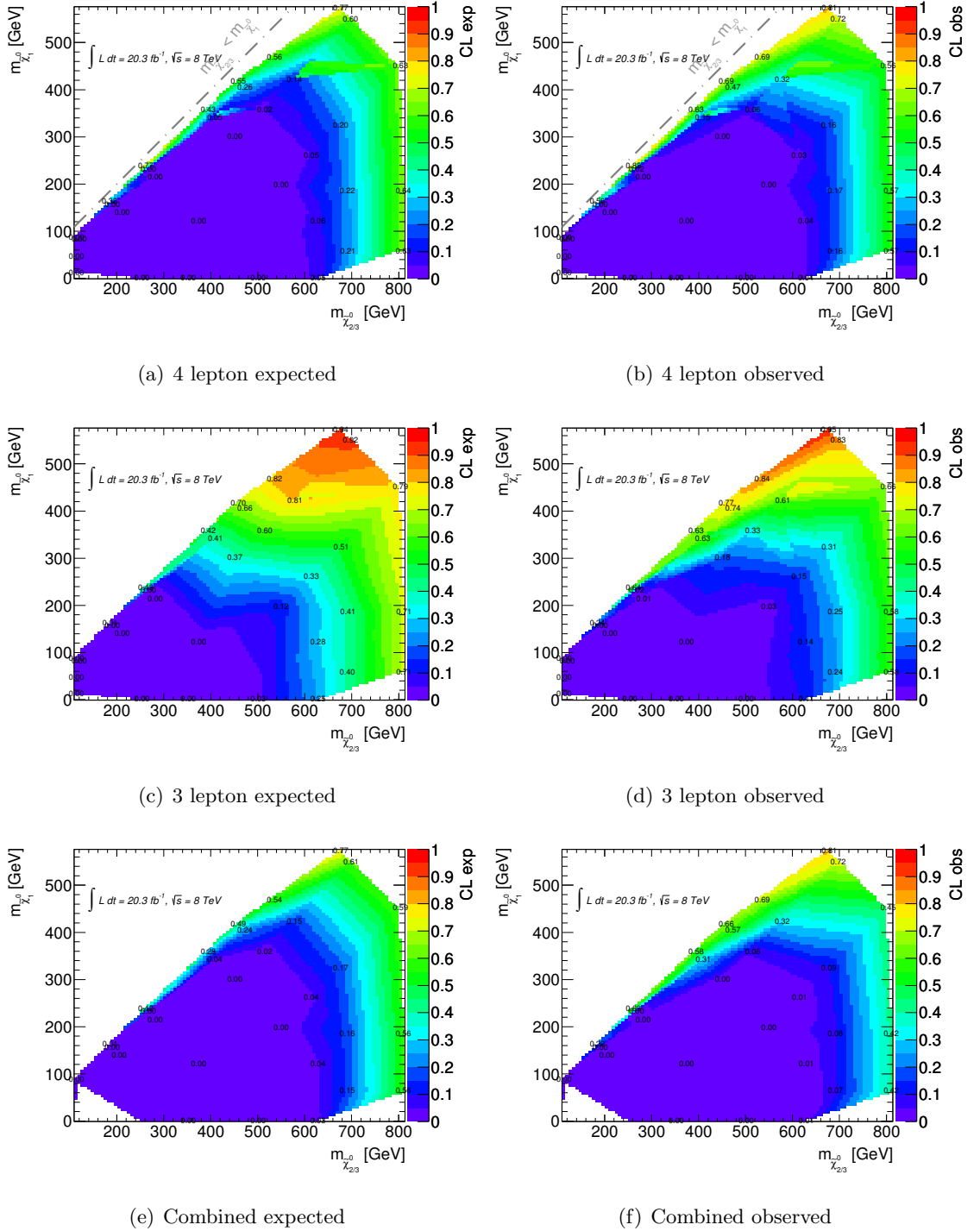


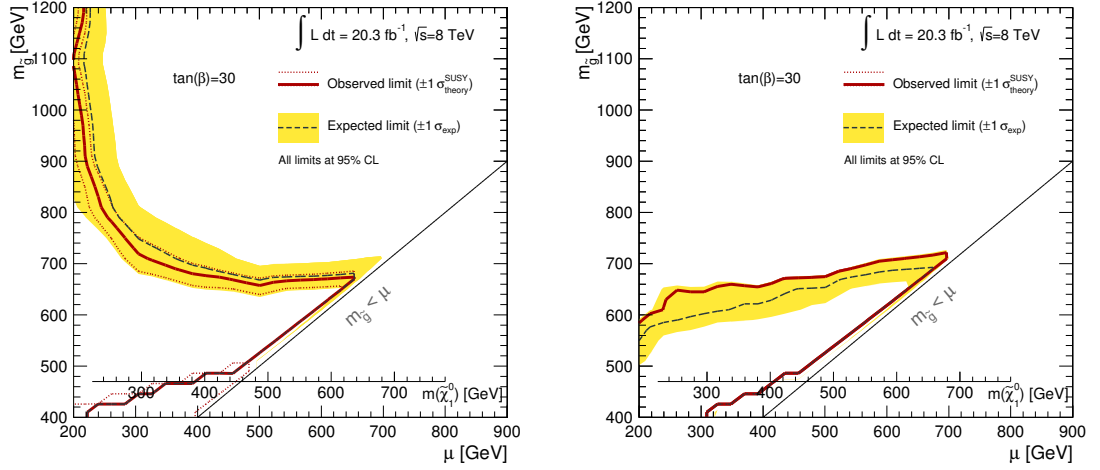
Figure 7.8: The expected (left) and observed (right) CL_S values on the $\tilde{\chi}_2^0 \tilde{\chi}_3^0$ via $\tilde{\ell}$ model for (a) and (b) the four lepton analysis, (c) and (d) the three lepton analysis and (e) and (f) the statistical combination of the two.

7.3.4 Combination in the GGM Scenario

Some signals targeted by the 3L analysis involve decays via either W and Z bosons or W and Higgs bosons, which could explain the sensitivity of the 3L SRs on the GGM scenario with $\tan\beta = 30$. In this version of the model, the $\tilde{\chi}_1^0$ NLSP decays via a mixture of Z bosons and Higgs bosons; the exact branching ratio to Higgs varies as a function of the parameter values. The exclusion limits produced by the four lepton analysis are less powerful on this GGM model than those for the model with $\tan\beta = 1.5$ which decays to Z bosons with a 97%BR. The 3L SRs are not sensitive to this version of the GGM model. Therefore a combination of the 3L and four lepton analyses is made on the GGM $\tan\beta = 30$ grid to produce improved 95% exclusion limits.

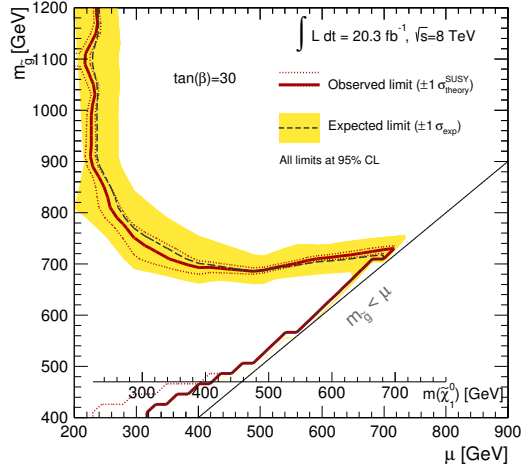
A statistical combination of the SR0 τ a, SR0 τ b, SR1 τ and SR2 τ a three lepton signal regions is performed, and this is then combined with the four lepton result, produced by statistically combining all three of the SRXZ regions. This is done within the same HIST-FITTER framework used for all other limit calculations in this thesis, and the correlation of systematics common between the two analyses is again taken into account. Figure 7.9 shows 95% CL exclusion limits from the three lepton analysis, the four lepton analysis, and the statistical combination of the two. The same convention for the expected and excluded limit lines is used, and the region contained below and to the left of these lines is the excluded parameter space. The exclusion limit produced with the three lepton SRs does not suggest that they will be helpful here, as no points in the top left of the plot are excluded. This region corresponds to the parameter space where electroweak decay processes dominate, and is the region where the four lepton analysis has some sensitivity, but is not covered by other searches focussing on the strong production on this grid [134]. However, the combined result shows a gain of around 20 GeV in the upper excluded μ value for the region with the lowest μ values and gluino masses above 900 GeV when compared to the four lepton exclusion limit. The cause for this improvement can be seen more clearly when considering the corresponding expected and observed CL_S values shown in Figure 7.10. The expected CL_S values for the points with gluino mass of 1100 GeV and 1200 GeV are all higher for the 3L analysis than the four lepton analysis, with the exception of the two points with μ values of 200 GeV. Points with lower gluino masses and μ values between 300 GeV and 600 GeV also have reasonable CL_S values for the 3L analysis, although they are not as good as the four lepton values. The expected CL_S values for combining the two analyses therefore predict an exclusion limit to higher μ values than with just the four lepton analysis. The expected CL_S values for points with μ of 300 GeV

and gluino masses of 1200, 1100, 1000, and 900 GeV are improved from 0.59, 0.55, 0.41 and 0.32 with the four lepton analysis to 0.35, 0.29, 0.32 and 0.31 with the combination. In addition, the observed CL_S values for the three lepton analysis are significantly higher than the expected values resulting in the observed CL_S values for the combination also being higher than the expected values in general.



(a) 4 lepton

(b) 3 lepton



(c) Combined

Figure 7.9: 95% CL exclusion limit on the GGM model with $\tan\beta = 30$ using (a) the four lepton analysis, (b) the three lepton analysis and (c) the statistical combination of the two.

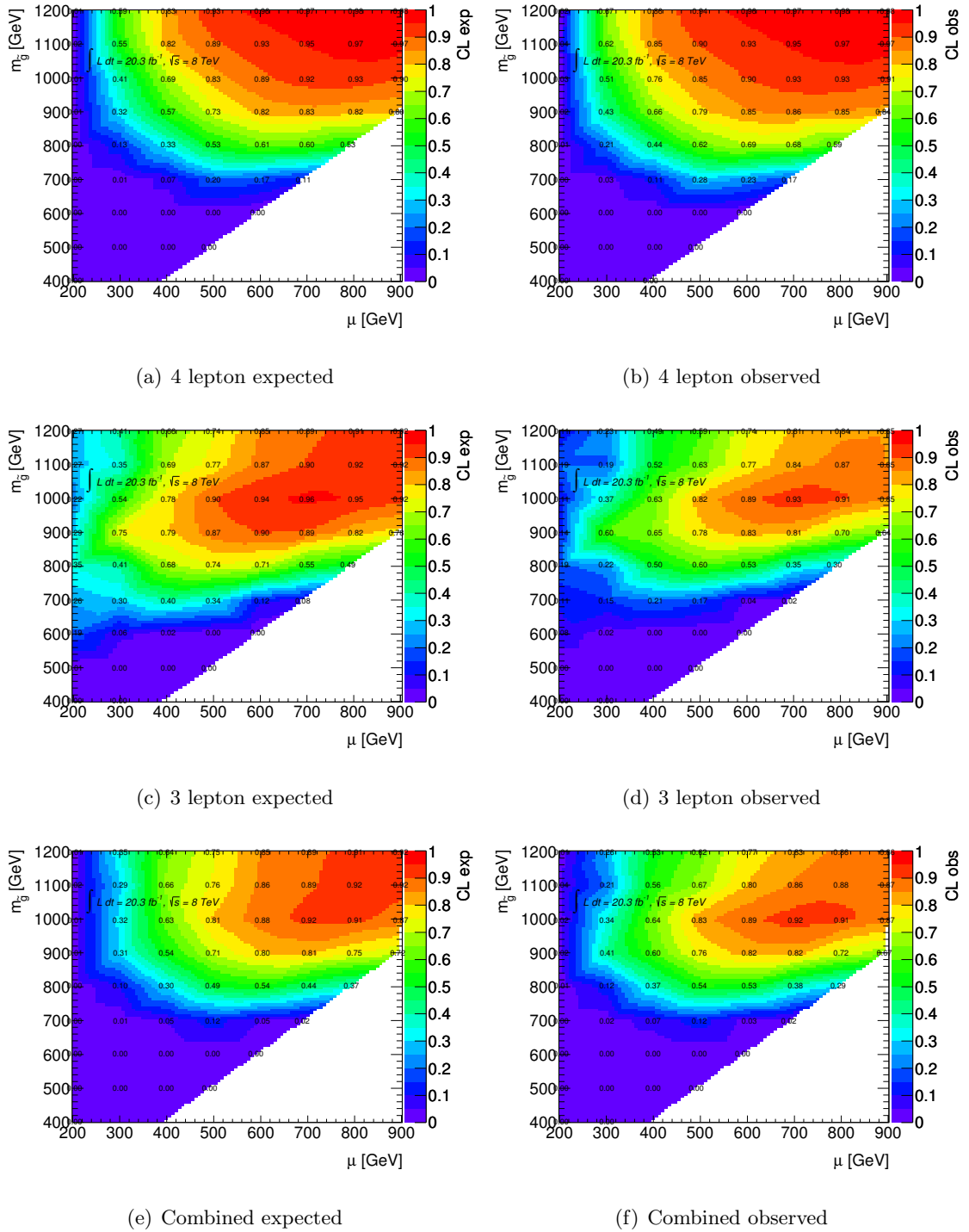


Figure 7.10: The expected (left) and observed (right) CL_S values on the GGM model with $\tan\beta = 30$ for (a) and (b) the four lepton analysis, (c) and (d) the three lepton analysis and (e) and (f) the statistical combination of the two.

7.3.5 Varying the Intermediate Slepton Mass

It has been assumed in the $\tilde{\chi}_0^2\tilde{\chi}_0^3$ via $\tilde{\ell}$ model that the intermediate slepton mass lies halfway between the mass of the $\tilde{\chi}_{2/3}^0$ degenerate NLSPs and that of the $\tilde{\chi}_1^0$ LSP. This assumption was made in order to simplify the scenario and allow exclusion limits to be set in terms of just two varied parameters (the LSP mass and NLSP mass). It is interesting however to investigate the effect of varying the intermediate slepton mass with respect to $m_{\tilde{\chi}_{2/3}^0}$, and instead fix $m_{\tilde{\chi}_1^0}$ to zero. ‘‘Slices’’ of points were produced for $m_{\tilde{\chi}_{2/3}^0}$ varying between 100 GeV and 700 GeV. The slepton mass is considered as 5%, 25%, 50%, 75%, or 95% of the $\tilde{\chi}_{2/3}^0$ mass in each of the five slices. 95% CL cross-section limits are then set for each case. The same four lepton signal regions are used for this as for the $\tilde{\chi}_0^2\tilde{\chi}_0^3$ via $\tilde{\ell}$ exclusion limits - all the SRXZ regions and either all the SRXnoZa or all the SRXnoZb regions are statistically combined. The three lowest NLSP mass points at 100 GeV, 150 GeV and 250 GeV all have lower CL_S values for the ‘‘a’’ regions and the remainder have lower CL_S values for the ‘‘b’’ regions, with the exception of the slice with slepton mass at 95%. For this scenario, only the two lowest mass points have lower CL_S values when using the ‘‘a’’ regions, the point at NLSP mass 250 GeV has a lower CL_S value resulting from the ‘‘b’’ regions.

The resulting 95% CL upper limits on the production cross-sections can be seen in Figure 7.11(a)-(e) with increasing slepton mass. The nominal scenario with the slepton mass set to 50% of the NLSP mass is almost identical to the case where it is set at 75% of the NLSP mass, especially for the points with higher NLSP mass. The three points at NLSP mass of 100 GeV, 150 GeV and 250 GeV are slightly higher in the 75% plot, equating to slightly less stringent cross-section limits in this instance. The limits for these three points are also lower in the 5% and 25% instances, by a more noticeable amount. For all of these slices, there is no difference regarding whether or not any of the points are excluded. This changes when considering the slice with slepton mass at 95% of the NLSP mass, which has visibly less stringent cross-section limits set for all points, and the two points at 100 GeV and 625 GeV NLSP mass are no longer excluded.

The changes resulting from the slepton mass variation can be seen more quantitatively by comparing the expected and observed CL_S values shown in Table 7.4. As the mass of the slepton gets further away from 50% of $m_{\tilde{\chi}_{2/3}^0}$ the CL_S values decrease, but this effect is not symmetrical, and the points with the slepton mass at 95% of $m_{\tilde{\chi}_{2/3}^0}$ all have higher CL_S values than the other slices. This can be explained by considering the mass available to the decay products in the mass frame of the $\tilde{\chi}_{2/3}^0$. When the slepton mass is very close

to that of the NLSP, the leptons produced in the first part of the decay chain - $\tilde{\chi}_{2/3}^0 \rightarrow \tilde{\ell}_R \ell$ - will be very low in p_T , and it will be much less likely that they will be accepted into the SRs unless the NLSPs are boosted. This is not so much the case for the other mass splittings considered, for example when the slepton is at 5% of $m_{\tilde{\chi}_{2/3}^0}$ the lepton produced in the second part of the decay - $\tilde{\ell}_R \rightarrow \tilde{\chi}_1^0 \ell$ - will have a higher p_T , as the slepton will also have transverse momentum from the remaining 95% of the $\tilde{\chi}_{2/3}^0$ mass. All leptons resulting from these events are more likely to have sufficient p_T to satisfy the selection criteria of the four lepton analysis.

Table 7.4: Observed and expected (beneath in brackets) CL_S values for each of the variable slepton mass slices considered for the $\tilde{\chi}_2^0 \tilde{\chi}_3^0$ via slepton scenario. The \checkmark symbol is used to denote masses which have CL_S values compatible with zero.

$m_{\tilde{\chi}_{2/3}^0}$ [GeV]	$m_{\tilde{\ell}_R}$ as a percentage of $m_{\tilde{\chi}_{2/3}^0}$				
	5%	25%	50%	75%	95%
100	\checkmark (\checkmark)	\checkmark (\checkmark)	\checkmark (\checkmark)	\checkmark (\checkmark)	0.08 (0.04)
150	\checkmark (\checkmark)	\checkmark (\checkmark)	\checkmark (\checkmark)	\checkmark (\checkmark)	\checkmark (\checkmark)
250	\checkmark (\checkmark)	\checkmark (\checkmark)	\checkmark (\checkmark)	\checkmark (\checkmark)	\checkmark (\checkmark)
350	\checkmark (\checkmark)	\checkmark (\checkmark)	\checkmark (\checkmark)	\checkmark (\checkmark)	\checkmark (\checkmark)
500	\checkmark (\checkmark)	\checkmark (\checkmark)	\checkmark (\checkmark)	\checkmark (\checkmark)	\checkmark (\checkmark)
625	0.06 (0.09)	0.04 (0.06)	0.04 (0.05)	0.02 (0.06)	0.7 (0.21)
700	0.25 (0.31)	0.21 (0.27)	0.19 (0.25)	0.07 (0.25)	0.15 (0.38)

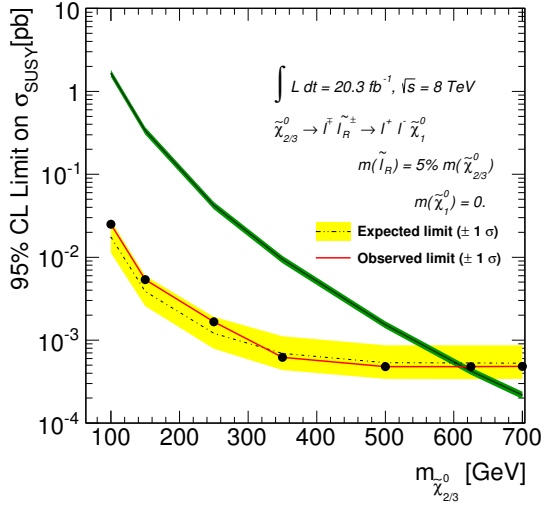
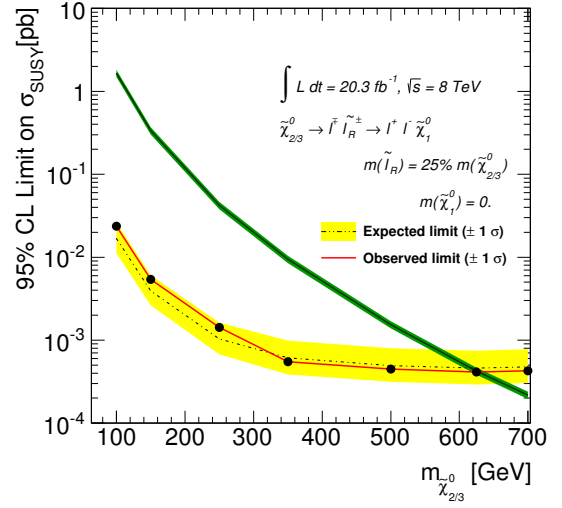
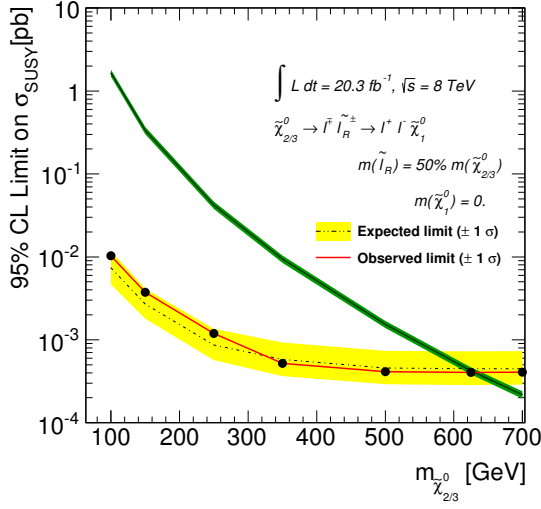
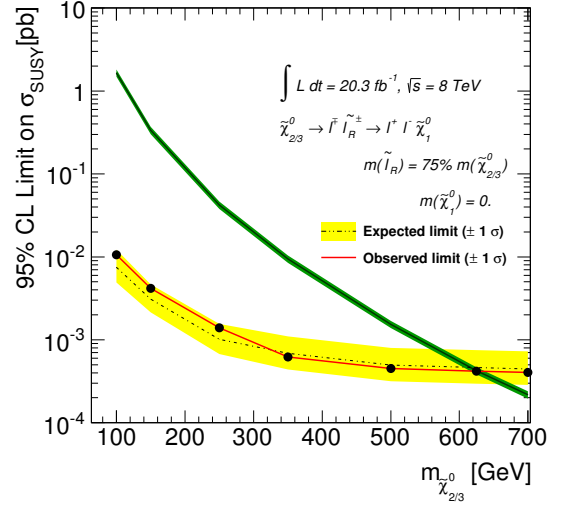
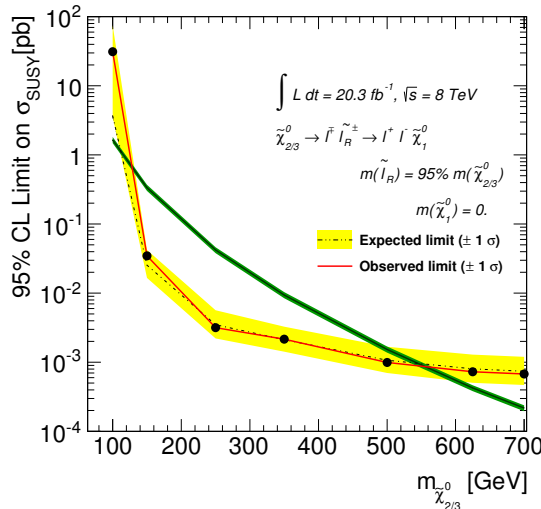
(a) $m_{\tilde{\ell}} 5\%$ (b) $m_{\tilde{\ell}} 25\%$ (c) $m_{\tilde{\ell}} 50\%$ (d) $m_{\tilde{\ell}} 75\%$ (e) $m_{\tilde{\ell}} 95\%$

Figure 7.11: The 95% CL upper cross-section limits on points from the $\tilde{\chi}_2^0 \tilde{\chi}_3^0$ via $\tilde{\ell}$ scenario with the intermediate slepton mass set at (a) 5% (b) 25% (c) 50% (d) 75% and (e) 95% of the $\tilde{\chi}_{2/3}^0$ mass.

Chapter 8

Conclusions

This thesis presents the best results produced to date by ATLAS on the search for supersymmetry in events with four or more leptons, using the full $\mathcal{L} = 20.3 \text{ fb}^{-1}$ 2012 dataset at $\sqrt{s} = 8 \text{ TeV}$. I was one of the main analysers contributing to these results, which are an extension and improvement on results published previously, to which I also made major contributions.

A wide range of signal scenarios including both R-parity conserving and R-parity violating models were targeted with optimised selection criteria applied to events containing four or more leptons. No significant deviation is observed between the expected Standard Model events and the data, within the statistical and systematic uncertainties. A statistical interpretation of the results was conducted in order to set 95% CL exclusion limits on parameters of the models considered, and model-independent limits on the visible cross-section for beyond-the-Standard Model scenarios. These results are complementary to the other ATLAS SUSY searches being carried out, in order to cover maximal SUSY scenarios with a full range of the final state signatures expected to be produced. Due to the low number of four lepton events expected from SM processes, this analysis makes a significant contribution, being sensitive to a number of simplified model processes down to smaller cross-sections.

For R-parity violating models where the LSP decays to electrons and muons, 95% CL limits were set on the masses of five different NLSPs: 1350 GeV for gluinos, 750 GeV for charginos, 490 (410) GeV for left-(right-)handed sleptons, and 400 GeV for sneutrinos. These constitute an improvement on the limits previously set by the four lepton analysis of 540 GeV for a chargino NLSP in this SUSY scenario. For newly considered models where the LSP decays to final states including taus, limits are set on the masses of four of these NLSPs: 950 GeV for gluinos, 450 GeV for charginos, and 300 (240) GeV for left-(right-

)handed sleptons. The parameter space which is excluded for the most simplified and the most “natural” models has been increased significantly by the data taken in Run 1 of the LHC, meaning that models which are slightly more complex need to be considered. The sensitivity of this analysis to a number of R-parity violating scenarios are very important in this light, in particular given that many of these do not have any limits set by CMS.

A set of simplified models considering $\tilde{\chi}_2^0\tilde{\chi}_3^0$ production were also explored with this analysis. For the scenario with decays via a slepton to the $\tilde{\chi}_1^0$ LSP, 95%CL exclusion limits were set on the $\tilde{\chi}_{2/3}^0$ mass of up to 620 GeV. For scenarios where the decay proceeds via a stau or Z boson, 95% CL limits were set on the production cross-sections. These are the strongest existing limits for this scenario, and will be improved even further by combining the result with the three lepton analysis result.

GGM models were also targeted with this analysis and 95% CL exclusion limits were set on relevant parameters. For the scenario with $\tan\beta=1.5$, gluino masses below 700 GeV were excluded for all μ values, and all gluino masses were excluded for μ values between 200 and 230 GeV. For the scenario with $\tan\beta=30$, gluino masses below 640 GeV were excluded for all μ values. This allows an exclusion limit to be set in the region of parameter space where electroweak decay processes dominate, which is not covered by any other SUSY analysis.

As an extension to the main body of results presented here, I have also worked on the combination of this analysis with other lepton-rich channels, for inclusion in a new publication in preparation. Improved limits are shown for R-parity conserving $\tilde{\chi}_2^0\tilde{\chi}_3^0$ production with decays via sleptons, and the GGM model with $\tan\beta=30$. Cross-section limits are also presented for $\tilde{\chi}_2^0\tilde{\chi}_3^0$ decays via sleptons when the slepton masses are varied from the nominal value. Varying the parameters which are fixed within the simplified models like this is crucial to assess whether there are regions of parameter space which are less accessible, or where SUSY could be “hiding”. Results from this publication will form the final word on SUSY in Run 1 at the LHC, giving the best limits for all accessible scenarios until results are produced with the Run 2 data.

Appendix A

Inner Detector Tracking Performance

A.1 Introduction

It is important to consider the performance of the tracking algorithms used for triggering in the HLT, in particular to check for any decreases in efficiency which could have occurred between the lower energy ($\sqrt{s} = 7$ TeV) data-taking period in 2011 and the data-taking period in 2012 with $\sqrt{s} = 8$ TeV. The increase in energy also led to an increase in the average pile-up present in each event from a mean average of 9.1 interactions per event in 2011 to a mean average of 20.7 interactions per event in 2012. Multiple interactions make it more difficult to accurately identify object tracks due to a higher number of tracks from pile-up. This would have a direct impact on any analyses using these triggers to select events.

The tracking algorithms used by the L2 trigger were discussed briefly in Section 3.8.2. The algorithm used for taus in Run-1 is referred to as “SiTrack” [137, 138] and uses a combinatorial approach to reconstruct tracks from the inside of the ID outwards. The tracks are seeded by forming pairs of spacepoints from the pixel and SCT detectors, and these are then extended to include spacepoints from the TRT. When an algorithm in this appendix is referred to as “L2”, this is really a reference to the SiTrack algorithm.

Results are included here for a study carried out by myself to assess the efficiency of the L2 and EF algorithms used for reconstructing taus in both the 2011 and 2012 data-taking periods. These form part of an official ATLAS publication for the performance of all HLT algorithms during Run-1, which is in progress at the time of writing.

A.2 Methodology

Dedicated HLT monitoring trigger chains are used to make an online selection of taus based solely on information from the calorimeters. The HLT tracking algorithms are still run, but the information is not used in the selection of events passing the trigger, in order to avoid bias when measuring the efficiency. The tracks which are reconstructed by the HLT for events which pass the monitoring triggers and correspond to taus are labelled as “test” tracks. These are then required to match to a “reference” track which is identified with the full offline tau reconstruction and located in the same RoI. The number of test tracks which can be matched to corresponding reference tracks is then converted to a percentage efficiency for the HLT tracking algorithms.

The offline tau candidates are reconstructed using anti- k_T jets with $p_T > 10$ GeV as seeds, which represents a generic and common setting for taus being used in analysis. They must also satisfy the medium tau identification criteria, which requires the medium JetBDT and medium ElectronBDT (described in Section 4.4.6) to be passed, as well as the muon veto. The test tracks are also required to satisfy a number of quality criteria, in order to only consider the efficiency for well-reconstructed cases. These are given by:

- $p_T > 1$ GeV
- number of hits in the “b-layer” of the pixel detector ≥ 1
- number of hits in the pixel detector ≥ 1
- total number of hits in the pixel and SCT detectors ≥ 7
- $|d_0| < 1$ mm
- $|z_0 \sin \theta| < 1.5$ mm.

This study is also restricted to one-prong tau candidates, which behave differently to three-prong candidates, and so both the test and reference tracks are required to correspond to taus with just one associated track. In order for a test track to be matched to a reference tau track, all tracks must pass the respective quality criteria, and the ΔR between them must be less than 0.2.

A.3 One-prong Tau Performance

Figures A.1(a) and (b) display the efficiency of the L2 and EF tau tracking algorithms as a function of the mean number of interactions per event $\langle \mu \rangle$ for data taken in 2011 and 2012

respectively. The datasets used in both instances do not correspond to the full datasets, but a proportion of runs taken from various points throughout the data-taking periods which gives acceptable levels of statistical uncertainty. The efficiency for the EF algorithms is expected to be higher, as these are very close to the offline selection algorithms, whereas the emphasis for the L2 tracking algorithms is on speed, in order to satisfy the lower latency available to the L2 trigger. The EF efficiency remains at approximately 99.5% for the vast majority of bins in both 2011 and 2012. The L2 algorithms are not significantly lower; in 2011 all bins show an L2 efficiency of more than 98%, and in 2012 the majority of points have an efficiency of approximately 98%. There are a few bins in the 2012 distribution which give L2 efficiencies between 95% and 98%, but these bins tend to contain less events, which is demonstrated by the larger error bars for these cases. The most important conclusion which can be drawn from these plots is that the performance of the algorithms was relatively independent of μ , as the distributions are flat, with decreases only seen for the μ values which are less common. This is also supported by Figures A.1(c) and (d), which give the EF and L2 efficiency in 2011 and 2012 as a function of the mean number of vertices reconstructed offline per event, which is related to μ .

Figures A.2(a) and (b) gives the efficiency of EF and L2 algorithms in 2011 and 2012 as a function of the reference track η . For both years the EF efficiency distribution is very flat with respect to η and the majority of bins have an efficiency of 100%. For the L2 algorithms the distributions are fairly flat in both years, achieving efficiencies of approximately 98% or higher in both data-taking periods. Figure A.2(c) and (d) give the equivalent efficiency distributions for 2011 and 2012 as a function of the reference track p_T . The efficiency of the EF algorithms is almost 100% for all bins in both years, but there is a turn-on in efficiency visible for the L2 algorithms. In 2011, the L2 efficiency has values of 92% and above for reference tracks with a $p_T < 3$ GeV, but for tracks with higher p_T the average efficiency of 98% or above is seen for all bins. In 2012 the same shape is seen, again with a p_T of approximately 3 GeV corresponding to the efficiency flattening to the average L2 value of approximately 98%. For reference tracks with a p_T higher than approximately 80 GeV the L2 efficiencies are also lower, but the error bars indicate that this is due to fewer events being present in the bins for these high p_T values.

The set of distributions presented in Figure A.3 give efficiencies as a function of the reference track ϕ . Figure A.3(a) shows the efficiency is flat for both EF and L2 when considered as a function of ϕ for the 2011 dataset. The EF efficiency is close to 100% in all bins, and the L2 efficiency remains above 98%. However, for the 2012 distribution

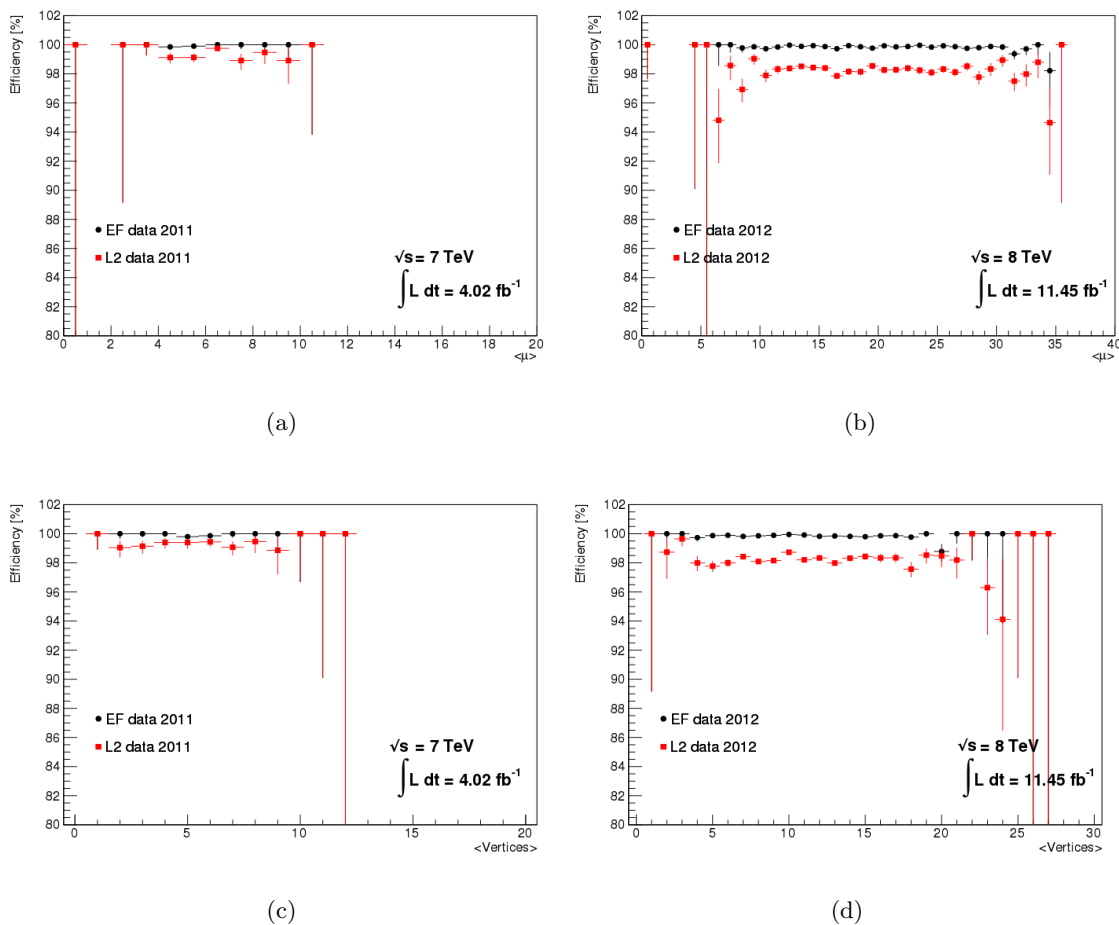


Figure A.1: The L2 and EF tracking efficiencies as a function of the average pileup interaction multiplicity, μ for (a) 2011 data and (b) 2012 data and as a function of the offline event vertex multiplicity for (c) 2011 and (d) 2012.

displayed in Figure A.3(b) this is not the case. The EF efficiency behaves as expected and has been observed in all other distributions, with a flat efficiency close to 100%. The L2 efficiency has a significant drop from approximately 99% to between 95% and 98% for a number of bins in the positive ϕ range of 1-2.5. I was involved in a number of detailed studies investigating this feature, for example considering the possibility of a detector defect in this region or a correlation between poor quality tracks and the problematic ϕ values. Figures A.3(c) and (d) show the effect on the distribution shape when the requirements for SCT hits are increased from 5 to 7 and when in addition the pixel hits required are increased from 1 to 2. An additional two hits being required in the SCT detector does not significantly alter the shape of the efficiency distribution, although it does increase the efficiency uniformly overall. When another pixel hits is also required in addition to this request though, the efficiency is very flat with respect to η . This

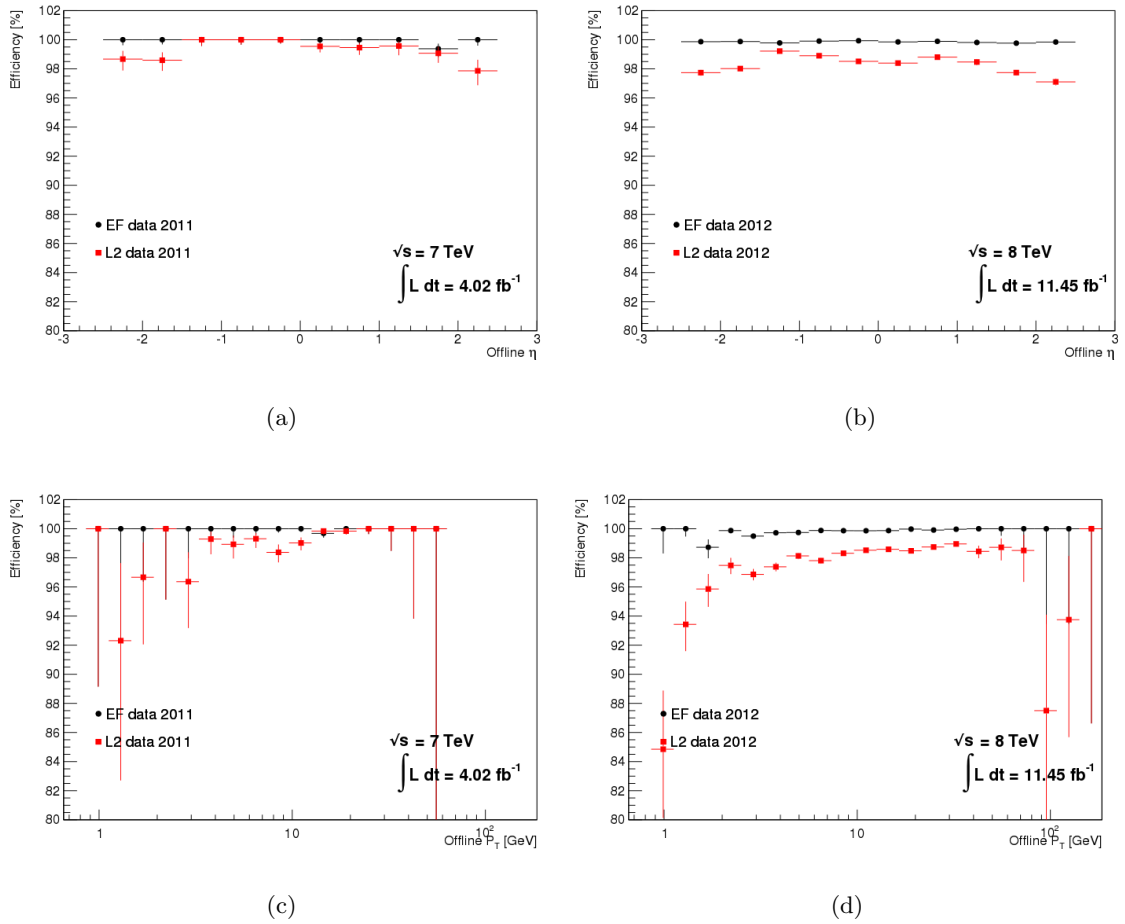


Figure A.2: The L2 and EF tracking efficiencies as a function of reference track pseudorapidity η for (a) 2011 and (b) 2012 and as a function of transverse momentum p_T for (c) 2011 and (d) 2012.

suggests that the tracks contributing to the poor efficiency in the high positive ϕ bins are disproportionately comprised of tracks with fewer hits in the ID, which causes a decrease in the efficiency of the L2 tracking algorithms. This was confirmed by comparing the hit information for tracks within this η region to that of all other tracks.

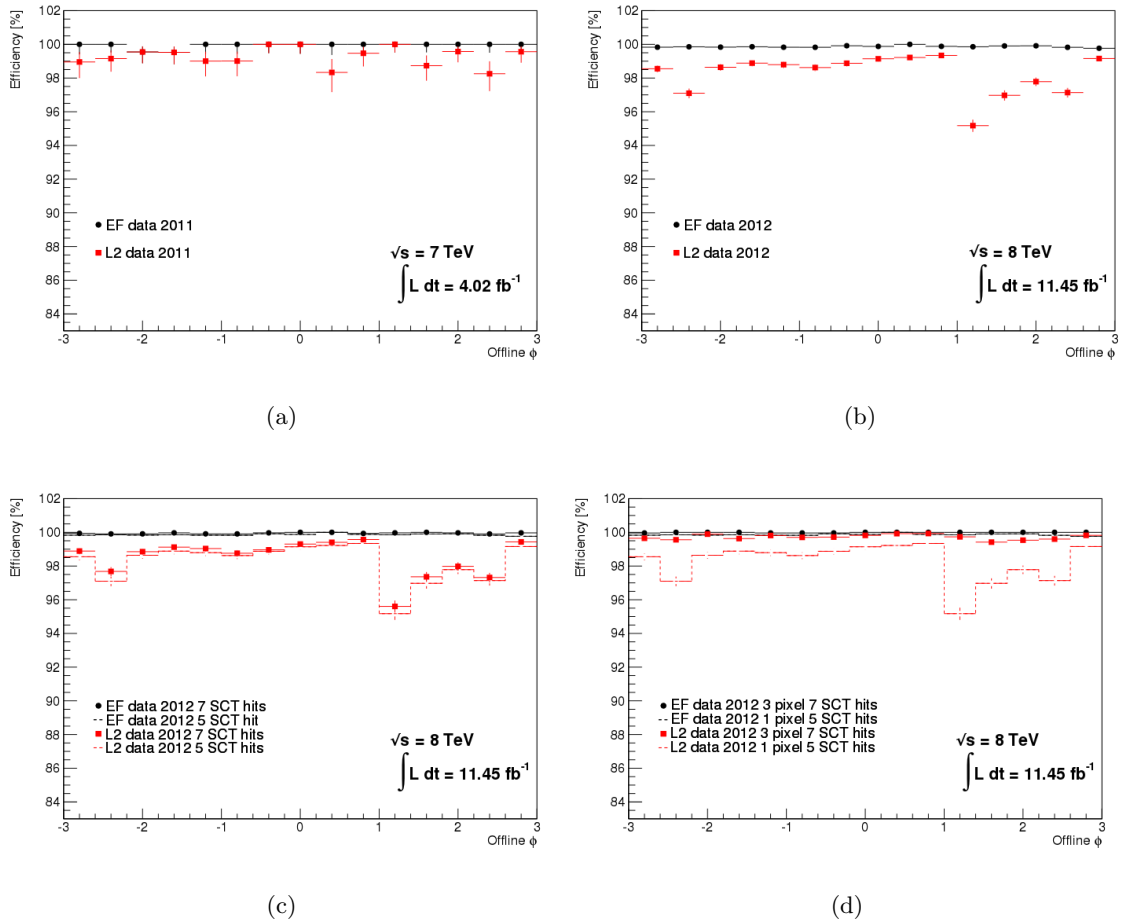


Figure A.3: The L2 and EF tracking efficiencies as a function of ϕ for (a) 2011 and (b) 2012 with standard selection, (c) with standard selection but requiring at least seven SCT clusters, or (d) requiring seven SCT clusters and also at least two pixel clusters

Appendix B

Generation and Properties of $\tilde{\chi}_2^0\tilde{\chi}_3^0$ Grids

B.1 Introduction

The four lepton analysis conducted on 13 fb^{-1} of the 8 TeV data collected in 2012 [97] included two supersymmetric scenarios for $\tilde{\chi}_2^0\tilde{\chi}_3^0$ production and decays via sleptons. In order to make these more comparable with the simplified models used in the electroweak SUSY group for $\tilde{\chi}_1^\pm\tilde{\chi}_2^0$ and $\tilde{\chi}_1^\pm\tilde{\chi}_1^\mp$ production they were simplified further to just one scenario with only two varied parameters. The $\tilde{\chi}_2^0$ and $\tilde{\chi}_3^0$ co-NLSPs were set to be degenerate in mass ($m_{\tilde{\chi}_2^0} = m_{\tilde{\chi}_3^0}$) and the slepton mass was fixed at halfway between the NLSP mass and the $\tilde{\chi}_1^0$ LSP ($m_{\tilde{\ell}} = \frac{m_{\tilde{\chi}_2^0} + m_{\tilde{\chi}_1^0}}{2}$). This allowed the exclusion limits to be calculated in the conventional LSP mass versus NLSP mass parameter space for the analysis published in 2014 [1]. In addition scenarios were added to also cover instances where the NLSPs decayed via Z bosons or staus. I was responsible for the re-design and subsequent MC sample generation for these models, and this appendix contains a description of the methods involved in this, as well as the calculation of systematics for the grid involving decays via staus, and some of the properties of the resulting $\tilde{\chi}_2^0\tilde{\chi}_3^0$ grids used by the four lepton analysis. Any plots relating to the $\tilde{\chi}_2^0\tilde{\chi}_3^0$ via slepton model were included in the auxiliary material of the most recent publication [1] (along with the equivalent plots for the GGM $\tan\beta = 30$ grid which I also produced), and all plots and numbers were produced by myself.

B.2 Sample Generation

MC samples for $\tilde{\chi}_2^0\tilde{\chi}_3^0$ production and subsequent decays via sleptons, staus or Z bosons were generated using MADGRAPH [100]. Data files containing only truth information were first generated privately with the MADGRAPH framework by myself in order to estimate the sensitivity of the four lepton analysis to each signal point. These “truth” samples were analysed with code which made selections on truth objects to emulate the four lepton analysis selections, including some object selection criteria, overlap removal, and application of the p_T thresholds used for the triggers. The acceptance was then calculated as the number of events satisfying these selections and the lepton multiplicity and Z-veto/selection requirements used by the SRs as a fraction of the total number of events. The decays via slepton grid used the $4\ell 0\tau$ multiplicity cut and the Z-veto (all cuts are those used for the signal regions, detailed in Section 5.4), the decays via stau grid used the combined acceptance for both the $3\ell 1\tau$ and $2\ell 2\tau$ multiplicity cuts and a Z-veto, and the decays via Z grid used the acceptance for $4\ell 0\tau$ after a Z-selection. Ideally the acceptance would be calculated for the SRs to be used on these grids, but due to the few events surviving once an E_T^{miss} or m_{eff} cut is also applied, and the fact that the SRs were re-optimised to suit these grids after generation, the acceptance after the Z-veto/selection was the next best option. The acceptance was used in combination with the LO cross-sections extracted from MADGRAPH (NLO cross-sections for the official analysis were later calculated with PROSPINO [103]) and the number of expected events passing the four lepton selection to roughly estimate the area of parameter space which could be probed with the four lepton analysis. This gave an indication of which mass values to use for samples for each of the three scenarios, which are described in Section 5.2. The efficiency of reconstructing the leptons was then assumed to be about 40% in the $4\ell 0\tau$ regions and 15% in the regions containing taus, and the number of events to request for each point was then calculated based on the formula:

$$\sigma = \frac{1}{\sqrt{E \times A \times N}}, \quad (\text{B.1})$$

where σ is the statistical uncertainty, E is the reconstruction efficiency, A is the acceptance and N is the number of events in the sample. The number of events was then increased until the statistical uncertainty fell below 5%, unless the sample size exceeded 50,000 events, in which case this was increased to 10% to minimize the number of events which needed to be generated.

Filters were used within the generation framework in order to increase the number of

generated events which would be useful for this analysis. For the $\tilde{\chi}_2^0\tilde{\chi}_3^0$ via slepton grid a filter was applied to require at least three light leptons present in the final state of each event, and the efficiency for this filter was then applied at analysis stage. The points generated with a mass splitting between the $\tilde{\chi}_1^0$ and $\tilde{\chi}_{2/3}^0$ of 20 GeV or 35 GeV had a more stringent filter which requires four light leptons applied. This was due to the lower acceptance for these small mass splitting points, as the leptons tend to have lower p_T values. For scenarios where the decay is via a stau, a filter requested three leptons which could be either electrons, muons or taus, but at least one of which had to be a light lepton. The scenarios with decays via a Z boson required the same as the bulk of the slepton grid, at least three light leptons.

I was also responsible for calculating the systematic uncertainties on the $\tilde{\chi}_2^0\tilde{\chi}_3^0$ via stau samples due to the ISR, FSR and QCD scale settings used within the generation. These sources of uncertainty are discussed in Section 6.3.3. This required the private generation of truth samples for these points with the settings varied up and down by one sigma for each of the three systematics. The scale uncertainty is calculated by varying the *matching scale* used within MADGRAPH to define which parts of the calculation are included in the matrix element, and which in the PDF. This has a default setting of 1, and is varied to 0.5 for the “down” setting and 2 for the “up” setting. The ISR systematic uncertainty is calculated by varying a parameter used within PYTHIA for the parton showering called PARP(64) [77], again from a nominal value of 1 to values of 0.5 and 2. This PARP(64) parameter scales the α_S and PDFs used. Similarly the FSR uncertainty is calculated by varying the PYTHIA parameter PARP(72) [77] by a factor of 0.5 and a factor of 2. The PARP(72) parameter sets the cut-off scale used for all running α_S calculations. The acceptance of events passing a truth-level emulation of the $3\ell 1\tau$ and $2\ell 2\tau$ SRs were then calculated and compared for each variation with the nominal value, and the difference was taken as the systematic uncertainty. The number of events required with each of these variations was calculated to ensure that there was a maximum statistical uncertainty on the results of 15%, but on average the statistical uncertainty was around 5%. The total systematic uncertainty from the ISR, FSR and scale sources was then calculated by summing the contributions in quadrature, and applying the largest variation (in either the upward or downward direction) symmetrically. The resulting uncertainties which are applied for the $\tilde{\chi}_2^0\tilde{\chi}_3^0$ via stau signal points are shown in Table B.1.

Table B.1: Total systematic uncertainty including variations to the ISR, FSR and scale settings used during generation, applied symmetrically to the $\tilde{\chi}_2^0\tilde{\chi}_3^0$ via stau points.

$m_{\tilde{\chi}_1^0}, m_{\tilde{\chi}_2^0, \tilde{\chi}_3^0}$	Uncertainty (%)
100,0	12.3
100,50	7.0
150,0	14.2
150,50	12.3
200,0	4.3
200,50	5.8
200,100	3.2
250,0	6.6
250,50	7.3
250,100	3.0
300,0	7.4
300,50	1.6
300,100	4.1
350,0	1.7

B.3 Properties of the $\tilde{\chi}_2^0\tilde{\chi}_3^0$ Grids

Once the official samples for the $\tilde{\chi}_2^0\tilde{\chi}_3^0$ samples were generated I was responsible for producing distributions of various useful properties of the signal points. Figures B.1(a) and (b) display a graphical representation of the NLO cross-sections calculated with PROSPINO [103] for the scenarios with decays via sleptons and staus respectively. The same convention is used as for the significance distributions and limit plots, with the mass of the LSP on the vertical axis and the mass of the NLSPs on the horizontal axis. For both decay modes the cross-section decreases as a function of increasing NLSP mass.

The acceptance for the official samples was calculated as the ratio of the number of events passing the SR selection to the total number of events in the sample. For the $\tilde{\chi}_2^0\tilde{\chi}_3^0$ via slepton grid, the signal region SR0noZa was used, and the resulting acceptance is displayed in Figure B.2(a). The acceptance is highest for the high NLSP mass, low LSP mass region of parameter space where it has values around 0.8. As the diagonal is approached the acceptance decreases to the lowest values of around 0.1, as a result of the lower p_T leptons produced in this region being less likely to pass the SR selection criteria. Figure B.2(b) shows the acceptance for $\tilde{\chi}_2^0\tilde{\chi}_3^0$ via stau signal events in the SR2noZa signal region as a function of the parameter space. The acceptance is approximately 0.1 for the

highest NLSP mass point, and decreases as the NLSP mass decreases to values around 0.01 for points with NLSP masses of 100 GeV. These are lower than the values for the slepton points, partly due to the difference in filters between the two, as there are more events which can satisfy the stau filter but not the SR2noZa selection criteria. Figures B.3(a) and (b) give the reconstruction efficiency for events from the slepton and stau samples respectively, in the SR0noZa and SR2noZa signal regions. The experimental uncertainties for each of the signal points from the slepton and stau grids are displayed in Figure B.4 in the same SRs - SR0noZa and SR2noZa. These do not include the statistical uncertainty arising from the MC sample sizes. The largest uncertainties on the slepton grid occur for the low mass splitting points near the diagonal, with values around 10-20%, whilst the majority of the grid has uncertainties around 7-8%. Values on the stau grid vary between 9.7% and 19.0%. The values for all properties calculated for the Z grid are displayed in Table B.2 as the points considered do not extend to LSP masses above 0 GeV. The same patterns with respect to increasing NLSP mass can be seen: the cross-sections decrease and the acceptance increases. The efficiencies vary between 0.05 and 0.25, between the values seen for the slepton and stau grids. The uncertainties are around 7% for all points except the one with the lowest NLSP mass of 100 GeV, which is also seen to have higher uncertainties in the other grids.

Table B.2: Acceptance, efficiency, signal systematic uncertainty and cross-section values for the $\tilde{\chi}_2^0\tilde{\chi}_3^0$ via Z grid. The acceptances, efficiencies and uncertainties are all calculated in the signal region SR0Z.

$m_{\tilde{\chi}_1^0}, m_{\tilde{\chi}_2^0, \tilde{\chi}_3^0}$	Acceptance	Efficiency	Uncertainty %	Cross-section [pb]
100,0	4.06e-05	0.14	24.24	1.5e-02
125,0	2.23e-04	0.23	7.35	6.6e-03
150,0	9.51e-04	0.18	7.40	3.3e-03
200,0	1.71e-03	0.11	7.04	1.0e-03
250,0	2.24e-03	0.06	6.95	4.1e-04
300,0	2.67e-03	0.07	7.00	1.9e-04

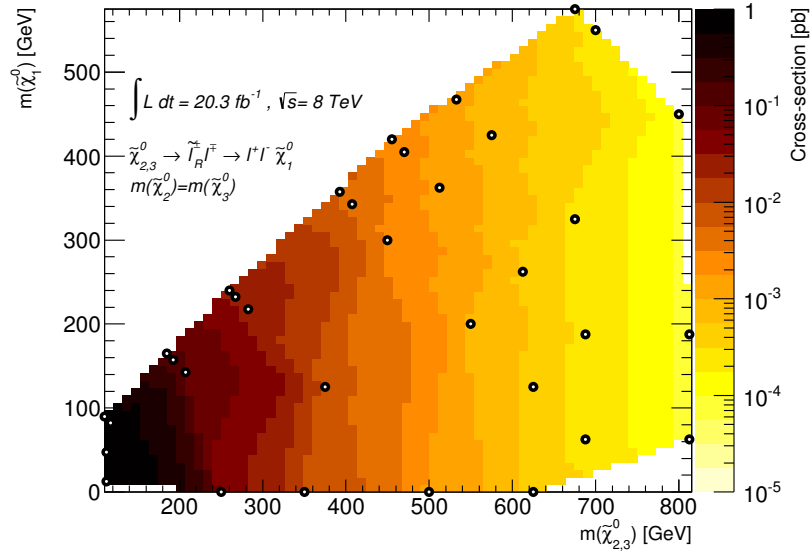
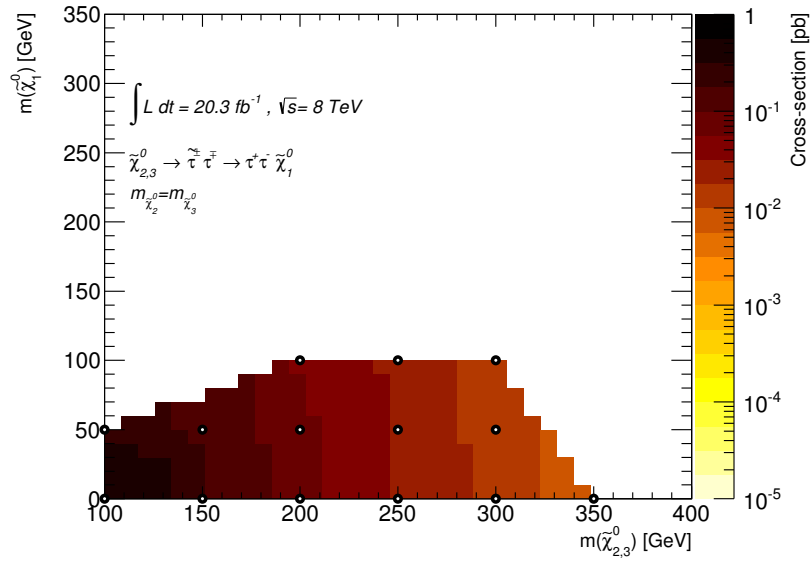
(a) $\tilde{\chi}_2^0 \tilde{\chi}_3^0$ slepton(b) $\tilde{\chi}_2^0 \tilde{\chi}_3^0$ stau

Figure B.1: The cross-section for the RPC simplified model $\tilde{\chi}_2^0 \tilde{\chi}_3^0$ grids with decays via (a) sleptons and (b) staus.

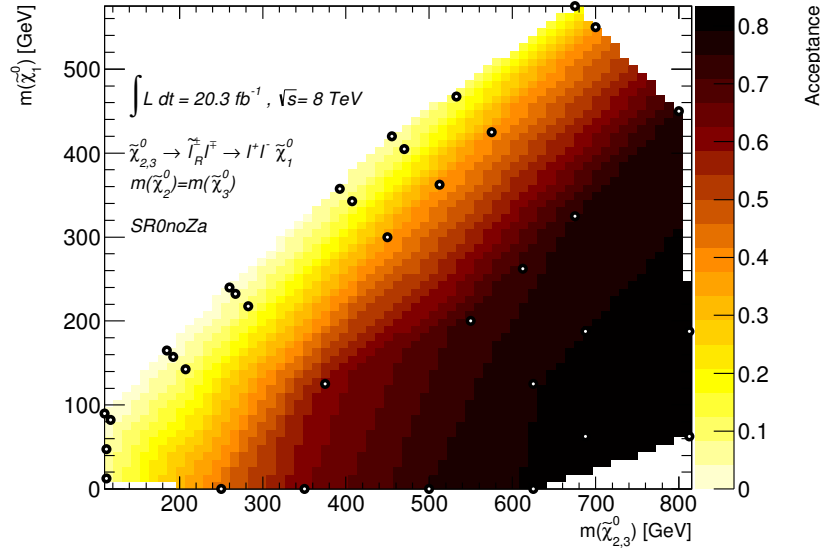
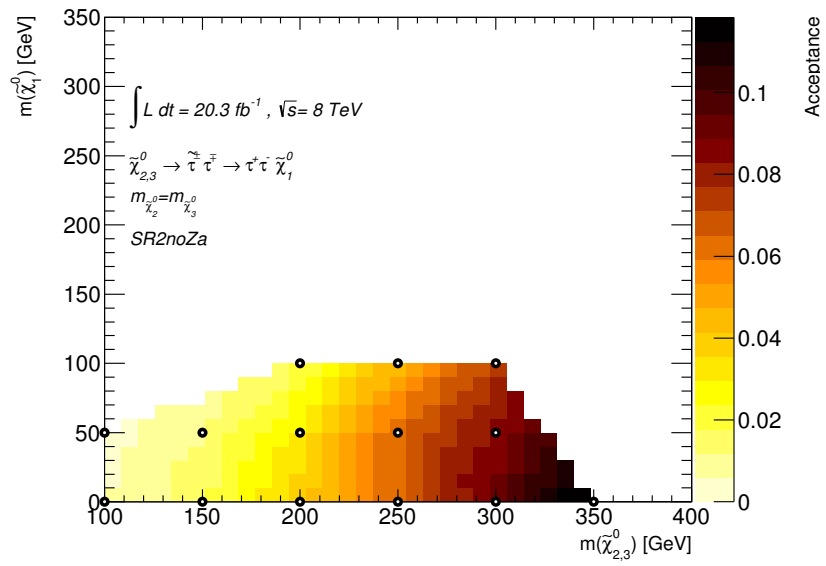
(a) $\tilde{\chi}_2^0 \tilde{\chi}_3^0$ slepton, SR0noZa(b) $\tilde{\chi}_2^0 \tilde{\chi}_3^0$ stau, SR2noZa

Figure B.2: The acceptance in selected signal regions for the RPC simplified model $\tilde{\chi}_2^0 \tilde{\chi}_3^0$ grids with decays via (a) sleptons and (b) staus.

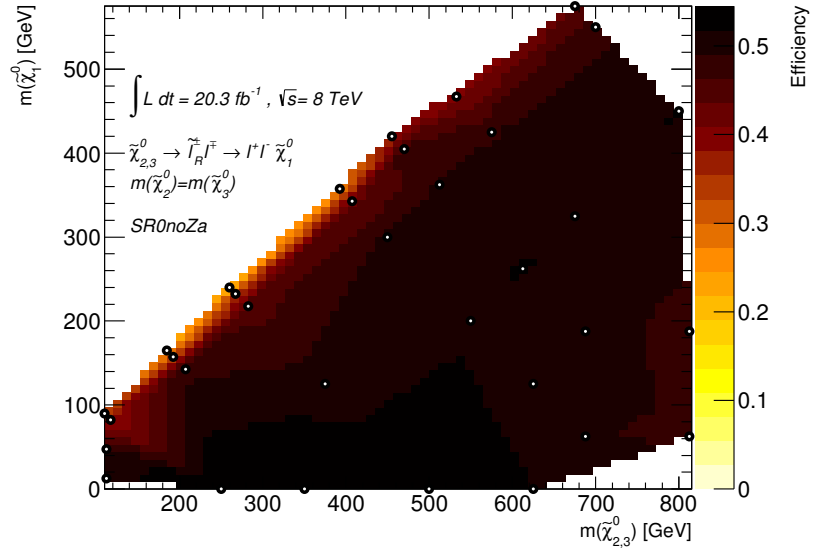
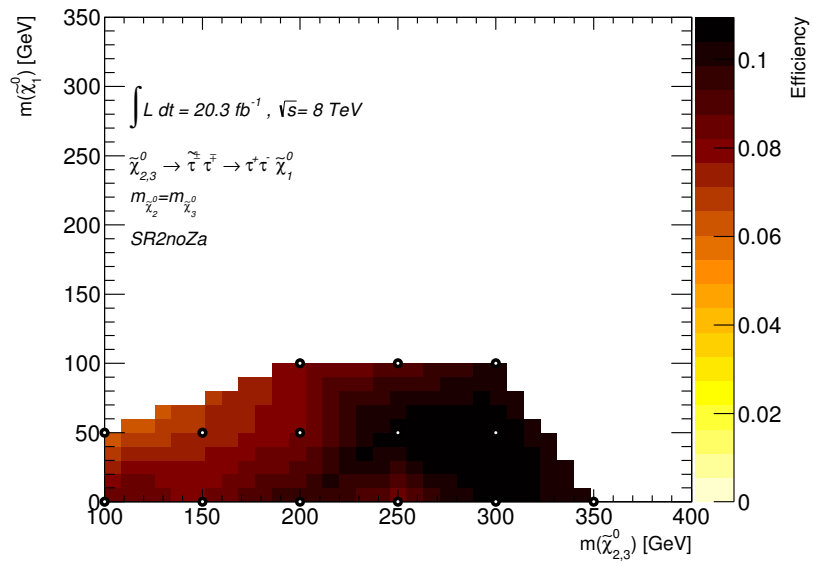
(a) $\tilde{\chi}_2^0 \tilde{\chi}_3^0$ slepton, SR0noZa(b) $\tilde{\chi}_2^0 \tilde{\chi}_3^0$ stau, SR2noZa

Figure B.3: The efficiency in selected signal regions for the RPC simplified model $\tilde{\chi}_2^0 \tilde{\chi}_3^0$ grids with decays via (a) sleptons and (b) staus.

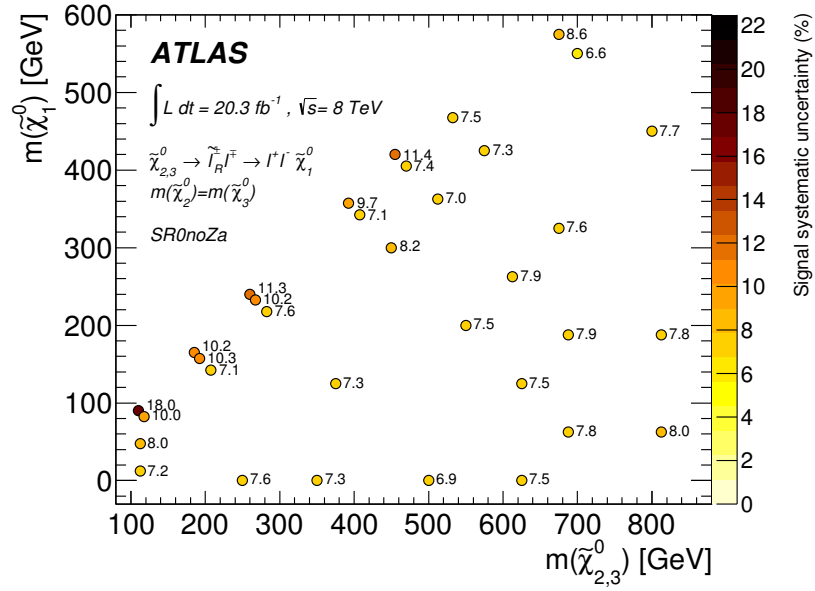
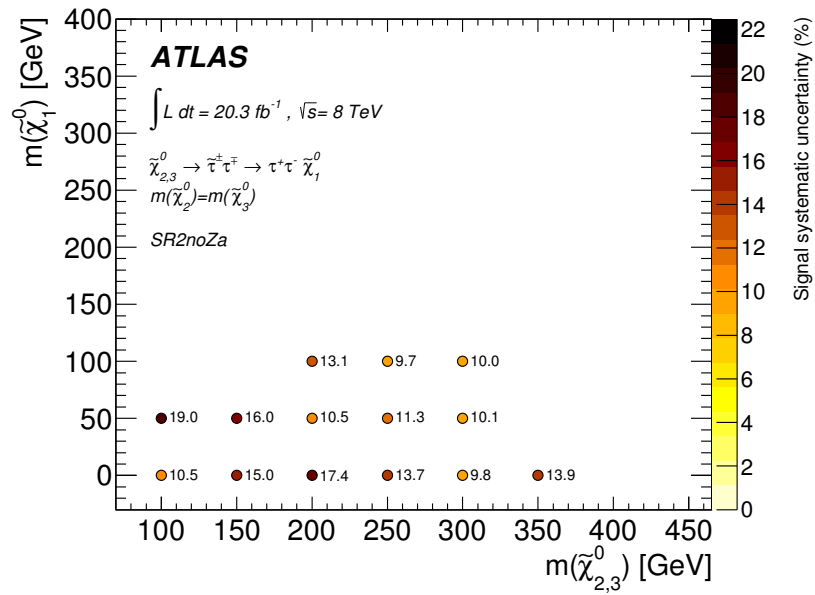
(a) $\tilde{\chi}_2^0 \tilde{\chi}_3^0$ slepton, SR0noZa(b) $\tilde{\chi}_2^0 \tilde{\chi}_3^0$ stau, SR2noZa

Figure B.4: Total uncertainty in selected signal regions for (a) the $\tilde{\chi}_2^0 \tilde{\chi}_3^0$ via slepton grid and (b) the $\tilde{\chi}_2^0 \tilde{\chi}_3^0$ via stau grid.

Appendix C

Systematic Uncertainties in the Signal Regions

This appendix contains tables summarising the systematic uncertainties arising from all included sources in each of the nine signal regions. All uncertainties are presented as a percentage, as one number for symmetric sources of uncertainty and one after the other for systematics where this is not the case. These are complementary to the figures and discussion found in [Section 6.3.4](#)

Table C.1: Summary of systematic uncertainties in the signal region SR0noZa for each of the irreducible background processes, the reducible processes and the total estimated background. Where two numbers are listed, the first gives the “down” systematic uncertainty and the second gives the “up” systematic uncertainty. All uncertainties are presented as a percentage, and the number of events estimated for each background process in this region is also displayed.

Systematic	ZZ	$t\bar{t} + V$	$t\bar{t} + Z$	VVV	Higgs	Reducible	Σ SM
Expected Events	0.29	0.07	0.8	0.19	0.27	0.006	1.6
Stat	± 8.7	± 13.7	± 21.6	± 8.4	± 11.8	± 2773.0	± 14.7
JES	3.3, -0.3	2.3, 0.0	0.7, -1.5	2.3, 1.1	-0.4, 2.8	-28.0, -14.5	1.1, -0.2
JER	± 11.2	± -0.1	± 0.3	± 2.8	± 3.6	± -73.2	± 2.9
ESF	-4.8, 5.0	-3.6, 3.6	-2.7, 2.8	-3.6, 3.7	-4.4, 4.5	39.4, -40.8	-3.4, 3.5
Generator	± 17.2	± 0.0	± 39.0	± 0.0	± 0.0	± -134.5	± 19.3
PDF	3.1, 3.2	0.0, 0.0	3.5, 3.5	0.0, 0.0	0.0, 0.0	-17.5, -18.2	-1.8, 1.8
Pileup	-2.3, 2.2	-0.4, -0.2	0.8, -1.5	0.4, -0.2	-1.3, 1.3	-2.0, 6.4	-0.2, -0.1
Pileup	0.0, -2.3	0.0, -0.4	0.0, 0.8	0.0, 0.4	0.0, -1.3	0.0, -2.0	0.0, -0.2
TauID SF	0.0, 0.0	0.0, 0.0	0.0, 0.0	0.0, 0.0	-0.0, 0.0	0.0, 0.0	-0.0, 0.0
Cross-section	-4.8, 4.8	-47.1, 47.1	-30.0, 30.0	-46.9, 46.9	-85.9, 85.9	287.0, -287.0	-21.3, 21.3
TES	0.0, 0.0	0.0, 0.0	0.0, 0.0	0.0, 0.0	0.0, 0.0	0.0, 0.0	0.0, 0.0
TEVSF	0.0, 0.0	0.0, 0.0	0.0, 0.0	0.0, 0.0	0.0, 0.0	0.0, 0.0	0.0, 0.0
Scale ST	-8.2, 14.6	0.0, -1.4	-2.1, -1.2	0.7, -0.3	4.5, 1.1	19.9, -19.9	-1.6, 2.1
Reso ST	± 4.0	± 1.6	± -2.9	± 0.9	± 1.0	± -25.6	± -0.4
Trigger	-5.0, 5.0	-5.0, 5.0	-5.0, 5.0	-5.0, 5.0	-5.0, 5.0	-5.0, 5.0	-5.0, 5.0
Lumi	± 2.8	± 2.8	± 2.8	± 2.8	± 2.8	± 2.8	± 2.8
e afr (WM)	0.0, 0.0	0.0, 0.0	0.0, 0.0	0.0, 0.0	0.0, 0.0	606.0, -1764.1	2.2, -6.3
mu afr (WM)	0.0, 0.0	0.0, 0.0	0.0, 0.0	0.0, 0.0	0.0, 0.0	-170.3, -891.0	-0.6, -3.2
tau afr (WM)	0.0, 0.0	0.0, 0.0	0.0, 0.0	0.0, 0.0	0.0, 0.0	0.0, 0.0	0.0, 0.0
5l (WM)	0.0, 0.0	0.0, 0.0	0.0, 0.0	0.0, 0.0	0.0, 0.0	0.0, 5.0	0.0, 0.0
closure (WM)	0.0, 0.0	0.0, 0.0	0.0, 0.0	0.0, 0.0	0.0, 0.0	-45.0, 45.0	-0.2, 0.2

Table C.2: Summary of systematic uncertainties in the signal region SR0noZb for each of the irreducible background processes, the reducible processes and the total estimated background. Where two numbers are listed, the first gives the “down” systematic uncertainty and the second gives the “up” systematic uncertainty. All uncertainties are presented as a percentage, and the number of events estimated for each background process in this region is also displayed.

Systematic	ZZ	$t\bar{t} + V$	$t\bar{t} + Z$	VVV	Higgs	Reducible	Σ SM
Expected Events	0.19	0.05	0.7	0.18	0.22	0.06	1.4
Stat	± 10.8	± 16.8	± 24.8	± 8.6	± 13.8	± 245.4	± 16.2
JES	2.2, 2.0	5.4, 0.0	3.2, 0.9	1.8, 0.8	-0.1, 1.5	-1.5, -0.2	2.2, 1.1
JER	± 9.9	± 3.6	± 4.9	± 2.7	± 6.8	± 3.2	± 5.5
ESF	-3.7, 3.8	-3.6, 3.7	-2.6, 2.7	-3.4, 3.6	-4.0, 4.1	2.8, -2.9	-2.9, 3.0
Generator	± 20.2	± 0.0	± 30.7	± 0.0	± 0.0	± -9.2	± 15.4
PDF	5.4, 4.7	0.0, 0.0	4.1, 4.2	0.0, 0.0	0.0, 0.0	-1.7, -1.6	-2.2, 2.2
Pileup	-1.5, 1.5	0.7, -0.9	0.3, -1.3	0.9, -0.9	-0.1, 0.1	-0.6, 1.0	0.0, -0.5
Pileup	0.0, -1.5	0.0, 0.7	0.0, 0.3	0.0, 0.9	0.0, -0.1	0.0, -0.6	0.0, 0.0
TauID SF	0.0, 0.0	0.0, 0.0	0.0, 0.0	0.0, 0.0	-0.0, 0.0	0.0, 0.0	-0.0, 0.0
Cross-section	-4.8, 4.8	-46.0, 46.0	-30.0, 30.0	-35.6, 35.6	-87.6, 87.6	21.9, -21.9	-21.0, 21.0
TES	0.0, 0.0	0.0, 0.0	0.0, 0.0	0.0, 0.0	0.0, 0.0	0.0, 0.0	0.0, 0.0
TEVSF	0.0, 0.0	0.0, 0.0	0.0, 0.0	0.0, 0.0	0.0, 0.0	0.0, 0.0	0.0, 0.0
Scale ST	-2.1, 0.9	0.1, -1.6	0.0, 1.3	-0.0, 0.8	0.3, -0.3	1.4, -1.4	-0.2, 0.7
Reso ST	± 1.4	± 0.0	± 0.2	± 0.8	± 2.1	± -0.8	± 0.7
Trigger	-5.0, 5.0	-5.0, 5.0	-5.0, 5.0	-5.0, 5.0	-5.0, 5.0	-5.0, 5.0	-5.0, 5.0
Lumi	± 2.8	± 2.8	± 2.8	± 2.8	± 2.8	± 2.8	± 2.8
e afr (WM)	0.0, 0.0	0.0, 0.0	0.0, 0.0	0.0, 0.0	0.0, 0.0	39.5, -89.9	1.7, -3.8
mu afr (WM)	0.0, 0.0	0.0, 0.0	0.0, 0.0	0.0, 0.0	0.0, 0.0	-49.8, 9.8	-2.1, 0.4
tau afr (WM)	0.0, 0.0	0.0, 0.0	0.0, 0.0	0.0, 0.0	0.0, 0.0	0.0, 0.0	0.0, 0.0
5l (WM)	0.0, 0.0	0.0, 0.0	0.0, 0.0	0.0, 0.0	0.0, 0.0	0.0, 5.0	0.0, 0.2
closure (WM)	0.0, 0.0	0.0, 0.0	0.0, 0.0	0.0, 0.0	0.0, 0.0	-62.0, 62.0	-2.6, 2.6

Table C.3: Summary of systematic uncertainties in the signal region SR0Z for each of the irreducible background processes, the reducible processes and the total estimated background. Where two numbers are listed, the first gives the “down” systematic uncertainty and the second gives the “up” systematic uncertainty. All uncertainties are presented as a percentage, and the number of events estimated for each background process in this region is also displayed.

Systematic	ZZ	$t\bar{t} + V$	$t\bar{t} + Z$	VVV	Higgs	Reducible	Σ SM
Expected Events	1.1	0.25	2.6	1	0.6	0	5
Stat	± 4.6	± 6.0	± 10.0	± 3.6	± 11.9	± -93.0	± 6.4
JES	2.8, 1.6	2.1, 1.8	-2.6, -3.3	1.0, 0.9	0.4, 5.2	1.6, 3.2	-0.4, -0.6
JER	± 7.3	± 1.1	± 0.8	± 1.9	± 3.3	± 2.0	± 2.6
ESF	-3.7, 3.9	-2.7, 2.8	-3.1, 3.1	-3.1, 3.1	-3.3, 3.4	-6.6, 6.8	-3.1, 3.2
Generator	± 7.2	± 0.0	± 31.5	± 0.0	± 0.0	± 24.1	± 15.5
PDF	3.0, 3.5	0.0, 0.0	1.4, 1.0	0.0, 0.0	0.0, 0.0	2.6, 2.6	-0.9, 0.9
Pileup	-2.5, 2.6	0.6, -0.6	0.3, -0.6	-0.0, 0.2	-0.8, 0.4	-0.8, 1.3	-0.4, 0.2
Pileup	0.0, -2.5	0.0, 0.6	0.0, 0.3	0.0, -0.0	0.0, -0.8	-0.0, -0.8	0.0, -0.4
TauID SF	0.0, 0.0	-0.0, 0.0	0.0, 0.0	0.0, 0.0	-0.0, 0.0	-0.0, -0.0	-0.0, 0.0
Cross-section	-4.5, 4.5	-50.0, 50.0	-30.0, 30.0	-48.7, 48.7	-32.7, 32.7	-43.1, 43.1	-18.0, 18.0
TES	0.0, 0.0	0.0, 0.0	0.0, 0.0	0.0, 0.0	0.0, 0.0	-0.0, -0.0	0.0, 0.0
TEVSF	0.0, 0.0	0.0, 0.0	0.0, 0.0	0.0, 0.0	0.0, 0.0	-0.0, -0.0	0.0, 0.0
Scale ST	-13.4, 18.3	-0.4, 1.0	-4.4, -3.2	-0.7, 1.3	-0.6, 3.3	-2.1, 1.6	-5.0, 2.7
Reso ST	± 3.1	± 0.1	± -0.4	± 0.1	± 4.0	± 1.7	± 0.8
Trigger	-5.0, 5.0	-5.0, 5.0	-5.0, 5.0	-5.0, 5.0	-5.0, 5.0	-5.0, 5.0	-5.0, 5.0
Lumi	± 2.8	± 2.8	± 2.8	± 2.8	± 2.8	± 2.8	± 2.8
e afr (WM)	0.0, 0.0	0.0, 0.0	0.0, 0.0	0.0, 0.0	0.0, 0.0	-73.1, 80.5	2.9, -3.2
mu afr (WM)	0.0, 0.0	0.0, 0.0	0.0, 0.0	0.0, 0.0	0.0, 0.0	31.4, -35.6	-1.3, 1.4
tau afr (WM)	0.0, 0.0	0.0, 0.0	0.0, 0.0	0.0, 0.0	0.0, 0.0	-0.0, -0.0	0.0, 0.0
5l (WM)	0.0, 0.0	0.0, 0.0	0.0, 0.0	0.0, 0.0	0.0, 0.0	-0.0, 5.0	0.0, -0.2
closure (WM)	0.0, 0.0	0.0, 0.0	0.0, 0.0	0.0, 0.0	0.0, 0.0	-31.0, 31.0	1.2, -1.2

Table C.4: Summary of systematic uncertainties in the signal region SR1noZa for each of the irreducible background processes, the reducible processes and the total estimated background. Where two numbers are listed, the first gives the “down” systematic uncertainty and the second gives the “up” systematic uncertainty. All uncertainties are presented as a percentage, and the number of events estimated for each background process in this region is also displayed.

Systematic	ZZ	$t\bar{t} + V$	$t\bar{t} + Z$	VVV	Higgs	Reducible	Σ SM
Expected Events	0.5	0.05	0.21	0.14	0.4	3.3	5
Stat	± 7.0	± 12.9	± 17.1	± 9.8	± 9.9	± 17.0	± 12.2
JES	1.8, 0.2	-1.7, 0.0	-4.5, -2.7	0.8, -0.6	0.0, -0.3	-0.0, 0.0	-0.0, -0.1
JER	± 5.3	± 1.1	± -0.9	± 1.2	± -1.4	± 0.0	± 0.5
ESF	-3.4, 3.5	-2.4, 2.5	-2.5, 2.6	-2.6, 2.6	-2.9, 3.0	0.1, -0.1	-0.8, 0.8
Generator	± 3.8	± 0.0	± 13.6	± 0.0	± 0.0	± -0.1	± 0.7
PDF	3.5, 2.8	0.0, 0.0	2.6, 2.0	0.0, 0.0	0.0, 0.0	-0.1, -0.0	-0.4, 0.3
Pileup	-0.8, 0.6	-0.2, -0.4	-1.0, 0.8	-0.4, -0.6	1.4, -1.0	0.0, -0.0	-0.0, -0.0
Pileup	3.5, -0.8	3.3, -0.2	3.6, -1.0	3.4, -0.4	3.6, 1.4	-0.1, 0.0	0.9, -0.0
TauID SF	-3.5, 3.5	-3.3, 3.3	-3.6, 3.6	-3.4, 3.4	-3.6, 3.6	0.1, -0.1	-0.9, 0.9
Cross-section	-4.8, 4.8	-50.0, 50.0	-30.0, 30.0	-44.4, 44.4	-80.9, 80.9	0.6, -0.6	-7.2, 7.2
TES	0.0, 0.0	-1.7, -1.7	0.0, 0.0	-0.9, -0.9	-0.1, -0.1	-0.5, -0.5	-0.4, -0.4
TEVSF	0.0, 0.0	0.0, 0.0	0.0, 0.0	0.0, 0.0	0.0, 0.0	0.0, 0.0	0.0, 0.0
Scale ST	-5.2, 3.2	0.0, -3.3	0.0, 0.0	-4.1, 0.9	-1.3, 0.5	0.0, -0.1	-0.8, 0.3
Reso ST	± 1.0	± 0.0	± -2.7	± -1.7	± 0.0	± 0.0	± -0.0
Trigger	-5.0, 5.0	-5.0, 5.0	-5.0, 5.0	-5.0, 5.0	-5.0, 5.0	-5.0, 5.0	-5.0, 5.0
Lumi	± 2.8	± 2.8	± 2.8	± 2.8	± 2.8	± 2.8	± 2.8
e afr (WM)	0.0, 0.0	0.0, 0.0	0.0, 0.0	0.0, 0.0	0.0, 0.0	-0.7, 0.9	-0.5, 0.6
mu afr (WM)	0.0, 0.0	0.0, 0.0	0.0, 0.0	0.0, 0.0	0.0, 0.0	-5.4, 6.1	-3.9, 4.3
tau afr (WM)	0.0, 0.0	0.0, 0.0	0.0, 0.0	0.0, 0.0	0.0, 0.0	-16.7, 24.1	-12.0, 17.2
5l (WM)	0.0, 0.0	0.0, 0.0	0.0, 0.0	0.0, 0.0	0.0, 0.0	0.0, 5.0	0.0, 3.6
closure (WM)	0.0, 0.0	0.0, 0.0	0.0, 0.0	0.0, 0.0	0.0, 0.0	-22.0, 22.0	-15.7, 15.7

Table C.5: Summary of systematic uncertainties in the signal region SR1noZb for each of the irreducible background processes, the reducible processes and the total estimated background. Where two numbers are listed, the first gives the “down” systematic uncertainty and the second gives the “up” systematic uncertainty. All uncertainties are presented as a percentage, and the number of events estimated for each background process in this region is also displayed.

Systematic	ZZ	$t\bar{t} + V$	$t\bar{t} + Z$	VVV	Higgs	Reducible	Σ SM
Expected Events	0.22	0.05	0.17	0.09	0.3	2.1	2.9
Stat	± 10.8	± 13.4	± 19.4	± 12.0	± 11.5	± 20.2	± 14.6
JES	1.4, 1.9	-0.1, 0.0	0.0, 0.0	-0.6, 0.3	1.7, 0.1	-0.0, 0.0	0.2, 0.2
JER	± 2.3	± -3.2	± 0.0	± 7.2	± 3.9	± -0.0	± 0.7
ESF	-2.9, 3.0	-2.4, 2.5	-2.8, 2.9	-2.6, 2.6	-2.8, 2.8	0.0, -0.0	-0.8, 0.8
Generator	± 7.1	± 0.0	± 21.2	± 0.0	± 0.0	± -0.1	± 1.3
PDF	4.1, 3.7	0.0, 0.0	2.2, 1.5	0.0, 0.0	0.0, 0.0	-0.0, -0.0	-0.3, 0.3
Pileup	-0.6, 0.4	-1.3, 0.6	0.2, -0.3	-1.2, 0.3	1.7, -1.1	0.0, 0.0	0.1, -0.1
Pileup	3.4, -0.6	3.5, -1.3	3.5, 0.2	3.6, -1.2	3.6, 1.7	-0.1, 0.0	0.9, 0.1
TauID SF	-3.4, 3.4	-3.5, 3.5	-3.5, 3.5	-3.6, 3.6	-3.6, 3.6	0.1, -0.1	-0.9, 0.9
Cross-section	-4.7, 4.7	-50.0, 50.0	-30.0, 30.0	-41.1, 41.1	-87.7, 87.7	0.8, -0.8	-9.2, 9.2
TES	0.0, 0.0	-1.8, -1.8	0.0, 0.0	-2.8, -2.8	0.0, 0.0	-0.5, -0.5	-0.5, -0.5
TEVSF	0.0, 0.0	0.0, 0.0	0.0, 0.0	0.0, 0.0	0.0, 0.0	0.0, 0.0	0.0, 0.0
Scale ST	-1.3, 2.5	0.0, -1.7	0.0, 0.0	0.0, 1.4	-1.6, 0.4	0.0, -0.0	-0.2, 0.2
Reso ST	± 0.9	± 0.0	± 0.0	± -0.0	± -4.8	± 0.0	± -0.4
Trigger	-5.0, 5.0	-5.0, 5.0	-5.0, 5.0	-5.0, 5.0	-5.0, 5.0	-5.0, 5.0	-5.0, 5.0
Lumi	± 2.8	± 2.8	± 2.8	± 2.8	± 2.8	± 2.8	± 2.8
e afr (WM)	0.0, 0.0	0.0, 0.0	0.0, 0.0	0.0, 0.0	0.0, 0.0	0.4, -0.5	0.3, -0.4
mu afr (WM)	0.0, 0.0	0.0, 0.0	0.0, 0.0	0.0, 0.0	0.0, 0.0	-7.5, 9.2	-5.4, 6.6
tau afr (WM)	0.0, 0.0	0.0, 0.0	0.0, 0.0	0.0, 0.0	0.0, 0.0	-19.1, 23.4	-13.7, 16.8
5l (WM)	0.0, 0.0	0.0, 0.0	0.0, 0.0	0.0, 0.0	0.0, 0.0	0.0, 5.0	0.0, 3.6
closure (WM)	0.0, 0.0	0.0, 0.0	0.0, 0.0	0.0, 0.0	0.0, 0.0	-31.0, 31.0	-22.3, 22.3

Table C.6: Summary of systematic uncertainties in the signal region SR1Z for each of the irreducible background processes, the reducible processes and the total estimated background. Where two numbers are listed, the first gives the “down” systematic uncertainty and the second gives the “up” systematic uncertainty. All uncertainties are presented as a percentage, and the number of events estimated for each background process in this region is also displayed.

Systematic	ZZ	$t\bar{t} + V$	$t\bar{t} + Z$	VVV	Higgs	Reducible	Σ SM
Expected Events	0.6	0.04	0.4	0.22	0.14	1.1	2.5
Stat	± 6.7	± 14.7	± 20.5	± 7.8	± 17.0	± 26.9	± 12.1
JES	2.8, -0.6	6.3, 0.0	9.0, 0.5	-0.3, -0.7	-1.2, -2.0	-0.4, 0.2	2.0, -0.2
JER	± 3.0	± 2.2	± -12.0	± -1.8	± -7.0	± 0.1	± -1.8
ESF	-2.7, 2.8	-2.1, 2.2	-2.3, 2.4	-2.2, 2.3	-2.4, 2.5	0.3, -0.3	-1.3, 1.3
Generator	± 12.9	± 0.0	± 17.7	± 0.0	± 0.0	± -1.2	± 4.3
PDF	4.0, 4.1	0.0, 0.0	2.6, 2.0	0.0, 0.0	0.0, 0.0	-0.3, -0.3	-1.1, 1.1
Pileup	-0.2, 0.2	1.8, -2.2	2.2, -1.8	0.7, -0.7	-0.5, 0.9	-0.1, 0.1	0.3, -0.3
Pileup	3.5, -0.2	3.6, 1.8	3.4, 2.2	3.5, 0.7	3.6, -0.5	-0.4, -0.1	1.8, 0.3
TauID SF	-3.5, 3.5	-3.6, 3.6	-3.4, 3.4	-3.5, 3.5	-3.6, 3.6	0.4, -0.4	-1.8, 1.8
Cross-section	-4.5, 4.5	-50.0, 50.0	-30.0, 30.0	-45.8, 45.8	-26.1, 26.1	1.8, -1.8	-6.9, 6.9
TES	0.0, 0.0	-2.1, -2.1	0.0, 0.0	0.0, 0.0	-0.5, -0.5	-1.6, -1.6	-0.7, -0.7
TEVSF	0.0, 0.0	0.0, 0.0	0.0, 0.0	0.0, 0.0	0.0, 0.0	0.0, 0.0	0.0, 0.0
Scale ST	-3.7, 2.9	0.0, 2.2	-1.2, -11.1	-1.8, 1.0	-1.2, 1.4	0.1, -0.3	-1.3, -1.1
Reso ST	± -0.6	± 0.0	± -14.6	± -0.3	± -0.4	± -0.0	± -2.7
Trigger	-5.0, 5.0	-5.0, 5.0	-5.0, 5.0	-5.0, 5.0	-5.0, 5.0	-5.0, 5.0	-5.0, 5.0
Lumi	± 2.8	± 2.8	± 2.8	± 2.8	± 2.8	± 2.8	± 2.8
e afr (WM)	0.0, 0.0	0.0, 0.0	0.0, 0.0	0.0, 0.0	0.0, 0.0	-12.5, 12.5	-5.3, 5.3
mu afr (WM)	0.0, 0.0	0.0, 0.0	0.0, 0.0	0.0, 0.0	0.0, 0.0	2.5, -8.8	1.1, -3.7
tau afr (WM)	0.0, 0.0	0.0, 0.0	0.0, 0.0	0.0, 0.0	0.0, 0.0	-28.6, 30.2	-12.2, 12.9
5l (WM)	0.0, 0.0	0.0, 0.0	0.0, 0.0	0.0, 0.0	0.0, 0.0	0.0, 5.0	0.0, 2.1
closure (WM)	0.0, 0.0	0.0, 0.0	0.0, 0.0	0.0, 0.0	0.0, 0.0	-17.0, 17.0	-7.2, 7.2

Table C.7: Summary of systematic uncertainties in the signal region SR2noZa for each of the irreducible background processes, the reducible processes and the total estimated background. Where two numbers are listed, the first gives the “down” systematic uncertainty and the second gives the “up” systematic uncertainty. All uncertainties are presented as a percentage, and the number of events estimated for each background process in this region is also displayed.

Systematic	ZZ	$t\bar{t} + V$	$t\bar{t} + Z$	VVV	Higgs	Reducible	Σ SM
Expected Events	0.15	0.023	0.13	0.05	0.2	3.4	4
Stat	± 11.9	± 20.0	± 51.8	± 16.1	± 12.0	± 13.4	± 11.7
JES	1.7, -0.5	0.0, 0.0	-7.4, 4.7	4.3, 1.3	-2.2, 1.7	-0.0, 0.0	-0.2, 0.2
JER	± 13.1	± 0.6	± 8.7	± 5.9	± 2.2	± -0.0	± 0.9
ESF	-1.3, 1.3	-0.8, 0.8	-4.0, 4.0	-1.3, 1.3	-1.8, 1.9	0.0, -0.0	-0.3, 0.3
Generator	± 17.3	± 0.0	± 42.9	± 0.0	± 0.0	± -0.0	± 1.5
PDF	3.5, 3.2	0.0, 0.0	8.4, 7.4	0.0, 0.0	0.0, 0.0	-0.0, -0.0	-0.3, 0.3
Pileup	-1.2, 0.8	3.8, -4.1	0.5, -1.9	-0.9, 1.1	-2.5, 2.9	0.0, -0.0	-0.1, 0.1
Pileup	7.3, -1.2	7.4, 3.8	6.1, 0.5	7.3, -0.9	7.1, -2.5	-0.0, 0.0	0.9, -0.1
TauID SF	-7.0, 7.3	-7.1, 7.4	-5.9, 6.1	-7.1, 7.3	-6.9, 7.1	0.0, -0.0	-0.9, 0.9
Cross-section	-4.8, 4.8	-50.0, 50.0	-30.0, 30.0	-42.9, 42.9	-82.8, 82.8	0.2, -0.2	-4.2, 4.2
TES	-0.6, -0.6	0.0, 0.0	0.0, 0.0	-3.5, -3.5	-2.9, -2.9	0.1, 0.1	-0.1, -0.1
TEVSF	0.0, 0.0	0.0, 0.0	0.0, 0.0	0.0, 0.0	0.0, 0.0	0.0, 0.0	0.0, 0.0
Scale ST	-4.5, 4.2	0.0, 0.0	6.8, -2.8	1.3, 2.8	-1.6, -1.2	0.0, -0.0	0.0, 0.0
Reso ST	± 3.1	± 0.0	± 11.4	± 3.5	± -2.0	± -0.0	± 0.4
Trigger	-5.0, 5.0	-5.0, 5.0	-5.0, 5.0	-5.0, 5.0	-5.0, 5.0	-5.0, 5.0	-5.0, 5.0
Lumi	± 2.8	± 2.8	± 2.8	± 2.8	± 2.8	± 2.8	± 2.8
e afr (WM)	0.0, 0.0	0.0, 0.0	0.0, 0.0	0.0, 0.0	0.0, 0.0	0.0, 0.0	0.0, 0.0
mu afr (WM)	0.0, 0.0	0.0, 0.0	0.0, 0.0	0.0, 0.0	0.0, 0.0	0.0, 0.0	0.0, 0.0
tau afr (WM)	0.0, 0.0	0.0, 0.0	0.0, 0.0	0.0, 0.0	0.0, 0.0	-13.4, 1.1	-11.5, 1.0
5l (WM)	0.0, 0.0	0.0, 0.0	0.0, 0.0	0.0, 0.0	0.0, 0.0	0.0, 5.0	0.0, 4.3
closure (WM)	0.0, 0.0	0.0, 0.0	0.0, 0.0	0.0, 0.0	0.0, 0.0	-30.0, 30.0	-25.9, 25.9

Table C.8: Summary of systematics in the signal region SR2noZb for each of the irreducible background processes, the irreducible processes and the total estimated background. Where two numbers are listed, the first gives the “down” systematic uncertainty and the second gives the “up” systematic uncertainty. All uncertainties are presented as a percentage, and the number of events estimated for each background process in this region is also displayed.

Systematic	ZZ	$t\bar{t} + V$	$t\bar{t} + Z$	VVV	Higgs	Reducible	Σ SM
Expected Events	0.11	0.016	0.27	0.04	0.13	2.5	3
Stat	± 14.2	± 23.6	± 49.2	± 17.4	± 14.4	± 14.3	± 12.4
JES	2.7, 0.1	0.0, 0.0	0.0, 0.0	-0.1, 5.3	-0.5, 0.5	-0.0, -0.0	0.1, 0.1
JER	± 10.8	± 0.8	± -2.9	± 2.7	± 3.6	± 0.0	± 0.3
ESF	-1.3, 1.4	-0.8, 0.8	-4.6, 4.6	-1.4, 1.4	-1.5, 1.5	0.0, -0.0	-0.5, 0.5
Generator	± 5.2	± 0.0	± 87.9	± 0.0	± 0.0	± -0.0	± 7.8
PDF	3.8, 3.8	0.0, 0.0	7.9, 6.9	0.0, 0.0	0.0, 0.0	-0.0, -0.0	-0.7, 0.6
Pileup	0.3, -0.2	2.5, -2.8	1.5, -1.0	-2.2, 2.8	-2.3, 3.0	-0.0, 0.0	0.0, 0.1
Pileup	7.2, 0.3	7.3, 2.5	7.3, 1.5	7.3, -2.2	7.1, -2.3	-0.0, -0.0	1.3, 0.0
TauID SF	-7.0, 7.2	-7.0, 7.3	-7.0, 7.3	-7.1, 7.3	-6.9, 7.1	0.0, -0.0	-1.3, 1.3
Cross-section	-4.8, 4.8	-50.0, 50.0	-30.0, 30.0	-39.2, 39.2	-89.0, 89.0	0.2, -0.2	-4.7, 4.7
TES	0.0, 0.0	0.0, 0.0	0.0, 0.0	-4.5, -4.5	-4.7, -4.7	0.1, 0.1	-0.2, -0.2
TEVSF	0.0, 0.0	0.0, 0.0	0.0, 0.0	0.0, 0.0	0.0, 0.0	0.0, 0.0	0.0, 0.0
Scale ST	-2.6, 2.5	0.0, 0.0	0.0, 0.0	0.0, -0.0	-0.1, 0.3	0.0, -0.0	-0.1, 0.1
Reso ST	± 2.4	± 0.0	± 0.0	± 4.7	± -0.3	± -0.0	± 0.1
Trigger	-5.0, 5.0	-5.0, 5.0	-5.0, 5.0	-5.0, 5.0	-5.0, 5.0	-5.0, 5.0	-5.0, 5.0
Lumi	± 2.8	± 2.8	± 2.8	± 2.8	± 2.8	± 2.8	± 2.8
e afr (WM)	0.0, 0.0	0.0, 0.0	0.0, 0.0	0.0, 0.0	0.0, 0.0	0.0, 0.0	0.0, 0.0
mu afr (WM)	0.0, 0.0	0.0, 0.0	0.0, 0.0	0.0, 0.0	0.0, 0.0	0.0, 0.0	0.0, 0.0
tau afr (WM)	0.0, 0.0	0.0, 0.0	0.0, 0.0	0.0, 0.0	0.0, 0.0	-17.5, 8.3	-14.2, 6.7
5l (WM)	0.0, 0.0	0.0, 0.0	0.0, 0.0	0.0, 0.0	0.0, 0.0	0.0, 5.0	0.0, 4.1
closure (WM)	0.0, 0.0	0.0, 0.0	0.0, 0.0	0.0, 0.0	0.0, 0.0	-33.0, 33.0	-26.8, 26.8

Table C.9: Summary of systematic uncertainties in the signal region SR2Z for each of the irreducible background processes, the reducible processes and the total estimated background. Where two numbers are listed, the first gives the “down” systematic uncertainty and the second gives the “up” systematic uncertainty. All uncertainties are presented as a percentage, and the number of events estimated for each background process in this region is also displayed.

Systematic	ZZ	$t\bar{t} + V$	$t\bar{t} + Z$	VVV	Higgs	Reducible	Σ SM
Expected Events	0.7	0.0018	0.035	0.04	0.14	0.9	1.8
Stat	± 6.1	± 70.8	± 42.6	± 17.6	± 8.3	± 33.8	± 17.1
JES	5.5, -4.2	0.0, 0.0	0.0, 0.0	3.3, 6.4	4.0, -5.5	-0.2, 0.2	2.4, -1.8
JER	± 2.9	± 0.0	± 5.7	± 1.1	± 3.6	± -0.1	± 1.5
ESF	-1.3, 1.3	0.0, 0.0	-1.9, 2.0	-1.5, 1.5	-1.4, 1.5	0.0, -0.0	-0.7, 0.7
Generator	± 7.4	± 0.0	± 42.9	± 0.0	± 0.0	± -0.2	± 3.0
PDF	4.4, 3.7	0.0, 0.0	3.3, 1.8	0.0, 0.0	0.0, 0.0	-0.1, -0.1	-1.7, 1.4
Pileup	-1.0, 1.0	0.7, -1.5	-1.9, 1.6	-0.7, 0.8	-0.5, 0.6	0.0, -0.0	-0.5, 0.4
Pileup	7.1, -1.0	7.3, 0.7	7.7, -1.9	7.4, -0.7	6.9, -0.5	-0.2, 0.0	3.5, -0.5
TauID SF	-6.9, 7.1	-7.0, 7.3	-7.5, 7.7	-7.1, 7.4	-6.7, 6.9	0.2, -0.2	-3.3, 3.5
Cross-section	-4.6, 4.6	-50.0, 50.0	-30.0, 30.0	-30.5, 30.5	-29.4, 29.4	0.2, -0.2	-3.0, 3.0
TES	-0.3, -0.3	0.0, 0.0	0.0, 0.0	0.0, 0.0	-0.6, -0.6	1.0, 1.0	0.3, 0.3
TEVSF	0.0, 0.0	0.0, 0.0	0.0, 0.0	0.0, 0.0	0.0, 0.0	0.0, 0.0	0.0, 0.0
Scale ST	-5.3, 4.0	0.0, 0.0	0.0, 0.0	-0.0, 0.3	-4.0, 3.0	0.2, -0.2	-2.2, 1.7
Reso ST	± 0.1	± 0.0	± 0.0	± 0.0	± -0.9	± 0.1	± 0.0
Trigger	-5.0, 5.0	-5.0, 5.0	-5.0, 5.0	-5.0, 5.0	-5.0, 5.0	-5.0, 5.0	-5.0, 5.0
Lumi	± 2.8	± 2.8	± 2.8	± 2.8	± 2.8	± 2.8	± 2.8
e afr (WM)	0.0, 0.0	0.0, 0.0	0.0, 0.0	0.0, 0.0	0.0, 0.0	0.0, 0.0	0.0, 0.0
mu afr (WM)	0.0, 0.0	0.0, 0.0	0.0, 0.0	0.0, 0.0	0.0, 0.0	0.0, 0.0	0.0, 0.0
tau afr (WM)	0.0, 0.0	0.0, 0.0	0.0, 0.0	0.0, 0.0	0.0, 0.0	-11.3, -8.6	-5.6, -4.3
5l (WM)	0.0, 0.0	0.0, 0.0	0.0, 0.0	0.0, 0.0	0.0, 0.0	0.0, 5.0	0.0, 2.5
closure (WM)	0.0, 0.0	0.0, 0.0	0.0, 0.0	0.0, 0.0	0.0, 0.0	-37.0, 37.0	-18.5, 18.5

Bibliography

- [1] ATLAS Collaboration, *Search for supersymmetry in events with four or more leptons in $s = 8$ TeV pp collisions with the ATLAS detector*, *Phys. Rev. D* (2014). [1](#), [59](#), [120](#), [126](#), [128](#), [130](#), [135](#), [139](#), [140](#), [141](#), [162](#)
- [2] W. N. Cottingham and D. A. Greenwood, *An introduction to the standard model of particle physics*. Cambridge, 1998. [2](#), [6](#)
- [3] M. E. Peskin and D. V. Schroeder, *An Introduction To Quantum Field Theory*. Westview Press, 1995. [2](#), [6](#)
- [4] ATLAS Collaboration, *Observation of a new particle in the search for the Standard Model Higgs boson with the ATLAS detector at the LHC*, *Phys.Lett.* **B716** (2012) [1–29](#), [arXiv:1207.7214 \[hep-ex\]](#). [2](#), [5](#), [19](#)
- [5] CMS Collaboration, *Observation of a new boson at a mass of 125 GeV with the CMS experiment at the LHC*, *Phys.Lett.* **B716** (2012) [30–61](#), [arXiv:1207.7235 \[hep-ex\]](#). [2](#), [5](#), [19](#)
- [6] S. P. Martin, *A Supersymmetry Primer*, [arXiv:9709356](#). [http://arxiv.org/abs/hep-ph/9709356](#). [3](#), [13](#), [17](#)
- [7] K. A. Olive et al., *Review of Particle Physics*, *Chin. Phys.* **38** no. 090001, (2014). [4](#), [5](#), [10](#), [17](#), [51](#), [93](#)
- [8] C. Rovelli, *Notes for a brief history of quantum gravity*, [arXiv:gr-qc/0006061](#). [4](#)
- [9] P. A. M. Dirac, *The Quantum Theory of the Electron*, *Proc. RS A: Math., Phys. and Eng.* **117** no. 778, (1928) [610–624](#). [5](#)
- [10] E. Majorana, *Teoria simmetrica dellelettrone e del positrone*, *Il Nuovo Cimento* **14** no. 4, (1937) [171–184](#). [5](#)
- [11] J. Beringer et al., *Review of Particle Physics**, *Phys. Rev. D* **86** (2012) [010001](#). [6](#)

- [12] J. Schwinger, *Quantum Electrodynamics. I. A Covariant Formulation*, [Phys. Rev. **74** \(1948\) 1439–1461](#). 6
- [13] R. P. Feynman, *Space-Time Approach to Quantum Electrodynamics*, [Phys. Rev. **76** \(1949\) 769–789](#). 6
- [14] S. Tomonaga, *On a Relativistically Invariant Formulation of the Quantum Theory of Wave Fields*, [Progress of Theoretical Physics **1** no. 2, \(1946\) 27–42](#). 6
- [15] K. J. Barnes, *Group Theory For The Standard Model Of Particle Physics And Beyond*. Taylor and Francis, 2010. 6
- [16] I. Aitchinson and A. Hey, *Gauge Theories in Particle Physics*. Bristol : Hilger, 1982. 7
- [17] F. Englert and R. Brout, *Broken Symmetry and the Mass of Gauge Vector Mesons*, [Phys. Rev. Lett. **13** \(1964\) 321–323](#). 7
- [18] P. W. Higgs, *Broken Symmetries and the Masses of Gauge Bosons*, [Phys. Rev. Lett. **13** \(1964\) 508–509](#). 7
- [19] T. W. B. Kibble, *Symmetry Breaking in Non-Abelian Gauge Theories*, [Phys. Rev. **155** \(1967\) 1554–1561](#). 7
- [20] S. L. Glashow, *Partial-symmetries of weak interactions*, [Nuclear Physics **22** no. 4, \(1961\) 579 – 588](#). 7
- [21] A. Salam, *Weak and Electromagnetic Interactions*, [Conf.Proc. **C680519** \(1968\) 367–377](#). 7
- [22] S. Weinberg, *A Model of Leptons*, [Phys. Rev. Lett. **19** \(1967\) 1264–1266](#). 7
- [23] T. Nakano and K. Nishijima, *Charge Independence for V-particles*, [Progress of Theoretical Physics **10** no. 5, \(1953\) 581–582](#). 7
- [24] M. Gell-Mann, *The interpretation of the new particles as displaced charge multiplets*, [Il Nuovo Cimento **4** no. 2, \(1956\) 848–866](#). 7
- [25] L. Ivarez Gaum and J. Ellis, *Eyes on a prize particle*, [Nature Phys. **7** \(2011\) 2–3](#). 8
- [26] M. Gonzalez-Garcia and M. Maltoni, *Phenomenology with Massive Neutrinos*, [Phys.Rept. **460** \(2008\) 1–129, arXiv:0704.1800 \[hep-ph\]](#). 10

- [27] V. C. Rubin and W. K. Ford, Jr., *Rotation of the Andromeda Nebula from a Spectroscopic Survey of Emission Regions*, *apj* **159** (1970) 379. 11
- [28] M. Markevitch et al., *Direct Constraints on the Dark Matter Self-Interaction Cross Section from the Merging Galaxy Cluster 1E 065756*, *The Astrophysical Journal* **606** no. 2, (2004) 819. <http://stacks.iop.org/0004-637X/606/i=2/a=819>. 11
- [29] L. Canetti, M. Drewes, and M. Shaposhnikov, *Matter and antimatter in the universe*, *New J. Phys.* **14** (2012). 11
- [30] A. H. Chamseddine, R. Arnowitt, and P. Nath, *Locally Supersymmetric Grand Unification*, *Phys. Rev. Lett.* **49** (1982) 970–974. 15
- [31] J. Ellis, D. Nanopoulos, and K. Tamvakis, *Grand unification in simple supergravity*, *Physics Letters B* **121** no. 23, (1983) 123 – 129. 15
- [32] M. Dine and A. E. Nelson, *Dynamical supersymmetry breaking at low-energies*, *Phys.Rev.* **D48** (1993) 1277–1287, [arXiv:hep-ph/9303230](https://arxiv.org/abs/hep-ph/9303230). 15
- [33] M. Dine, A. E. Nelson, and Y. Shirman, *Low-energy dynamical supersymmetry breaking simplified*, *Phys.Rev.* **D51** (1995) 1362–1370, [arXiv:hep-ph/9408384](https://arxiv.org/abs/hep-ph/9408384). 15
- [34] M. Dine, A. E. Nelson, Y. Nir, and Y. Shirman, *New tools for low-energy dynamical supersymmetry breaking*, *Phys.Rev.* **D53** (1996) 2658–2669, [arXiv:hep-ph/9507378](https://arxiv.org/abs/hep-ph/9507378). 15
- [35] L. Randall and R. Sundrum, *A Large mass hierarchy from a small extra dimension*, *Phys.Rev.Lett.* **83** (1999) 3370–3373, [arXiv:hep-ph/9905221](https://arxiv.org/abs/hep-ph/9905221). 15
- [36] L. Randall and R. Sundrum, *Out of this world supersymmetry breaking*, *Nucl.Phys.* **B557** (1999) 79–118, [arXiv:hep-th/9810155](https://arxiv.org/abs/hep-th/9810155). 15
- [37] G. F. Giudice, M. A. Luty, H. Murayama, and R. Rattazzi, *Gaugino mass without singlets*, *JHEP* **9812** (1998) 027, [arXiv:hep-ph/9810442](https://arxiv.org/abs/hep-ph/9810442). 15
- [38] J. Ellis, J. Hagelin, D. Nanopoulos, K. Olive, and M. Srednicki, *Supersymmetric relics from the big bang*, *Nuclear Physics B* **238** no. 2, (1984) 453 – 476. 18
- [39] J. Alwall, P. C. Schuster, and N. Toro, *Simplified models for a first characterization of new physics at the LHC*, *Phys. Rev. D* **79** (2009) 075020. <http://link.aps.org/doi/10.1103/PhysRevD.79.075020>. 18

- [40] D. Alves et al., *Simplified models for LHC new physics searches*, Journal of Physics G: Nuclear and Particle Physics **39** no. 10, (2012) 105005.
<http://stacks.iop.org/0954-3899/39/i=10/a=105005>. 18
- [41] D. Larson, J. Dunkley, G. Hinshaw, E. Komatsu, M. Nolta, et al., *Seven-Year Wilkinson Microwave Anisotropy Probe (WMAP) Observations: Power Spectra and WMAP-Derived Parameters*, *Astrophys.J.Suppl.* **192** (2011) 16,
[arXiv:1001.4635](https://arxiv.org/abs/1001.4635) [[astro-ph.CO](#)]. 19
- [42] Planck Collaboration, P. Ade et al., *Planck 2013 results. XVI. Cosmological parameters*, *Astron.Astrophys.* **571** (2014) A16, [arXiv:1303.5076](https://arxiv.org/abs/1303.5076) [[astro-ph.CO](#)]. 19
- [43] CMS Collaboration, S. Chatrchyan et al., *Measurement of the $B(s)$ to $\mu^+ \mu^-$ branching fraction and search for B^0 to $\mu^+ \mu^-$ with the CMS Experiment*, *Phys.Rev.Lett.* **111** (2013) 101804, [arXiv:1307.5025](https://arxiv.org/abs/1307.5025) [[hep-ex](#)]. 19
- [44] LHCb Collaboration, R. Aaij et al., *Measurement of the $B_s^0 \rightarrow \mu^+ \mu^-$ branching fraction and search for $B^0 \rightarrow \mu^+ \mu^-$ decays at the LHCb experiment*, *Phys.Rev.Lett.* **111** (2013) 101805, [arXiv:1307.5024](https://arxiv.org/abs/1307.5024) [[hep-ex](#)]. 19
- [45] *LEP design report*, Tech. Rep. CERN-LEP-84-01 (1984).
<http://cds.cern.ch/record/102083?ln=en>. 19, 21
- [46] R. R. Wilson, *The Tevatron*, *Phys.Today* **30N10** (1977) 23–30. 19
- [47] G. L. Kane, C. F. Kolda, L. Roszkowski, and J. D. Wells, *Study of constrained minimal supersymmetry*, *Phys.Rev.* **D49** (1994) 6173–6210,
[arXiv:hep-ph/9312272](https://arxiv.org/abs/hep-ph/9312272) [[hep-ph](#)]. 19
- [48] “Atlas 2011 supersymmetry summary plot.”. 19
- [49] “Cms 2011 supersymmetry summary plot.”. 19
- [50] “Atlas 2012 supersymmetry summary plot.”
https://atlas.web.cern.ch/Atlas/GROUPS/PHYSICS/CombinedSummaryPlots/SUSY/ATLAS_SUSY_Summary/ATLAS_SUSY_Summary.png. 20
- [51] “Cms 2012 supersymmetry summary plot.”. 20
- [52] L. Evans and P. Bryant, *LHC machine*, *Journal of Instrumentation* **08001** no. 3, (2008). 21

- [53] P. Lebrun, S. Myers, O. Brüning, and R. Ostojic, *LHC Design Report*, CERN-2004-003-V-1 (2004). <http://cds.cern.ch/record/782076>. 21
- [54] C. Lefèvre, *The CERN accelerator complex*, Dec., 2008. <http://cds.cern.ch/record/1260465?ln=en>. 22
- [55] ATLAS Collaboration, *The ATLAS experiment at the CERN large hadron collider*, Journal of Instrumentation **08003** (2008). <http://iopscience.iop.org/1748-0221/3/08/S08003>. 21, 25, 27, 29, 31, 32, 34
- [56] CMS Collaboration, *The CMS experiment at the CERN LHC - 2008_JINST_3_S08004.pdf*, 2008. http://jinst.sissa.it/LHC/CMS/2008_JINST_3_S08004.pdf. 21
- [57] LHCb Collaboration, *The LHCb Detector at the LHC - 2008_JINST_3_S08005.pdf*, 2008. http://jinst.sissa.it/LHC/LHCb/2008_JINST_3_S08005.pdf. 21, 39
- [58] ALICE Collaboration, *The ALICE experiment at the CERN LHC - 2008_JINST_3_S08002.pdf*, 2008. http://jinst.sissa.it/LHC/ALICE/2008_JINST_3_S08002.pdf. 21
- [59] ATLAS Collaboration, *ATLAS public luminosity plots*, 2013. https://twiki.cern.ch/twiki/bin/view/AtlasPublic/LuminosityPublicResults#Multiple_Year_Collision_Plots. 24
- [60] ATLAS Collaboration, *Luminosity determination in pp collisions at $\sqrt{s} = 7$ TeV using the ATLAS detector at the LHC*, The European Physical Journal C **71** no. 4, (2011) 1630, 1101.2185. 23
- [61] G. Hallewel and N. Wermes, *ATLAS pixel detector*,. <https://cds.cern.ch/record/381263?ln=en>. 27
- [62] M. Capeans et al., *ATLAS Insertable B-Layer Technical Design Report*, CERN-LHCC-2010-013 (2010). <http://cds.cern.ch/record/1291633?ln=en>. 27
- [63] ATLAS Collaboration, *Performance of the ATLAS Trigger System in 2010*, The European Physical Journal C **72** no. 1, (2012) 1849, arXiv:1110.1530. 36
- [64] R. Frhwirth, *Application of Kalman filtering to track and vertex fitting*, Nucl. Instr. Meth. **262** (1987) 444–450. 37

- [65] ATLAS Collaboration, *ATLAS computing technical design report*, ATLAS-TDR-017 (2010). [http://link.springer.com/article/10.1140/\\$%2Fepjc/\\$%2Fs10052-010-1429-9](http://link.springer.com/article/10.1140/$%2Fepjc/$%2Fs10052-010-1429-9). 39
- [66] G. Barrand et al., *GAUDI A software architecture and framework for building HEP data processing applications*, *Comput. Phys. Commun.* **140** (2001) 45–55. 39
- [67] W. Lukas, *Fast Simulation for ATLAS: Atlfast-II and ISF*, *J. Phys.: Conf. Ser.* **396** no. 022031, (2012). 40, 45
- [68] A. Buckley et al., *General-purpose event generators for LHC physics*, *Physics Reports* **504** (2011) 145–233. 42
- [69] J. M. Campbell, J. Huston, and W. Stirling, *Hard Interactions of Quarks and Gluons: A Primer for LHC Physics*, *Rept.Prog.Phys.* **70** (2007) 89, [arXiv:hep-ph/0611148](https://arxiv.org/abs/hep-ph/0611148) [[hep-ph](#)]. 42
- [70] M. Dobbs and J. B. Hansen, *The HepMC C++ Monte Carlo event record for High Energy Physics*, *Comput.Phys.Commun.* **134** (2001) 41–46. 42
- [71] V. Gribov and L. Lipatov, *Deep inelastic e p scattering in perturbation theory*, *Sov. J. Nucl. Phys.* **15** (1972) 438–450. 42
- [72] G. Altarelli and G. Parisi, *Asymptotic freedom in parton language*, *Nucl. Phys. B* **126** no. 2, (1977) 298–318. 42
- [73] H1 and ZEUS Collaborations, *Combined Measurement and QCD Analysis of the Inclusive ep Scattering Cross Sections at HERA*, *JHEP* **109** (2010). 43, 108
- [74] B. Everitt, *The Cambridge dictionary of statistics*. Cambridge University Press, 2002. 44
- [75] T. Gleisberg et al., *Event generation with SHERPA 1.1*, *JHEP* **0902** no. 007, (2009). 44, 69
- [76] G. Corcella et al., *HERWIG 6.5: an event generator for Hadron Emission Reactions With Interfering Gluons (including supersymmetric processes)*, *JHEP* **0101** no. 010, (2001). 44, 69
- [77] T. Sjostrand et al., *PYTHIA 6.4 Physics and Manual*, *JHEP* **0605** no. 026, (2006). 44, 65, 69, 164

- [78] R. D. Field, *The Underlying Event in Hard Scattering Processes*,
<http://arxiv.org/abs/hep-ph/0201192>. 44
- [79] J. Butterworth et al., *Multiparton Interactions in Photoproduction at HERA*, *Z. Phys.* **C72** (1996) 637–646. 44
- [80] GEANT4 Collaboration, *Geant4a simulation toolkit*, *Nucl. Instrum. Meth. A* **506** (2003) 250–303. 44
- [81] Lampl, W. and others, *Calorimeter Clustering Algorithms: Description and Performance*, ATL-LARG-PUB-2008-002 (2008).
<https://cdsweb.cern.ch/record/1099735>. 48
- [82] ATLAS Collaboration, *Electron efficiency measurements with the ATLAS detector using the 2012 LHC proton-proton collision data*, ATLAS-CONF-2014-032 (2014).
<http://cds.cern.ch/record/1706245>. 48, 49
- [83] ATLAS Collaboration, *Expected electron performance in the ATLAS experiment*,
<http://cds.cern.ch/record/1345327/files/ATL-PHYS-PUB-2011-006.pdf>. 48, 49, 56
- [84] R. Nicolaidou, L. Chevalier, S. Hassani, J. F. Laporte, E. L. Menedeu, and A. Ouraou, *Muon identification procedure for the ATLAS detector at the LHC using Muonboy reconstruction package and tests of its performance using cosmic rays and single beam data*, *J. Phys.: Conf. Ser* **219** (2010). 49
- [85] ATLAS Collaboration, *Measurement of the muon reconstruction performance of the ATLAS detector using 2011 and 2012 LHC protonproton collision data*, *European Physical Journal C* **74** no. 3130, (2014). 50
- [86] ATLAS Collaboration, *Properties of Jets and Inputs to Jet Reconstruction and Calibration with the ATLAS Detector Using Proton-Proton Collisions at $\sqrt{s} = 7$ TeV*,
<http://cds.cern.ch/record/1281310/files/ATLAS-CONF-2010-053.pdf>. 50
- [87] W. Lampl et al., *Calorimeter Clustering Algorithms:Description and Performance*, Tech. Rep. ATL-LARG-PUB-2008-002.ATL-COM-LARG-2008-003 (2008). 50
- [88] M. Cacciari, G. Salam, and G. Soyez, *The anti-kt jet clustering algorithm*, *JHEP* **4** (2008). 51

- [89] ATLAS Collaboration, *Jet energy measurement and its systematic uncertainty in proton–proton collisions at $s = 7$ TeV*, <http://arxiv.org/abs/1406.0076>. 51
- [90] ATLAS Collaboration, *Determination of the tau energy scale and the associated systematic uncertainty in proton-proton collisions at $\sqrt{s} = 7$ TeV with the ATLAS detector at the LHC in 2011*, Tech. Rep. ATLAS-CONF-2013-044 (2013). 52
- [91] ATLAS Collaboration, *Performance of the Reconstruction and Identification of Hadronic Tau Decays in ATLAS with 2011 Data*, Tech. Rep. ATLAS-CONF-2012-142 (2012). 52
- [92] ATLAS Collaboration, *Performance of the Reconstruction and Identification of Hadronic Tau Decays with ATLAS*, Tech. Rep. ATLAS-CONF-2011-152 (2011). 52
- [93] ATLAS Collaboration, *Performance of the Reconstruction and Identification of Hadronic Tau Decays in ATLAS with 2011 Data*, Tech. Rep. ATLAS-CONF-2012-142 (2012). 52, 58
- [94] ATLAS Collaboration. <https://twiki.cern.ch/twiki/bin/view/AtlasPublic/TauPublicCollisionPlots>. 52
- [95] ATLAS Collaboration, *Performance of missing transverse momentum reconstruction in proton-proton collisions at $\sqrt{s} = 7$ TeV with ATLAS*, *Eur. Phys. Journal C* **72** no. 1844, (2012). 53
- [96] ATLAS Collaboration, *Search for supersymmetry in events with four or more leptons in $s = 7$ TeV pp collisions with the ATLAS detector*, *JHEP* (2012). 59, 137
- [97] ATLAS Collaboration, *Search for supersymmetry in events with four or more leptons in 21fb1 of pp collisions at $s = 8$ TeV with the ATLAS detector*, ATLAS-CONF-2013-036 (2013). <https://cds.cern.ch/record/1532429>. 59, 162
- [98] P. Meade, N. Seiberg, and D. Shih, *General Gauge Mediation*, *Prog.Theor.Phys.Suppl.* **177** (2009) 143–158, [arXiv:0801.3278](https://arxiv.org/abs/0801.3278). 64
- [99] G. Giudice and R. Rattazzi, *Theories with gauge mediated supersymmetry breaking*, *Phys.Rept.* **322** (1999) 419–499, [arXiv:hep-ph/9801271](https://arxiv.org/abs/hep-ph/9801271) [hep-ph]. 64
- [100] J. Alwall et al., *MadGraph 5 : Going Beyond*, *JHEP* **1106** no. 128, (2011). 65, 69, 112, 163

- [101] M. Bahr et al., *Herwig++ Physics and Manual*, *Eur. Phys. J.* **C58** (2008) 639–707. 65
- [102] P. M. Nadolsky et al., *Implications of CTEQ global analysis for collider observables*, *Phys. Rev.* **D78** no. 013004, (2008). 65, 108
- [103] W. Beenakker et al., *Squark and gluino production at hadron colliders*, *Nucl. Phys.* **B492** (1997) 51–103. 66, 111, 163, 165
- [104] P. Nason, *A New method for combining NLO QCD with shower Monte Carlo algorithms*, *JHEP* **0411** no. 040, (2004). 69
- [105] T. Sjostrand et al., *A Brief Introduction to PYTHIA 8.1*, *Comput. Phys. Commun.* **178** (2008) 852–867. 69
- [106] G. P. N. Kauer, *Inadequacy of zero-width approximation for a light Higgs boson signal*, *JHEP* **1208** no. 116, (2012). 69
- [107] B. W. S. Frixione, *Matching NLO QCD computations and parton shower simulations*, *JHEP* **0206** no. 029, (2002). 69
- [108] M. L. Mangano et al., *ALPGEN, a generator for hard multiparton processes in hadronic collisions*, *JHEP* **0307** no. 001, (2003). 69
- [109] B. P. Kersevan and E. Richter-Was, *The Monte Carlo event generator AcerMC versions 2.0 to 3.8 with interfaces to PYTHIA 6.4, HERWIG 6.5 and ARIADNE 4.1*, *Comp. Phys. Comms.* **184** (2013) 919–985. 69
- [110] *Computational Geometry: Algorithms and Applications*. Springer-Verlag, 3 ed., 2008. 88
- [111] G. Cowan, *Statistical Data Analysis*. Clarendon Press, 1998. 89, 132, 133
- [112] J. Campbell and R. Ellis, *$ttW+$ production and decay at NLO*, *JHEP* **1207** (2012). 107
- [113] A. Kardos, Z. Trocsanyi, and C. Papadopoulos, *Top quark pair production in association with a Z-boson at next-to-leading-order accuracy*, *Phys. Rev. D* **85** (2012). 107
- [114] J. Butterworth et al., *Single Boson and Diboson Production Cross Sections in pp Collisions at $s=7$ TeV*, Tech. Rep. ATL-COM-PHYS-2010-695 (2010). 107

- [115] S. Dittmaier et al., *Handbook of LHC Higgs Cross Sections: 2. Differential Distributions*, CERN-2012-002 (2012). 107
- [116] ATLAS Collaboration, *Performance assumptions for an upgraded ATLAS detector at a High-Luminosity LHC*, Tech. Rep. ATL-PHYS-PUB-2013-004 (2013). <https://cds.cern.ch/record/1527529>. 107
- [117] http://www.hep.ucl.ac.uk/pdf4lh/PDF4LHC_practical_guide.pdf. 108
- [118] S. Alekhin et al., *The PDF4LHC Working Group Interim Report*, [arXiv:1101.0536](https://arxiv.org/abs/1101.0536). 108
- [119] ATLAS Collaboration, *Electron performance measurements with the ATLAS detector using the 2010 LHC proton-proton collision data*, *Eur. Phys. J.* **C72** (2012). 108
- [120] ATLAS Collaboration, *Measurement of the muon reconstruction performance of the ATLAS detector using 2011 and 2012 LHC proton-proton collision data*, *Eur. Phys. J.* **C74** (2014). 109
- [121] ATLAS Collaboration, *Determination of the tau energy scale and the associated systematic uncertainty in proton-proton collisions at $s=8\text{TeV}$ with the ATLAS detector at the LHC in 2012*, Tech. Rep. ATLAS-CONF-2013-044 (2013). <https://cdsweb.cern.ch/record/1544036>. 109
- [122] ATLAS Collaboration, *Identification of the Hadronic Decays of Tau Leptons in 2012 Data with the ATLAS Detector*, Tech. Rep. ATLAS-CONF-2013-064 (2013). <https://cds.cern.ch/record/1562839>. 109
- [123] ATLAS Collaboration, *Jet energy scale and its systematic uncertainty in proton-proton collisions at $\sqrt{s}=7\text{ TeV}$ with ATLAS 2011 data*, Tech. Rep. ATLAS-CONF-2013-004 (2013). <https://cds.cern.ch/record/1509552?ln=en>. 109
- [124] ATLAS Collaboration, *Jet energy resolution and selection efficiency relative to track jets from in-situ techniques with the ATLAS Detector Using Proton-Proton Collisions at a Center of Mass Energy $s = 7\text{ TeV}$* , Tech. Rep. ATLAS-CONF-2010-054 (2010). <https://inspirehep.net/record/1204034?ln=en>. 109

- [125] ATLAS Collaboration, *Improved luminosity determination in pp collisions at $s=7$ TeV using the ATLAS detector at the LHC*, *Eur.Phys.J.* **C73** no. 8, (2013) 2518, [arXiv:1302.4393 \[hep-ex\]](#). 110
- [126] M. Kramer et al., *Supersymmetry production cross sections in pp collisions at $\sqrt{s} = 7$ TeV*, Tech. Rep. CERN-PH-TH-2012-163 (2012), [arXiv:1206.2892](#). 111
- [127] D. Lopez Mateos and E. W. Hughes, *Measurement of multi-jet production cross section at a center-of-mass energy of 7 TeV at the large hadron collider with the ATLAS detector*,. <https://cds.cern.ch/record/1363353/export/hx?ln=en>. 112
- [128] A. L. Read, *Presentation of search results: the CLs technique*, *JPhys G: Nucl. and Part. Phys.* **28** (2002). 131
- [129] CMS Collaboration, *Search for anomalous production of multilepton events in pp collisions at $s = 7$ TeV*, *Journal of High Energy Physics* **2012** no. 6, (2012). 137
- [130] DELPHI Collaboration, *Searches for supersymmetric particles in $e+e$ collisions up to 208 GeV and interpretation of the results within the MSSM*, *Eur. Phys. J.* (2003) 421, [arXiv:hep-ex/0311019](#). 138
- [131] OPAL Collaboration, *Search for Chargino and Neutralino Production at $\sqrt{s} = 192$ -209 GeV at LEP*, *Eur. Phys. J.* **C35** (2004) 1, [arXiv:hep-ex/0401026](#). 138
- [132] ALEPH Collaboration, *Search for charginos nearly mass degenerate with the lightest neutralino in $e+e$ - collisions at centre-of-mass energies up to 209GeV*, *Phys. Lett.* **533B** (2002) 223, [arXiv:hep-ex/0203020](#). 138
- [133] L3 Collaboration, *Search for Charginos and Neutralinos in $e+e$ - collisions at $s = 189$ Gev*, *Phys. Lett.* **472B** (2000) 420, [arXiv:hep-ex/9910007](#). 138
- [134] ATLAS Collaboration, *Search for supersymmetry in events containing a same-flavour opposite-sign dilepton pair, jets, and large missing transverse momentum in $s=8$ TeV pp collisions with the ATLAS detector*, [arXiv:1503.03290 \[hep-ex\]](#). 138, 148
- [135] ATLAS Collaboration, *Search for direct production of charginos and neutralinos in events with three leptons and missing transverse momentum in $\sqrt{s} = 8$ TeV pp collisions with the ATLAS detector*, *J. High Energy Phys.* **1404** (2014) 169. 142, 143

- [136] M. Baak, G. Besjes, D. Cote, A. Koutsman, J. Lorenz, et al., *HistFitter software framework for statistical data analysis*, [arXiv:1410.1280 \[hep-ex\]](#). 144
- [137] P. Bernat, *Architecture and Performance of the Inner Detector Trigger of the ATLAS detector*, Tech. Rep. ATL-DAQ-PROC-2012-032, ATL-COM-DAQ-2012-082 (2012). 156
- [138] PESA Core Algorithms Group Collaboration, S. Armstrong, *Algorithms for the ATLAS High Level Trigger*, Tech. Rep. ATL-DAQ-2003-002, ATL-COM-DAQ-2003-013, CERN-ATL-DAQ-2003-002 (2003). 156